McMaster University

Doctoral Thesis

Biophysics of Blood Membranes

Author:
Sebastian Himbert, M.Sc., B.Sc.

Supervisor:
Dr. Maikel Rheinstädter

A Thesis
Submitted to the School of Graduate Studies
in Partial Fulfillment of the Requirements
for the Degree of Doctor of Philosophy

Doctor of Philosophy (2021) McMaster University
Physics and Astronomy Hamilton, Ontario, Canada

TITLE: Biophysics of Blood Membranes

AUTHOR: Sebastian Himbert, M.Sc., B.Sc.

SUPERVISOR: Dr. Maikel Rheinstädter

NUMBER OF PAGES: xiv, 166

MCMASTER UNIVERSITY

Abstract

Faculty of Sciences
Department of Physics and Astronomy

Doctor of Philosophy

Biophysics of Blood Membranes

by Sebastian Himbert, M.Sc., B.Sc.

Red blood cells (RBCs) are the predominant cell type in blood and have a two-layered outer shell which is composed of a cytoskeleton network tethered to a cytoplasmic membrane. In this thesis, I study the structure and mechanical properties of the RBC's cytoplasmic membrane (RBCcm) on the nanoscale and utilize this knowledge to functionalize this biological structure on a molecular level. In a first case study, I measure the membrane's bending rigidity from thermal fluctuations observed in X-ray diffuse scattering (XDS) and Neutron Spin Echo (NSE) experiments, as well as Molecular Dynamics (MD) simulations. I provide evidence of the RBCcm's highly deformable nature with a bending rigidity that is substantially softer as compared to synthetic membranes. The methods are applied to RBCs that were stored for up to 5 weeks. I demonstrate that storage of RBCs leads to an increased fraction of liquid ordered membrane domains and an increased bending rigidity.

RBCs are ideal for pharmaceutical applications as they provide access to numerous targets in the body, however lack specificity. Functionalizing the cytoplasmic membrane is thus a prerequisite to use these cells in biotechnology. I develop protocols throughout two studies to tune the membrane's lipid and protein composition. I investigate the impact of synthetic lipid molecules on the membrane's structure and demonstrate that small molecules can be encapsulated into liposomes that are formed from these hybrid membranes. Further, I provide direct evidence that the SARS-CoV 2 spike protein can be anchored into the RBCcm through a detergent mediated insertion protocol. These virus-like particles are observed to trigger seroconversion in mouse models, which demonstrates the potential of functionalized RBC in biotechnology.

Acknowledgements

This thesis would not have been possible without the tremendous help and support of a number of people.

Firstly, I would like to express my gratitude to my supervisor and mentor Dr. Maikel Rheinstädter. His contagious enthusiasm, patience, flexibility, and encouragement made it easy to be excited about every project. He shaped me as a person, professionally and personally, throughout the last 5 years and I will always remember his lessons.

A special thanks also goes to all the fantastic group members of Dr. Rheinstädter's laboratory: Rick, Lili, Adree, Matt, Isabella, Kate, Renée, Telmah , Quinn, Udi, Hannah, Alix, and Tetyana, thank you for being amazing colleagues and great friends.

I had the privilege of working and collaborating with outstanding people throughout the PhD program. A special thanks goes to Dr. John Nagle, who has been an incredible help in understanding and finalizing our work on membrane bending. My sincere thanks goes to the group of Dr. Todd Hoare (Michael, Eva, and Madeline), the group of Dr. Guiseppe Melacini (Rashik), the group of Dr. Harald Stöver (Samantha, Sheilan, and Mitchell), the group of Dr. Christian Wagner (Alexander), the group of Dr. Dawn Bowdish (Braeden), Dr. Janos Junhasz, Dr. Syed Quadri, Dr. William Sheffield, and Dr. Angelo D'Alessandro for allowing me to use their instruments, providing samples, and letting me explore science outside of physics.

I would also like to acknowledge the NIST Center for Neutron Research for accepting my proposal and granting me access to their unique facility. Thank you to the Canadian Blood Services and the numerous donors for providing samples for the research in this thesis.

Finally, I would like to acknowledge the support of my family and friends over the years. I couldn't have finished this PhD without them. I would especially like to express my gratitude to my parents Susanne and Stefan, and my sister, Caroline. Thank you for supporting me in good and tough times throughout my life and helping me to become the person I am today.

This brings me to my partner, Elaine. We only met during the PhD program, but she has become a truly important part in my life. Thank you for all the adventures and for bringing the fun and joy into my life.

Glossary

q_1	q_z position of the first order lamellar peak.
B	Membrane interaction modulus
$\tilde{\mathbf{B}}$	Magnetic filed
CBS	Canadian Blood Services
CPD-SAGM	Citrate Phosphate Dextrose and Saline-Adenine-Glucose-Mannitol buffer. 100 ml contain 0.33 g citric acid, 2.63 g sodium citrate, 0.25g sodium dihydrogen phosphate, 3.4 g dextrose, 0.88 g sodium chloride, 0.02 g adenine and 0.53 g Mannitol
CPU	Central Processing Unit in a computer
CUDA	Compute Unified Device Architecture
d	Lamellar repeat distance
D	Length of the primary coils in a NSE Instrument
Erythro-VLPs	Erythrocyte based Virus-Like Particles
η_c	Caillé Parameter
$F(q_z)$	Form factor
ghosts	Empty RBC that consists of the RBCcm and remains of the spectrin cytoskeleton
GPU	Graphics Processing Unit in a computer

h	Distance of the neutral surface relative to the bilayer mid-plane
h_C	Height of the hydrocarbon tails in one monolayer
hematocrit	RBC fraction that separates after the centrifugation from a whole blood sample
$I(\mathbf{Q}, \tau)$	Intermediate scattering function
$J_0(x)$	Zero-order Bessel function
K_A	Area compressibility modulus
$\mathbf{k}_i$	Wave-vector of the incident wave
$\mathbf{k_f}$	Wave-vector of the scattered wave
κ	Bending modulus
$\tilde{\kappa}$	Dynamic modulus measured in an NSE experiment when using the ZG-Theory
k_B	Boltzmann constant
L	Sample-detector distance
$\overline{L_z}$	Average out-of-plane patch size of coherently scattering membrane patches
$\overline{L_r}$	Average in-plane patch size of coherently scattering membrane patches
λ	Wavelength of a wave; $\lambda = 1.5481$ Å in the case of X-ray photons (Cu-α anode); $\lambda = \lambda_{DB} = \frac{h}{m_n \lvert\mathbf{v}\rvert}$ in the case of neutrons with mass m_n and velocity $\lvert\mathbf{v}\rvert$
lysis buffer	Buffer consisting of 3 Vol% PBS in ultra pure water (resistivity 18.2 MΩ·cm)
MD	Molecular Dynamics
N	Number of bilayers in a stack
$\overline{N}$	Number of Lamor precessions in NSE experiment

netCAD	Network Center for Applied Development from the Canadian Blood Services
NSE	Neutron Spin Echo
PA	Phosphatidic Acid
PBS	Phosphate Buffer Saline containing sodium cloride (137 mM), potassium cloride (2.7 mM), sodium phosphate (10 mM) and potassium phosphate (1.8 mM)
PC	Phosphatidylcholine
PE	Phosphatidylethanolamine
PG	Phosphatidylglycerol
PI	Phosphatidylinositol
PL	Glycerophospholipid
PS	Phosphatidylserine
Ψ	Real space azimuth coordinate
$\langle P_z \rangle$	Polarization of the scattered neutron beam in an NSE experiment
$\mathbf{q}$	Scattering vector
$\mathbf{Q}$	Wavevector of the thermal membrane fluctuations
$q_{\|\|}$	Radial component of the scattering vector $\mathbf{q}$
q_Ψ	Azimuth component of the scattering vector $\mathbf{q}$
$\mathbf{q}_r$	In-plane component of the scattering vector $\mathbf{q}$
q_z	Out-of-plane component of the scattering vector $\mathbf{q}$
$\mathbf{r}$	Real space coordinate parallel to the membrane surface; $\mathbf{r} = (x, y) = (r\cos(\Psi), r\sin(\Psi))$

r	Real space radial coordinate
RBC	Red blood cell, also referred to as erythrocyte
RBCcm	Red blood cell's cytoplasmic membrane
RH	Relative Humidity
$\rho_m^{flat}(z)$	Scattering length density of a flat, static membrane
$S(\mathbf{q})$	Structure factor
σ_r	Variance of the in-plane patch size of coherently scattering membrane patches
σ_z	Variance of the of-of-plane patch size of coherently scattering membrane patches
SARS-CoV-2	Severe Acute Respiratory Syndrome Coronavirus 2
SM	Sphingomylin
S-Protein	SARS-CoV-2 spike Protein
τ	Fourier time
T	Temperature
θ	Meridional scattering angle
$\delta u_n(r)$	Height-height pair correlation function of a fluctuating bilayer
$u(\mathbf{r})$	Local spatial deviations of the bilayer center in the out-of-plane direction
$\mathbf{v}$	Velocity (of Neutrons)
w_x	Distance of a pixel on the 2-dimensional detector from to position of the direct, *i.e.* unscattered, beam
χ^2	Chi-square function in the described least square fitting routine

XDS	X-ray Diffuse Scattering
ξ	Caillé parameter
Ξ	Azimuth scattering angle
XRD	X-ray Diffraction
z	Real space coordinate axis; orthogonal to the membrane surface
ZG-Theory	Theory of membrane fluctuations and prediction of the intermediate scattering function by Anton Zilman and Rony Granek

Contents

Chapter 1

Preface

Blood is an essential transport mechanism and has a pivotal role in human metabolism. This fluid is composed of non-cellular blood plasma and a cellular fraction, of which red blood cells (RBCs) represent the predominant cell type. These unique cells deliver oxygen and are characterized by a simple structure with no internal organelles. They have a two-layered shell that is composed of a cytoskeleton tethered to a cytoplasmic membrane.

This thesis is divided in two parts. First, I study, at the nanoscale, the structure and mechanical properties of the RBC's cytoplasmic membrane (RBCcm). Second, I use the insight gained from the first section to functionalize this biological structure on a molecular level.

RBCs are forced to undergo numerous deformations when passing through the vascular system. This sets stringent demands on the mechanical properties of the cell's shell. The RBCcm is expected to dominate the elastic behavior on nanometer length scales [1], which is most relevant for cellular processes that take place between the fibrils of the cytoskeleton. Studying mechanical properties of biological cell membranes on this length scale is challenging. In the first half of this thesis, I measure the RBCcm's structure in X-ray diffraction (XRD) experiments and determine its bending rigidity from thermal fluctuations in X-ray Diffuse Scattering (XDS) and Neutron Spin Echo (NSE) experiments, as well as Molecular Dynamics (MD) simulations. I develop protocols to extract the RBCcm from RBC and prepare them in a suitable manner for both experimental techniques: as solid supported stack (XDS) and as nanometer-sized liposomes (NSE). I further implement a parallelized computer program to analyze signals measured in XDS experiments. Models for MD simulations are developed to match the experimentally probed lipid composition of the membrane. These methods are applied to membranes that are extracted from freshly collected RBCs as well as from cells that are stored for up to 5 weeks. I demonstrate that the RBCcm is a highly

deformable structure with a bending rigidity that is substantially softer than synthetic membrane analogues.

The second half of this thesis focuses on the synthesis of functionalized RBCcms. RBCs can reach nearly any part of the human body as they pass through the vascular system. This makes them ideal carriers for pharmaceuticals, as they provide direct access to numerous targets. However, the apparent advantage of these endogenous cells is often limited due to their of lack of specificity. This can be overcome by functionalizing the cell's membrane. Of course, a good understanding of the RBCcm's structure on nanometer length scale is an essential prerequisite to altering its composition on the molecular level. I demonstrate that the membrane can be modified with synthetic lipid molecules to adjust membrane thickness, order, and charge. Furthermore, I anchor the spike protein (S-Protein) of the SARS-CoV-2 (severe acute respiratory syndrome coronavirus 2) into the RBCcm to synthesize virus-like particles that lead to seroconversion in mouse models.

1.1 Thesis Overview

This thesis is written such that scientists who are not necessarily experts in this field can understand and appreciate the achievements of my PhD work. It has a sandwich structure, where I first introduce the underlying concepts before presenting four major first-author publications in my portfolio. A list of all of my scientific contributions can be found in Sec. 1.2.

Chapter 2 presents the relevant scientific background to the reader. RBCs as an integral part of blood are introduced, and the structure of their outer shell is described with a special emphasis on the lipid composition of the cells' cytoplasmic membrane. Further, membrane deformations in the form of compression and bending of membranes are discussed, and effects of the membrane's composition on its deformability are reviewed. The underlying theory of XRD and XDS experiments on solid supported membranes is introduced, together with the most important concepts of NSE and MD simulations.

Chapter 3 presents an overview of the sample preparation methods and analysis tools. The isolation of the RBC membrane is described, together with its preparation as a solid supported membrane stack and nanometer-sized liposome. It follows a walk-through of how the membrane composition can be tuned with respect to lipid and protein content. A central achievement in this thesis is the measurement of the RBC membrane's bending modulus from XDS experiments

and the development of a Graphics Processing Unit (GPU) accelerated analysis program. The measurement procedures on the in-house X-ray diffractometer are described, followed by an illustration of the implemented algorithm. Finally, I explain how neutron spin echo experiments were performed and how computer models for molecular dynamic simulations were developed.

Chapters 4-7 then focus on the scientific findings of this thesis, which can be broadly divided in two parts. The first two publications study the structure and mechanical properties of the RBCcm membrane, while the later two publications focus the functionalization of this biological structure and their uses in biotechnology.

Paper I measures the bending modulus of the RBCcm with a combination of XDS, NSE, and MD simulations. Paper II applies the developed methods to membranes that were extracted from stored RBCs. Paper III demonstrate that the RBCcm can be doped with synthetic lipid molecules and form a homogeneous hybrid structure on the nanoscale. This sets the base for Paper IV, where virus-like particles were synthesized by anchoring the SARS-CoV-2 spike protein into the RBCcm. These so-called Erythro-VLPs were observed to trigger seroconversion in mouse models.

1.2 Scientific Contributions

1.2.1 First Author Publications

7. S. Himbert, A. D'Alessandro, S. M. Qadri, M. J. Majcher, T. Hoare, W. P. Sheffield, M. Nagao, J. F. Nagle, and M. C. Rheinstädter The Bending Rigidity of Red Blood Cell Membranes, *in preparation*

6. S. Himbert, S. M. Qadri, P. Schubert, W. P. Sheffield, A. D'Alessandro, and M. C. Rheinstädter. Storage of red blood cells leads to an increased membrane order and bending rigidity, *submitted*

5. S. Himbert, I. Passos Gastaldo, R. Ahmed, S. Ros, J. Juhasz, B. Cowbrough, H. D. H. Stöver, G. Melacini, D. M. E. Bowdish, and M. C. Rheinstädter. Erythro-VLPs: Embedding SARS-CoV-2 spike proteins in red blood cell based proteoliposomes leads to pronounced antibody response in mouse models, *submitted*

4. S. Himbert, L. Zhang, R. J. Alsop, V. Cristiglio, G. Fragneto, and M. C. Rheinstadter. Anesthetics significantly increase the amount of intramembrane water in lipid membranes, Soft Matter, 2020, DOI:10.1039/D0SM01271H

3. S. Himbert, M. J. Blacker, A. Kihm, Q. Pauli, A. Khondker, K. Yang, S. Sinjari, M. Johnson, J. Juhasz, C. Wagner, H. D. H. Stover, M. C. Rheinstädter, Hybrid erythrocyte liposomes: functionalized red blood cell membranes for molecule encapsulation, Advanced Biosystems, 1900185.

2. S. Himbert, R. J. Alsop, M. Rose, L. Hertz, A. Dhaliwal, J. M. Moran-Mirabal, C. P. Verschoor, D. M. E. Bowdish, L. Kaestner, C. Wagner, and M. C. Rheinstädter, The Molecular Structure of Human Red Blood Cell Membranes from Highly Oriented, Solid Supported Multi-Lamellar Membranes, Scientific Reports 7 (39661), (2017)

1. S. Himbert, M. Chapman, D. W. Deamer, and M. C. Rheinstädter, Organization of Nucleotides in Different Environments and the Formation of Pre-Polymers, Scientific Reports 6 (31285), (2016)

1.2.2 Other Publications

12. M. Majcher, **S. Himbert**, F. Vito, G. V. Jensen, M. C. Rheinstädter, N. Smeets, and T. Hoare, Investigating the Kinetics and Structure of Network Formation in Charged UV-Photopolymerizable Starch Nanoparticle (SNP) Network Hydrogels via Very Small Angle Neutron Scattering (vSANS) and Dynamic Hybrid Rheology, *in preparation*

11. H. Krivić, **S. Himbert**, R. Sun and M. C. Rheinstädter, Erythro-PmBs: A Highly Selective Polymyxin B Delivery System Using Antibody-Conjugated Hybrid Erythrocyte Liposomes, *submitted*

10. E. Mueller, **S. Himbert**, M. J. Simpson, M. Bleuel, M. Rheinstädter, T. Hoare. Cationic, Anionic, and Amphoteric Dual pH/Temperature-Responsive Degradable Microgels via Self-Assembly of Functionalized Oligomeric Precursor Polymers. Macromolecules, 54, 1, 351–363 (2021)

9. R. Bider, T. Lluka, **S. Himbert**, A. Khondker, S. Qadri, W. P. Sheffeld and M. Rheinstadter, Stabilization of lipid membranes through partitioning of the blood bag plasticizer 2 di-2 ethylhexyl phthalate (DEHP)", Langmuir, 36(40), 11899-11907 (2020)

8. I. Passos-Gastaldo, **S. Himbert**, U. Ram, M. Rheinstädter The Effects of Resveratrol, Caffeine, β-Carotene, and Epigallocatechin Gallate (EGCG) on Amyloid-β Aggregation in Synthetic Brain Membranes. Molecular Nutritious Food Research, 2000632 (2020)

7. M. J. Majcher, C. L. McInnis, D. Kinio, R. J. Alsop, **S. Himbert**, M. C. Rheinstädter, N.M.B. Smeets, T. Hoare, Photopolymerized-Polymerizable Starch Nanoparticle (SNP) Network Hydrogels, Carbohydrate Polymers, 236, 115998.

6. J D. Nickels, M. D. Smith, R. J. Alsop, **S. Himbert**, A. Yahya, D. Cordner, P. Zolnierczuk, C. Stanley, J. Katsaras, X. Cheng, M. C. Rheinstädter, Lipid Rafts: Buffers of Cell Membrane Physical Properties, J. Phys. Chem. B, 123 (9), pp 2050-2056 (2019)

5. A. Khondker R. J. Alsop, **S. Himbert**, J. Tang, A.-C. Shi, A. P. Hitchcock, and M. C. Rheinstädter, Membrane-Modulating Drugs Impact on Cross-β Sheet Aggregates of Amyloid25-35 Peptides in Anionic Unsaturated Lipid Membranes, Scientific Reports 8:12367 (2018)

4. R. J. Alsop, **S. Himbert**, K. Schmalzl, and M. C. Rheinstädter, Aspirin Locally Disrupts the Liquid Ordered Phase, Royal Society Open Science, 5(2), 171710 (2018)

3. S. Himbert The Molecular Structure of Human Red Blood Cell Membranes from Highly Oriented, Solid Supported Multi-Lamellar Membranes, Master Thesis, Saarland University, Saarbrücken, Germany
https://macsphere.mcmaster.ca/handle/11375/21637

2. S. Quint, A. F. Christ, A. Guckenberger, **S. Himbert**, L. Kaestner, S. Gekle, and C. Wagner. 3D tomography of cells in micro-channels. Applied Physics Letters, 111(10), 103701 (2017)

1. U. Gill, T. Sutherland, **S. Himbert**, Y. Zhu, M. C. Rheinstädter, E. D. Cranston, and J. M. Moran-Mirabal. Beyond buckling: humidity-independent measurement of the mechanical properties of green nanobiocomposite films. Nanoscale, 9(23), 7781-7790 (2017)

1.2.3 Patents

3. M. C. Rheinstädter, **S. Himbert**, I. Passos-Gastaldo, "Biological Membranes with Embedded Proteins and Methods of Making and Uses Thereof", U.S. Provisional Pat. Ser. No. 63/201,115 , filed April 13, 2021

2. M. C. Rheinstädter, **S. Himbert**, M. J. Blacker, "Hybrid Biological Membranes, Methods of Making and uses Thereof", U.S. Provisional Pat. Ser. No. 62/951,586, filed December 20, 2019

1. M. C. Rheinstädter, **S. Himbert**, R. J. Alsop, J. M. Moran-Mirabal, S. Saem, D. M. E. Bowdish, Biological Membrane-Based Sensor, U.S. Pat. Ser. No. 62/413,652, filed December 13, 2018

1.2.4 Contributed Talks

22. S. Himbert, M. C. Rheinstädter; *The Nanoscopic Bending Rigidity of Red Blood Cell Membranes*; Invited talk at the CINS Seminar (July 29, 2021), Virtual, (July 29, 2021)

21. S. Himbert, M. C. Rheinstädter; *The Nanoscopic Bending Rigidity of Red Blood Cell Membranes*; CAP Meeting 2021 (June 06 – June 11, 2021), Virtual, (June 09, 2021)

20. S. Himbert, M. C. Rheinstädter; *Erythro-VLPs: Embedding SARS-CoV-2 Spike Proteins in Red Blood Cell Based Proteoliposomes*; CAP Meeting 2021 (June 06 – June 11, 2021), Virtual, (June 08, 2021)

19. S. Himbert, M. C. Rheinstädter; *Erythro-VLPs: Embedding SARS-CoV-2 Spike Proteins in Red Blood Cell Based Proteoliposomes*; BSC Meeting 2021 (May 25 – May 28, 2021), Halifax/Virtual, Canada, (May 25, 2021)

18. S. Himbert, M. C. Rheinstädter; *Erythro-VLPs: Embedding SARS-CoV-2 Spike Proteins in Red Blood Cell Based Proteoliposomes*; ACS Spring Meeting 2021 (April 05 – April 16, 2021), Virtual, (April 14, 2021)

17. S. Himbert, M. C. Rheinstädter; *The Nanoscopic Bending Rigidity of Red Blood Cell Membranes*; ACS Spring Meeting 2021 (April 05 – April 16, 2021), Virtual, (April 14, 2021)

16. S. Himbert, M. C. Rheinstädter; *The Nanoscopic Bending Rigidity of Red Blood Cell Membranes*; 7th European Joint Theoretical /Experimental Meeting on Membranes (April 07 – April 09, 2021), Graz/Virtual, Austria, (April 07, 2021)

15. S. Himbert, M. C. Rheinstädter; *Super-Human Red Blood Cells to Fight Diseases*; European Red Cell Society Meeting in Pavia (September 11, 2020), Italy, (September 11, 2020)

14. S. Himbert, M. C. Rheinstädter; *The Bending Rigidity of Red Blood Cell Membranes Determined from Solid-Supported Multi-lamellar Membranes*; 2019 CINS Meeting in Hamilton, Canada, (October 25 – October 26, 2019) (October 25, 2019)

13. S. Himbert, M. C. Rheinstädter; *The Bending Rigidity of Red Blood Cell Membranes Determined from Solid-Supported Multi-lamellar Membranes*; Annual Meeting of the Canadian Biophysical Society in Toronto, Canada, (May 28rd – May 31, 2019) (May 29, 2019)

12. S.Himbert, M. C. Rheinstädter; *Under the Radar: Bionic Blood Cells to Fight Diseases*; Invited talk at the Pint of Science Festival in Hamilton, Canada, (May 20 May 22, 2019) (May 21st, 2019)

11. S. Himbert, M. C. Rheinstädter; *The Bending Rigidity of Red Blood Cell Membranes Determined from Solid-Supported Multi-lamellar Membranes*; Chemical Biophysics Symposium in Toronto, Canada, (May 03 05, 2019) (May 5, 2019)

10. S. Himbert, M. C. Rheinstädter; *The Molecular Structure of Human Red Blood Cell Membranes from Highly Oriented, Solid Supported Multi-Lamellar Membranes*; Membranes Beyond Conference in Hamilton, Canada, (July 02 – July 04, 2018) (July 02, 2018)

9. S. Himbert, M. C. Rheinstädter; *The Molecular Structure of Human Red Blood Cell Membranes from Highly Oriented, Solid Supported Multi-Lamellar Membranes*; Chemical Biophysics Symposium in Toronto, Canada, (May 04. – May 06, 2018) (May 05, 2018)

8. S. Himbert, C. Wagner and M. C. Rheinstädter; *The Molecular Structure of Human Red Blood Cell Membranes from Highly Oriented, Solid Supported Multi-Lamellar Membranes*; 21st European Red Cell Society Meeting in Heidelberg, Germany, (April 27 - May 1st, 2017) (April 27, 2017)

7. S. Himbert, C. Wagner and M. C. Rheinstädter; *Organization of Nucleotides in Different Environments: Implications for the Formation of First RNA under Prebiotic conditions*; Springmeeting of the DPG (German Physics Association) in Dresden, Germany, (March 19 - March 24, 2017), (April 27 - May 1st, 2017) (March 24, 2017)

6. S. Himbert, C. Wagner and M. C. Rheinstädter; *Red Blood Cell Ghosts for biomedical applications: Blood on a Chip*; Cell Physics Conference in Saarbrücken, Germany, (June 22 - June 24, 2016), (April 27 - May 1st, 2017) (June 24, 2016)

5. S. Himbert, C. Wagner and M. C. Rheinstädter; *Red Blood Cell Ghosts for biomedical applications: Blood on a Chip*; Cell Physics Conference in Saarbrücken, Germany, (June 22 - June 24, 2016), (April 27 - May 1st, 2017) (June 24, 2016)

4. S. Himbert, M. C. Rheinstädter; *Red Blood Cell Ghosts for biomedical applications: Blood on a Chip*; CAP Congress in Ottawa, Ontario, Canada (June 13 - June 17, 2016), (April 27 - May 1st, 2017) (June 15, 2016)

3. S. Himbert, M. C. Rheinstädter; *Organization Of Nucleotides In Different Environments*; CAP Congress in Ottawa, Ontario, Canada (June 13 - June 17, 2016), (April 27 - May 1st, 2017) (June 13, 2016)

2. S. Himbert, M. C. Rheinstädter; *Organization Of Nucleotides In Different Environments*; Chemical Biophysics Symposium in Toronto, Ontario, Canada (May 13 - May 15, 2016), (April 27 - May 1st, 2017) (May 14, 2016)

1. S. Himbert, C. Ruloff and C. Wagner; *Hydrodynamic interactions between two optical trapped Chlamydomonas rheinhardii*; Living Fluids Conference in Marrakesh, Morocco, (October 9 October 11, 2014) (October 10, 2014)

1.2.5 Poster Presentation

4. S. Himbert, M. C. Rheinstädter; *Erythro-VLPs: Embedding SARS-CoV-2 Spike Proteins in Red Blood Cell Based Proteoliposomes*; 7th European Joint Theoretical / Experimental Meeting on Membranes (April 07 – April 09, 2021), Graz/Virtual, Austria, (April 07, 2021)

3. S. Himbert, M. C. Rheinstädter; *The Molecular Structure of Human Red Blood Cell Membranes from Highly Oriented, Solid Supported Multi-Lamellar Membranes*; MIRA and Labarge Research Day (December 12, 2019), Hamilton, Canada, (December 12, 2019)

2. S. Himbert, M. C. Rheinstädter; *The Molecular Structure of Human Red Blood Cell Membranes from Highly Oriented, Solid Supported Multi-Lamellar Membranes*; 2018 BPS Meeting in San Francisco, USA, (February 17 February 21, 2018) (February 19, 2018)

1. S. Himbert, M. C. Rheinstädter; *From Nucleotides to RNA: Searching for the Origins of Life*; Cell Physics Conference in Saarbrücken, Germany, (July 22 - July 24, 2016) (July 23, 2016)

Chapter 2

Introduction

2.1 Red Blood Cells and Their Shell

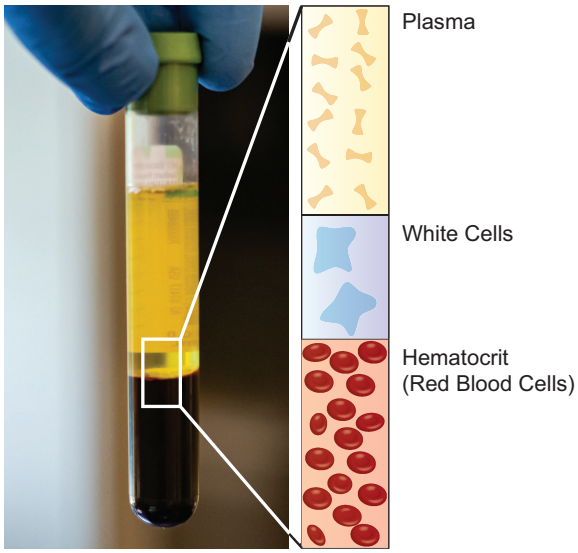

FIGURE 2.1: A whole blood sample can be separated into its components through centrifugation

Red blood cells (RBCs; also referred to as erythrocytes) are the most abundant cell type in the human body [2] and, as the name suggests, are an integral part of blood. Pumped by the heart, blood circulates through the vascular system and supplies cells with oxygen and nutrients. It can be separated into a cellular and non-cellular fraction through centrifugation as seen in Figure 2.1. The non-cellular fraction is commonly known as blood plasma . The cellular fraction is comprised

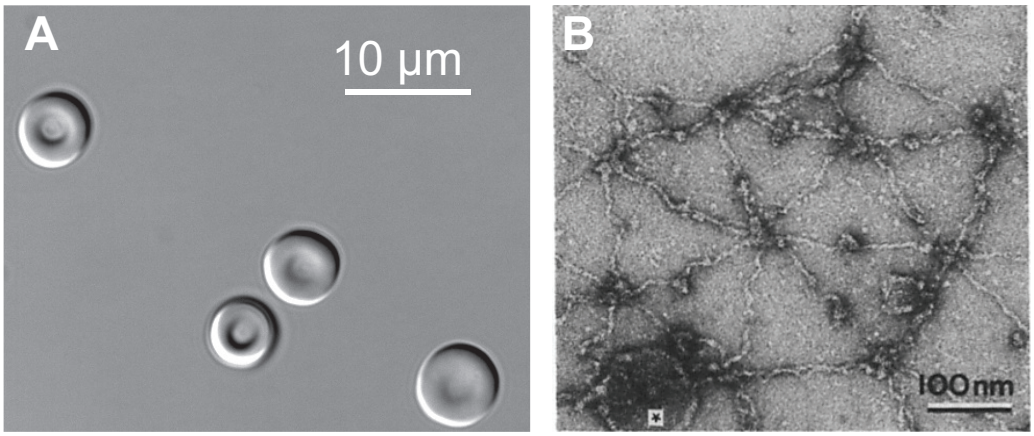

FIGURE 2.2: **A** RBCs under a DIC-Microscope: The cells are characterized by a discocyte shape with a thicker outer rim and an indent in their center. **B** Electron microscopic picture of the RBC's outer shell which is comprised of a cytoskeleton tethered to a cytoplasmic membrane. The image in **B** was taken from [4] with permission from the publisher (see Appendix B)

of white blood cells, platelets and RBCs [3]. The fraction of RBCs per blood volume is often referred to as the hematocrit. RBCs appear under the microscope as round disks with a diameter of $\approx$7 μm and a central indent (Figure 2.2 A). Cells with this shape are commonly referred to as discocytes [5].

The cells' primary purpose is the oxygen transport in the human body. Oxygen diffuses across the cell's outer shell and binds reversibly to the protein hemoglobin [3]. It is not surprising that the cells interior lacks internal structures, such as a nucleus and mitochondria [3], in favor of more volume for this oxygen binding protein . This protein is also responsible for the cell's red color [3].

The outer shell of RBCs consists of two layers: a cytoplasmic membrane (RBCcm) tethered to a spectrin cytoskeleton [4]. This composite structure can be seen in the electron microscope image in Figure 2.2 C: The cytoskeleton forms a triangular filament network parallel to the cytoplasmic membrane. The distance between tethers is $\approx$80 nm [4].

A popular model of the cytoplasmic membrane is the fluid mosaic model [6], which describes this structure as a 2-dimensional fluid-like lipid bilayer with embedded proteins. More than 50 of these membrane proteins have been characterized for the RBCcm [7].

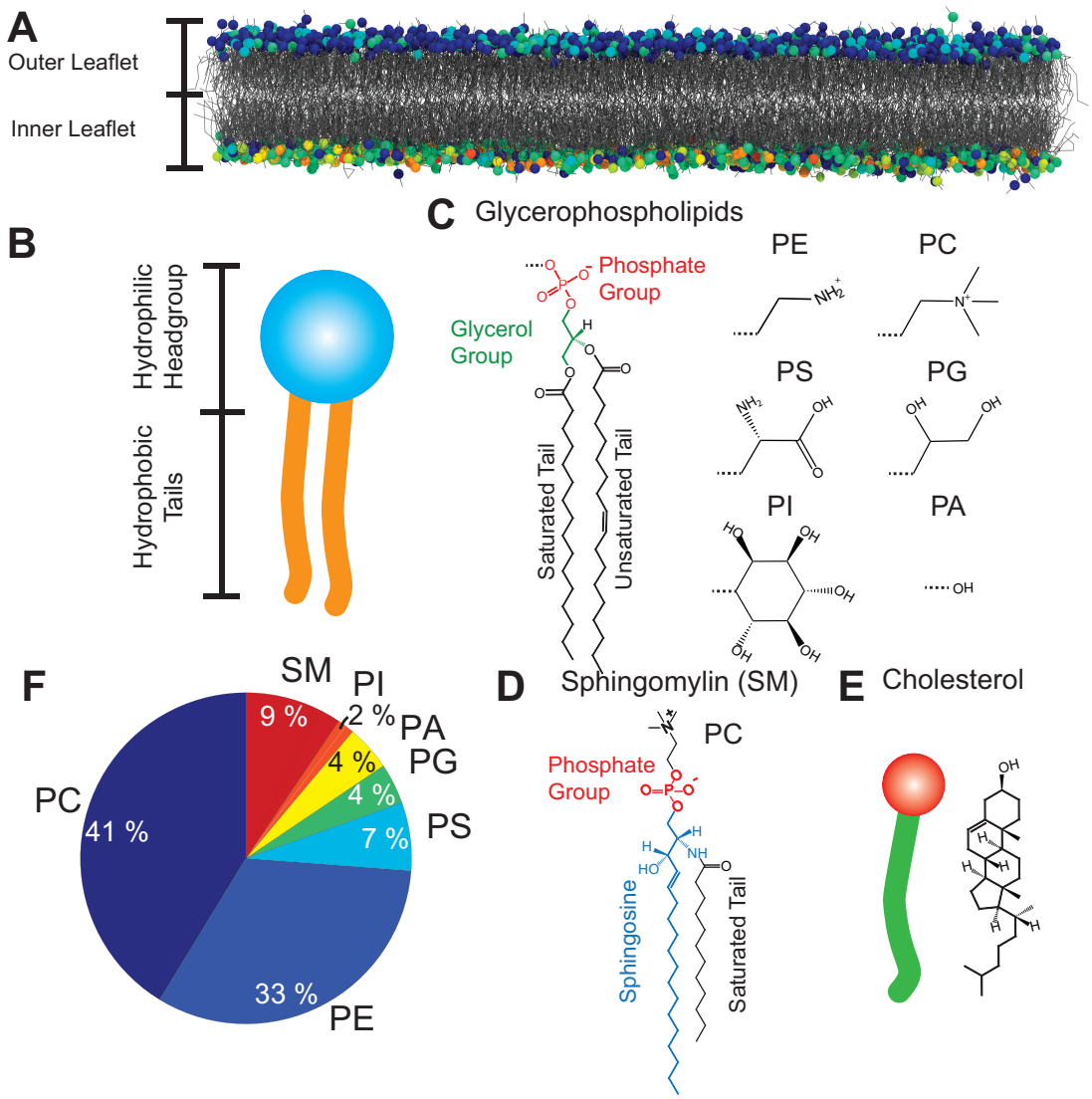

FIGURE 2.3: **A** A lipid membrane is formed by two layers (leaflets) of molecules known as lipids. **B** The structure of glycerophospholipids and sphingomyelin can be divided in a hydrophilic headgroup and two hydrophobic tails. **B-E** Chemical structure of glycerophospholipids, sphingomyelin and cholesterol. Common headgroups are: Phosphatidylcholine (PC), Phosphatidylethanolamine (PE), Phosphatidylserine (PS), Phosphatidylglycerol (PG), Phosphatidic Acid (PA) and Phosphatidylinositol (PI). **F** Lipidomics of an RBC membrane.

The lipid bilayer is a ≈5 nm [8] thick membrane formed by two layers (referred to as leaflets) of molecules known as lipids (Figure 2.3 A). Membrane lipids are amphiphilic, *i.e.*, they have a hydrophilic and a hydrophobic part [9]. The molecules orient themselves such that the hydrophobic parts of both leaflets face towards each other while the hydrophilic part is exposed to the aqueous environment [9]. There is a variety of different lipids in a typical mammalian membrane. Notable examples include glycerophospholipids (PLs), sphingomyelin (SM) and cholesterol.

The molecular structure of PL and SM is characterized by a hydrophilic headgroup and flexible hydrophobic tails, as seen in Figure 2.3 B. PLs are built around a glycerol moiety. Two of the carbon atoms are esterified to two fatty acids chains (tails) with the third carbon atom bound to a polar headgroup (see Figure 2.3 C) [9]. Common headgroups include Phosphatidylcholine (PC), Phosphatidylethanolamine (PE), Phosphatidylserine (PS), Phosphatidylglycerol (PG), Phosphatidic Acid (PA) and Phosphatidylinositol (PI) [9]. The fatty acid tails can vary in length, *i.e.*, the number of carbon atoms per tail and in the degree of saturation, *i.e.*, the number of double bonds between the carbon atoms in the tail [9]. Table A.1 in the Appendix lists a selection of lipid molecules with their respective abbreviations that will be used throughout this thesis. SM is built around sphingosine with an attached fatty acid chain and a PC headgroup (Figure 2.3 D).

Unlike PL and SM, cholesterol is dominated by a rigid structure formed by hydrocarbon rings (Figure 2.3 E). It is highly abundant in cell membranes, with molar ratios between 20 mol% and 50 mol% [10], and aligns itself upright along the bilayer normal.

The lipid composition (also known as lipidomics) of the RBCcm can be determined in mass spectroscopy experiments and was also provided by the group of Dr. Angelo D'Alessandro (Columbia University) for the Molecular Dynamics simulations in this thesis (see Chapter 3). The abundance of PL and SM is graphed in Figure 2.3 F. PC and PE glycerophospholipids are the most abundant molecules in the membrane followed, by SM. PS, PG, PA and PI lipids account for ≈20 % of the membrane. Importantly, these lipids are asymmetrically distributed between the two leaflets [7]. PC and SM lipids are predominantly found in the outer leaflet of the membrane while the majority of PE and PI lipids as well as all PS and PG lipids are located on the inner leaflet [7]. The cholesterol content of RBC has been reported between 30 mol% and 50 mol% [11, 12].

Experiments on model lipid systems that contain saturated, unsaturated PLs and cholesterol (known as raft-forming mixture) [13–15] have shown that membranes containing cholesterol form a patchy structure. Heterogeneities have been

also reported in the RBCcm [16, 17]. The cholesterol molecule is preferably located in areas with saturated lipid tails where it straightens the lipid tails and leads to a reduced area per lipid [18]. These cholesterol-rich patches are referred to as *rafts* which are a manifestation of the liquid ordered (l_o) lipid phase [19]. The surrounding, less ordered, lipid patches are referred to as liquid disordered (l_d) domains [19]. In my Master's thesis, I measured the RBCcm's structure in XRD experiments [8] and demonstrated that the membrane is a patchy structure with nanometer-sized (diameter <3 nm) l_o and l_d lipid domains [8]. In XRD experiments, the scattering signal is measured for several hours and the observed domain structure is thus suggested to be persistent throughout the measurement time. Molecular Dynamics simulations however, suggest that theses domains are the effect of ongoing mixing and de-mixing processes in the membrane [20, 21].

2.2 Bending of Membranes

Many biological processes, such as mobility, cell division and vesicle trafficking, are intrinsically related to a cell membrane's ability to undergo deformation [22–24]. In this section, we will discuss the mathematical foundations to describe membrane bending and compression, and introduce the bending modulus κ and the area compression modulus K_A. We will first focus our discussion on model lipid bilayers before elaborating on the deformation of RBC membranes. In-plane will hereafter refer to the coordinates parallel to the membrane surface (x-y-plane) and the out-of-plane direction is defined as axis perpendicular to the membrane surface (z-axis).

2.2.1 Deforming A Lipid Bilayer

Let us consider two types of deformation of a lipid bilayer: in-plane compression and bending. A simple picture that helps us understanding the deformation of lipid bilayers is depicted in Figure 2.4: Lipid molecules can be thought of as being connected by springs that each undergo compression and stretching when the membrane is deformed [25].

Intuitively, we can understand in-plane compression as the compression of springs between the lipid molecules. Of course, this compression comes with an energy cost. It can be expressed as [25]

$$F_{Compress} = \frac{K_A}{2}\frac{\Delta a^2}{a_0}, \tag{2.1}$$

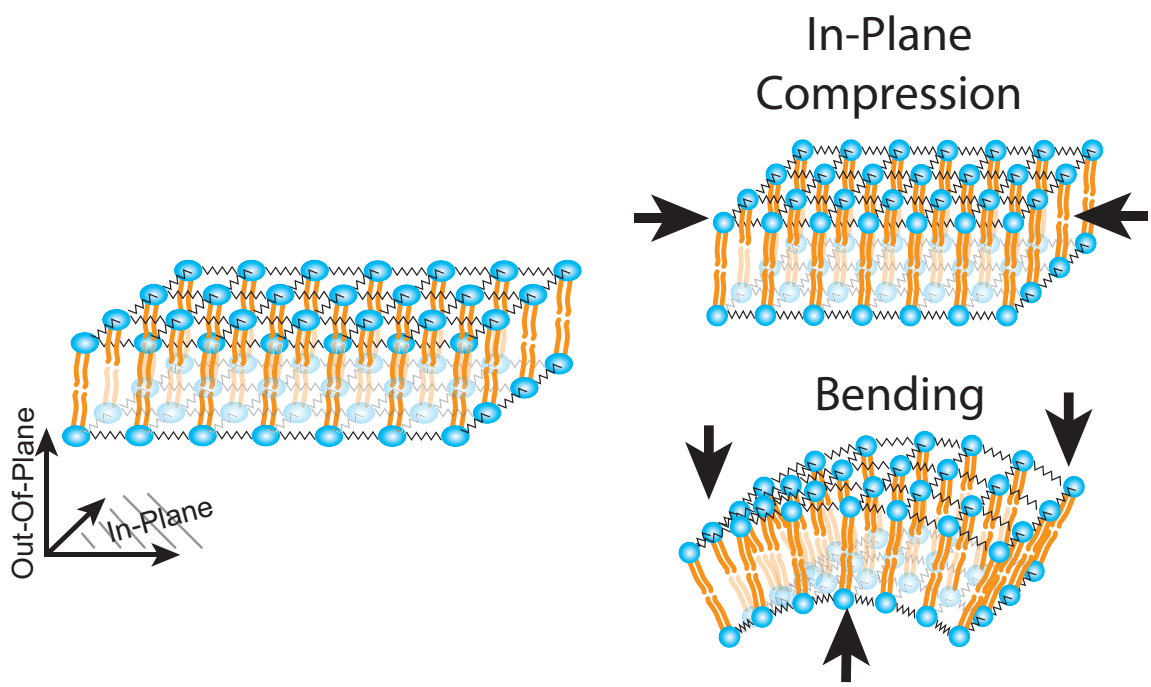

FIGURE 2.4: A lipid bilayer can be pictured as a lattice of lipid molecules connected by springs. The two types of deformation, in-plane compression and bending, can be thus understood as the stretching and compression of these springs.

where Δa refers to the change of the membrane area relative to the uncompressed area a_0. K_A is a material property known as the area compression modulus [25]. $F_{Compress}$ has the unit of an energy and it is consequently clear that K_A is required to have the unit of *force/length*. We can thus understand K_A as a measure of the force needed, per dimension, to compress a lipid bilayer by a certain length.

The in-plane compression deforms both monolayers evenly. This changes when a bilayer is bent from its flat state. Returning to our rudimentary model of springs between lipids, bending requires an uneven stretching and compression of springs along the out-of-plane coordinate. This is illustrated in Figure 2.4, where springs in the lower leaflet are compressed while those in the upper leaflet are stretched. The energy cost resulting from bilayer bending is well accepted to be described by [25]

$$F_{Bend} = \frac{\kappa}{2} \int_A da (\nabla^2 u(x,y))^2, \tag{2.2}$$

where $u(x, y)$ describes local spatial deviations of the bilayer center in the out-of-plane direction, κ is the membrane's bending modulus, and A is the area covered by the membrane. Equation 2.2 is widely referred to as the Helfrich-Canham-Evans functional [25]. κ is an additional material property that measures the amount of energy that is needed to bend a membrane.

Both K_A and κ characterize the membrane's deformability and several experimental methods have been developed to measure these entities. A particularly popular technique is micropipette aspiration (MA), which can be applied to whole cells and artificially formed liposomes. A small bulge is formed by sucking a section of the membrane into a micropipette with an opening of a few micrometers. This deformation is then visually inspected under a microscope and both material properties can be determined from a shape analysis of the formed bulge [26–30].

This approach is taken further by the formation of membrane nanotubes (NT). A nanometer-sized section (diameter $\approx$ 100 nm) of the membrane is pulled out of a liposome with an optical tweezer and κ can be determined from the applied pulling force [30–32]. The membrane's elastic properties can also be measured indirectly from a spectral analysis of flickering of cells under a microscope [33–35], as well as optical interferometric techniques [5, 36].

In addition, techniques such as XDS [37, 38] and NSE spectrometry [39–41] have become standard methods to determine the membrane's bending modulus from thermal membrane fluctuations but have been limited thus far to artificially formed lipid bilayers [42–44] as they either require a large volume (a typical NSE sample consists of 20 ml with a membrane mass concentration of $\approx$20 mg/ml) or well organized solid supported membrane stacks (XDS). It is important to note that the measured values can vary when comparing different experimental methods. For instance, the bending modulus for DMPC has been reported over a range between κ=7-30 k_BT (Table 3.4 in [45]).

The area compression modulus of synthetically assembled membranes ranges between 230 and 290 mN/m and was found to vary little with respect to tail saturation and tail length [25, 46]. In contrast, the bending modulus κ is reported to vary significantly with both lipid characteristics. Rawicz *et al.* [46] showed that single component lipid bilayers becomes stiffer with increasing tail length in saturated and mono unsaturated tails, from $\approx$12 k_BT for diC 13:0 PC to $\approx$30 k_BT for diC 22:1 PC. No significant difference was observed for molecules with a single monounsaturated tail (SOPC) as compared to molecules with two unsaturated tails (DOPC) [46].

An important question concerns the effect of cholesterol on the membrane's mechanical properties. Table 2.1 lists literature values of κ and K_A for different

Lipid	Method	κ (k_BT)	K_A (mN/m)	References
DMPC				
0 mol% Cholesterol	XDS	13±1‡	-	[47]
30 mol% Cholesterol	XDS	65±7‡	-	
SOPC				
0 mol% Cholesterol	XDS	22±2‡	-	
30 mol% Cholesterol	XDS	33±3‡	-	[48]
50 mol% Cholesterol	XDS	33±3‡	-	
SOPC				
0 mol% Cholesterol	MA	-	290±17*	[49]
50 mol% Cholesterol	MA	-	1130±110*	
DOPC				
0 mol% Cholesterol	XDS	18±2‡	-	
30 mol% Cholesterol	XDS	18±2‡	-	[48]
50 mol% Cholesterol	XDS	18±2‡	-	
DOPC				
0 mol% Cholesterol	NT	26±3*	-	[50]
30 mol% Cholesterol	NT	23±3*	-	
DOPC				
0 mol% Cholesterol	MA	16±2*		[51]
30 mol% Cholesterol	MA	15±4*	-	
DOPC				
30 mol% Cholesterol	NT	20±6‡	-	[52]
DOPC				
0 mol% Cholesterol	MA	-	310±20*	[49]
50 mol% Cholesterol	MA	-	870±20*	
diC 22:1 PC				
0 mol% Cholesterol	XDS	29±3‡	-	[48]
30 mol% Cholesterol	XDS	30±3‡	-	

TABLE 2.1: A summary of values reported for the bending rigidity κ in the literature (* Error represents the standard error of the mean; ‡ Error represents the error estimate from a least square fit and applying the proper error propagation)

lipid-cholesterol mixtures. One may intuitively speculate that cholesterol's rigid nature increases the membrane's rigidity, which can indeed be observed in a fully

saturated lipid bilayer: The addition of cholesterol in DMPC bilayers (30 mol%) led to a 5-fold increase in κ in XDS experiments (see Table 2.1). However, the effect is significantly reduced when there is a single monounsaturated chain (1.5-fold increase in κ in SOPC bilayers) and vanishes when both chains are unsaturated (see table entries for DOPC) and with increasing tail length (see table entry for di22:1 PC). This contrasts with the area compression modulus which increases in the presence of cholesterol in all reported lipid mixtures (see Table. 2.1).

Biological membranes, are often composed of hundreds of different molecule species, which raises the question of how mechanical properties scale in multi-component lipid mixtures. A striking result was published by Brüning *et al.* [53], who reported a low $\kappa = 1.8 \pm 0.3$ k_BT in a DMPC:DOPC mixture (molar ratio 1:1). This is surprising since κ of DMPC and DOPC have been independently reported to be >10 k_BT [46, 48, 53, 54] and the result thus contradicts the intuitive hypothesis of an averaged bending modulus in lipid mixtures. The same change was observed when doping DMPC with lipid 1,2-dioleoyl-3-trimethylammonium-propane (DOTAB) [53].

Several studies have confirmed the trend of a lowered κ in lipid mixtures [55–57], though not consistently [51, 57] and a comprehensive study is still lacking.

2.2.2 Deformation of Red Blood Cell Membranes

The deformability of the RBC's outer shell is of particular interest as these cells are required to undergo various deformations when passing through the vascular system. Strikingly, the cells can pass through constrictions where the aperture is much smaller than the cell's diameter [58].

This extraordinary flexibility is the result of the unique construction of their shell: a 2-dimensional spectrin cytoskeleton tethered to a cytoplasmic membrane. This composite structure of coupled layers leads to a wavelength, *i.e.*, length scale dependent bending modulus [1]. The cells bending stiffness is solely effected by the cytoplasmic membrane at length scales < 400 nm but becomes influenced by the interplay between both layers on cellular levels [1].

This becomes apparent in experiments where values of κ over a wide range between 5 and 230 k_BT have been reported [26, 28, 33–36, 59]. Importantly, when measuring RBC's elasticity on small length scales, values for κ of 5 k_BT have been reported [34, 36]. A summary of experimentally determined values of κ is listed in Table 1 in Paper I [60] (see Chapter 4).

The RBC's bending modulus can be measured through MA [26] which generally analyzes deformations on cellular length-scales or through a spectral analysis

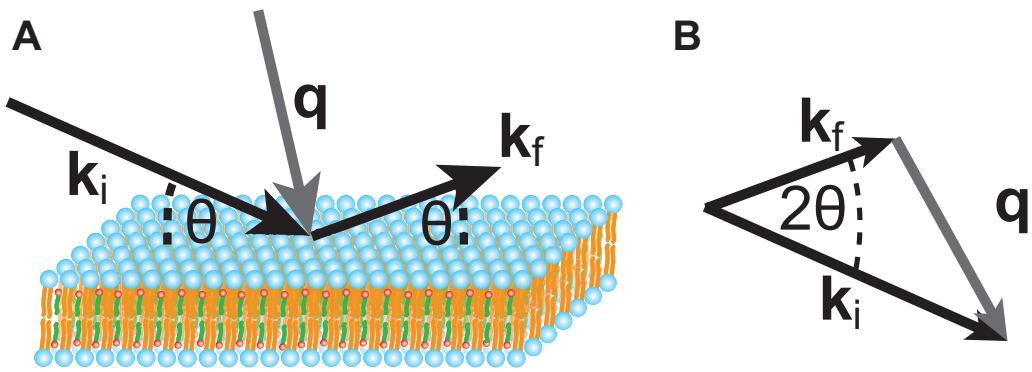

FIGURE 2.5: **A** Diagram illustrating a scattering experiment: A wave with wave vector $\mathbf{k}_i$ is incident on a membrane and a wave with the new wave vector $\mathbf{k_f}$ is scattered. **B** The scattering vector $\mathbf{q}$ is defined as the momentum transfer (see Equation 2.4)

of the cell's membrane fluctuations. The length-scale of this last method is solely limited by the resolution with which membrane fluctuations can be probed. The smallest length scale can be achieved, when measuring out-of-plane membrane fluctuations in XDS and NSE experiments, as it will be discussed in the next section. These techniques have been thus far limited to synthetic lipid bilayer due to experimental challenges, but have been applied for the first time to RBC membranes as part of this thesis [60, 61].

2.3 Basics of Elastic Scattering Techniques

Resolving the structure and dynamics of RBC membranes on molecular length scales is experimentally challenging. Scattering techniques, such as X-ray and neutron scattering, have the advantage of probing membranes in a hydrated environment while allowing high-resolution structural and dynamical analysis.

A typical scattering experiment is sketched in Figure 2.5. A wave (X-ray or neutron) with a wave vector $\mathbf{k}_i$ is incident on a membrane under the angle θ. The wave vector is proportional to the momentum, $\mathbf{p}_i = \hbar\mathbf{k}_i$, and its absolute value is related to the wavelength λ through

$$|\mathbf{k}_i| = |2\pi/\lambda_i| \,. \tag{2.3}$$

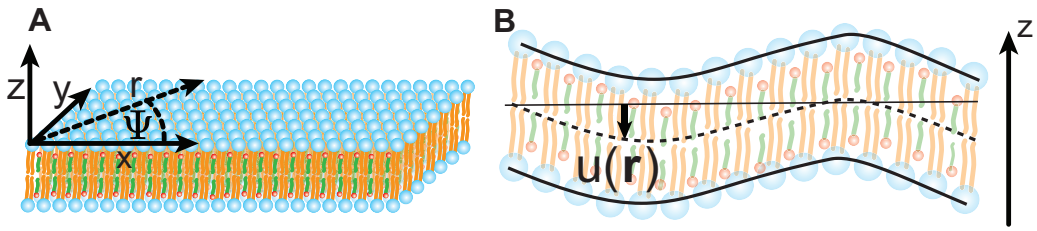

FIGURE 2.6: **A** The membrane shall be oriented such that the z axis is normal to the membrane surface (out-of-plane direction). In-plane coordinates are described by the two dimensional vector $\mathbf{r} = (x, y) = (r\cos(\Psi), r\sin(\Psi))$. **B** Membrane out-of-plane fluctuations are described by local deviations $u(\mathbf{r})$ of the bilayer center in the z-direction.

The energy is given by $E = \frac{hc}{\lambda}$ (for X-ray photons; c is the speed of light) and $E = \frac{h^2}{2m_n\lambda_{DB}^2}$ (for neutrons; $\lambda_{DB} = \frac{h}{m_n|\mathbf{v}|}$ is the de Broglie wavelength, m_n is neutron's mass and $|\mathbf{v}|$ is neutron's velocity). A wave with the new wave vector $\mathbf{k}_f$ is scattered off the membrane and we can define the scattering vector $\mathbf{q}$ as the momentum transfer

$$\mathbf{q} = \mathbf{k}_i - \mathbf{k}_f. \tag{2.4}$$

The geometric relation between the wave vectors and $\mathbf{q}$ is sketched in Figure 2.5 B.

It is best to understand scattering experiments as a measurement of correlations: elastic scattering provides insight into spatial correlations in the sample, *i.e.*, structure; inelastic scattering measures temporal correlations, *i.e.*, dynamics.

This section will focus on elastic scattering where the energy is invariant and $|\mathbf{k}_i| = |\mathbf{k}_f|$. Inelastic scattering will be addressed in Section 2.4.

Molecular structures, such as RBC membranes, consist of numerous atoms, each contributing to the total measured scattered intensity. Let us consider a flat membrane as sketched in Figure 2.6 A (proteins are omitted for clarity). The membrane is aligned such that the z coordinate is normal to the membrane's surface (out-of-plane direction) and any location parallel to the membrane's surface (in-plane direction) is described by the two dimensional vector $\mathbf{r} = (x, y)$. It is convenient to use cylindrical coordinates for the following discussion, *i.e.*, $\mathbf{r} = (r\cos(\Psi), r\sin(\Psi))$.

Let the scattering length density $\rho_m^{flat}(z)$ describe the distribution of scattering centers along the out-of-plane direction in a static, flat membrane. We can further account for out-of-plane fluctuations of the membrane as illustrated in Figure 2.6 B. Such fluctuations can be described by local deviations $u(\mathbf{r})$ of the bilayer center in the z-direction (see Figure 2.6 B). The out-of-plane scattering length density profile of a fluctuating membrane can then be expressed as [62]

$$\rho_m^{fluc}(z) = \rho_m^{flat}(z - u(\mathbf{r})). \tag{2.5}$$

Diffraction experiments in this thesis were performed on stacks of RBCcms and the following discussion will thus focus on this specific geometry as sketched in Figure 2.7. Such a stack can be pictured as N single membranes, each shifted by nd in the z direction, where d is the average lamellar repeat distance, and n can take discrete integer values ($n = 1, 2, ..., N$). We can consequently express the out-of-plane scattering length density [62]

$$\rho(z) = \sum_{n=0}^{N} \rho_m^{flat}(z - u_n(\mathbf{r}) - nd), \tag{2.6}$$

where $u_n(\mathbf{r})$ refers to the local deviations of the center of n-th membrane in the z-direction. Note that each membrane has been assigned an individual $u_n(\mathbf{r})$ and is assumed to fluctuate independently.

Returning to scattering experiments, let us now calculate an expression for the measured intensity. Scattering theory teaches us that each volume element dV of a sample contributes $\rho(z)dV$ to the sample's scattering with a phase factor $e^{i(q_z z + \mathbf{q}_r \mathbf{r})}$ [63]. Here, q_z and $\mathbf{q}_r = (q_{||}\cos(q_\Psi), q_{||}\sin(q_\Psi))$ are the out-of-plane and in-plane component of the scattering vector. It follows for the measured intensity [63]

$$I \propto \left| \int_V \rho(z) e^{i(q_z z + \mathbf{q}_r \mathbf{r})} d^3 r \right|^2. \tag{2.7}$$

A typical X-ray diffraction experiment collects scattering signal over several hours

and we consequently measure the thermal averaged intensity ($I \rightarrow \langle I \rangle$). Combining Equation 2.6 and 2.7, we can write [62]

$$\begin{aligned}
\langle I \rangle &= \left\langle \left| \int_V d^3r \sum_{i=0}^{N} \rho_m^{flat}(z - u_n(\mathbf{r}) - nd) e^{iq_z z + i\mathbf{q}_r \mathbf{r}} \right|^2 \right\rangle \\
&= \left\langle \left| \int_V d^3r \sum_{i=0}^{N} \rho_m^{flat}(z') e^{iq_z(z' + u_n(\mathbf{r}) + nd) + i\mathbf{q}_r \mathbf{r}} \right|^2 \right\rangle \\
&= \left| \int_V dz' \rho_m^{flat}(z') e^{iq_z z'} \right|^2 \left\langle \left| \int d^2r \sum_{i=0}^{N} e^{iq_z(u_n(\mathbf{r}) + nd) + i\mathbf{q}_r \mathbf{r}} \right|^2 \right\rangle \\
&= |F(q_z)|^2 \langle S(\mathbf{q}) \rangle, \qquad (2.8)
\end{aligned}$$

where we utilized the substitution $z = z' + nd + u(\mathbf{r})$. $F(q_z)$ is the form factor and corresponds to the Fourier transformation of the membrane's scattering length density profile. The structure factor $S(\mathbf{q})$ is the Fourier transformation of spatial correlations in the sample that originate from the periodic stacking of membranes and from out-of-plane membrane fluctuations.

The theory thus far implicitly assumed a membrane stack with an infinite expansion. Of course, this assumption is insufficient to describe a realistic experiment. A limiting factor in the out-of-plane direction is the number of membranes that can be stacked with a sufficient degree of order. The in-plane direction is limited by the sample's dimensions (10×10 mm^2), the footprint of the beam (diameter of 200 μm) on the sample, but most importantly, by the size of coherently scattering membrane patches (diameter of ≈500 Å). These patches are different from the lipid domains that will be discussed below and need to be understood as finite blocks of N stacked membranes. The sample then consists of numerous of these blocks.

Deriving the structure factor for such a patchy sample is lengthy and is described in detail in [64] and [65]. Briefly, one can assume cylindrical patches with a Gaussian distributed diameter L_r (average patch size $\overline{L_r}$ and variance σ_r) and a Gaussian distributed height L_z (average patch size $\overline{L_z}$ and variance σ_z) and define

size effect functions [65]

$$H(z) = \int_z^\infty dL_z \frac{1}{\sigma_z} \exp(-(L_z - \overline{L_z})^2/2\sigma_z^2)(L_z - z)/d, \tag{2.9}$$

$$\begin{aligned} H(r) &= \int_r^\infty dL_r \frac{1}{\sigma_r} \exp(-(L_r - \overline{L_r})^2/2\sigma_z^2) L_r^2 \\ &\times \begin{cases} 0 & \mathrm{r}/L_r > 1 \\ \cos^{-1}(r/L_r) - r/L_r\sqrt{1-(r/L_r)^2} & \mathrm{r}/L_r \leq 1. \end{cases} \end{aligned} \tag{2.10}$$

We can further assume the membrane patch can be isotropic along the azimuth axis and integrated out the Ψ dependency [64, 65]. The in-plane vector $\mathbf{r}$ can be replaced with its radial component r [65].

The structure factor then has the form [65]

$$\begin{aligned} S(q_z, q_{||}) &= \sum_{n=-\infty}^{n=\infty} H_z(nd) e^{iq_z nd} \int_0^\infty r dr H_r(r) J_0(q_{||} r) e^{iq_z \delta u_n(r)} \\ &= \sum_{n=-\infty}^{n=\infty} H_z(nd) \cos(q_z nd) \int_0^\infty r dr H_r(r) J_0(q_{||} r) e^{iq_z \delta u_n(r)}, \end{aligned} \tag{2.11}$$

where J_0 is the zero order Bessel function and $\delta u_n(r)$ is the height-height pair correlation function.

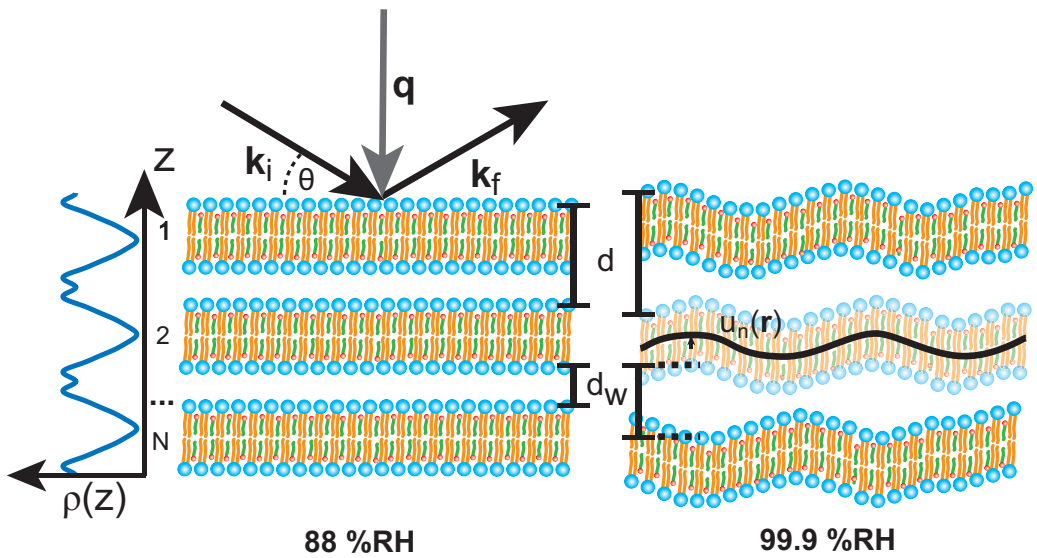

FIGURE 2.7: Diagram of a scattering experiment on a stack of membranes. Each bilayer has the identical scattering length density ρ_z and the membranes are placed at a lamellar repeat distance d from each other. The space between neighboring membranes is filled with hydration water and the thickness d_w of this water layer is controlled by the environments RH. This water layer thickness is small (measured to be around $d_w \approx 13$ Å) at 88 % RH which consequently suppresses out-of-plane membrane fluctuations. Well hydrated samples (99.9 % RH) on the other hand have a substantial ($d_w \approx 28$ Å) water layer between the membranes enabling out-of-plane fluctuations of each membrane.

Solid supported RBCcms in this thesis were measured at 88 % and at 99.9 % relative humidity (RH). Controlling the samples' environment with respect to the RH allows to tune the amount of hydration water in the space between neighboring membranes. The average thickness d_w of this water layer at 88 % RH was measured to be around $d_w \approx 13$ Å which leaves little space for out-of-plane membrane fluctuations ($u_n(\mathbf{r}) \approx 0$). $\sum_{n=-\infty}^{n=\infty} H_z(nd)\cos(q_z nd)$ in the structure factor is non-zero for

$$q_z = \frac{2\pi}{nd}, \tag{2.12}$$

when assuming an infinite stack of RBCcms. The specular intensity profile ($\mathbf{q}_{||} = 0$) is thus a series of defined intensity peaks and the position of the n-th peak is

defined by Equation 2.12. The location of the first order lamellar peak (n =1) will be hereafter referred to as q_1.

An exemplary measurement of a stack of RBCcm at 88 % RH is shown in Fig 2.8 A. Details of the experimental setup are discussed in Chapter 3. A series of $\tilde{N}$ peaks are observed. We can use Equation 2.12 to determine the membrane lamellar repeat distance from the observed peak positions to $d = 55.4 \pm 0.5$ Å.

It is important to appreciate that Equation 2.8 teaches us that each peak corresponds to a measurement of $|F(q_z)|^2$ probed at discrete values $q_z^{(l)}$, with $l = 1, ..., \tilde{N}$. The form factor is given by the Fourier transformation of the scattering length density $\rho_m^{flat}(\mathbf{r}, z)$ and is generally a complex quantity. However, the form factor becomes real - $F_n = \sqrt{I_l q_z^{(l)}}$ - in the case of stacks of centro-symmetric membranes and we can determine the RBCcm's scattering length density from a discrete 1-dimensional inverse Fourier transformation [66]:

$$\rho(z) = \frac{2}{d} \sum_{l=1}^{\tilde{N}} \sqrt{I_l q_z^{(l)}} \nu_l \cos\left(l z q_z^{(l)}\right). \tag{2.13}$$

Here, ν_l are phase factors that can take values of ± 1 (in the case of centro-symmetry). The choices of ν_n can be assessed by fitting a periodic function [67]

$$T(q_z) = \sum_{l=0}^{\tilde{N}} \sqrt{I_l q_z^{(l)}} \mathrm{sinc}\left(\frac{1}{2} d_z q_z - \pi l\right) \tag{2.14}$$

to the data. This method of reconstructing the scattering length density from specular scattering will be hereafter referred to as *1-dimensional Fourier analysis*. The method can be applied in neutron and X-ray diffraction experiments. I have used used this method to determine the water concentration across lipid bilayers in the presence of anesthetics [68] and in my publications [61] and [21].

The achievable resolution of the scattering length density depends on the maximal number of lamellar peaks measured in an experiment. Measurements at 88 % RH showed up to 7 orders of lamellar peaks in contrast to measurements at 99.9 % RH (maximal 2 peaks were detected) and were therefore used for the structural analysis.

Hydrating RBCcm at 99.9 % RH leads to an influx of bulk water in the space in between the stacked membranes. The water layer thickness in this environment can not be measured directly as the detected two orders of lamellar peaks are insufficient for a 1 dimensional Fourier analysis. However, we can estimate a

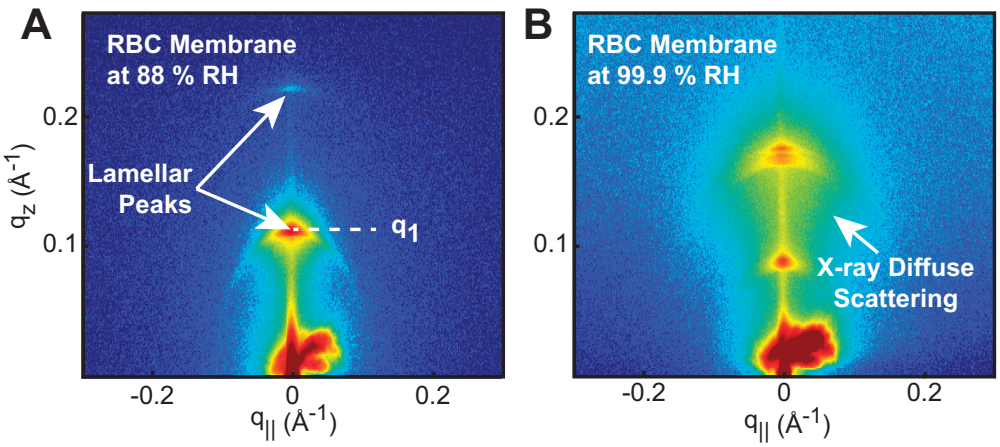

FIGURE 2.8: 2-dimensional X-ray intensity maps recorded on a stack of RBCcms. Measurements were performed at 88 % RH (**A**) and 99.9 % RH (**B**). The most intense scattering is specular ($q_{||} = 0$) in both scans and the signal consists of a series of defined lamellar peaks. Importantly, a cloud of diffuse off-specular scattering was observed in measurements at 99.9 %RH. This off-specular scattering ($q_{||} \neq 0$) is caused by thermal out-of-plane fluctuations of membranes in the stack.

water layer thickness of ≈28 Å, when assuming that the membrane's thickness remains consistent when hydrating the sample. This leaves substantially more space for out-of-plane membrane fluctuations in this environment and $u(\mathbf{r})$ no longer vanishes.

The effect can be seen in Figure 2.8 B, where out-of-plane membrane fluctuations lead to a cloud of off-specular scattering around the lamellar peaks known as X-ray diffuse scattering (XDS).

XDS originates from a change in the structure factor (Equation 2.11), where we now need to consider the height-height pair correlation function $\delta u_n(\mathbf{r})$.

This leaves us with the task of finding a sufficient model to describe fluctuations of the RBC membrane. A popular equation that determines the free energy of a membranes' out-of-plane fluctuations in stacks of synthetic lipid bilayers has been invoked in the literature [65, 69]:

$$H = \int_A d^2r \sum_{n=0}^{N-1} \left(\frac{1}{2}\kappa \left(\nabla_r^2 u_n(\mathbf{r}) \right)^2 + \frac{1}{2}\frac{B}{d}(u_{n+1}(\mathbf{r}) - u_n(\mathbf{r}))^2 \right). \tag{2.15}$$

Of course, one contribution to this free energy is the membrane's resistance to bending (first term in Equation 2.15; see discussion in Section 2.2). However, we need to remember that our sample consists of stacks of RBCcms, which leads to a hindrance of out-of-plane fluctuations due to interactions with neighboring membranes. This interaction is modeled in Equation 2.15 by $F_{Interaction} = \frac{B}{2d}(u_{n+1}(\mathbf{r}) - u_n(\mathbf{r}))^2$, where B is a modulus that accounts for attractive and repulsive forces [62].

Calculating the height-height pair correlation function from Equation 2.15 is lengthy and non-trivial and has been described in detail in [62]. Briefly, membrane fluctuations are governed by thermal energy and can be separated into normal modes by transforming the out-of-plane displacement $u_n(\mathbf{r})$ into Fourier space ($u_n(\mathbf{r}) \rightarrow U_n(\mathbf{Q})$). $\mathbf{Q}$ spans the Fourier space of the membrane fluctuations and differs form the scattering vector $\mathbf{q}$. The free energy functional in Equation 2.2 decouples in Fourier space [62]. The equipartition theorem then assigns $\frac{1}{2}$ k_BT of energy to each normal mode [62]. This allows to calculate the power spectrum of the membrane fluctuations. In Fourier space, the height-height pair correlation function is proportional to this power spectrum [62] and an analytical expression of $\delta u_n(\mathbf{r})$

$$\delta u_n(\mathbf{r}) = \frac{2\eta_c}{q_1^2} \int_0^\infty dx \frac{1 - J_0(r/\xi\sqrt{2x})(\sqrt{1+x^2} - x)^{2n}}{x\sqrt{1+x^2}} \tag{2.16}$$

can be derived [62], where $J_0(x)$ is the zero order bessel function and ξ and η_c are known as Caillé parameters which relate to the bending modulus κ and the membrane interaction modulus B through [65]

$$\eta_c = \frac{k_B T q_1^2}{8\pi\sqrt{B\kappa}} \quad \text{and} \quad \xi^4 = \frac{\kappa}{B}. \tag{2.17}$$

Here, k_B is the Boltzmann constant and T is the temperature.

It has been emphasized above that out-of-plane membrane fluctuations lead to off-specular scattering in diffraction experiments. Equation 2.11 and Equation 2.16 teach us that this XDS signal is influenced by the membrane's bending modulus κ and interaction modulus B. This influence can be seen in Figure 2.9 A and B where 2-dimensional maps of $S(q)$ are shown for two settings of κ and B. κ=6.3 k_BT and B=$2.4 \cdot 10^{-6}$ k_BT/Å^4 mimics a soft membrane and κ=25.4 k_BT and B=$6.2 \cdot 10^{-7}$ k_BT/Å^4 mimics a rigid membrane. The specular signal ($q_{||}$=0) is still dominated by a series of defined lamellar peaks and shows little variation between both structure factors (see Figure 2.9 C). This changes, in the out of plane

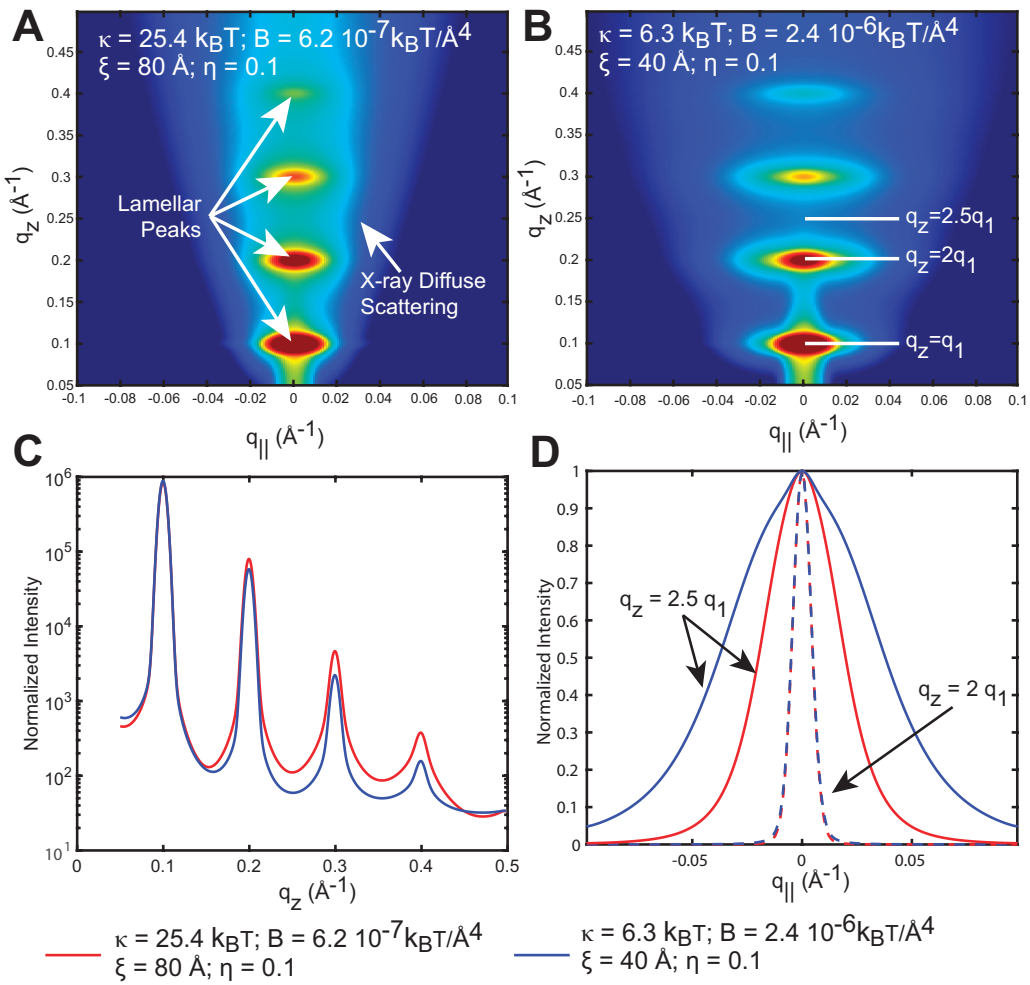

FIGURE 2.9: **A** 2-dimensional map of $S(\mathbf{q})$ at values of κ=6.3 k_BT and B=2.4 $\cdot 10^{-6}$ k_BT/Å^4. **B** 2-dimensional map of $S(\mathbf{q})$ at values of κ=25.4 k_BT and B=6.2 $\cdot 10^{-7}$ k_BT/Å^4. **C** Normalized line-cuts of $S(\mathbf{q})$ taken at $q_z = 2q_1$ and $q_z = 2.5q_1$. **D** Normalized line-cuts of $S(\mathbf{q})$ taken at $q_{||} = 0$.

direction (see Figure 2.9 D): The diffuse signal in between peaks extends further in the in-plane direction for softer membranes as compared to rigid membranes.

One can consequently determine both, the bending modulus κ and the interaction modulus B, independently by fitting the structure factor $S(q_z, q_{||})$ to experimental data. This method has been developed in the groups of Dr. John Nagle and Dr. Stephanie Tristram-Nagle at Carnegie Mellon University and has been

thus far applied to synthetic membrane mixtures [37, 54, 70, 71].

In my publications [60, 61], I apply this method to RBC membranes. Diffuse scattering signals were measured on an in-house diffractometer and a GPU accelerated fit program was implemented for the analysis. The algorithm will be addressed in Chapter 3.

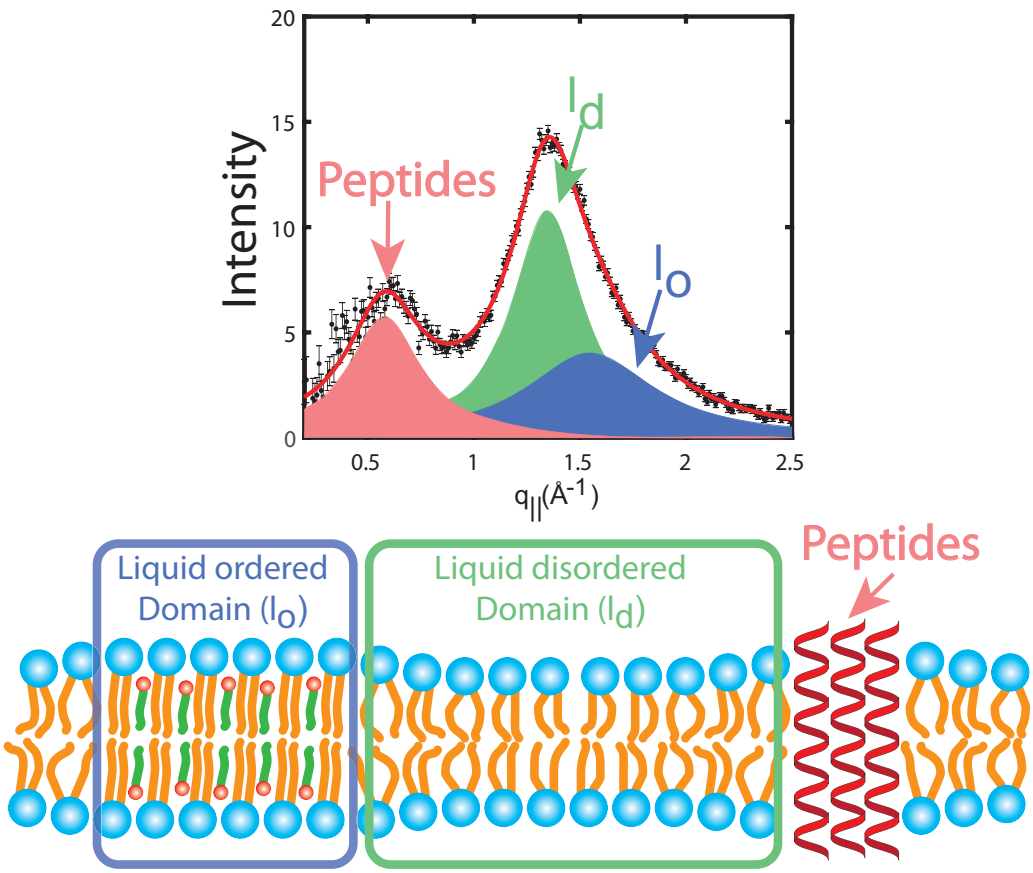

FIGURE 2.10: A wide range in-plane scan of stacks of RBCcm reveals three peaks that can be assigned to a peptide signal and two lipid signals that originate from liquid ordered l_o and liquid disordered l_d domains.

We so far focused on out-of-plane correlations: The periodicity of stacked membranes manifests in the observed lamellar peaks and height-height pair correlations are probed indirectly by X-ray diffuse scattering. We implicitly ignored any in-plane dependency and pictured the membrane to be homogeneous in this

direction. This is an insufficient description as the membrane is composed of individual lipid molecules with embedded proteins. The in-plane structure can be probed in a in-plane scan (see Section 3.2). A scan of a RBC membrane is depicted in Figure 2.10. Three peaks are detected for stacked RBC membranes. Two peaks originate from aforementioned l_o and l_d lipid domains (blue and green peak) [8]. The third peak results from α-helical coiled-coiled peptide structures [8].

This X-ray analysis was originally developed for synthetic lipid bilayers and there are several caveats that need to be adressed when applying the methods to RBC membranes.

First we need to remember that the outer shell of RBC is a composite structure of a RBCcm tethered to a cytoskeleton and both components affect the shell's fluctuations. However, the determined electron density profile, measured at 88 % RH, does not indicate the presence of a cytoskeleton between the membrane layers and spectrin filaments are likely ruptured during the preparation process [8]. It is thus plausible to interpret the measured XDS signal as results of fluctuations of the RBCcm.

It is well known that the RBCcm is asymmetric, which raises the question of whether the discussed 1-dimensional Fourier analysis is applicable (absence of centro-symmetry). Multilamellar stacks of RBCcm are formed through liposome fusion when RBC liposomes are dried on a silicon wafer. This process does not allow controlling of the membrane's orientation within the stack: Either of the leaflets can face up or down (along z). We consequently measure membranes with an ensemble of different orientations and it is plausible to assume an average symmetric scattering length density $\rho(\mathbf{r}, z)$.

2.4 Neutron Spin Echo Spectrometry

The elastic scattering theory can be generally applied to X-ray and neutron scattering. The following section, however, focuses on the specifics of neutron scattering and the concept of NSE spectrometry.

The previous section introduced elastic scattering as a measurement of spatial correlations in the sample. Membrane dynamics is not measured directly. This limitation can be overcome in inelastic scattering experiments where we allow the wave's energy to change during the scattering process, *i.e.*, $\mathbf{k}_i \neq \mathbf{k}_f$. It is best to understand inelastic scattering as a measurement of a system's response to an external disturbance.

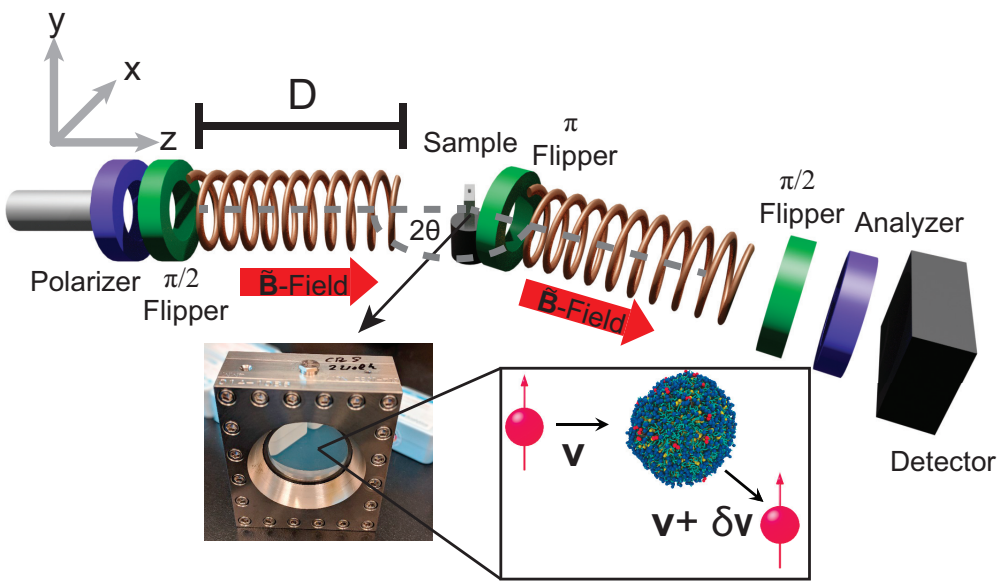

FIGURE 2.11: Setup of a neutron spectrometer. Incoming neutrons are first polarized before passing two magnetic coils before and after interacting with the sample. The neutrons spin is undergoing lamor precession when passing through this magnetic field. A change in the neutron's velocity can be measured by comparing the spin orientation at the beginning and at the end of the instrument. The sample studied in this thesis consists of *RBC liposomes* immersed in heavy water (D_2O)

A harmonic oscillator can be used as a simple example to illuminate this concept. Elongating the system out of equilibrium (disturbance) results in a periodic, oscillating motion (response). Of course, the oscillator can be damped which results in a periodic motion with an exponentially decaying amplitude. The system is called over-damped if any periodic motion is suppressed. The response function in this last scenario is an exponential decay.

We can picture membrane fluctuations very much like the oscillator in our rudimentary example. An obvious question that arises from this analogy is whether membrane dynamics in an aqueous environment is harmonic, damped, or over-damped.

NSE spectrometry is a suitable technique to address this question.

This instrument uses the neuton's magnetic moment to probe velocity changes

of the scattered neutrons. First, it is important to remind ourselves that neutrons undergo Larmor precession when passing through a magnetic field ($\tilde{\mathbf{B}}$) if the neutron is polarized perpendicular to the field. The frequency of this precession can be written as [72]

$$\omega_L = \gamma|\tilde{\mathbf{B}}|, \tag{2.18}$$

where γ is the gyromagnetic ratio ($\gamma_{neutron} = -1.83\ \frac{\text{rad}}{\text{s T}}$ [73]).

The setup of an NSE spectrometer is sketched in Figure 2.11. The z-axis shall be parallel to neutron's direction of motion and the x-y-plane is perpendicular to the neutron's direction of motion. The manipulation of the neutron's spin orientation throughout the instrument is visualized in Figure 2.12. First, the incoming neutron beam is polarized with the magnetic moment pointing in the z-direction before being flipped by 90° around the x-axis by a $\frac{\pi}{2}$ flipper [72]. The neutron's spin is then pointing in the y direction. This is required for the neutron's spin to undergo Lamor precession in the subsequent magnetic field coil before interacting with the sample. The magnetic field in this coil results in the neutron's spin to precess through an angle [72]

$$\Phi = \omega_L t = \gamma|\tilde{\mathbf{B}}|\frac{D}{|\mathbf{v}|}, \tag{2.19}$$

where D is the length of the magnetic field coil and $\mathbf{v}$ is the neutron's velocity. The phase angle is determined as $(\Phi \mod (2\pi))$ and the number of precessions is $\overline{N} = \frac{\Phi}{2\pi}$. Importantly, a wide wavelength spread ($\lambda/\delta\lambda$<18% for the used instrument [72]; see Chapter 3) results in the complete depolarization of the beam before the sample.

A second magnetic field coil is placed at a scattering angle 2θ relative to the incoming beam. The scattered neutron's spin is flipped by 180° (π-flipper) before being guided through this secondary coil [72]. This is experimentally realized by a π flip of the neutron's spin orientation (phase angle $-(\Phi \mod (2\pi))$) prior entering the secondary coil [72].

Let's first consider an elastically scattered neutron. The neutron's wavelength and velocity is invariant and the number of precessions in both magnetic coils is identical. Consequently, the neutrons' polarization is the same before the first and after the second magnetic coil (this is referred to as the *Echo* condition [72]).

In the case of inelastic scattering, the neutron's change in velocity results in an unequal number of Lamor precessions in both magnetic coils causing the final

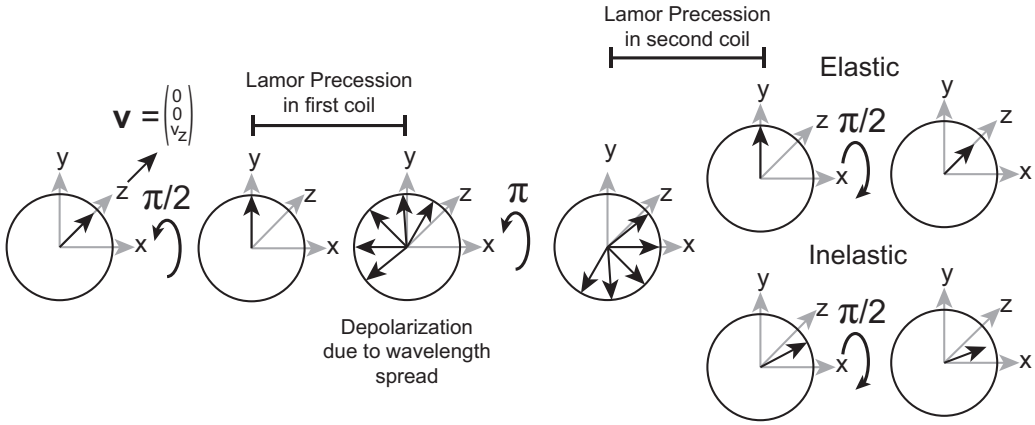

FIGURE 2.12: The orientation of the neutron's magnetic moment throughout the instrument: Neutrons are first polarized and the spin orientation is flipped. The magnetic moment experiences Lamor precession in the two subsequent magnetic field coils. Inelastically scattered neutrons show an unequal polarization before the first magnetic coil and after the second magnetic coil as a result of the neutron's change in velocity. The energy transfer can be thus measured by analyzing the neutron's polarization.

spin orientation to differ from the initial polarization. This results in an attenuated polarization measured by the analyzer-detector combination [72].

It has been shown that the polarization $\langle P_z \rangle$ of the scattered neutron beam can be written as [72, 74]

$$\langle P_z \rangle = \int f(\lambda) d\lambda \int S(\mathbf{q}, \omega) \cos(\omega\tau)\, d\omega = \int f(\lambda) I(\mathbf{Q}, \tau) d\lambda. \tag{2.20}$$

Here, $f(\lambda)$ is the wavelength distribution of the incoming neutron beam, $I(\mathbf{Q}, \tau)$ is the intermediate scattering function and

$$\tau = \gamma \left(\frac{m_n}{h}\right)^2 \frac{\lambda^3}{2\pi} \left|\tilde{B}\right| D \tag{2.21}$$

is the Fourier time [72].

$$S(\mathbf{q}, \omega) = \frac{1}{2\pi\hbar} \int \int G(\mathbf{r}, t) e^{i(\mathbf{q}\mathbf{r} - \omega t)} d\mathbf{r} dt, \tag{2.22}$$

is the scattering function and gives the probability that scattering changes the energy of a system by an amount $\hbar\omega = E_i - E_f$ and its momentum $\hbar\mathbf{q}$ ($= \hbar\mathbf{k}_i -$

$\hbar\mathbf{k}_f$) [73]. It corresponds to the Fourier transformation of the time dependent self pair-correlation function [75]

$$G(\mathbf{r},t) = \left\langle \sum_{i,j} e^{i\mathbf{q}\left[\mathbf{r}_i(t)-\mathbf{r}_j(0)\right]} \right\rangle, \tag{2.23}$$

where $\mathbf{r}_i$ is the time-dependent coordinate of a single atom.

Measuring the spin orientation as function of the Fourier time τ consequently allows measuring the Fourier transformation of the scattering function which is just the time-dependent self pair-correlation function itself [74].

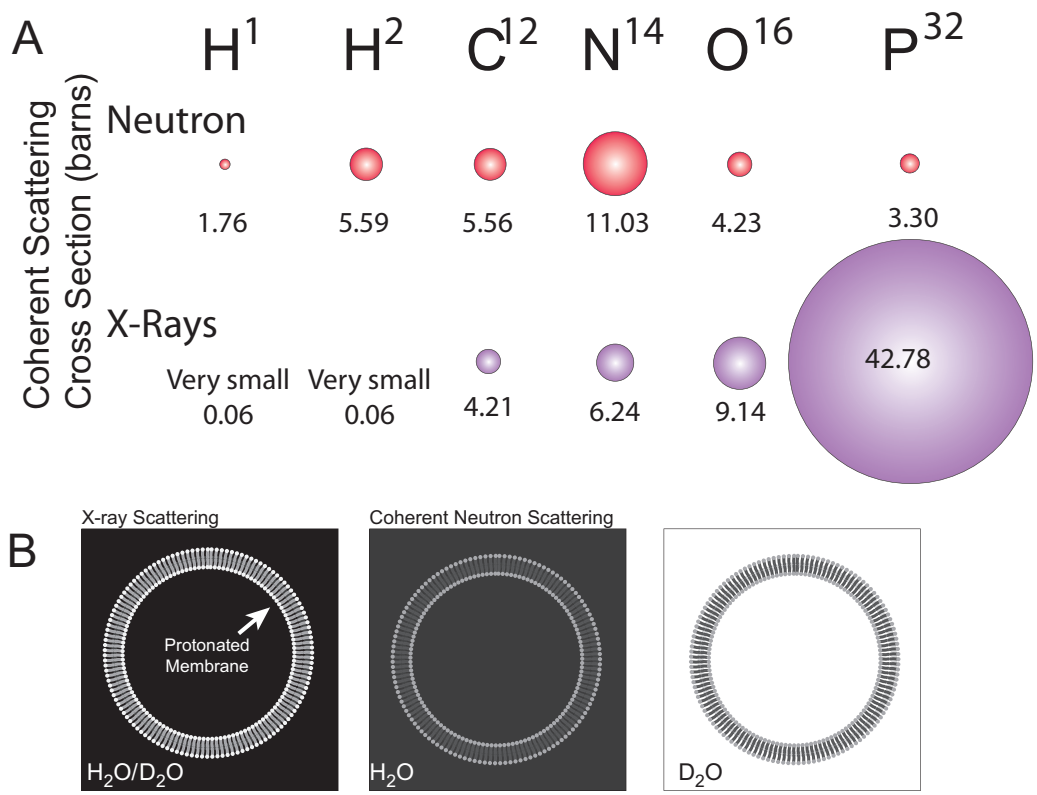

FIGURE 2.13: **A**: A list of X-ray and neutron cross sections for selected elements. **B**:A liposome seen by X-ray and neutron scattering. The significant contribution of hydrogen in neutron scattering experiments substantially reduces contrast. The contrast can be enhanced by replacing the solvent with heavy water D_2O.

This is a good place to discuss the sample studied in this thesis. Membrane fluctuations were measured on RBC liposomes with a diameter of ≈200 nm (verified through dynamic light scattering and small angle neutron scattering) that were immersed in heavy water (deuterium hydroxide; D_2O). The sample was then filled in a custom built titanium holder (see Chapter 3) and placed in the NSE spectrometer.

The use of heavy water was indispensable in order to achieve a high contrast between the solvent and membrane. Contrast refers to a difference of the scattering efficiency between two materials and allows X-ray's and neutrons to distinguish between materials in the sample [76]. The scattering efficiency is quantified by the scattering cross section σ. The unit of σ is barn=100 fm^2. Figure 2.13 visualizes σ for a selection of elements commonly found in organic material.

Hydrogen is certainly the most abundant element in the studied sample as it is an integral part of organic molecules and water. This element scatters X-rays very weakly ($\sigma = 0.06$ barn) but contributes substantially ($\sigma = 1.76$ barn) in a neutron scattering experiment resulting in a loss of contrast between the membrane and water. This is illustrated in Figure 2.13 B: A phospholipid vesicle immersed in H_2O is seen by X-rays through the high contrast created by the the electron rich head groups (phosphorous) of the membrane. This contrast is much weaker when imaging this vesicle with neutrons.

The contrast can be enhanced by selectively substituting hydrogen with its isotope deuterium which has a ≈5× higher neutron scattering cross section compared to hydrogen. This can be done by either immersing the liposomes in heavy water (D_2O) or using deuterated lipid molecules. Of course, this last option is unfeasible for the study of RBC membranes as it would require to change the donors metabolism to a heavy (deuterium based) diet.

Returning to the question raised at the beginning of this section we can now use NSE to determine whether membranes in an aqueous environment show, damped oscillatory dynamics or over-damped dynamics. NSE spectrometry measures the wave vector dependent self pair-correlation function in the time domain, which is distinct in both scenarios [72].

The collected data from RBC vesicles [60] show an intermediate scattering function that follows a stretched exponential decay demonstrating the over-damped dynamics of the membrane fluctuations.

Quantifying the measured decay requires a good theoretical understanding of the observed membrane fluctuations. This problem was first addressed by Anton Zilman and Rony Granek (ZG-Theory) [75]. They describe membrane fluctuations by the Helfrich-Canham-Evans functional (Equation 2.2) in combination

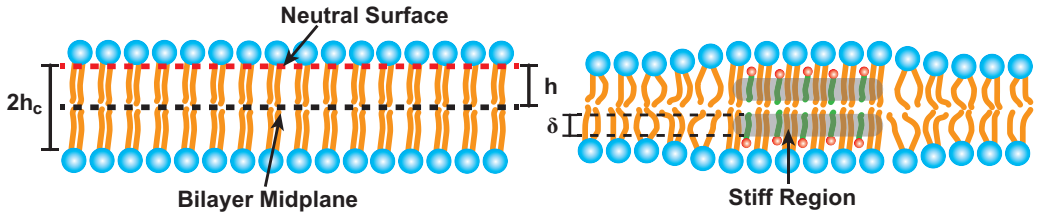

FIGURE 2.14: Measuring the bending modulus from NSE experiments requires knowledge of the area compression modulus K_A. Two models are discussed: the coupled monolayer model and the cholesterol model. The left panel shows the location of the conceptual neutral surface which is widely believed to be located at the interface between the hydrophilic heads and the hydrophobic core. The right panel shows the stiff region with a thickness δ used in the *cholesterol* model. It is assumed to be the height of cholesterol's stiff hydrocarbon rings.

with hydrodynamics [77] and their primary result can be written

$$I(q,\tau)/I(q,0) = \exp\left[-\left(\Gamma_{ZG}\tau\right)^{2/3}\right], \tag{2.24}$$

where

$$\Gamma_{ZG} = 0.025\left(\frac{k_B T}{\tilde{\kappa}}\right)^{1/2}\left(\frac{k_B T}{\eta}\right) q^3. \tag{2.25}$$

Here, Γ_{ZG} is the q-dependent relaxation rate, η is the solute viscosity, k_B is the Boltzmann constant, T is the sample temperature and $\tilde{\kappa}$ is the dynamic bending modulus.

We immediately recognize the stretched exponential dependency (stretch factor $2/3$) of the intermediate scattering function. The most striking perception, however, is that the model relates the decay constant Γ_{ZG} to the membrane's material property $\tilde{\kappa}$.

The ZG-Theory initially introduced $\tilde{\kappa}$ as the static bending modulus κ. However, bending moduli obtained by NSE and the ZG-Theory were initially much larger than values obtained by other methods [78–80]

This controversy was eventually resolved for lipid bilayer vesicles by Watson *et al.* [81] by taking the friction between both leaflets into account [78] and expressing

$$\tilde{\kappa} = \kappa + h^2 K_A, \tag{2.26}$$

where h is location of the membrane's neutral surface relative to the bilayer midplane. This neutral surface indicates the location in each monolayer where stretching and compression modes are decoupled from bending modes [78, 82].

It is important to appreciate that Equation 2.26 contains both the bending modulus κ and the area compression modulus K_A. We have learned in Section 2.2 that both moduli can scale very differently in synthetic lipid bilayer membranes: K_A is independent of the tail length while κ increases ($\approx 2\times$) for longer tails. Importantly, cholesterol increases K_A ($\approx 3\times$) but has little effect on a bilayers bending rigidity when there are saturated tails.

Equation 2.26 also shows that we can not determine both moduli independently from a single fit and a good model is required to decouple both parameters. Of course, such a model has to account for the effects of tail length, tail saturation, the cholesterol concentration, and potentially the presence of proteins.

Currently, such a coherent model is missing but several approaches aim to overcome this limitation. A particularly popular model is the coupled monolayer model (*cmm*). It writes

$$K_A = 48 \frac{\kappa}{2h_c}^{2}, \tag{2.27}$$

where h_C is the height of the hydrocarbon tails in one monolayer. Using this relation, Equation 2.25 can be rewritten

$$\Gamma_{nse}^{cmm} = 0.025 \left(\frac{k_B T}{\kappa \left(1 + 48(h/2h_c)^2\right)} \right)^{1/2} \left(\frac{k_B T}{\eta} \right) q^3. \tag{2.28}$$

The exact location of the position of the neutral surface within a bilayer is unknown but it is generally believed to be located at the interface between the headgroup region and the hydrophobic tails (see Figure 2.14 for clarification) [40]. A value of $h/2h_c = 0.5$ is thus commonly used in the literature [40].

It is important to appreciate that the *cmm* results in an invariant factor, $\left(1 + 48(h/2h_c)^2\right)$, in the decay constant and does not account for effects of the membrane composition on K_A. Especially the effect of cholesterol on K_A is not considered as has been recently emphasized [78, 83].

Cholesterol's structure differs significantly from lipid molecules and is dominated by rigid sterol rings with a height $\delta \approx 9$ Å. An alternative approach was suggested [78, 84]:

$$K_A = 12\kappa/\delta^2. \tag{2.29}$$

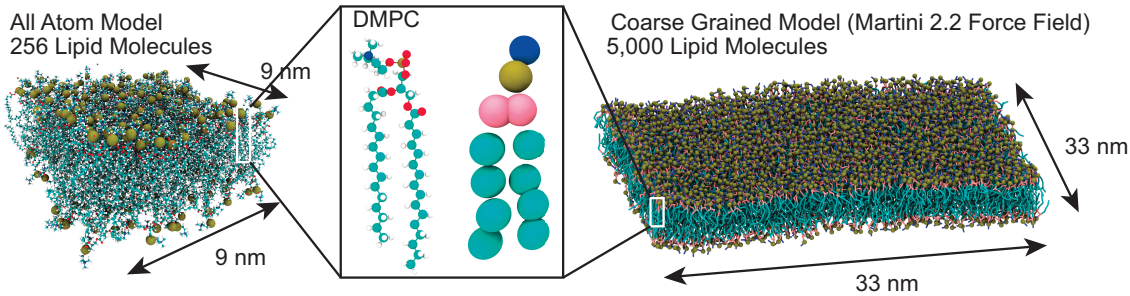

FIGURE 2.15: Comparison between all-atom and coarse grained MD models: All-atom simulations represent every atom as individual bead. Coarse grained simulations group several atoms together to reduce the number of beads in the system and ultimately allow the simulation of larger structures. Water molecules are omitted from both membrane patches for clarity

This model, hereafter referred to as the *cholesterol model*, assumes a stiff region with a height δ in the bilayer corresponding to the rigid hydrocarbon rings of the cholesterol molecule as sketched in Figure 2.14. Consequently.

$$\Gamma_{nse}^{chol} = 0.025 \left(\frac{k_B T}{\kappa \left(1 + 12(h_c/\delta)^2\right)} \right)^{1/2} \left(\frac{k_B T}{\eta} \right) q^3. \tag{2.30}$$

This alternative model leads to a $\approx$3.25$\times$ lowering of the measured bending modulus.

RBC membranes are rich in cholesterol and we consequently used the cholesterol model for the analysis of the collected NSE data.

2.5 Molecular Dynamics Simulations

X-ray and neutron diffraction experiments provide measurements of structure and dynamics on molecular length scales averaged over a large ensemble of molecules. Information about individual molecules is lost in these techniques. It is often challenging - especially with multiplex structures such as RBC membranes - to model the experimental results as it has been especially emphasized in the previous section. MD simulations on the other hand provide insight into the dynamics of single molecules but are often limited to small system sizes due to computational constraints.

MD Simulations attempt to numerically solve a N-Body problem. Every atom in a molecular structure is represented as a bead. Chemical bonds are optionally defined as relative constraints (relative distance and bond angle) between two or more beads. A MD simulation is then performed by first dividing the desired time frame t_{total} in finite steps dt (typically 1-20 fs). For every time step, the computer calculates the force that is acting on every atom by summing over all interactions with the surrounding atoms. The equations of motion are then solved for every bead and the new bead positions are recorded. This constitutes a single simulation step. For every subsequent step, the computer re-evaluates the forces and equations of motion using the latest bead positions. This process is repeated until the desired time t_{total} is reached.

The approach of representing every atom by a single bead is referred to as *all-atom simulation*. The left panel of Figure 2.15 shows a bead model on the example of the lipid DMPC. Carbon atoms are visualized in cyan, oxygen in red, phosphorous in gold, nitrogen in blue and hydrogen in white.

The approach taken in MD simulations may sound intuitively simple but it is important to appreciate that they remain computationally intense despite improvements on the underlying algorithms: The required computation-time scales with the number of atoms in the system and ultimately limits the simulation's complexity. Determining the exact interactions between all atoms would require calculating the exact quantum mechanical forces at every time-step of the simulation. To optimize this process, pre-determined approximations to the exact interactions, so-called *force fields*, are used to determine the forces between atoms in the system. A variety of force fields is available to simulate complex molecular assemblies. A well accepted and validated *all-atom force field* is the *charmm 36* force field [85].

A three dimensional render of an all-atom membrane model (charmm 36) with 256 lipid molecules is depicted in Figure 2.15. It contains 27,392 beads (including 24 water molecules per lipid; omitted for clarity in Figure 2.15) and can be simulated at a speed of $<$50 ns/day on the GPU accelerated setup described in Chapter 3. The systems spans only $\approx 9 \times 9$ nm^2 but provides detailed insight into the dynamics of small molecular assemblies. I have used all-atom models to study the interactions of antibiotics [68] and my students have designed models that mimic brain membranes and the plastisizer Di(2-ethylhexyl)phthalate (DEHP) [86].

Modern force fields are optimized to reproduce experimental observations and allow a realistic insight into the dynamics of molecules. They are also well suited to determine static material properties such as the membrane's bending modulus from the power spectrum of out-of-plane fluctuations of the membrane

model. Deriving an expression of the power spectrum is lengthy but has been shown in the literature [82, 87]. It follows the same approach that was introduced in Section 2.3 when describing the derivation of Equation 2.16. The membrane fluctuations are separated into normal modes by a Fourier Transformation ($u_n(\mathbf{r}) \rightarrow U_n(\mathbf{Q})$) and the free energy functional in Equation 2.2 decouples in Fourier space. The equipartition theorem then assigns $\frac{1}{2}$ k_BT of energy to each normal mode. This allows to calculate the power spectrum of the membrane fluctuations. The membrane, again, is isotropic along the azimuth axis and the spectrum only depends on the radial component $Q_{||}$ of the vector $\mathbf{Q}$ and can be written [87]

$$\left\langle |h(Q_{||})|^2 \right\rangle = \frac{k_B T}{\kappa Q_{||}^4}. \tag{2.31}$$

The spectrum thus follows a $Q_{||}^4$ dependency and is proportional to the reciprocal of the bending modulus κ. Determining κ from MD simulations and Eq. 2.31 requires a sufficient sampling of the low-$Q_{||}$ regime (long wavelength fluctuations). This requires long simulations ($t > 1$ μs) of patches >30×30 nm^2. Membrane patches of a few hundred lipid molecules are too small for this analysis making all-atom simulations computationally expensive for this purpose.

Coarse grained simulations have been developed and aim to overcome these limitations. In this type of simulation, multiple atoms are grouped together and are represented by one single bead which reduces the number of beads in the simulated system and allows the simulation of larger systems. The grouping of atoms in a given molecule varies from force field to force field and is determined by an iterative process that aims to reproduce results from all-atom simulations and experimental observations. Numerous coarse grained force fields have been developed and are tested against experimental findings to accurately represent large scale dynamics such as membrane domain formation and membrane undulations. The widely accepted Martini 2.2 force field [88] has been used throughout this thesis. A coarse grained model of DMPC (Martini 2.2) is depicted in Figure 2.15 B. The two tails of DMPC have 14 carbon atoms and 29 hydrogen atoms, each, and are represented by 4 beads per tail. A model of the RBCcm has been developed and is described in Chapter 3. I have used MD simulations to study the mixing behavior of synthetic lipids in hybrid RBC membranes [21]; investigated the Triton-X 100 mediated insertion of the SARS-CoV 2 spike protein into RBC membranes [89] and determined the bending modulus in RBC membrane mimics [60, 61].

Chapter 3

Methods

3.1 Sample Preparation

Several sample preparation protocols were developed for the projects in this thesis. A summary of the different methods is presented in Figure 3.1.

Preparation of RBC Ghosts

The preparation of RBC ghosts was first introduced by Dodge *et al.* in 1963 [90]. RBC ghosts are empty RBCs that consist of the RBCcm and remains of the spectrin cytoskeleton. The hemoglobin is removed from the cell in a four-step process that will be detailed below. Their name originates from their colorless appearance under a microscope.

NSE experiments require an especially large sample volume (each sample consists of 20 ml solution with a RBC liposome mass concentration of ≈20 mg/ml) and the protocol was thus optimized to achieve a high yield. Either whole blood or leukocyte-reduced transfusion red cell concentrates (RC) can be used to prepare RBC ghosts.

Whole blood samples (see Figure 3.2 A) were collected from volunteers in 10 ml heparinized blood collection tubes. RCs were provided by the Canadian Blood Service's (CBS's) Network Center for Applied Development (netCAD, Vancouver, BC) and stored in standardized PVC plastic bags in a citrate phosphate dextrose and saline-adenine-glucose-mannitol (CPD-SAGM) solution. 100 ml contain 0.33 g citric acid, 2.63 g sodium citrate, 0.25g sodium dihydrogen phosphate, 3.4 g dextrose, 0.88 g sodium chloride, 0.02 g adenine and 0.53 g mannitol [91]. The storage bags were stored at 4 °C until use.

In the case of RCs, 5 ml RC was mixed with 5 ml phosphate buffer saline (PBS). This buffer contained sodium chloride (137 mM), potassium chloride (2.7 mM),

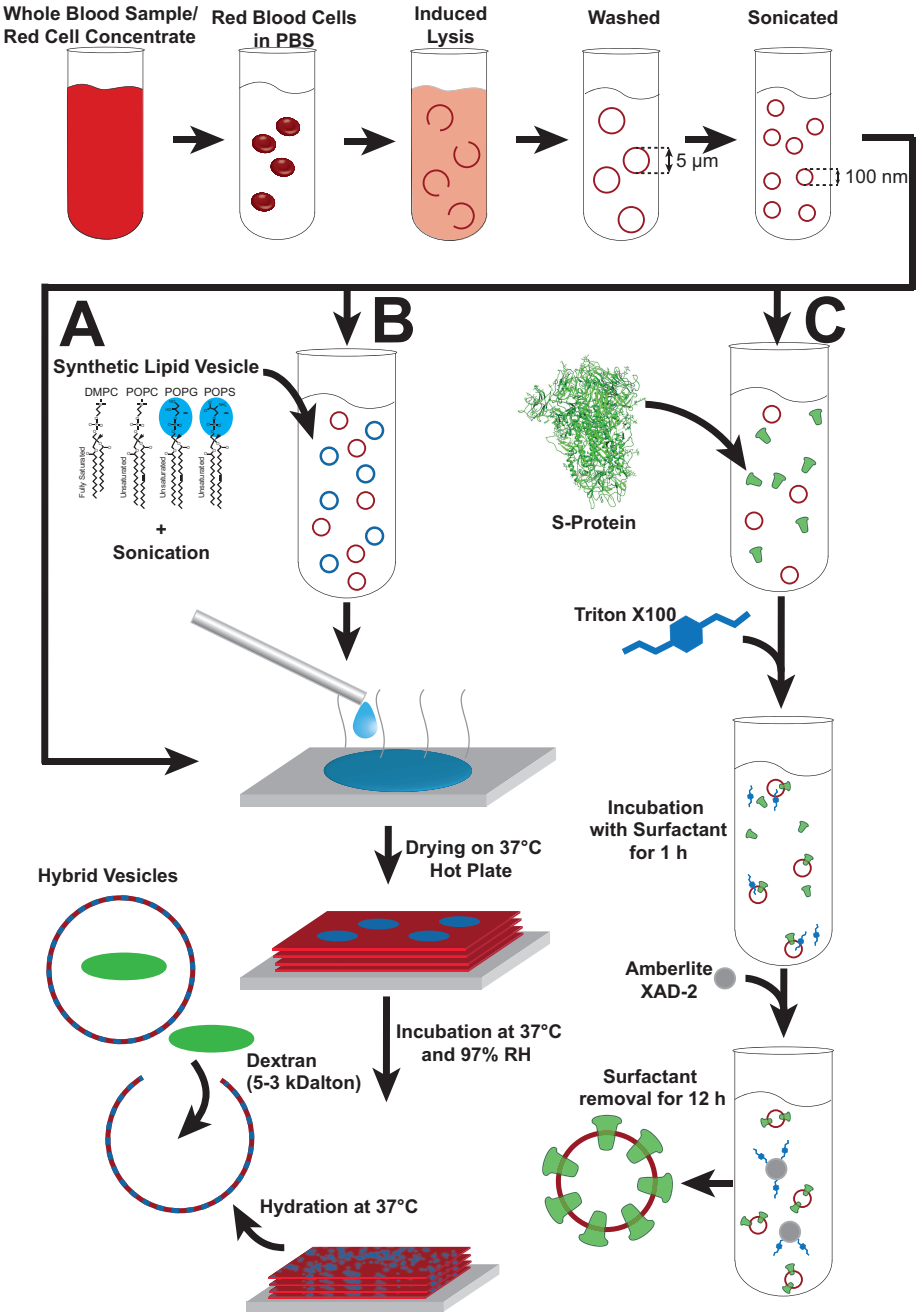

FIGURE 3.1: Summary of the preparation protocols developed in this thesis: First, RBC ghosts were prepared from isolated RBCs through induced lysis and subsequent washing. These resulting RBC liposomes were further processed following three different strategies: **A** Solid supported RBCcms were prepared by applying the solution on a silicon wafer and allowing them to slowly dry. **B** Optionally, the liposomes were modified with synthetic lipid molecules. **C** Proteins such as the S-protein can be anchored into the RBCcm's through a detergent mediated insertion process.

sodium phosphate (10 mM), and potassium phosphate (1.8 mM), and was prepared from tablets purchased from Sigma-Aldrich (Product Number P4417) mixed with ultra-pure water (resistivity 18.2 MΩ·cm). The ion concentration and osmolarity match those found in the human body reducing the risk of cell damage.

The collected samples were then centrifuged for 10 min at 4,000 g, resulting in the separation of RBCs from blood plasma (Figure 3.2 B-C). The red, RBC-rich fraction, is commonly referred to as hematocrit. The supernatant was removed and replaced with fresh *PBS*. The sample was centrifuged for additional 10 min at 4,000 g. This process of centrifugation with subsequent buffer exchange was repeated two more times. A *lysis buffer* was prepared by mixing 16 ml *PBS* with 484 ml ultra pure water and chilled at ≈4 °C. The pH was adjusted to pH 8 prior to cooling by adding potassium hydroxide under continuous monitoring of the solution's pH. The RBCs were exposed to osmotic stress by mixing hematocrit with this *lysis buffer* at a concentration of 6 vol%. This induces hemolysis, *i.e.* the rupture of the cell with a subsequent release of hemoglobin. The ratio of hematocrit to lysis buffer was lowered to 3 vol% for the RC samples after an inadequate lysis in these samples was observed. The tubes were immediately placed on ice for 30 min to avoid a fast re-closing of the ruptured cells.

The solution was subsequently centrifuged at 4,000 g for 1 h resulting in a pellet consisting of empty RBC. The centrifuge was pre-chilled to ≈4 °C. The supernatant was removed and replaced with fresh *lysis buffer*. This step of centrifugation with subsequent buffer exchange was repeated four times until the supernatant was found to be clear and a white pellet was observed on the bottom of the tube (see Figure 3.2 D-H). The samples were stored on ice in between steps. Potential inconsistencies in the preparation protocol due to interruptions in the cooling chain and or variations in the *lysis buffer*'s pH resulted in a red coloring of the sample indicative of an inadequate rupturing of the cells. Such samples were disposed to ensure a consistent sample quality.

The prepared RBC ghosts were visually inspected under a microscope and had a diameter between 1 μm and 10 μm. Such large structures and especially the remaining spectrin cytoskeleton are undesirable for the preparation of solid supported membranes as they result in a poor level of order in the stacks [8]. Therefore, I combined the pellet from multiple reaction tubes (typically 6×15 ml reaction tubes are prepared from a 10 ml blood sample) in a single 1.5 ml reaction tube and the volume was adjusted to 500 μl. The sample was then tip-sonicated with 20×5 s pulses at a power of 100 W. Note that the reaction tube was placed on ice during sonication to prevent the sample from overheating. The sample was subsequently centrifuged at 20,000 g for 20 minutes to remove any larger residues.

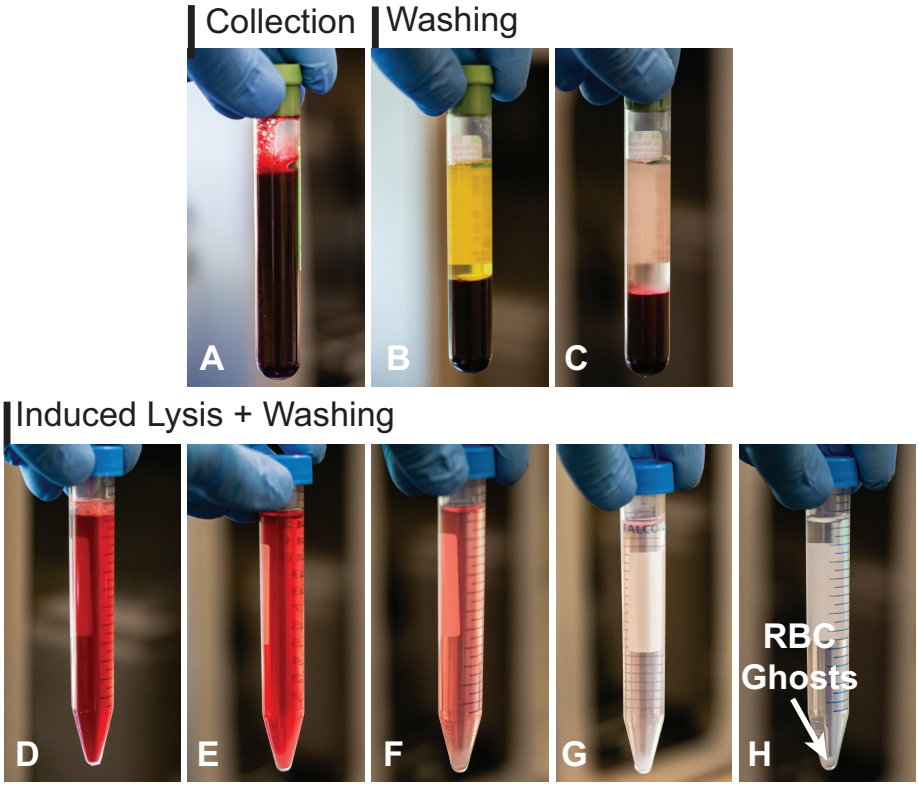

FIGURE 3.2: Sample tube throughout the preparation of RBC ghosts. First, RBC are isolated through centrifugation and washed with PBS buffer (**A**-**C**). **D** The RBCs are then exposed to osmotic stress by mixing hematocrit with *lysis buffer* at a concentration of 6 Vol%. The released heamoglobin is subsequently washed out (**E**-**H**)

This results in liposomes with a diameter of ≈200 nm (verified with dynamic light scattering) that will be hereafter referred to as *RBC liposome solution*. Remains of the cytoskeleton were no longer detectable in fluorescent microscopy experiments [8] and are likely ruptured during sonication.

10 ml of a whole blood sample yielded ≈500 μl of final solution at a membrane concentration of ≈14 mg/ml (verified through drying the sample) [8]. RBC liposomes were used for all further preparation that will be outlined in the following paragraphs.

Preparation of Solid Supported RBC Cytoplasmic Membranes

The formation of well-aligned multilamellar stacks of RBCcm is a prerequisite for a high-resolution structural analysis in XRD experiments and has been first introduced by Himbert *et al.* [8]. The protocol was optimized throughout this PhD.

100 mm diameter, 300 μm thick silicon wafers were pre-cut into 10×10 mm^2 chips. The wafers were cleaned with a solution of 15 ml sulfuric acid and 5 ml hydrogen peroxide (Piranha solution) resulting in a hydrophilic surface. Each wafer was then thoroughly rinsed with ≈50 ml of ultra pure water and placed on a hot plate (37 °C) in a 3-dimensional orbital shaker. 100 μl of the *RBC liposome solution* was pipetted slowly onto the wafer. The sample was covered with a tilted petri dish lid to allow the membrane solution to slowly dry over ≈12 h. The dried wafers were then incubated for 24 h at 97 % relative humidity and 37 °C by placing the samples in a sealed container with a saturated K_2SO_4 solution. This incubation step promotes the fusion of the dried RBC liposomes, resulting in a stack of RBCcms parallel to the silicon substrate.

Tuning the Lipid Composition of the RBC's Cytoplasmic Membrane

This section of the protocol is also described in my publication *Hybrid Erythrocyte Liposomes: Functionalized Red Blood Cell Membranes for Molecule Encapsulation* (Paper III) [21].

Aqueous solutions of synthetic lipid mixtures were prepared by dissolving 14 mg of lipids in 1 ml of ultra pure water. The solution appeared cloudy due to the formation of larger multilamellar liposomes ($1-10$ μm) and was subsequently tip-sonicated 20 times for 10 s each at a power of 100 W until the solution became clear. This sonicated solution will be referred to as *Lipid solution*. The *RBC liposome solution* was then mixed with the *lipid solution* in the desired ratio and tip-sonicated 20 times for 5 s each. The reaction tube was placed on ice to prevent the sample from overheating and subsequently centrifuged at 20,000 g for 20 minutes to remove any larger residues. In my publication [21], I studied the impact of DMPC, POPC, POPS and POPG onto the RBCcm's structure. Ratios of 1:4, 2:3, 1:1, 3:2, 4:1, and 9:1 (*RBC liposome solution*:*lipid solution*) were prepared for DMPC and POPC. The impact of POPS and POPG were studied in ratios of 4:1 and 9:1.

The homogeneous fusion of the RBC and synthetic membrane species requires

a two step process [21]. First, the solution is dried on to a silicon wafer as described above. This creates a 2-dimensional confinement of the membrane mixture. However, distinct, micrometer-sized patches of RBC-rich and RBC-poor areas were initially observed. Both membranes fused together during a subsequent incubation of the sample at 37 °C and 97 % relative humidity after which a patchy structure of the membrane was no longer detectable under the microscope.

Hybrid liposomes were synthesized by placing the silicon wafers in a reaction tube filled with 2 ml of ultra pure water with subsequent bath sonication for 1 h at 37 °C. This re-hydrates the membrane stack, resulting in the formation of multilamellar hybrid liposomes.

Molecules can be encapsulated within the liposomes by adding the molecule of interest at a concentration of 1 mg/ml to the aqueous solution when incubating the wafer. The sample was then centrifuged for 20 min at 20,000 g. The supernatant was removed and replaced with ultra pure water. This washing step was repeated twice to isolate the liposomes. This protocol was demonstrated in my publication [21] by using fluorescein labeled dextran (3 - 5 kDalton).

Anchoring Proteins in the RBC's Cytoplasmic Membrane

This section of the protocol is also described in my publication *Erythro-VLPs: anchoring SARS-CoV-2 spike proteins in erythrocyte liposomes* (Paper IV) [89]. The SARS-CoV-2 spike protein (S-Protein) was embedded into the RBCcm through a Triton-X 100 mediated insertion protocol to prepare erythrocyte-based virus-like particles (Erythro-VLPs).

Full-length S-protein was purchased from Acrobiosystems (SPN-C52H4). The protein was delivered in a lyophilized form and the sample also contained trehalose. This cryoprotectant was first removed through analytical size-exclusion chromatography with a Superdex 200 increase 10/300 analytical gel filtration column (GE Healthcare). The S-protein was eluted with ultra pure water and subsequently lyophilized.

The lyophilized state was preferred as it conveniently allows mixing the S-Protein and the RBC-liposomes by simply resuspending the S-Protein in 50 μl of the *RBC liposome solution*. The surfactant Triton-X 100 (9002-93-1, Sigma-Aldrich) was added at a concentration of 25 mM in order to promote the insertion of the protein into the RBCcm. The effect of Triton-X 100 is two fold: it solubilizes the membrane and stabilizes the trans-membrane domain. The sample was allowed to incubate for 3 h.

Of course it is required to remove Triton-X 100 from the solution. This was done by adding an excess of Amberlite XAD-2 (9003-70-7, Sigma-Aldrich). These non-polar polystyrene beads are commonly used to remove surfactants, such as Triton-X 100. The sample was incubated at room temperature for another 12 h. To remove any remaining Triton-X 100, not removed by the beads, the supernatant containing Erythro-VLPs was injected into an analytical gel filtration column and eluted with 8-fold diluted *PBS*.

3.2 X-ray Diffraction Experiment

3.2.1 Experimental Setup

X-ray diffraction experiments were performed on a RIGAKU SmartLab Diffractometer. A photograph of the setup is shown in Figure 3.3 A and the primary components are sketched in Figure 3.3 B. The instrument is equipped with a 9 kW CuKα rotating anode tube and a RIGAKU HyPix-3000 2-dimensional semiconductor detector. Multilayer optics consisting of a focusing mirror, a 5 degree soller collimator, and a 5 mm monocapillary collimator provide a circular beam with a diameter of $\approx$200 μm, a divergence of 0.008 rad and an intensity of 10^8 counts/mm^2·s. The wavelength is $\lambda = 1.5418$ Å with a spread of $\frac{\Delta\lambda}{\lambda}$=1 %.

The detector has an array of 775$\times$385 pixels, each measuring 100$\times$100 μm^2. Each pixel is a single photon counter with a bit-depth of 32 bit, in contrast to the widely used CCD based detectors which have a typical bit-depth of 16 bit. A beam-block was installed to attenuate the intensity from the direct, *i.e.* non-scattered, beam.

All samples were placed in a sealed humidity-controlled aluminum chamber during the measurements, as depicted in Figure 3.3 C. Aluminum is opaque for X-rays, so windows are machined on either side of the chamber and are sealed with a 13 μm thick kapton foil. This polymeric material was chosen for its high transmittance for X-rays and it's defined background; the diffraction signal of the Kapton windows consists of a powder diffraction peak at $|\mathbf{q}|$ $\approx$0.45 Å^{-1} (half-width at half-maximum $\approx$0.05 Å^{-1}). The sample is placed on a stage in the center of the chamber. A basin at the bottom of the chamber below the sample is filled with a saline solution. The temperature in the chamber is not controlled as the ambient temperature inside the X-ray machine is $\approx$30 °C. The humidity inside the chamber is controlled through the choice of salt and the salinity of the saline solution. Measurements on RBCcm were generally performed with two humidity

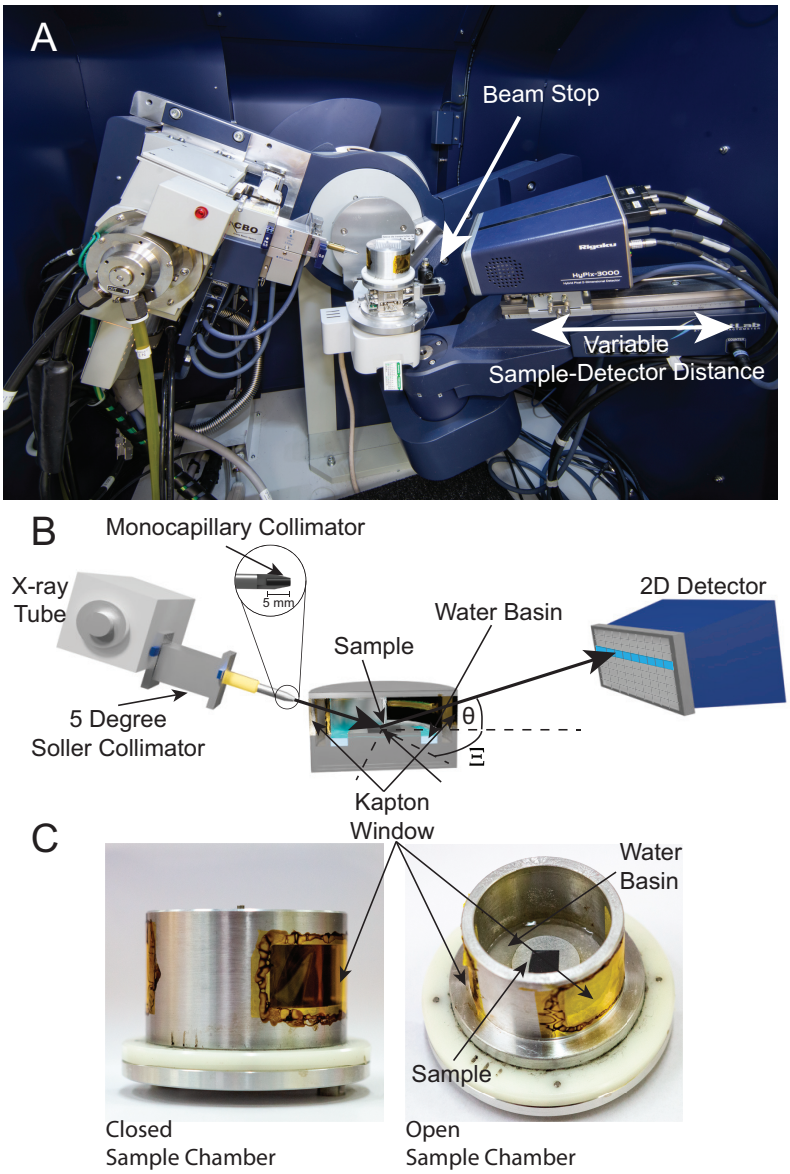

FIGURE 3.3: The setup of the X-ray diffraction machine is photographed in **A** and schematically sketched in **B**. The central components: X-ray tube, collimator optics, humidity chamber and detector are marked in the graphics. Close-up images of the open and closed sample chamber are presented in **C**.

settings: at ≈88 % RH using a saturated *KCl* solution and at 99.9 % RH by using a 40 mg/ml K_2SO_4 solution. The dry sample environment results in a small spacing between the membranes with suppressed out-of-plane fluctuations and was found to be ideal for high resolution structure determination of RBCcms. A measurement of the RBCcm's bending modulus κ and interaction modulus B requires the membrane stack to be in a fully hydrated state with a finite lamellar repeat distance d. RBC samples were found to be unstable when measured at 100 % RH. The membranes were found to be highly hygrosopcic and swell until the sample washed off the silicon wafer. The humidity was therefore lowered to 99.9 % RH.

Both the X-ray tube and the detector are mounted on movable arms and move on spherical coordinates. The detector moves along the meridional angle θ and the azimuth angle Ξ, while the source's movement is restricted to the meridional angle (see Figure 3.3 B for angle assignment). This avoids any movement of the sample during the measurement. The components q_z and $q_{||}$ of the scattering vector are perpendicular and parallel to the membrane surface, and can be determined from

$$q_z = \frac{4\pi \sin(\theta)}{\lambda} \qquad (3.1)$$
$$q_{||} = \frac{4\pi \sin(\Xi/2)}{\lambda}.$$

The instrument also allows the adjustment of the angular resolution of the measurement through manipulating the sample-detector distance L between ≈150 mm and ≈350 mm. This setting is not motorized and requires calibration after every adjustment using the instrument's control software.

A θ-scan is performed by first choosing a detector-sample distance and a fixed azimuth angle. The X-ray tube is then moved along the meridional angle θ thus altering the incident angle of the X-ray beam. The scattered intensity is then recorded by the 2-dimensional detector. However, only the pixel row which matches the specular condition in its center is read out for a given setting of θ (see blue highlighted pixel in Figure 3.3 B). The detector then follows along the meridional axis to cover the entire q-range of interest.

Multiple measurement protocols were used to collect the data presented in this thesis and are listed in Table 3.1. The in-plane scan was optimized to probe the RBCcm's in-plane structure; the out-of-plane scan was used to measure the lamellar repeat distance d and the electron density profile from a 1-dimensional Fourier analysis. The diffuse scan was optimized to measure XDS.

Scan	Parameters	q-range
In-Plane Scan	2 Scans (Panorama) L =150 mm 2θ=0-26° Ξ_0=12° and Ξ_0=35° 88 % relative humidity	$q_z = 0 - 1.9$ Å^{-1} $q_{\|\|} = 0 - 3.4$ Å^{-1}
Out-Of-Plane Scan	1 Scan L =350 mm 2θ=0-10° Ξ_0=0° 88 % relative humidity	$q_z = 0 - 0.8$ Å^{-1} $q_{\|\|} = -0.45 - 0.45$ Å^{-1}
Diffuse Scan	4 Scans (Integrated) L =350 mm 2θ=0-4° Ξ_0=0° 99 % relative humidity	$q_z = 0 - 0.3$ Å^{-1} $q_{\|\|} = -0.45 - 0.45$ Å^{-1}

TABLE 3.1: Parameters and q-range of the performed scans. Panorama refers to the stitching of two scans to cover a larger in-plane q-range; For integrated scans 4 scans with the same settings are performed and the intensities are added.

3.2.2 Analysis

The instrument saves the recorded data in the open *.img* file-format. The analysis capabilities of RIGAKU's proprietary software are limited, so a customized analysis library was developed in MATLAB.

Each file contains a 4096 byte long header formatted in the *American Standard Code for Information Interchange* (ASCII) followed by 32-bit binarized image data and can be read using MATLAB built-in functions. Scaled q_z and $q_{||}$ axis are not included in the file and need to be reconstructed from the instruments geometry.

It is important to recognize that the 2-dimensional flat detector subtends the spherical coordinate system spanned by the meridional angle θ and the azimuth angle Ξ and consequently measures a distorted image. This distortion can be corrected when taking into account the geometry of the X-ray instrument and the data acquisition by the detector. Let us first discuss pixels located at $q_{||} = 0$ Å^{-1}. It was emphasized above that the detector only records the pixel row matching the specular condition in its center and moves along the meridional angle otherwise.

Each pixel at $q_{||} = 0$ Å^{-1} thus covers a small fraction on the meridional arc. The data are consequently not distorted and the scattering angle for pixel k can be determined from L and the pixel height of 0.1 mm to be

$$\theta_k = \frac{0.1k}{L}\frac{360}{2\pi}. \tag{3.2}$$

This changes in the in-plane direction, as can be seen in Figure 3.4. The pixel position of the direct beam p_d on the detector at $\Xi = 0$ is measured by the instrument and is stored in the header. We can use this information to calculate the distance w_x of a given pixel in a single detector row to p_d. We can then determine the azimuth angle of pixel l as

$$\Xi_l = \Xi_0 + \tan^{-1}\left(\frac{w_x}{L}\right)\frac{360}{2\pi}, \tag{3.3}$$

where we account for a possible offset Ξ_0 of the detector. The out-of-plane and in-plane component of the scattering vector can be then calculated using Equation 3.2, once both angles are determined for a given dataset.

The developed library allows further options for the handling of multiple scans. Two or more scans can be summed to enhance statistics. Alternatively, scans at different settings of Ξ_0 can be stitched together resulting in a single scan that covers a larger $q_{||}$ range.

The 2-dimensional X-ray signals can be reduced in three different ways. Data can be integrated within a rectangular box either along the $q_{||}$ axis or the q_z axis. This option is used to determine out-of-plane intensity profiles ($q_{||} = 0$ Å^{-1}) and XDS profiles (see below). Alternatively, pixels for a fixed value $|\mathbf{q}|$ can be integrated. This last option is used to calculate 1-dimensional in-plane scattering profiles from a 2-dimensional intensity map. An exemplary 1-dimensional in-plane scattering profiles is depicted in Fig. 2.10 A.

The bending modulus κ and the membrane interaction modulus B can be measured independently from XDS signal, as it was introduced in Chapter 2. First, two 1-dimensional line cuts, each at a fixed value $q_z = q_z^1$ and $q_z = q_z^2$ (typical, $q_z^1 = 2q_1$ $q_z^2 = 2.5q_1$) were extracted from a 2-dimensional X-ray intensity map and then fitted simultaneously to Equation 2.11. Calculating $S(q_z, q_{||})$ is computationally intense and a program was thus written in C++ to analyze XDS data. The algorithm was based on the program introduced in [65] but was modified to allow for GPU acceleration with the Compute Unified Device Architecture (CUDA) provided by the Nvidia Corporation.

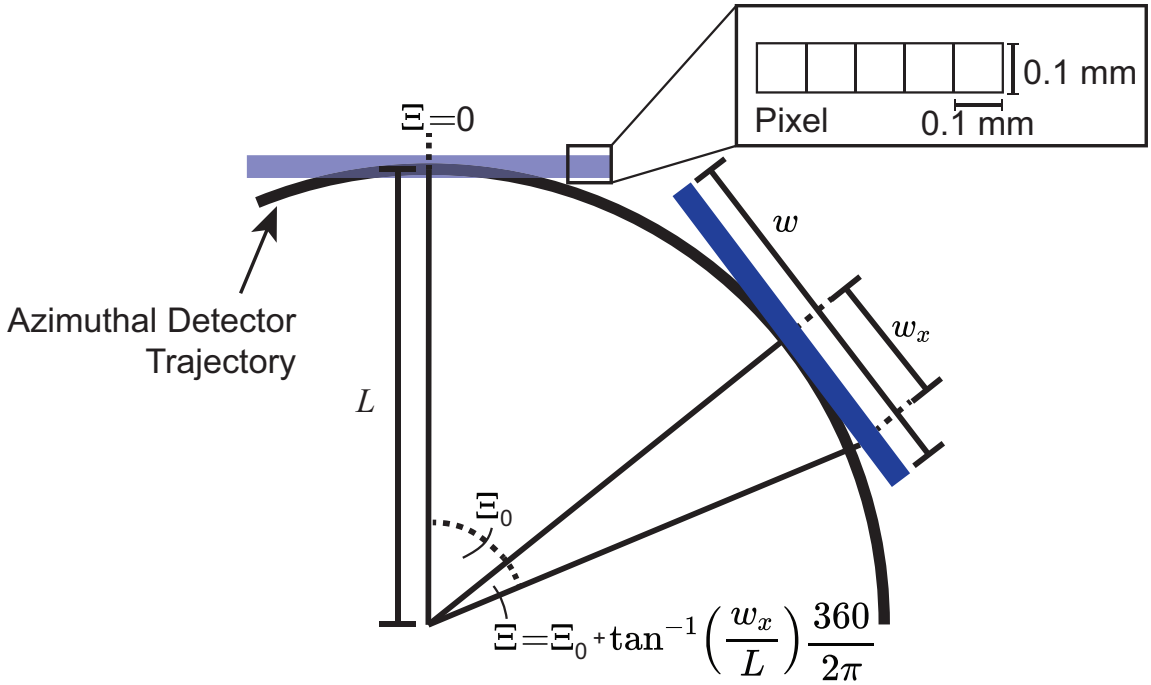

FIGURE 3.4: Instrument geometry in the in-plane direction. The flat detector (shown in blue) subtends the spherical in-plane coordinate system spanned by the azimuth angle Ξ and consequently measures a distorted picture. The azimuth angle Ξ can be calculated from Equation 3.3

GPU acceleration generally works by splitting the computation workload of a given problem between multiple processors. However, this requires the algorithm to be parallelizable, as can be explained on the example of numeric integration: the widely used trapezoidal rule splits the range of an integral into finite steps and approximates the integral by a sum of finite trapezoids. It is clear that the areas of the individual trapezoids solely depend on the number of steps and are independent of each other. They can be calculated *in parallel*. Adaptive methods such as the *gsl_integration_qagiu* algorithm adjust the number of steps dynamically during the algorithm's run-time to ensure a faster convergence. The number of trapezoids and the size of each trapezoid changes throughout the algorithm and thus requires a *serial* processing of these methods.

The CUDA toolkit allows splitting of a processing job into *threads* that are grouped in *blocks*. The number of *threads* per *block* is a hardware specific quantity. The maximum number of *block* is independent of the hardware and is only

limited by the CUDA toolkit [92]. As a result, a processing job can be split into as many *threads* as required. Of course, it should be remembered that the effective speed gain is limited by the hardware. The single Geforce GTX-1080 TI graphics card that was used for this thesis has 3584 physical CUDA cores and allows 1024 *threads* per *block*.

The flow diagram of the implemented algorithm is depicted in Figs. 3.5 and Figure 3.6. The program uses the *program_options* toolbox from the *boost* C++ library to handle user input and can operate in two modes: It can calculate the 2-dimensional structure factor for a given q_z and $q_{||}$ range, or it can fit a provided data set.

Both routines rely on an algorithm that calculates the structure factor for given values q_z, $q_{||}$, ξ, η and q_1. Calculating and fitting the structure factor in Equation 2.11 is non-trivial due to the nested integration and summation and requires computational approximations. First, it is important to appreciate that we can isolate a term that solely depends on q_z from the structure factor

$$\Lambda(r) = \sum_{n=-\infty}^{n=\infty} H_z(nD)\cos(q_z nD)G(r,n,q_z),, \tag{3.4}$$

allowing us to rewrite Equation 2.11

$$S(q_z, q_{||}) \quad = \quad \int_0^\infty rdrH_r(r)J_0(q_{||}r)\Lambda. \tag{3.5}$$

We can consequently calculate $\Lambda(r)$ only once for a given q_z before solving the integration in Equation 3.5 numerically for the desired values of $q_{||}$ (hereafter referred to as $q_{||}$-profile).

Furthermore, the functions $H_r(r)$ and $H_z(nD)$ were introduced to account for the finite size of membrane domains. This is convenient as it reduces the required range for n and r [62].

The first step in calculating $\Lambda(r)$ is to compute the height-height paircorrelation function $\delta u_n(r)$. It is computationally useful to use Equation 2.16 for $n < 30$ and $r < 1000$ and employ the widely accepted approximation [65]

$$\delta u_n(r) = \frac{4\eta_1}{q_1^2}\left[\gamma \ln\left(\frac{r}{\xi}\right) + 0.5E_1\left(\frac{r^2}{4n\xi^2}\right)\right] \tag{3.6}$$

for all other values for n and r. Further, it is important to appreciate that both equations for $\delta u_n(r)$ are independent of the scattering vector $\mathbf{q}$. Importantly, we

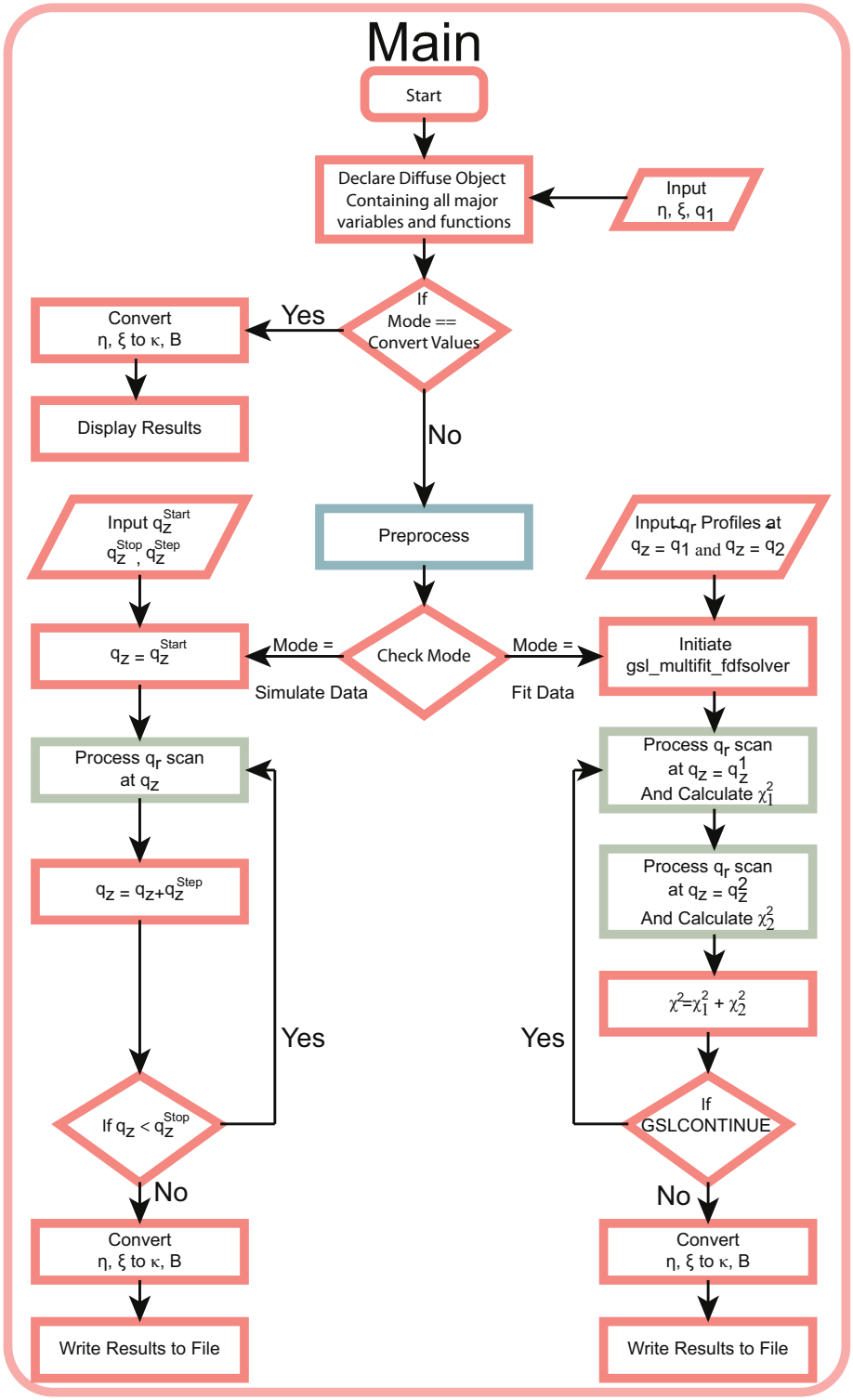

FIGURE 3.5: Flow diagram of the main program structure. Critical subroutines are highlighted in light blue and light green, and are visualized in greater detail in Figure 3.6.

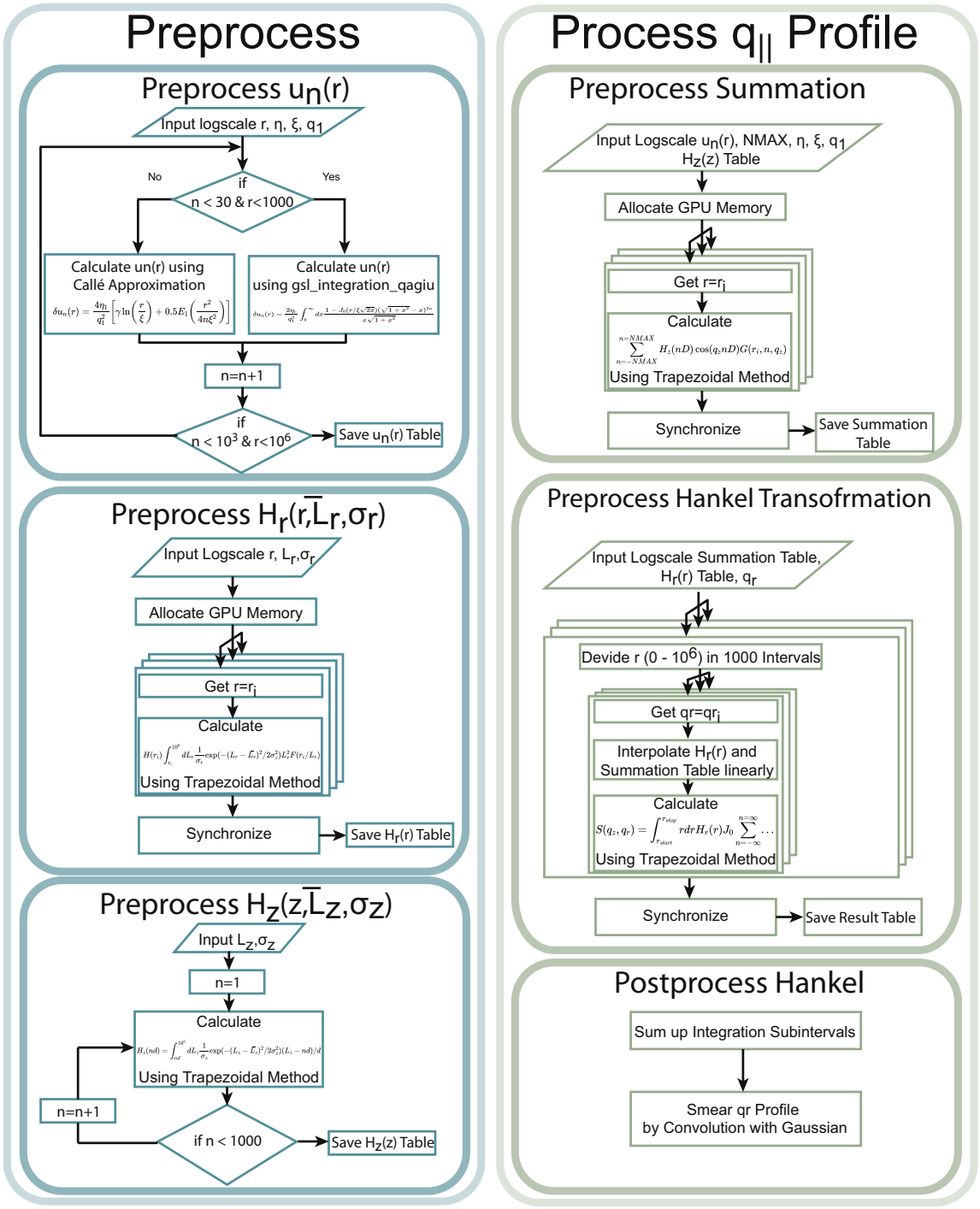

FIGURE 3.6: Flow diagram of the subroutines. The program pre-calculates arrays of the height-height paircorrelation function $\delta u_n(r)$ and the finite size effect functions (Eqs. 2.9 and 2.10) before calculating a single $q_{||}$ profile for given values of q_z, $q_{||}$, ξ, η and q_1.

can introduce the transformation $r = \bar{r}\xi$, where $\bar{r}$ is the radius for $\xi = 1$ and η=1. Any other combination of (ξ, η) can then be calculated by simply rescaling r:

$$\delta u_n(r, \xi, \eta) = \eta \delta u_n(\xi \bar{r}, 1, 1). \tag{3.7}$$

This enables us to calculate an array of $\delta u(r, 1, 1)$ at the beginning of the algorithm for logarithmically spaced floating point values $10^{-4} < r < 10^6$ and linearly spaced integer values $0 < n < 1000$. Equation 3.7 is then applied to calculate an array for $\delta u(r, \xi, \eta)$.

The integration in Equation 2.16 is performed numerically using the adaptive *gsl_integration_qagiu* algorithm provided by the GNU scientific library [93]. The trapezoidal rule can not be used due to the apparent singularity in the integrand in Equation 2.16 ($x \to 0$).

In the same way, arrays for $H_r(r)$ and $H_z(nd)$ (see Equation 2.9 and Equation 2.10) are pre-calculated. Again, logarithmically spaced floating-point values $10^{-4} < r < 10^6$ (10,000 values in total) and linearly spaced integer values $0 < n < 1000$ were used in the calculation.

The calculation of $H_r(r)$ is further accelerated using the CUDA toolkit by splitting the process into 10 *blocks* with 1024 *threads* each. Each *thread* then calculates the integration in Equation 2.10 for fixed values r and n and stores the results in an array.

In the next step, the algorithm calculates $\Lambda(r)$ (Equation 3.4) for integer values of $-1000 < n < 1000$ using the array entries from all predetermined functions. This process is split into 2 *blocks* with 1024 *threads* each. Each *thread* solely calculates the summation in Equation 3.4 for a given value r and stores the results in an array.

Finally, the program calculates Equation 3.5. The numerical integration is performed using the trapezoidal rule with $1 < r < 10^6$ and a step width of 1 Å. Values of Λ between the grid points of the predetermined arrays are determined from cubic interpolation. This process is once again parallelized. 2 *blocks* with 1024 *threads* each are defined, where each *thread* is instructed to compute the integration for a fixed value q_r.

Equation 2.11 represents the structure factor for a finite membrane stack, but does not account for characteristics of the X-ray instrument. In a real-world experiment, the structure factor is convoluted with the beam's footprint on the sample. The beam profile in the described setup is circular with a Gaussian distribution with a standard deviation of $\sigma_q = 0.004$ in both spatial directions. The determined $q_{||}$ profile is thus convoluted with a Gaussian distribution to account for this beam geometry.

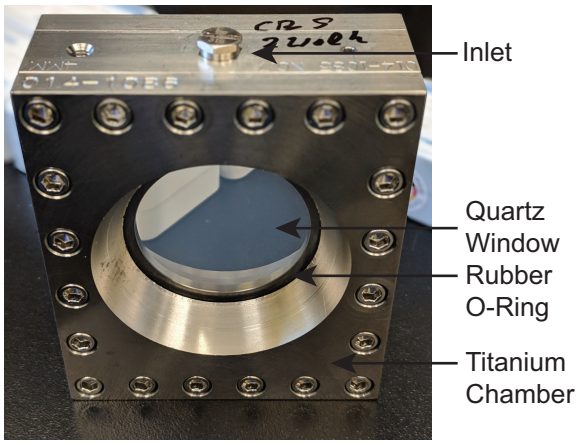

FIGURE 3.7: Sample chamber used for the NSE experiements: A circular cavity within a titanium block is sealed with quartz windows and rubber O-rings

Multiple $q_{||}$-profiles are calculated by looping through multiple setting of q_z to calculate a 2-dimensional scan of the structure factor $S(q_z, q_{||})$.

The bending modulus κ and the membrane interaction modulus B can be determined independently from XDS data by fitting the calculated structure factor at two different values of $q_z = q_z^{(1)}$ and $q_z = q_z^{(2)}$ to the experimental data.

For this purpose, a Levenberg-Marquardt least square fit was implemented using the *gsl_multimin_fminimizer* from the GNU Scientific library [93]. The function to be minimized is given by the sum of the squared residuals

$$\chi^2 = \chi^2(q_z^{(1)}) + \chi^2(q_z^{(2)}) = (Y_1[k] - y_1[k])^2/\sigma_1[k] + (Y_2[k] - y_2[k])^2/\sigma_2[k], \quad (3.8)$$

where $Y_j[k]$ is the interpolated value of $S(q_z, q_{||})$ at discrete values $q_z^{(j)}$ and $q_r^{(k)}$ and $y_j[k]$ are the corresponding experimental values. $\sigma_1[k]$ and $\sigma_2[k]$ are the experimental errors.

3.3 Neutron Spin Echo

One paper discussed in this thesis contains NSE measurements. Experiments were performed on the NGA-NSE spectrometer at the NIST Center for Neutron Research (NCNR) in Gaithersburg, MD, U.S.A. [94].

The sample consisted of RBC liposomes with a diameter of ≈200 nm immersed in heavy water (D_2O). The diameter was verified by dynamic light scattering prior shipping the samples to the NCNR and by small angle neutron scattering on site. Samples were filled in a custom made sample holder provided by the

NCNR, as depicted in Figure 3.7. The holder consists of a titanium block with a circular cavity with a diameter of 40 mm and a depth of 4 mm (capacity 20 ml). The cavity is sealed with quartz windows and rubber O-rings on either side. The entire holder is held together tightly by screwed titanium retainers.

Measurements were performed at q = 0.0523 Å^{-1}, 0.0664 Å^{-1}, 0.0794 Å^{-1} and 0.0959 Å^{-1} using wavelengths of λ = 8 and 11 Å, with a wavelength spread $\Delta\lambda/\lambda$ ≈0.18 [72], providing access to Fourier times ranging from 0.01 to 100 ns. The sample temperature was controlled by a recirculation bath with an accuracy of ±1 °C. All experiments were performed at a sample temperature of 37 °C. NSE data were corrected for instrumental resolution and solvent background using the DAVE software package [95]. Fits of the Zilman-Granek theory to the experimentally probed intermediate scattering function were performed in MATLAB using the spec1D library provided by the Institute Laue Langevin, Genoble, France.

3.4 Molecular Dynamics Simulations

MD simulations were performed on a GPU accelerated computer workstation using GROMACS Version 5.1.4. The device is equipped with a 40 Core central processing unit (CPU, Intel(R) Xeon(R) CPU E5-2630 v4 @ 2.20GHz), 130 GB random-access memory (RAM) and three graphic processing units (GPU, 2 × NVIDIA 1080 TI + 1 × GeForce GT 730).

Membrane models were created using the CHARMM-GUI membrane-builder (http://charmm-gui.org/) [96, 97] and the Martini force field 2.2 [97].

Martini is a coarse-grained force field, as was introduced in Chapter 2 and was specifically designed to simulate bio-molecules [88]. A RBCcm model can thus only approximate the exact membrane composition.

A program was written to represent the experimentally determined lipidomics with molecules that are available in the Martini force field. A flow diagram of this mapping program is shown in Figure 3.8. The program aims to represent each experimentally determined lipid with a Martini molecule by matching the tail length and degree of saturation.

This is done through calculating an error coefficient for every available model lipid. This error value is composed of an error of saturation E_{sat} and an error of tail length E_{tail}. E_{sat} is the difference in tail saturation between the model and the experimental lipid. In the same way, E_{tail} was defined as the difference in tail length. Let us illustrate this on the example of di22:1 PC. In Martini, each bead can represent multiple CH_2 groups and one model lipid can mimic an ensemble

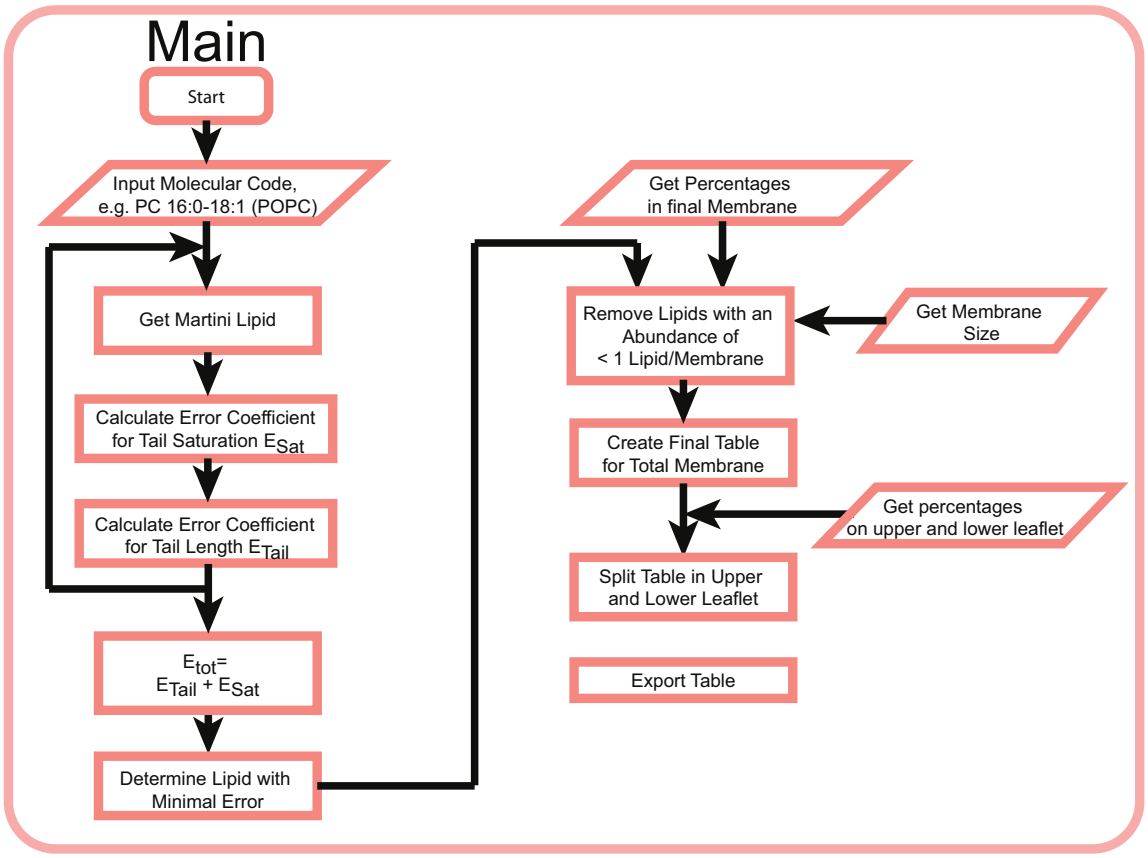

FIGURE 3.8: Flow diagram of the program used to map experimental lipidomics to available molecules in the Martini force field.

of tail lengths. The Martini lipid with two identical, 16-18 carbon atoms long tails and two double bonds per tail would result in an error value of $E = E_{sat} + E_{tail} = 2 \cdot (2-1) + 2 \cdot (22-18) = 10$. The Martini lipid with the smallest error value was then used for each experimental lipid respectively.

A membrane patch was then created from the list of mapped molecules by matching the relative lipid concentration to the experimental abundance. The finite size of the patch requires some molecules to have a concentration of less than one molecule per patch. These molecules were ignored when building the final model.

RBCcms are known to be asymmetric, with PS and PE lipids preferably located on the inner leaflet [7]. This asymmetry between different lipid species was

adjusted by using values for the compositional asymmetry published in previous coarse grained plasma membrane simulations [20]. For a given species, the simulated lipid population was split among both leaflets to match the relative abundance. For instance, PC lipids were split in a ratio of 3:1 between the upper and lower leaflet. Thus, simulated PC lipids were placed 75 % in the upper leaflet and 25 % in the lower leaflet.

RBCcms have a high cholesterol level of up to 50 mol% [90], which was consequently used in the design of the membrane patch. However, concentrations as low as 30 mol% have been used in the simulations of stored RBCcms to mimic maximal changes in the cholesterol concentration throughout storage [61].

The calculation of the fluctuation spectrum from simulation data requires an accurate interpolation of the function $u(\mathbf{r})$ at every time step of the simulation. To remind the reader, $u(\mathbf{r})$ describes local deviations of the bilayer center in the out-of-plane direction.

This is done by first calculating these local out-of-plane deviations for the headgroups of both leaflets respectively. The position of the headgroup beads of all lipid molecules (minus cholesterol) was exported in steps of 4 ns and the z position from all beads was interpolated using the 2-dimensional cubic interpolation provided by the MATLAB's built-in *griddata* function for both leaflets respectively. $u(\mathbf{r})$ was then determined by calculating the average displacement of the upper and lower leaflet. The 2-dimensional power spectrum was then determined using the built-in MATLAB function *fft2*. This spectrum was averaged over all exported time frames and subsequently reduced to a 1-dimensional spectrum. First, the reciprocal coordinates Q_x and Q_y were determined for all pixels. The 2-dimensional power spectrum was then integrated along concentric rings with $\sqrt{Q_x^2 + Q_y^2} = Q_{||} = const$. This spectrum was then fit to Equation 2.31 in the low $Q_{||}$-regime ($q < 0.1$ Å^{-1}) to determine the membrane's bending modulus κ.

Chapter 4

Paper I: The Bending of Red Blood Cell Membranes

4.1 Preface to: The Bending of Red Blood Cell Membranes

In this publication, we study the bending of the RBCcm on the nanoscale with a combination of XDS and NSE experiments as well as MD simulations.

The membranes are extracted from a freshly collected blood sample and are prepared as solid supported stacks (XDS) and RBC liposomes (NSE) as it was introduced in Chapter 3.

XDS experiments are conducted on the described in-house instrument using the optimized measurement protocol (see Table. 3.1). The analysis of XDS data is computationally challenging and requires the GPU accelerated computer program that is described in Chapter 3.

NSE experiments are performed on the NSE instrument at the NCNR in Gaithersburg, MD, USA. The bending modulus from these measurements was initially 10× higher than values obtained from XDS and MD simulations when using the *cmm* model in the analysis. However, this discrepancy is eventually resolved when considering the cholesterol concentration (≈50 mol% [11]) in the RBCcm and consequently applying the cholesterol model as it is emphasized in Chapter 2.

The experiments are complemented by MD simulations where a coarse grained model is specifically designed to mimic the RBC's lipidomics that is provided by Dr. Angelo D'Alessandro from Columbia University.

We measure a bending modulus between 2 and 5 k_BT, which is substantially lower than previously reported values on purely synthetic membranes.

To the best of my knowledge, this is the first time that the combination of these three techniques was applied to a biological membrane.

Status: in preparation

Author Contributions:

- Experimental Concept: **Sebastian Himbert**, Maikel Rheinstädter
- Sample Preparation: **Sebastian Himbert**, Syed M. Quadri, William P. Sheffield
- DLS Experiment: **Sebastian Himbert**, Michael J. Majcher, Todd Hoare
- Neutron Experiments: **Sebastian Himbert**, Michihiro Nagao, Maikel Rheinstädter
- X-ray Experiments: **Sebastian Himbert**, Maikel Rheinstädter
- Analysis Software Development: **Sebastian Himbert**
- MD Model Development: **Sebastian Himbert**, Angelo D'Alessandro
- Data Analysis: **Sebastian Himbert**, John F. Nagle, Maikel Rheinstädter
- Manuscript Preparation: **Sebastian Himbert**, John F. Nagle, Maikel Rheinstädter

The Bending Rigidity of the Red Blood Cell Cytoplasmic Membrane

Sebastian Himbert,[1,2] Angelo D'Alessandro,[3,4] Syed M. Qadri,[5] Michael J. Majcher,[6] Todd Hoare,[6] William P. Sheffield,[7] Michihiro Nagao,[8,9,10] John F. Nagle,[11,*] and Maikel C. Rheinstädter[12,13,†]

[1] *Department of Physics and Astronomy, McMaster University, Hamilton, ON, L8S 4M1, Canada*
[2] *Origins Institute, McMaster University, Hamilton, ON, L8S 4M1, Canada*
[3] *Department of Pathology and Cell Biology, Columbia University Vagelos College of Physicians and Surgeons and New York-Presbyterian Hospital, New York, NY 10032, USA*
[4] *University of Colorado Denver-Anschutz Medical Campus, Aurora, CO 80045, USA*
[5] *Faculty of Health Sciences, Ontario Tech University, Oshawa, ON L1H 7K4, Canada*
[6] *Department of Chemical Engineering, McMaster University, Hamilton, ON L8S 4M1, Canada*
[7] *Department of Pathology and Molecular Medicine, McMaster University, Hamilton ON L8S 4M1, Canada*
[8] *Center for Neutron Research, National Institute of Standards and Technology, Gaithersburg, MD 20899, USA*
[9] *Department of Physics and Astronomy, University of Delaware, Newark, DE 19716, USA*
[10] *Department of Physics, University of Maryland, Maryland, MD 20742, USA*
[11] *Department of Physics, Carnegie Mellon University, Pittsburgh, PA 15213, USA*
[12] *Department of Physics and Astronomy, McMaster University, Hamilton, ON L8S 4M1, Canada*
[13] *Origins Institute, McMaster University, Hamilton, ON L8S 4M1, Canada*

(Dated: September 23, 2021)

An important mechanical property of cells is the membrane bending modulus, κ. In the case of red blood cells (RBCs) there is a composite membrane consisting of a cytoplasmic membrane and an underlying spectrin cytoskeleton. Literature values of κ are puzzling, as they are reported over a wide range, from 5 to 230 k_BT. To disentangle the contribution of the cytoplasmic membrane from the spectrin network, we investigated the bending of red blood cell cytoplasmic membranes (RBCcm) in the absence of spectrin and also no ATP. We used a combination of X-ray diffuse scattering (XDS), neutron spin-echo (NSE) spectrometry and Molecular Dynamics (MD) simulations. Our results indicate values of κ of order 4 to 6 k_BT, relatively small compared to literature values for intact RBC membranes, and for most single component lipid bilayers. We suggest that this relative softness may have biological advantage.

Keywords: red blood cell membrane, bending modulus, blood storage

SIGNIFICANCE

It has been challenging to understand the widely disparate reported values of the bending rigidity of the complex RBC shell. By isolating the membrane of red blood cells and removing the spectrin network, we determined that the bending modulus of just the RBCcm cytoplasmic membrane is quite small compared to the value obtained for the entire macroscopic RBC shell. This makes sense because the cytoplasmic membrane should dominate the elastic behavior at length scales smaller than the 80 nm length scale of the spectrin mesh, and this is the length scale that is relevant for oxygen permeability and other biochemical processes that should be facilitated by a soft, fluid membrane environment.

Cellular functions, such as mobility, division and vesicle trafficking, are intrinsically related to a cell's ability to comply to deformation.[1–3]. In the case of red blood cells (RBCs) that have no internal structure, this ability depends upon its two-dimensional "shell", which consists of a spectrin cytoskeleton tethered to a cytoplasmic membrane.

A suite of techniques has been used to study cell elasticity. Mechanical properties on cellular length scales are measured by micropipette aspiration[4], while atomic force microscopy (AFM)[5] probes elastic behavior on the nanoscale. Cell stiffness is studied indirectly by spectral analysis of flickering of cells under a microscope[6–8], as well as optical interferometric techniques[9,10].

A particularly appropriate measure of elasticity is the bending modulus κ, which gives the energy required to bend away from the resting state. Table 1 shows values for the bending modulus κ of RBCs that have been reported over the years, ranging from 5 to 230 k_BT[4,6–9,11,12]. A reasonable hypothesis for this disparity is that the bending modulus depends on the length scale of the measurements.[13] On length scales smaller than the mesh size of the cytoskeleton of $\approx$ 80 nm, the average bending modulus could be due mostly to the cytoplasmic membrane, while the spectrin network would add a contribution at longer length scales. When measuring RBC elasticity on small length scales, values for κ of 5 k_BT[7] and 7 k_BT,[14] have been reported in contrast to the much larger values for length scales of the entire RBC[4,8,11,12]. According to the above hypothesis, this would imply a substantial bending modulus for the

* nagle@cmu.edu
† rheinstadter@mcmaster.ca

Technique	κ (k_BT)	Lengthscale (μm)	Reference
Literature	RBC		
Optical Tweezer	68	1-7	12
Diffraction Phase Microscopy	219	0.7-7	11
Micropipette Aspiration Buckling	43	1-2	4
Reflection Interference Microscopy	97	1-2	8
Reflection Interference Microscopy	5	0.25-3	7
Diffraction Phase Microscopy	20	0.1-5	10
Reanalysis of[10]	14,25	0.1- 5	13
Diffraction Phase Microscopy	7	0.1-5	9
This paper	RBCcm		
Diffuse X-ray Scattering	2 - 6		
Neutron Spin Echo	4 - 7		
Molecular Dynamics	4		

TABLE 1. A summary of values reported for the bending rigidity, κ, of discocytic intact ghost red blood cells from the literature and our RBC_{cm} membranes.

cytoskeleton. It may be noted, however, this is inconsistent with a report that the bending modulus of the cytoskeleton is very small.[15]

Supposing that the bending modulus of the cytoplasmic membrane is only of order 6 k_BT, it is noteworthy that this κ is significantly smaller than bending rigidities reported for single component lipid bilayers of similar thickness that have values of κ typically between 15 and 50 k_BT[16–29]. It is further intriguing that the cytoplasmic membrane contains considerable cholesterol which is conventionally thought to stiffen lipid membranes, although that depends on the lipid.[20]

Here we measure the bending rigidity of the RBC's cytoplasmic membrane to clearly separate the elastic contribution of the membrane from that of the spectrin network. We will call these RBCcm. Our samples also have no ATP, which has sometimes been reported to affect membrane fluctuations[12,30], but sometimes not[11]. Solid-supported multi-lamellar RBC membrane stacks were prepared for measurements of X-ray diffuse scattering (XDS), and unilamellar RBC liposomes were prepared for neutron spin-echo (NSE) spectroscopy. We also performed coarse grained MD simulations of multicomponent membranes that essentially matched the lipid composition of the RBC membranes in the experiments. Table 1 shows our values of κ to facilitate comparison with literature values.

RESULTS

X-ray diffuse scattering

The geometry of X-ray reflectivity experiments on stacks of membranes is depicted in Fig. 1 A. The most intense scattering is specular ($q_{||} = 0$ Å^{-1}); as shown in Fig. 1 B this includes peaks due to the average lamellar repeat distance in the stack of membranes, and it includes the sharp line of reflectivity from the silicon substrate. Only two lamellar repeat spacing peaks are visible for

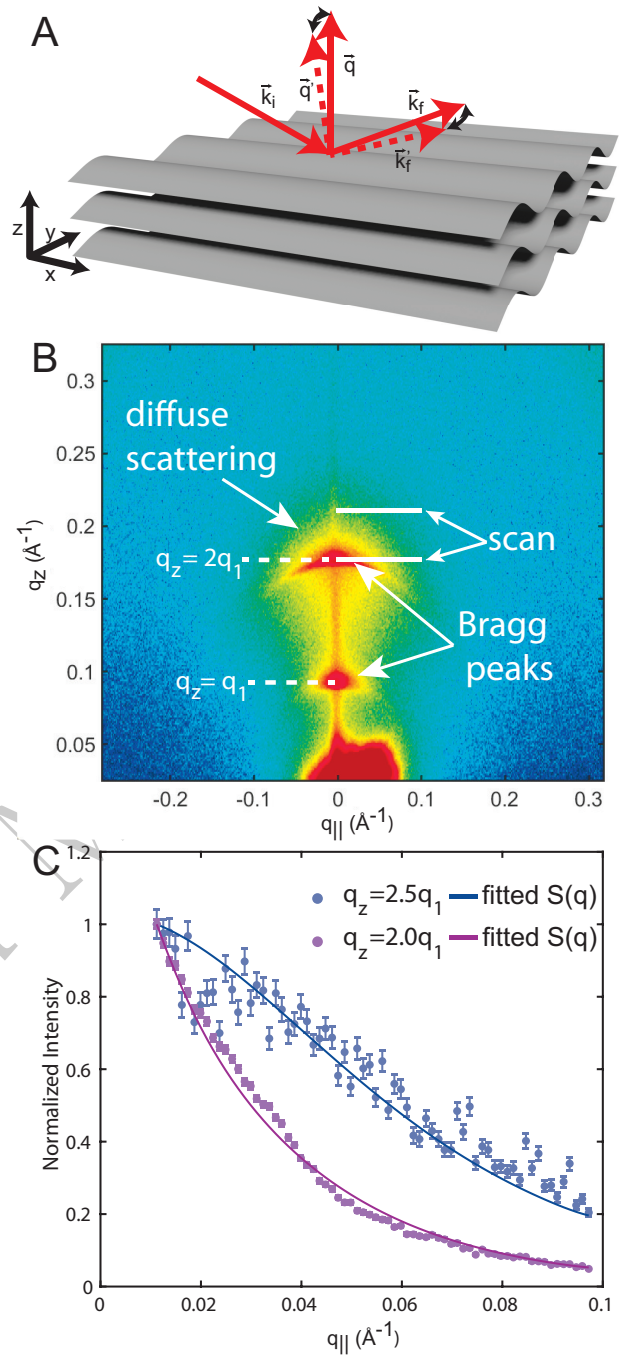

FIG. 1. **A** Schematic of a stack of fluctuating membranes and the geometry of specular ($q_{||} = 0$) and off-specular ($q_{||} \neq 0$) X-ray scattering. **B** q-space X-ray intensity map of a solid supported RBC membrane stack. Two orders of lamellar peaks surrounded by diffuse X-ray intensity are visible. The white lines show the locations and ranges of the data presented in the next panel. **C** Off-specular intensities at $q_z = 2q_1$ and $q_z = 2.5q_1$, normalized to the respective X-ray intensity at $q_{||} = 0.01$ Å^{-1}). Fits of the structure factor $S(q)$ following Eq. (4) are shown as solid lines.

the RBC samples, indicating a high degree of structural disorder within each membrane. The first order peak was observed at q_1=0.084 Å^{-1} corresponding to a membrane d-spacing of d = 74.8 Å. Most importantly for elastic properties, a cloud of diffuse off-specular scattering was observed. Fig. 1 C displays the $q_{||}$ dependence for $q_z = 2q_1$ and $q_z = 2.5q_1$.

Off-specular scattering ($q_{||} \neq 0$ Å^{-1}) is due to thermal fluctuations of membrane undulation modes and compression modes of the stack of membranes. The energy of these fluctuations is given by smectic liquid crystal elastic theory as[22,31]

$$H = \int_A d^2r \sum_{n=1}^{N-1} \frac{1}{2}\left(\kappa\left(\nabla_{||}^2 u_n\right)^2 + B(u_{n+1}-u_n)^2\right), \tag{1}$$

where u_n is the locally varying displacement. κ is the bending modulus, B is the compression modulus, N is the number of membranes and d is the lamellar spacing between neighboring membranes. Given values of κ and B this model predicts the structure factor $S(q_z, q_{||})$[32] which contains the important $q_{||}$ dependence of the diffuse scattering intensity. The best values for the samples were obtained by varying κ and B to provide the best fit of this model to the off-specular diffuse intensity. Values of κ=2 k_BT and B=2·10^{-7} k_BT/Å^4 were determined, and are listed in Table 1.

Neutron spin echo

Membrane dynamics are measured in unilamellar vesicles by NSE. The precession of the neutron spin in a well-defined magnetic field is used to determine the energy transfer between neutrons and membranes on length scales of ≈10 nm. The basic set up of the experiment is shown in Fig. 2 A. Nanometer sized RBC liposomes were immersed in D_2O and mounted in a custom-made titanium chamber. Details of the experimental setup are described in *Materials & Methods*. The liposome size distribution was measured by dynamic light scattering (DLS) and small angle neutron scattering (SANS) prior to the experiment, giving respective diameters of 199 ± 3 nm (polydispersity index: 0.1 ± 0.01) and 189.8± 5.5 nm (polydispersity index: 0.15 ± 0.03), as shown in Fig. S2 in the *Supplementary Material*. Data for the intermediate scattering function were fitted to the Zilman and Granek[33] theory, as shown by solid lines in Fig. 2. The inset shows the decay constant Γ versus q. These values of Γ were then used to obtain the dynamical bending modulus $\tilde{\kappa}$ using

$$\Gamma(q) = 0.025\left(\frac{k_BT}{\tilde{\kappa}}\right)^{1/2}\left(\frac{k_BT}{\eta}\right)q^3, \tag{2}$$

where k_BT is thermal energy and η is the solvent viscosity.

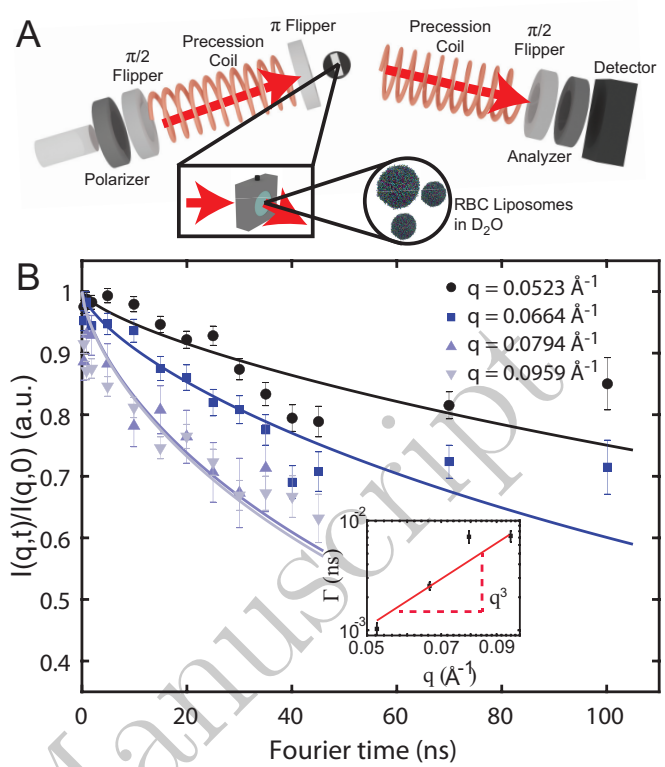

FIG. 2. **A** Experimental setup of the NSE experiment. 6 ml of RBC liposomes immersed in D_2O at a concentration of 20 mg/ml were filled in custom made titanium/quartz chambers provided by the NIST Center for Neutron Scattering (NCNR). **B** Intermediate scattering function $I(q,t)/I(q,0)$ at q =(0.0523, 0.0664, 0.0794 and 0.0959) Å^{-1}. Data were fitted by Eq. (9). The inset shows the determined decay constant Γ is graphed versus the scattering vector q. Data were fitted with a q^3 dependency as predicted by the Zilman-Granek (ZG) Theory and a bending modulus of 4 k_BT was determined using the *cholesterol model*.

The theory of Watson and Brown[34] relates the dynamical bending modulus $\tilde{\kappa}$ to the customary bending modulus κ by the formula

$$\tilde{\kappa} = \kappa + h^2 K_A, \tag{3}$$

that also involves the area compressibility modulus K_A and the distance h of the neutral surface of each monolayer from the bilayer midplane. To obtain κ it is necessary to eliminate K_A. As detailed in *Materials and Methods*, the value of κ = 4 k_BT listed in Table 1 is the result of a model that is appropriate for bilayers with a high concentration of cholesterol.[35]

Molecular dynamics simulations

We used results from mass spectrometry on extracted lipids from native RBCs[36] for the composition of the RBC membranes. The cholesterol concentration was

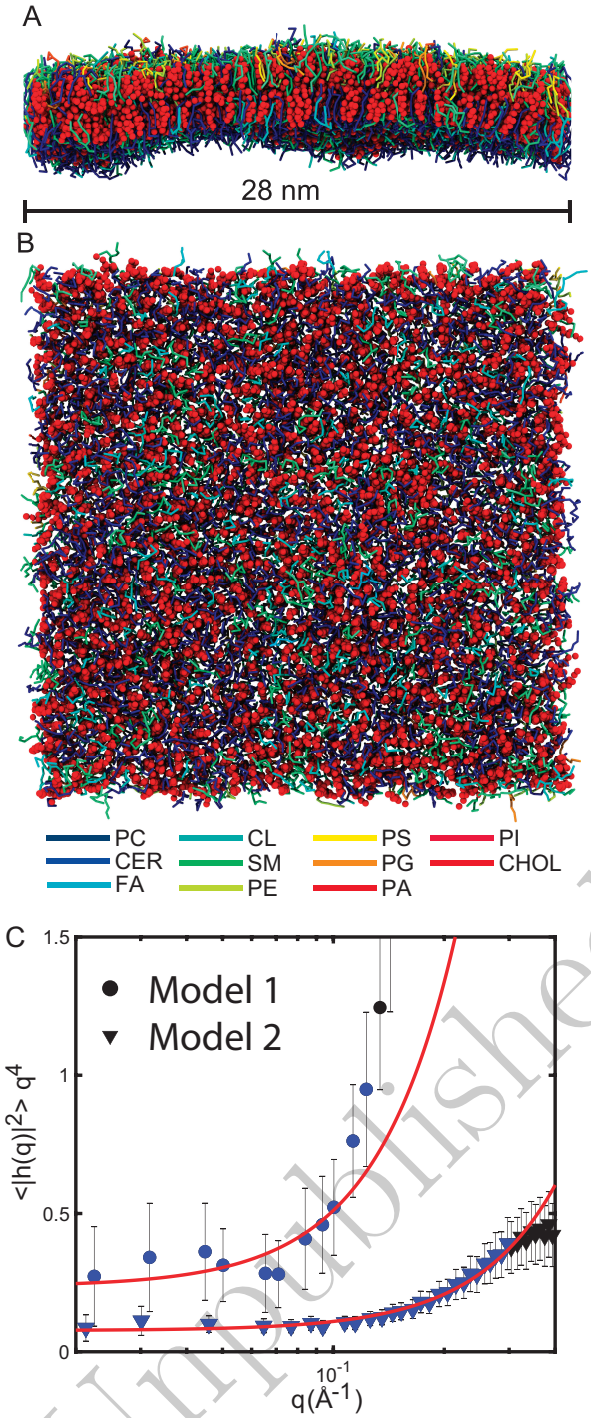

FIG. 3. 3-dimensional renders of the *undulation simulation* after 1 μs (side-view **A** and top-view **B**). Lipid molecules are represented by rods representing intra-molecular bonds. Each lipid species (Phosphatidylcholine, PC; Ceramide, CER; Monoglucosyl lipids, MG; Diacylglycerol lipids, DG; Fatty acids, FA; Sphingomyelin, SM; Phosphatidylethanolamine, PE; Phosphatidylserine, PS; Phosphatidylglycerol, PG; Phosphatidic acid, PA; Phosphatidylinositol, PI) are represented by different colors indicated in the legend. Cholesterol (CHOL) is symbolized by red spheres. **C** The fluctuation spectrum determined from the *undulation simulation* averaged over the last 800 ns. The fit of Eq. (12) onto the data is depicted as red solid line. The fit range was $q < 0.2$Å^{-1}

not determined but taken from[37] reporting a cholesterol to lipid ratio of ≈ 1. Two membrane models containing $\approx$ 5,000 molecules forming a patch of $\approx$ 30 nm $\times$30 nm were created. For the first model, the determined membrane composition was recreated in coarse grained MD simulations by mapping experimental lipids to the molecules available in the MARTINI force-field. This model will be referred to as *Model 1* In second model, we removed any lipid molecule with more than 2 unsaturated bonds per tail. We will call this model *Model 2*. Cholesterol accounted for 50 mol% of both membrane models. Details about the mapping process can be found in *Materials & Methods* and the model composition is listed in Tab. S1 in the *Supplementary Material*. Fig. 3 A and B show a 3-dimensional rendering of *Model 1* (side- and top-view).

The undulation spectrum was determined and is shown in Fig. 3 C. It has a q^4 dependency in the low-q regime (q <0.2 Å^{-1}) in good agreement with the Helfrich–Canham (HC) theory (Eq. (12)). This theory models the membrane as an elastic sheet and is only valid for length scales much larger than the membrane thickness, *i.e.* small q[38,39]. The measured spectrum consequently differs from the q^4 dependency for q >0.2 Å^{-1} due to molecular tilt that is characterized by the tilt modulus K_t[40]. Fits of Eq. (12) for values of q <0.2 Å^{-1} are displayed as a red solid line from which the bending modulus and tilt modulus were determined to be κ =4.2±0.8 k_BT and K_t=3.63±1 k_BT. Determining the bending modulus in asymmetric membranes is non-trivial because an uneven area per lipid in both leaflets[41] can potentially induce curvature, which can impact the results. Simulations on membrane patches with symmetrized upper and lower leaflet were thus conducted. We find values of 5 and 6 k_BT, respectively (shown in Fig. S4 in the *Supplementary Material*), in good agreement with the asymmetric membrane that confirm our results. The bending rigidity and the membrane's tilt modulus were both found to increase in *Model 2* and values of $\kappa = 13 \pm 0.6$ k_BT and $K_t = 30.4 \pm 1.5$ k_BT were determined.

DISCUSSION

The bending rigidity of red blood cells has been reported many times, as shown in Table I. Interestingly, the smallest $\kappa = 5$ k_BT came from the same lab as one of the largest values.[7,8] Likewise, the value of 20 k_BT was later reduced to 7 k_BT[10,14]. The disparate experimental results have been appropriately described as puzzling[8,13]. However, correlation of the magnitude of κ with the length scale of the experiments has been noted,[13] with the larger values generally coming from measurements on the length scale of the whole cell, such as buckling in an aspiration pipette experiment[4], spectral analysis of membrane fluctuations observed in microscopy experiments (κ=97 k_BT[8], κ=68 k_BT[12], κ=218 k_BT[11]) and deformations induced by optical

tweezers (κ=67 k_BT[12]). The smaller values in Table I by Brochard *et al.* (κ=12 k_BT,[6]), and Park *et al.* (κ=7 k_BT[9]), Zilker *et al.* (κ=5 k_BT[7]) come from length scales of the order of the wavelength 400 *nm* of the optical methods employed. Our results for κ are a bit smaller. One might be tempted to attribute this to even smaller length scale of 1-10 nm of our three methods. However, this would be misleading because there is only one true value of the Helfrich κ for a homogeneous RBCcm membrane, which is independent of length scale. This value will apparently change at small length scales due to second order local features, such as molecular tilt, that are not included in the first order Helfrich theory. This is clearly revealed by the high q simulation results in Fig. 3.

Unfortunately, we can not use higher order elastic theory with our NSE data because there is no existing analysis. While a higher order analysis of XDS data has been employed to obtain the higher order tilt modulus for single component bilayers[24], our RBC data are not strong enough to employ that analysis. Nevertheless, the higher order analysis shows that inclusion of a tilt modulus increases the value of κ for typical bilayers by 25-50%. For RBCcm we can make an independent estimate of the increase in κ due to the higher order theory, as described in *Supplementary Material*. This estimate gives the upper range value of 6 k_BT, shown in Table 1 for the XDS method.

As has been widely recognized, the reason that the RBCs' κ appears to be length scale dependent is that previous methods have measured the apparent κ for the composite structure of a bilayer tethered to a spectrin network and it was previously speculated that these apparent controversial results can be explained by the complex interplay between the membrane bilayer and the cellular cytoskeleton[8]. While the cytoplasmic membrane is homogeneous on the lateral length scale of 10 nm, the spectrin cytoskeleton has a mesh size of order 80 nm. As has been emphasized[13,42], one would therefore expect a corresponding crossover with varying length scale in the value of an effective bending modulus κ, especially if that is the primary parameter in the analysis. The most recent analysis[9] recognized this and included other parameters combined with theory for dynamic optical measurements to obtain $\kappa = 6.7\pm3.3$ k_BT for the cytoplasmic membrane but with a disconcertingly small value of K_A = 15.5±2.5 μN/m for the area compressibility modulus compared to directly measured values.[4?]

In contrast, we have measured κ on length scales smaller than the bond length of the cytoskeleton to probe the bending rigidity of the RBC_{cm} directly. Using our prepration protocol of sonication with subsequent centrifugation of RBC ghosts[43], spectrin filaments were no longer detectable by fluorescent microscopy. In addition, the d-spacing in XDS experiments together with electron density profiles are inconsistent with the presence of cytoskeleton structures between membranes in the solid supported stack. We thus argue that our results measure the bending modulus of the cytoplasmic RBC membrane in the absence of the spectrin cytoskeleton. While our values tend to be smaller than those of Park *et al.*[9], their measurements were in an excess of 100 nm length scale, somewhat larger than the cytoskeleton network, so an even larger difference might have been expected. In any case, there is considerable overlap within the considerable quoted uncertainties for κ.

These considerations for the two experimental methods lead us to suggest that RBCcm have a value of κ in the range of 4 to 6 k_BT. Even though this is a rather large uncertainty range, it is still significant in that the bending modulus of the RBCcm is relatively small compared to most pure lipid bilayers, such as POPC, for which κ is of order 20 k_BT[18]; this is also the value that we obtained by our analysis of POPC XDS data in this study to confirm the validity of our implementation of the XDS method.

The MD simulations were conducted in the absence of any proteins in order to specifically study the influence of the lipid membrane on the bending modulus. The analysis of the XDS experiment is based on smectic elastic theory and does not include potential protein induced local curvature. Simulating a bilayer in the absence of proteins thus allows a direct comparison between both methods and provides insight into the contribution of the lipid bilayer to the membranes' bending rigidity. The simulated value of κ essentially agrees with those from XDS and NSE. This suggests that κ can in first order be well approximated by the properties of just the lipid membrane.

The observed low bending rigidity in the experiment and simulation is surprising as it contrasts values that are typically measured on synthetic membranes (20 $k_BT < \kappa < 50$ k_BT) and may be well attributed to the large lipid diversity in this biological membrane. A particularly interesting observation in this context is the increase in both the bending rigidity and tilt modulus in the simulation of *Model 2*. This suggest that the softness may be partially explained by the presence of lipids with higher degrees of tail unsaturation within the RBCcm.

The nanoscopic regime is most relevant for cellular processes which take place between the ribs of the cytoskeleton. Especially the non-active transport of small molecules is intrinsically related to the membrane's properties on small length scales[44]. Specifically, red blood cells are required to efficiently exchange oxygen across the membrane and one may speculate that this soft nature at the small length scale is physiologically valuable.

In summary, we have studied the bending of red blood cell membranes by combining X-ray diffuse scattering, neutron spin echo spectrometry and molecular dynamics simulations. We determine values for κ for the cytoplasmic component of the RBC between 4 to 6 k_BT, which is rather softer than most single component lipid bilayers. This leads us to suggest that nature has designed the RBC to be soft for regions involved in the permeability of oxygen while providing overall stiffness for the macroscopic elasticity of the complex shell.

MATERIALS & METHODS

This research was approved by the Hamilton Integrated Research Ethics Board (HIREB) under approval number 1354-T. Informed consent was obtained from all blood donors. The authors confirm that all methods were performed in accordance with the relevant guidelines and regulations. Certain trade names and company products are identified in order to specify adequately the experimental procedure. In no case does such identification imply recommendation or endorsement by the National Institute of Standards and Technology, nor does it imply that the products are necessarily the best for the purpose.

Preparation of RBC liposomes

10 ml of blood samples were collected from volunteers in heparanized blood collection tubes. RBC liposomes were then prepared from all samples following a previously published protocol[43]. Briefly: The blood was washed twice and the RBCs were isolated by successive centrifugation and replacing the supernatant with phosphate saline buffer (PBS). The cells were exposed to osmotic stress by mixing hematocrit with lysis buffer (3 % PBS buffer, pH 8) at a volume fraction of 5 %. The lysis buffer was pre-chilled to ≈ 4 °C and the reaction tube was immediately stored on ice to prevent a fast re-closing of the ruptured cells. Hemoglobin and other cellular compartments were removed through multiple washing steps, as demonstrated in[43]. The protocol results in a white pellet containing empty RBC vesicles, commonly known as RBC ghosts.

These RBC ghosts were suspended in heavy water (D_2O) in the case of the NSE experiment: the supernatant was removed from the pallet and the tube was refilled with D_2O. The sample was centrifuged at 20,000 g for 20 minutes and the resulting supernatant was subsequently replaced with D_2O. This step was repeated twice. This buffer exchange was obmitted when preparing the samples for the XDS experiment.

The resulting ghost solution was then tip sonicated 20 times for 5 s each at a power of 100 W. The reaction tube was placed on ice during sonication to prevent the sample from overheating. Afterwards, the tube was centrifuged for 15 min at ≈ 20,000 g. This additional centrifugation step was found to be an efficient method for removing remaining undesired structures from the solution: The supernatant consists of a solution of large unilamellar vesicles (LUV, Diameter: 199 nm , PID = 0.1) while any larger structures sediment into a pellet. This supernatant has an approximate concentration of ≈ 14 mg/ml[43] and will be hereafter referred to as the *membrane solution*.

Multi-lamellar, solid supported membranes were prepared for the X-ray experiments. Membranes from the *membrane solution* were applied onto single-side polished silicon wafers. 100 mm diameter, 300 μm thick silicon wafers were pre-cut into 10×10 mm^2 chips. The wafers were functionalized with a solution of 15 ml sulfuric acid and 5 ml hydrogen peroxide (Piranha solution) resulting in a hydrophilic surface. This strong oxidizing agent removes all organic contaminants on the surface, but does not disturb the native silicon oxide layer. Each wafer was then thoroughly rinsed with ≈ 50 ml of ultra pure water (18.2 MΩ·cm) and placed on a hot plate (37 °C) in a 3-dimensional orbital shaker. 100 μl of the *membrane solution* was pipetted slowly onto the wafer. The sample was covered with a tilted lid of a petri dish and to allow the membrane solution to slowly dry within ≈ 12 h. The dried wafers were further incubated prior to the experiment at 97 % relative humidity and 37 °C for 72 h by placing the samples in a sealed container with a saturated K_2SO_4 solution. This allows the membranes to assemble into an oriented multilamellar stacked structure. Given the concentrations above, this translates into a thickness of the membrane stack of ≈18 μm, when assuming an average area per lipid of 0.5 nm^2, an average molar mass per lipid molecule of 700 g/mol and a membrane thickness of 6 nm.

The *membrane solution* suspended in D_2O were used for the neutron spin-echo experiments to create a strong scattering contrast between the protonated RBC membranes and the surrounding solution. The liposome solution was brought to a final concentration of 20 mg/ml. First the sample was centrifuged at 20,000 g for 20 minutes and the supernatant replaced by D_2O. This process was repeated twice. ≈ 6 ml of this solution was filled in custom made sample holders provided by the NIST Center for Neutron Scattering (NCNR). All samples were sealed prior to the shipment to the National Institute of Standards and Technology (NIST) in Gaithersburg, MD, U.S.A. The vesicle diameter was measured using DLS prior to shipment and a diameter of 199 nm (polydispersity index = 0.1) was determined. The diameter was further confirmed in small angle neutron scattering experiments at NIST simultaniously to the NSE experiments. A value of 189.6 nm (polydispersity index = 0.145) was determined confirming that the vesicle did not aggregate during shipment. Importantly, the SANS data showed no multilamellar peak confirming that the vesicles have a unilamellar structure.

X-ray diffraction

X-ray scattering experiments were performed using a rotating anode instrument equipped with a Rigaku HyPix-3000 2-dimensional semiconductor detector. Details of the experimental setup and protocol can be found in the *Supplementary Material*. The membrane bending modulus κ and the membrane interaction modulus B and were determined from measurements of the diffuse scattering when the membranes were well-hydrated from water vapor close to 100 % relative humidity. The analysis was similar to previous studies[17–21,32], although the different experimental setup required a modification that is detailed in *Supplementary Material*. Basically, the $q_{||}$ dependence of the intensity $I(q_z, q_{||})$ is proportional to a constant times the so-called structure or interference factor $S(q_z, q_{||})$. (The constant is related to the electron density profile which is not of concern in this paper and is a simple linear fitting parameter for each q_z.) For obtaining moduli, the focus is the structure factor[32],

$$S(q_z, q_r) = \sum_{n=-\infty}^{n=\infty} H_z(nd, L_z, \sigma_z)\cos(q_z nd) \times \int_0^\infty r dr H_r(r, L_r, \sigma_r) J_0 \exp(-q_z^2 \delta u_n(r)/2), \quad (4)$$

where d is the average repeat spacing of the membranes in the stack, J_0 is the zero order Bessel function[32], $H_z(z, L_z, \sigma_z)$ and $H_r(r, L_r, \sigma_r)$ account for finite domain sizes within the sample; L_r and L_z are the average domain sizes with variances σ_r and σ_z in the lateral and out-of-plane directions[32]. The height-height pair correlation function $\delta u_n(r)$ follows from Eq. (1) that defines κ and B

$$\delta u_n(r) = \frac{2\eta_c}{q_1^2} \int_0^\infty dx \frac{1 - J_0(r/\xi\sqrt{2x})(\sqrt{1+x^2} - x)^{2n}}{x\sqrt{1+x^2}} \quad (5)$$

in which the Caillé η_c parameter[46] and an in-plane correlation length ξ are related to the bending modulus κ and the membrane interaction modulus B by

$$\eta_c = \frac{k_B T q_1^2}{8\pi\sqrt{B\kappa}} \quad \text{and} \quad \xi^4 = \frac{\kappa}{B} \quad (6)$$

This model was fit simultaneously to the intensities at $q_z = 2.0q_1$ and $q_z = 2.5q_1$ to obtain values of κ and B with results shown in Fig. 1 C. Further details of the numerical calculation of the structure factor in Eq. (4) are described in the *Supplementary Material*.

Only two orders of lamellar repeat spacing were detected for solid supported RBC membranes, limiting the analysis of the membrane fluctuations to the low-q_z regime. The observed diffuse X-ray signal is secondarily sensitive to the domain size[17,32], so the primary fit was repeated for different values of L_r and the fit with the smallest ξ^2 was found for L_r=500 Å.

The direct application of the XDS method gives values of $\kappa \approx 2$ k_BT that we believe are too small. The main reason is that molecular tilt was not included in Eq. (1) because our experimental setup gave too low signal/noise to provide a meaningful fit to an extra parameter. Inclusion of tilt generally increases κ by 25-50% as the tilt modulus K_t varies from 90 mN/m to 50 mN/m when κ is of order 20 k_BT[47]. As mentioned in the discussion, we have used the simulation results for K_t to estimate how much the RBC$_{cm}$ κ might change if the XDS data were strong enough to fit for K_t. We prepared several sets of emulated structure factor data with different values of κ_{emu}, all with the simulated value of K_t. We then fit these emulations with the tilt independent XDS analysis program used for actual data to obtain κ_{fit} values. The emulated data that returned κ_{fit} closest to the value of 2 k_BT had a value of κ_{emu} that was about 6 k_BT.

This provides the upper estimate for the XDS value shown in Table 1. We also note that the structure factor for the emulated data had very weak peaks for orders three and higher, in agreement with the primary data shown in Fig. 1.

Those intensities are a product of the structure factor and the form factor squared; the latter could also have extinctions, but invoking extinctions is not necessary to account for the absence of higher order peak which comes about just from the effect of small values of the elastic moduli on the structure factor.

Our fitting routine was tested on a POPC bilayer. The observed 2-dimensional X-ray scattering pattern is shown in Fig. S3 A and the corresponding diffuse profiles are depicted in Fig. S3 B including fits to the data. The determined bending modulus of 20.8±1 k_BT is in good agreement with the earlier 20.3 k_BT[48] and the more recent tilt independent value of 19.2 k_BT,[47] which further supports the use of this analysis for RBCs.

Neutron spin-echo spectroscopy

Neutron Spin-Echo (NSE) experiments were performed on the NGA-NSE spectrometer at the NIST Center for Neutron Research (NCNR) in Gaithersburg, MD, U.S.A.[49]. While X-ray diffuse scattering measures nearly instantaneous snapshots of the disorder caused by the fluctuations, NSE measures the relaxation rates of those fluctuations which are affected by transport properties like viscosity as well as the static bending modulus. Measurements were performed at $q = 0.0523$ Å^{-1}, 0.0664 Å^{-1}, 0.0794 Å^{-1} and 0.0959 Å^{-1} using neutron wavelengths of $\lambda = 8$ and 11 Å, with a wavelength spread $\Delta\lambda/\lambda \approx 0.18$, providing access to Fourier times ranging from 0.01 to 100 ns. Temperature was controlled to 37 °C by a recirculation bath within an accuracy of ±1 °C. Data were corrected for instrumental resolution and solvent background using the DAVE software package[50].

According to the generally accepted theory of Zilman and Granek (ZG theory)[33] the intermediate scattering function of liposomes follows

$$I(q,t)/I(q,0) = \exp\left[-\left(\Gamma_{ZG}t\right)^{2/3}\right], \tag{7}$$

where the decay constants $\Gamma_{ZG}(q)$ are used in Eq. (2) to obtain the NSE dynamic bending modulus $\tilde{\kappa}$.

It has been previously discussed[51] that vesicle diffusion can contribute to the scattering signal observed in an NSE experiment in the low q-regime. While diffusion dominates NSE relaxation for $qR \ll 25$, the influence becomes negligible for our vesicle radius ($R =$ 100 nm) and a bending rigidity $\kappa < 20$ k_BT (see Fig. 1 in[51]).

Eq. (3) relates the dynamical bending modulus $\tilde{\kappa}$ to the customary bending modulus κ. The most important step to obtaining the true bending modulus κ is to relate K_A to κ. The relation

$$K_A = 48\frac{\kappa}{(2D_c)^2}, \tag{8}$$

where $2D_c$ is the thickness of the hydrocarbon region, has been used[24] for NSE experiments on pure lipid bilayers. (We note that[24] incorrectly calls Eq. (8) the *polymer brush model*. Instead, the factor 48 assumes uncoupled monolayers, and the polymer brush model would replace 48 by 24.) Assuming Eq. (8) and Eq. (3), Eq. (2) can be written as

$$\Gamma_{nse}^{pb} = 0.025\left(\frac{k_BT}{\kappa(1+48(h/2D_c)^2)}\right)^{1/2}\left(\frac{k_BT}{\eta}\right)q^3. \tag{9}$$

It is often assumed that the neutral surface (defined as the location in each monolayer where stretching is decoupled from bending[52]) is close to the boundary D_c of the hydrocarbon chains and the head group, in which case $h/D_c = 1$. Previous studies of the electron density of red blood cell membranes report a head-head group distance (membrane thickness) of 46 Å[43]. Using these results, the thickness of the hydrophobic core is estimated to be $2D_c = 36$ Å. Using the uncoupled monolayer model results in a value of $\kappa = 15 \pm 1.6$ k_BT.

Pan *et al.*[20] pointed out that conventional models, the uncoupled monolayer model in Eq. (8), the coupled monolayer model, and the polymer brush model, did not account for κ and K_A data as cholesterol was added to lipid bilayers. Evan Evans provided an alternative theory that assumed a stiff region in both uncoupled monolayers with a length of $\delta = 9$ Å. This resulted in

$$K_A = 12\frac{\kappa}{\delta^2} \tag{10}$$

Consequently,

$$\Gamma_{nse}^{chol} = 0.025\left(\frac{k_BT}{\kappa\left(1+12(h/\delta)^2\right)}\right)^{1/2}\left(\frac{k_BT}{\eta}\right)q^3. \tag{11}$$

Using $h = h_c$ and $\delta = 9$ Å, the result for this cholesterol model is $\kappa = 4.1\pm0.4$ k_BT when no diffusion correction was made and $\kappa =$ 7±0.4 k_BT when a diffusion correction was made; this is the range of values we display in Table 1 for our NSE results.

Molecular dynamics simulations

MD simulations were performed on a GPU accelerated computer workstation using GROMACS Version 5.1.4. A RBC membrane model was designed using the CHARMM-GUI membrane-builder (http://charmm-gui.org/)[53,54] and the Martini forcefield 2.2[54]. The system represents a membrane patch of ≈ 34 nm × 34 nm with about 2,500 lipid molecules on each leaflet and 37 water molecules per lipid corresponding to a well hydrated state of the membrane.

The lipid composition of the membrane patch was adjusted to match the experimental lipidomic findings of fresh red blood cells[36]. Each lipid species was mapped to available models in the Martini force field: First, an error coefficient was calculated for every available model lipid. This error value is composed of an error of saturation E_{sat} and an error of tail length E_{tail}. E_{sat} was chosen to be the difference in tail saturation between the model and the experimental lipid. In the same way E_{tail} was defined as the difference in tail length. For instance, given an experimental Lipid: 18:2-14:1; a corresponding Martini lipid 18:1-16:1 would result in an error value of $E = E_{sat} + E_{tail} = 1 + 2 = 3$. The Martini lipid with the smallest error value was then used for each experimental lipid respectively. The cholesterol concentration was taken from[37]

which reported that cholesterol accounts for 50 mol% of the RBC membrane.

RBC membranes are known to be asymmetric, with PS and PE lipids preferably located on the inner leaflet. This asymmetry between different lipid species was adjusted according to the widely accepted experimental findings by Dodge *et al.*[37]. For a given species the simulated lipid population was split among both leaflets to match the relative experimental findings. For instance, phosphatidylcholine (PC) lipids were reported to be split in a ratio of 3:1 between the upper and lower leaflet. Thus from all simulated PC lipids 75 % were placed in the upper and 25 % were placed in the lower leaflet. Details about the exact lipid composition of each model can be found in the *Supplementary Material* in Table S1. Fig S5 visualizes the relative concentrations of lipid species in the membrane model.

Simulations were equilibrated for 80 ns in the NPT ensemble (constant pressure and temperature), and then run for 2 μs. Only the final 800 ns were analyzed, after affirming the membrane had reached equilibrium by determining the area per lipid. Prior to each simulation run, the system was allowed to equilibrate for simulated 5 ns. The simulation used a 1 fs time step, a short range van der Waal cutoff of 1.1 nm and a potential-shift-verlet coulomb modifier. Periodic boundary conditions were applied to all spacial directions. Neighbor lists were updated in intervals of 20 steps. The temperature coupling was controlled by a v-rescale thermostat at a constant pressure of 1 bar using Parrinello-Rahman semi-isotropic weak coupling (τ=12 ps; compressibility β=3·10^{-4} bar^{-1}). The fluctuation spectrum of the membrane was determined as detailed in the *Supplementary Material*. The spectrum is governed by a q^4 dependency according to the Helfrich–Canham (HC) theory. The bending modulus was determined by fitting the lower q-regime (q <0.1 Å^{-1}) to

$$\langle |h(q)|^2 \rangle = \frac{k_B T}{\kappa q^4} + \frac{k_B T}{K_t q^2} \tag{12}$$

Determining the bending modulus in asymmetric membranes is non-trivial due to potentially induced curvature resulting from an uneven area per lipid in both leaflets[41]. Simulations on membrane patches with symmetrized upper and lower leaflet were used to verify the results from the asymmetric simulation. The resulting fluctuation spectra are presented in Fig. S4 in the *Supplementary Material*. The bending moduli agree within 1 k_BT and thus confirm the results that we obtained for the asymmetric membrane.

Dynamic light scattering

The size distribution of the liposomes was measured by dynamic light scattering (DLS) using a Brookhaven 90Plus particle analyzer running Particle Solutions Software (Version 2.6, Brookhaven Instruments Corporation) with a 659 nm laser and a 90° detection angle. Each measurement was performed at a count rate between 200 and 500 kilocounts/s for 2 min. The scattering signal at the position of the detector fluctuates due to the diffusion of liposomes in the solution. The instrument directly measures the diffusion constant D of the liposomes by fitting the cross-correlation function of the time signal measured by the detector. This is related to the particle size via the Stokes-Einstein relation: $D = \frac{k_B T}{6\pi\eta r}$, where η is the dynamic viscosity of the solution, k_B is the Boltzmann constant, T is the sample temperature and r is the radius of the LUVs, assumed to be spherical. All measurements were performed at 25°C on 1 ml of sample containing ≈ 20 mg/ml of erythrocyte liposomes.

Lipidomics analysis

Lipidomics

Samples were resolved as described[?] , over an ACQUITY HSS T3 column (2.1 × 150 mm, 1.8 μm particle size (Waters, MA, USA) using an aqueous phase (A) of 25 % acetonitrile and 5 mM ammonium acetate and a mobile phase (B) of 50 % isopropanol, 45 % acetonitrile and 5 mM ammonium acetate. Samples were eluted from the column using either the solvent gradient: 0-1 min 25 % B and 0.3 ml/min; 1-2 min 25-50 % B and 0.3 ml/min, 2-8 min 50-90 % B and 0.3 ml/min, 8-10 min 90-99 % B and 0.3 ml/min, 10-14 min hold at 99 % B and 0.3 ml/min, 14-14.1 min 99-25 % B and 0.3 ml/min, 14.1-16.9 min hold at 25 % B and 0.4 ml/min, 16.9-17 min hold at 25 % B and resume flow of 0.3 ml/min. Isocratic elution of 5 % B flowed at 250 μl/min and 25 °C or a gradient from 0- 5 % B over 0.5 min; 5-95 % B over 0.6 min, hold at 95 % B for 1.65 min; 95-5 % B over 0.25 min; hold at 5 % B for 2 min, flowed at 450 μl/min and 35 °C[?] . The Q Exactive mass spectrometer (Thermo Fisher Scientific, San Jose, CA, USA) was operated independently in positive or negative ion mode, scanning in Full MS mode (2 μscans) from 150 to 1500 m/z at 70,000 resolution, with 4 kV spray voltage, 45 sheath gas, 15 auxiliary gas.

MS2 analyses for untargeted lipidomics

For untargeted lipidomics, dd-MS2 was performed at 17,500 resolution, AGC target = $1 \cdot 10^5$, maximum IT = 50 ms, and stepped NCE of 25, 35 for positive mode, and 20, 24, and 28 for negative mode, as described in Stefanoni *et al.*[?] and applied to similar samples (*i.e.*, stored RBCs) in D'Alessandro *et al.*[?] .

Quality control and data processing

Calibration was performed prior to analysis using the PierceTM Positive and Negative Ion Calibration Solutions (Thermo Fisher Scientific). Acquired data was then converted from .raw to .mzXML file format using Mass Matrix (Cleveland, OH, USA). Samples were analyzed in randomized order with a technical mixture (generated by mixing 5 μl of all samples tested in this study) injected every 10 runs to qualify instrument performance. This technical mixture was also injected three times per polarity mode and analyzed with the parameters above, except CID fragmentation was included for unknown compound identification (10 ppm error for both positive and negative ion mode searches for intact mass, 50 ppm error tolerance for fragments in MS2 analyses – further details about the database searched below).

Metabolite assignment and relative quantitation

Metabolite assignments, isotopologue distributions, and correction for expected natural abundances of deuterium, ^{13}C, and ^{15}N isotopes were performed using MAVEN (Princeton, NJ, USA)[?] , against an in house library of deuterated lipid standards (SPLASH LIPIDOMIX Mass Spec Standard, Avanti Lipids) and in house libraries of 3,000 unlabeled (MSMLS, IROATech, Bolton, MA, USA; IroaTech ; product A2574 by ApexBio; standard compounds for central carbon and nitrogen pathways from SIGMA Aldrich, St Louis, MO, USA) and labeled standards (see below for the latter). Untargeted lipidomics analyses were performed with the software LipidSearch (Thermo Fisher, Bremen, Germany). Results from lipidsearch were exported as a library and additional discovery mode analyses were performed with standard workflows using

Compound Discoverer 2.1 SP1 (Thermo Fisher Scientific, San Jose, CA). From these analyses, metabolite IDs or unique chemical formulae were determined from high-resolution accurate intact mass, isotopic patterns, identification of eventual adducts (e.g., Na^+ or K^+, etc.) and MS2 fragmentation spectra against the KEGG pathway, HMDB, ChEBI, and ChEMBL databases.

ACKNOWLEDGEMENTS

This research was funded by the Natural Sciences and Engineering Research Council of Canada (NSERC), the Canada Foundation for Innovation (CFI) and the Ontario Ministry of Economic Development and Innovation. M.C.R. is the recipient of an Early Researcher Award of the Province of Ontario and a University Scholar of McMaster University. S.M.Q. was the recipient of a Postdoctoral Fellowship from Canadian Blood Services. The funders had no role in study design, data collection and analysis, decision to publish, or preparation of the manuscript. Access to NGA-NSE was provided by the Center for High Resolution Neutron Scattering, a partnership between the National Institute of Standards and Technology and the National Science Foundation under Agreement No. DMR-2010792.

REFERENCES

[1] Kirchhausen T (2012) Bending membranes. *Nature Cell Biology* 14(9):906–908.

[2] McMahon HT, Gallop JL (2005) Membrane curvature and mechanisms of dynamic cell membrane remodelling. *Nature* 438(7068):590–596.

[3] McMahon HT, Boucrot E (2015) Membrane curvature at a glance. *Journal of Cell Science* 128(6):1065–1070.

[4] Evans EA (1983) Bending elastic modulus of red blood cell membrane derived from buckling instability in micropipet aspiration tests. *Biophysical Journal* 43(1):27–30.

[5] Radmacher M (2002) 4.-Measuring the elastic properties of living cells by the atomic force microscope. *Methods in Cell Biology* 68(1):67–90.

[6] Brochard F, Lennon J (1975) Frequency spectrum of the flicker phenomenon in erythrocytes. *Journal de Physique* 36(11):1035–1047.

[7] Zilker A, Ziegler M, Sackmann E (1992) Spectral analysis of erythrocyte flickering in the 0.3–4-μm^{-1} regime by microinterferometry combined with fast image processing. *Physical Review A* 46(12):7998.

[8] Strey H, Peterson M, Sackmann E (1995) Measurement of erythrocyte membrane elasticity by flicker eigenmode decomposition. *Biophysical Journal* 69(2):478–488.

[9] Park Y, et al. (2010) Measurement of red blood cell mechanics during morphological changes. *Proceedings of the National Academy of Sciences* 107(15):6731–6736.

[10] Popescu G, et al. (2006) Optical measurement of cell membrane tension. *Physical Review Letters* 97(21):218101.

[11] Evans J, Gratzer W, Mohandas N, Parker K, Sleep J (2008) Fluctuations of the red blood cell membrane: relation to mechanical properties and lack of atp dependence. *Biophysical Journal* 94(10):4134–4144.

[12] Betz T, Lenz M, Joanny JF, Sykes C (2009) Atp-dependent mechanics of red blood cells. *Proceedings of the National Academy of Sciences* 106(36):15320–15325.

[13] Auth T, Safran S, Gov NS (2007) Fluctuations of coupled fluid and solid membranes with application to red blood cells. *Physical Review E* 76(5):051910.

[14] Park Y, et al. (2010) Measurement of red blood cell mechanics during morphological changes. *Proceedings of the National Academy of Sciences* 107(15):6731–6736.

[15] Gov N, Zilman A, Safran S (2003) Cytoskeleton confinement and tension of red blood cell membranes. *Physical Review Letters* 90(22):228101.

[16] Dimova R (2014) Recent developments in the field of bending rigidity measurements on membranes. *Advances in Colloid and Interface Science* 208:225–234.

[17] Liu Y, Nagle JF (2004) Diffuse scattering provides material parameters and electron density profiles of biomembranes. *Physical Review E* 69(4):040901.

[18] Kučerka N, Tristram-Nagle S, Nagle JF (2006) Structure of fully hydrated fluid phase lipid bilayers with monounsaturated chains. *The Journal of Membrane Biology* 208(3):193–202.

[19] Tristram-Nagle S, Nagle JF (2007) Hiv-1 fusion peptide decreases bending energy and promotes curved fusion intermediates. *Biophysical Journal* 93(6):2048–2055.

[20] Pan J, Tristram-Nagle S, Nagle JF (2009) Effect of cholesterol on structural and mechanical properties of membranes depends on lipid chain saturation. *Physical Review E* 80(2):021931.

[21] Nagle JF, Jablin MS, Tristram-Nagle S, Akabori K (2015) What are the true values of the bending modulus of simple lipid bilayers? *Chemistry and Physics of Lipids* 185:3–10.

[22] Rheinstädter MC, Häussler W, Salditt T (2006) Dispersion relation of lipid membrane shape fluctuations by neutron spin-echo spectrometry. *Physical Review Letters* 97:048103.

[23] Pabst G, Kučerka N, Nieh MP, Rheinstädter M, Katsaras J (2010) Applications of neutron and x-ray scattering to the study of biologically relevant model membranes. *Chemistry and Physics of Lipids* 163(6):460 – 479.

[24] Nagao M, Kelley EG, Ashkar R, Bradbury R, Butler PD (2017) Probing elastic and viscous properties of phospholipid bilayers using neutron spin echo spectroscopy. *The Journal of Physical Chemistry Letters* 8(19):4679–4684.

[25] Kelley EG, Butler PD, Ashkar R, Bradbury R, Nagao M (2020) Scaling relationships for the elastic moduli and viscosity of mixed lipid membranes. *Proceedings of the National Academy of Sciences* 117(38):23365–23373.

[26] Chakraborty S, et al. (2020) How cholesterol stiffens unsaturated lipid membranes. *Proceedings of the National Academy of Sciences* 117(36):21896–21905.

[27] Hu M, Diggins IV P, Deserno M (2013) Determining the bending modulus of a lipid membrane by simulating buckling. *The Journal of Chemical Physics* 138(21):214110.

[28] Eid J, Razmazma H, Jraij A, Ebrahimi A, Monticelli L (2020) On calculating the bending modulus of lipid bilayer membranes from buckling simulations. *The Journal of Physical Chemistry B* 124(29):6299–6311.

[29] Eid J, Greige-Gerges H, Monticelli L, Jraij A (2021) Elastic moduli of lipid membranes: Reproducibility of AFM measures. *Chemistry and Physics of Lipids* 234:105011.

[30] Park Y, et al. (2010) Metabolic remodeling of the human

red blood cell membrane. *Proceedings of the National Academy of Sciences* 107(4):1289–1294.

[31] Helfrich W (1978) Steric interaction of fluid membranes in multilayer systems. *Zeitschrift für Naturforschung A* 33(3):305–315.

[32] Lyatskaya Y, Liu Y, Tristram-Nagle S, Katsaras J, Nagle JF (2000) Method for obtaining structure and interactions from oriented lipid bilayers. *Physical Review E* 63:011907.

[33] Zilman A, Granek R (1996) Undulations and dynamic structure factor of membranes. *Physical Review Letters* 77:4788–4791.

[34] Watson MC, Peng Y, Zheng Y, Brown FL (2011) The intermediate scattering function for lipid bilayer membranes: From nanometers to microns. *The Journal of Chemical Physics* 135(19):194701.

[35] Nagle JF, et al. (2021) A needless but interesting controversy. *Proceedings of the National Academy of Sciences* 118(20).

[36] Stefanoni D, et al. (2020) Red blood cell metabolism in rhesus macaques and humans: comparative biology of blood storage. *Haematologica* 105(8):2174.

[37] Dodge JT, Phillips GB (1967) Composition of phospholipids and of phospholipid fatty acids and aldehydes in human red cells. *Journal of Lipid Research* 8(6):667–675.

[38] Brown FL (2008) Elastic modeling of biomembranes and lipid bilayers. *Annual Reviews Physical Chemistry* 59:685–712.

[39] Fowler PW, et al. (2016) Membrane stiffness is modified by integral membrane proteins. *Soft Matter* 12(37):7792–7803.

[40] May ER, Narang A, Kopelevich DI (2007) Role of molecular tilt in thermal fluctuations of lipid membranes. *Physical Review E* 76(2):021913.

[41] Hossein A, Deserno M (2020) Spontaneous curvature, differential stress, and bending modulus of asymmetric lipid membranes. *Biophysical Journal* 118(3):624–642.

[42] Lipowsky R, Girardet M (1990) Shape fluctuations of polymerized or solidlike membranes. *Physical review letters* 65(23):2893.

[43] Himbert S, et al. (2017) The molecular structure of human red blood cell membranes from highly oriented, solid supported multi-lamellar membranes. *Scientific Reports* 7:39661.

[44] Ghysels A, et al. (2019) Permeability of membranes in the liquid ordered and liquid disordered phases. *Nature Communications* 10(1):1–12.

[45] HW GL, Wortis M, Mukhopadhyay R (2002) Stomatocyte–discocyte–echinocyte sequence of the human red blood cell: Evidence for the bilayer–couple hypothesis from membrane mechanics. *Proceedings of the National Academy of Sciences* 99(26):16766–16769.

[46] Caillé A (1972) X-ray scattering by smectic-A crystals. *C.R. Acad. Sci. Ser. B* 274:891–893.

[47] Nagle JF, Mathai JC, Zeidel ML, Tristram-Nagle S (2007) Theory of passive permeability through lipid bilayers. *J. Gen. Physiol.* 131:77–85.

[48] Kučerka N, et al. (2005) Structure of fully hydrated fluid phase DMPC and DLPC lipid bilayers using x-ray scattering from oriented multilamellar arrays and from unilamellar vesicles. *Biophysical Journal* 88:2626–2637.

[49] Rosov N, Rathgeber S, Monkenbusch M (1999) Neutron spin echo spectroscopy at the NIST center for neutron research in *ACS Symposium Series*. (American Chemical Society), pp. 103–116.

[50] Azuah R, et al. (2009) Dave: A comprehensive software suite for the reduction, visualization, and analysis of low energy neutron spectroscopic data. *Journal of Research of the National Institute of Standards and Technology* 114:341.

[51] Mell M, et al. (2013) Bending stiffness of biological membranes: What can be measured by neutron spin echo? *The European Physical Journal E* 36(7):75.

[52] Safran S (2018) *Statistical thermodynamics of surfaces, interfaces, and membranes.* (CRC Press).

[53] Jo S, Kim T, Iyer VG, Im W (2008) Charmm-gui: a web-based graphical user interface for charmm. *Journal of Computational Chemistry* 29(11):1859–1865.

[54] Qi Y, et al. (2015) Charmm-gui martini maker for coarse-grained simulations with the martini force field. *Journal of Chemical Theory and Computation* 11(9):4486–4494.

[55] Guinier A, Fournet G, Yudowitch KL (1955) *Small-angle scattering of X-rays.* (Wiley New York).

SUPPLEMENTARY MATERIAL TO: THE BENDING RIGIDITY OF THE RED BLOOD CELL CYTOPLASMIC MEMBRANE

X-ray diffraction experiment

X-ray diffraction measurements were performed using CuKα X-rays (λ=1.5418 Å) generated by a RIGAKU SmartLab rotating anode instrument operated at 9 kW. The focusing multi-layer optics provided a high intensity circular beam with a diameter of $\approx$ 200 μm and an angular divergence of 0.008 rad with monochromatic X-ray intensities of 10^8 counts/mm^2·s. The instrument is equipped with a Rigaku HyPix-3000 2-dimensional semiconductor detector with an array of (n, m) pixels of size 100 μm^2. We note that this detector counts single photons in every pixel in contrast to widely used CCD based instruments. The geometry of the instrument is sketched in Fig. S1.

Both source and detector were moved on spherical coordinates around the stationary horizontal sample allowing to control the incident angle θ. As θ was varied, the scattering intensity measured by the detector was read only for the pixel row matching the specular condition in its center as indicated by the blue highlighted pixels in Fig. S1. These intensities at q_z were then recorded at the corresponding q_z value in the data set shown in Fig. 1 B in he main text, which was used for analysis.

The sample holder was a sealed chamber with two double walled kapton windows on either side. A basin at the bottom below the sample was filled with aqueous solution and the humidity inside the chamber was controlled by the salinity of this solution. Ultra pure water was used for experiments performed near 100 % RH and the d-spacing of a POPC sample was as large as is obtained for fully hydrated unoriented multilamellar vesicles in bulk water. The RBC samples at 100 % RH had an unbounded d-spacing due to the presence of charged lipids, so the humidity was tuned to 99 % RH by using a 40 mg/ml K_2SO_4 solution to obtain a finite D necessary for analysis of the moduli[32]. The temperature inside the chamber was 37 °C.

We emphasize that the sample remained horizontal throughout the measurement. This differs from the earlier protocol[17] in which the sample was rocked while the synchrotron source and the detector remained fixed. In that protocol the intensity at each pixel came from a trajectory in q space whereas each pixel in the present protocol received intensity from only one point in q space; this simplified the XDS analysis which was rewritten for this setup, following instructions from[32]. While simpler, calculating the structure factor in Eq. (4) was still computationally challenging. First a table of $\delta u_n(r)$ was calculated numerically for $n \leq$30 and $r \leq$1000 Å using logarithmic steps in r. For $n >$30 and 1000 Å$< r < 10^6$ Å the approximation proposed by Callié was used as in[32]:

$$\delta u_n(r) = \frac{4\eta_1}{q_1^2}\left[\gamma \ln\left(\frac{r}{\xi}\right) + 0.5E_1\left(\frac{r^2}{4n\xi^2}\right)\right] \tag{S13}$$

The same way, tables were calculated for $H_r(r, L_r, \sigma_r)$ and $H_z(z, L_z, \sigma_z)$. Then the summation in Eq. (4) ($n \leq$1000) was calculated from these predetermined tables using a GPU accelerated algorithm. The Hankel transformation in Eq. (4) was then calculated using the Simpson-rule allowing this step to be accelerated through the GPU. Levenberg-Marquardt least square fitting (GNU Scientific library) was then used to obtain the K_C and B values for which $S(q)$ best fit the data, necessarily allowing each value of q_z a different normalization factor related to the electron density profile of the membrane. Data used were the measured X-ray intensity slices at $q_z = 2q_1$ and $q_z = 2.5q_1$. The program is available upon request from the authors of this paper. Interestingly, essentially the same values of K_C and B were

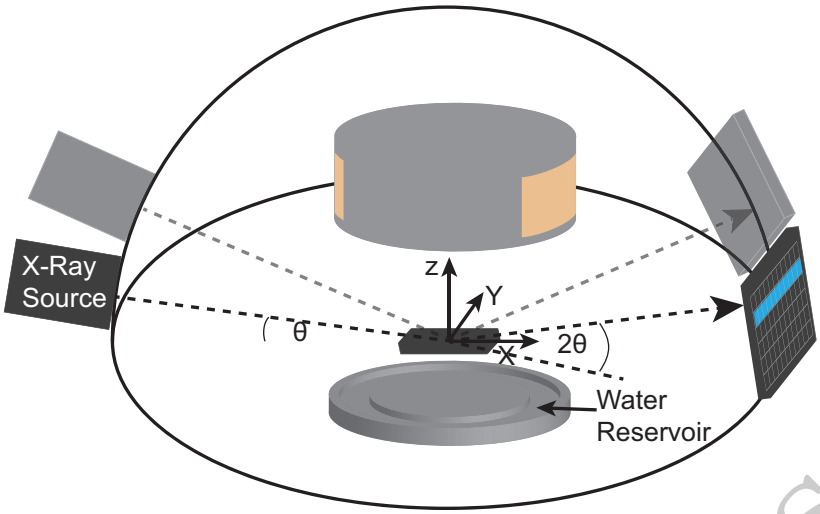

Figure S1. Schematic illustration of the instrumental setup. The X-ray source and the 2-dimensional detector, mounted on movable arms, were simultaneously rotated by $\pm\theta$ relative to the fixed horizontal sample. The detector recorded only the pixel row indicated by the blue highlighted pixels whose center was at the specular relative to the incident angle θ. The double walled aluminum chamber consisted of a lid with two double walled kapton windows on either side. A solution reservoir beneath the sample provided the desired relative humidity inside the tightly sealed chamber when the lid was attached.

obtained by fitting all q_z slices between $q_z = 2q_1$ and $q_z = 2.5q_1$ using the program for the original experimental protocol.[17]. Also, for the control POPC, the range of q_z for fitting was moved to $q_z = 3q_1$ and above, as in previous studies[17], because the diffuse scattering is more robust compared to the specular due to the larger bending modulus. Again, both methods of fitting gave essentially the same values of the moduli.

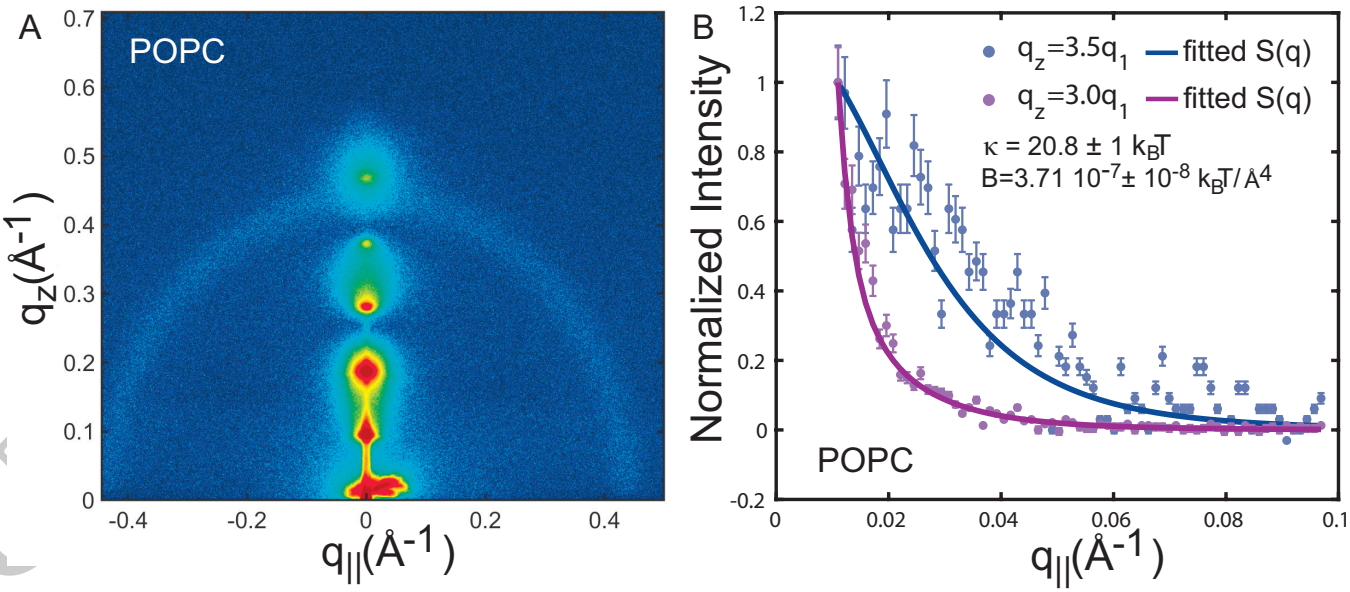

Figure S2. **A** 2-dimensional intensity map of a POPC bilayer measured at 100 % relative humidity. **B** Diffuse profile extracted at q_z=3q_1 and 3.5q_1. Fits of S(q) (Eq. (4)) are shown as solid lines.

Small angle neutron scattering (SANS)

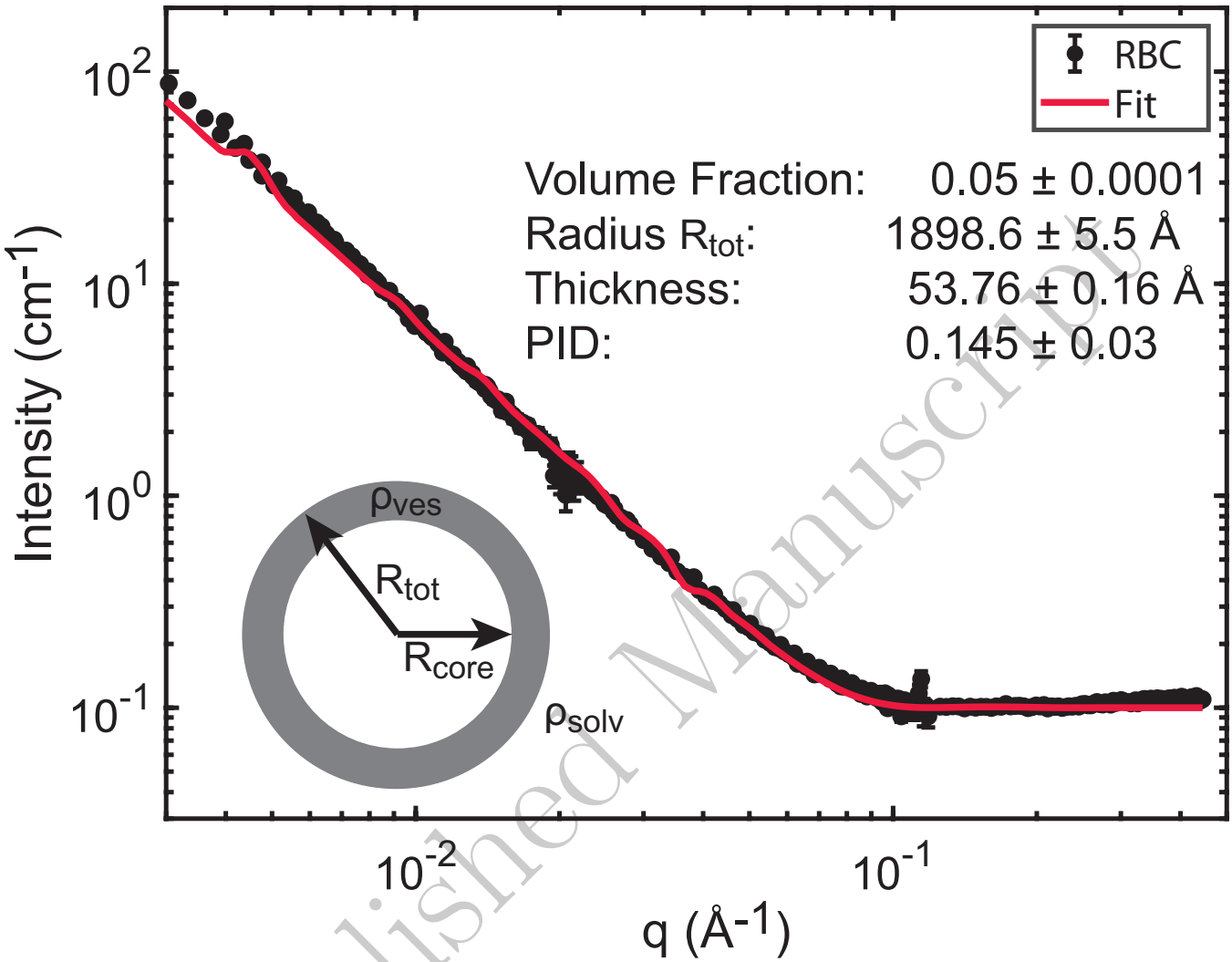

Figure S3. SANS spectra recorded on RBC liposomes in D_2. Data were fit to a vesicle model (Eq. S14) and the fit is presented as solid red line.

SANS experiments were conducted using the 30 m SANS NGB30 at the NIST Center for Neutron Research (NCNR, Gaithersburg, MD). Sample-to-detector distances of 1 and 4 m with a neutron wavelength of 6 Å were used together with the 13 m lens configuration of the instrument with a neutron wavelength of 8.4 Å to measure a q range between 0.001 and 1 $Å^{-1}$. RBC liposomes in D_2O were loaded into NCNR's custom quartz sample holders (diameter 19 mm and thickness 1 mm, corresponding to a volume of $\approx$ 800 μl per sample). The low q range data were acquired by counting for 120 min using the 13 m Lens configuration, the medium q range data were acquired by counting for 10 min using the 4 m distance, and the high q range data were acquired for 5 min using the 1 m detection distance. The three ranges were reduced and merged using Igor Pro Version 6.37 and macros provided by the NIST-NCNR. The data were fit to the vesicle model[55] using SASVIEW version 5.0.2. The structure factor in this model is given as:

$$S(q) = \frac{\varphi}{V_{shell}} \left[\frac{3V_{core}(\rho_{solvent} - \rho_{shell})J_1(qR_{core})}{qR_{core}} + \frac{3V_{tot}(\rho_{shell} - \rho_{solvent})J_1(qR_{tot})}{qR_{tot}} \right]^2 + \text{Background} \quad \text{(S14)}$$

where φ is the volume fraction, V_{shell} is the membrane volume, V_{core} is the volume of the vescile core and $V_{total} = V_{shell} + V_{core}$. J_1 is the first order bessel function. R_{core} and R_{tot} referring to the core radius and total vesicle radius respectively.

Molecular dynamics simulation

MD simulations were performed on a GPU accelerated computer using GROMACS Version 5.1.4. The device is equipped with a 40 Core central processing unit (CPU, Intel(R) Xeon(R) CPU E5-2630 v4 @ 2.20GHz), 130 GB random-access memory (RAM) and three graphic processing units (GPU, 2 × NVIDIA 1080 TDI + 1 × GeForce GT 730).

The fluctuation spectrum was determined as follows: First the upper and lower leaflet was indext using the spliptleaflets program. The position of C1 Beads from DPGG, OPGG, FPGG, and DFGG, as well as GL1 beads from FPMG, OPMG, DPMG, were exported between 200 ns and 2 μs in steps of 4 ns for each leaflet separately together with the position of the PO4 Beads from the remaining lipid molecules. The Z position from all atoms was interpolated using a 2-dimensional cubic interpolation provided by the MATLAB built-in *griddata* function for both leaflets respectively. The membrane undulation-profile was then determined by calculating the average undulation of the upper and lower leaflet. The 2-dimensional spectrum was then determined using built-in MATLAB function. The scaling of the spectrum was verified using the program provided by the authors of[39] and a simulation of a POPC bilayer. A value of κ =19±2 $k_B T$ was determined, as shown in Fig. S4 in the *Supplementary Material*, in good agreement with previously published results.

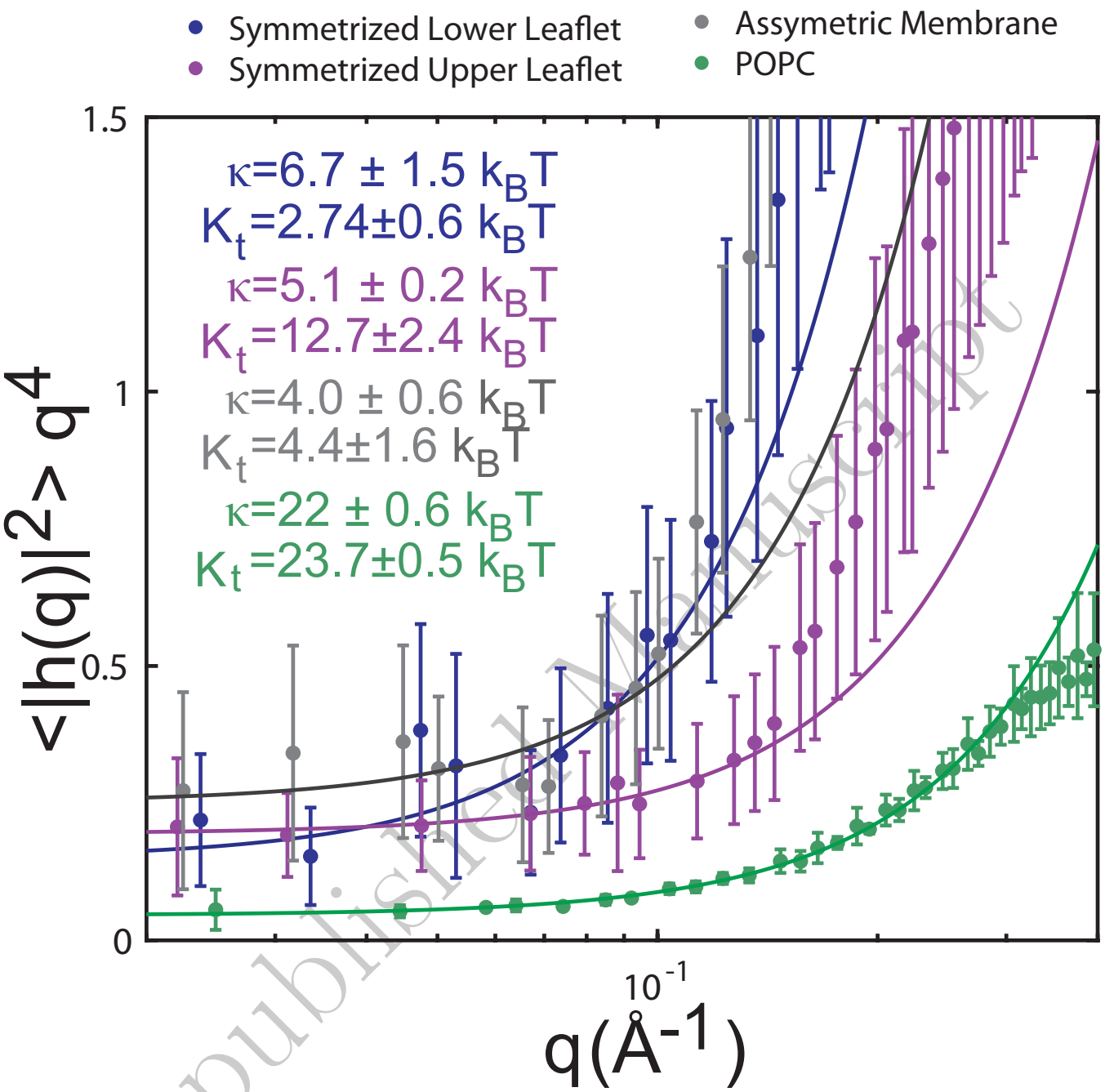

Figure S4. Fluctuation spectra determined from simulations of a POPC bilayer and symmetrisized versions of the asymmetric membrane patch. Bending moduli of κ=19.7±2 k_BT, κ=4.1±1 k_BT and κ=3.1±0.8 k_BT were determined for POPC, and membranes with a symmetric upper and lower leaflet respectively.

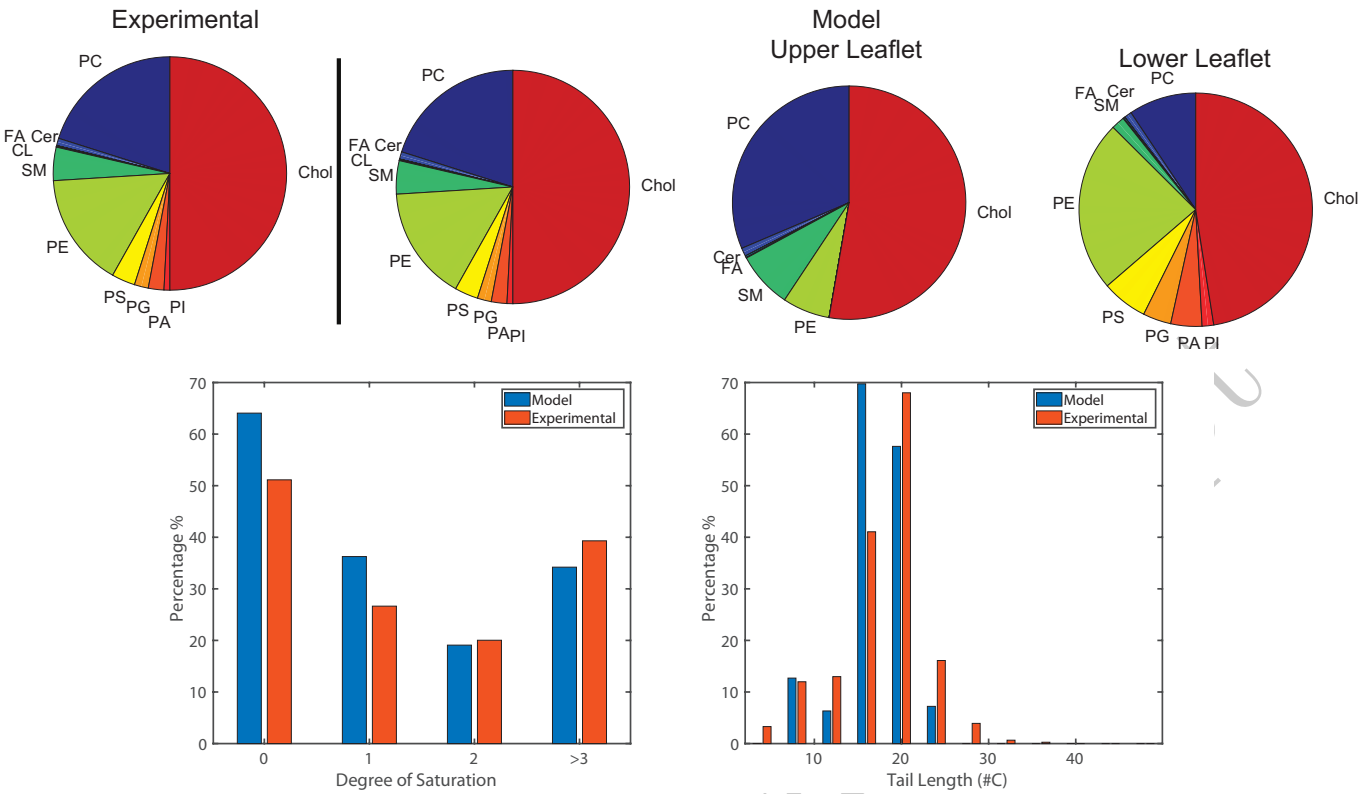

Figure S5. **A** Experimentally determined composition of red blood cell membrane as reported by[36]. **B** Lipidomics of the implemented coarse grained MD simulation model. The asymmetry of the membrane was created by distributing lipids between both leaflets according to experimental findings by[37].**C** Comparison of the degree of tail saturation in the experimental and model membrane. **D** Comparison between the lipid tail length of the experimental and model membrane.

Chapter 5

Paper II: Storage of red blood cells leads to an increased membrane order and bending rigidity

5.1 Preface to Paper II

This project is conducted in collaboration with CBS. The effect of long term storage on the RBCcm's structure and bending rigidity is studied by XRD, XDS and MD simulations.

RC is provided by the CBS and stored for 2 and 5 weeks, respectively. Solid supported stacks of RBCcms are prepared from these samples and are compared to the structure and mechanical properties of a fresh RBC sample.

We experimentally observe a 6 % increase in the fraction of l_o domains in stored RBC membranes together with an increase membrane thickness and lipid order. At the same time, the size of both, l_o and l_d domains decrease by 25 %. Importantly, the membrane's bending modulus κ is found to increase from 1.9 k_BT to 5.3 k_BT in XDS experiments.

We further develop coarse grained MD models in collaboration with Dr. Angelo D'Alessandro to replicate the changes of the RBCcm's lipid composition during storage. The simulations are conducted at cholesterol levels of 30 mol% and 50 mol% to study the maximal potential change in the membrane's cholesterol levels during storage.

The MD simuluations confirm the experimentally observed changes in the l_o and l_d membrane domains, however do not show an increase in the membrane's bending modulus. This suggests that the increase in bending rigidity in stored RBC is not the effect of cholesterol and changes in the RBCcm's lipid composition but is potentially linked to integral proteins.

Status: submitted

Author Contributions:

- Experimental Concept: **Sebastian Himbert**, Maikel Rheinstädter
- Sample Preparation: **Sebastian Himbert**, Syed M. Quadri, Peter Schubert, William P. Sheffield
- X-ray Experiments: **Sebastian Himbert**, Maikel Rheinstädter
- Analysis Software Development: **Sebastian Himbert**
- MD Model Development: **Sebastian Himbert**, Angelo D'Alessandro
- Data Analysis: **Sebastian Himbert**, Maikel Rheinstädter
- Manuscript Preparation: **Sebastian Himbert**, Maikel Rheinstädter

Blood bank storage of red blood cells alters RBC cytoplasmic membrane order and bending rigidity

Sebastian Himbert[1,2,‡], Syed M. Qadri[3], William P. Sheffield[4,5], Peter Schubert[6,7], Angelo D'Alessandro[8,9], Maikel C. Rheinstädter[1,2*]

1 Department of Physics and Astronomy, McMaster University, Hamilton, ON, Canada
2 Origins Institute, McMaster University, Hamilton, ON, Canada
3 Faculty of Health Sciences, Ontario Tech University, Oshawa, ON, Canada
4 Department of Pathology and Molecular Medicine, McMaster University, Hamilton, ON, Canada
5 Centre for Innovation, Canadian Blood Services, Hamilton, ON, Canada
6 Centre for Innovation, Canadian Blood Services, Vancouver, British Columbia, Canada.Centre for Innovation, Canadian Blood Services, Vancouver, British Columbia, Canada.
7 Centre for Blood Research, University of British Columbia, Vancouver, British Columbia, Canada.
wor **8** Department of Pathology and Cell Biology, Columbia University Vagelos College of Physicians and Surgeons and New York-Presbyterian Hospital, New York, New York, USA
9 University of Colorado Denver-Anschutz Medical Campus, Aurora, Colorado, USA.

‡ himberts@mcmaster.ca
* Department of Physics and Astronomy, McMaster University, ABB-241, 1280 Main Street West, Hamilton, Ontario L8S 4M1, Canada; Phone: +1-(905)-525-9140-23134, Fax: +1-(905)-546-1252, E-mail:rheinstadter@mcmaster.ca

Abstract

Blood banks around the world store blood components for several weeks ensuring its availability for transfusion medicine. Red blood cells (RBCs) are known to undergo compositional changes during storage, which may impact the cells' function and eventually the recipients' health. Using mass spectrometry, we observed slight changes in the lipidomics of the RBC's cytoplasmic membrane (RBCcm) related to the degree of saturation and tail length. A potential increase of the cholesterol content has been previously reported, from $\approx$ 30 mol% to 50 mol%. However, little is known about the impact of these changes on the RBC cytoplasmic membrane's (RBCcm's) molecular assembly and mechanical properties. The RBCcm of the cells was extracted and the effect of storage on the membranes' molecular structure and bending rigidity was investigated by a combination of X-ray diffraction (XRD), X-ray diffuse scattering (XDS) and coarse grained Molecular Dynamics (MD) simulations. We provide evidence for an increased fraction (6 %) of liquid ordered (l_o) domains in stored RBCcms, and an increased lipid packing in these domains, leading to an increased membrane thickness and membrane order. The size of both, l_o and liquid disordered (l_d) lipid domains was found to decrease with increased storage time by up to 25 %. XDS experiments reveal a storage dependent increase in the RBCcm's bending modulus κ by a factor of 2.8, from 1.9 k_BT to 5.3 k_BT. The origin of this increase in membrane stiffness is likely not a result of the increased cholesterol concentration, as it was not observed in MD simulations containing only lipids and cholesterol.

Introduction

The long term storage of blood components is essential in transfusion medicine. Blood is first collected from donors and processed into different components, after which they are stored until needed in hospitals around the world. The maximal allowed storage time is 5 to 6 weeks in most countries, depending on the jurisdiction. Red cell concentrate (RC) refers to the concentrated RBC fraction of blood and there is some evidence that the use of older RC in transfusion is accompanied by clinical consequences, such as rapid clearance from the bloodstream of the recipient of membrane-damaged RBCs [1, 2], inflammatory reactions [3], multiple organ dysfunction [4, 5, 5] and an increased mortality [5–8]. It is known that RBCs - the most abundant cell type in blood - undergo numerous biochemical, and structural changes during storage, resulting in a decreased resistance against oxidative stress [9–11], damaged membranes [10, 12–14] and reduced deformability [15–19].

The RBCs' unique ability to deform is intrinsically related to complex interplay between the spectrin skeleton and the membrane, forming the outer layer of the cell. When deformations occur on the nanoscale, *i.e.*, smaller than the spacing between cytoskeleton tethers, the mechanical properties of the RBCcm become dominant [20]. This regime is in particular important for molecular processes, such as the non-active transport of small molecules across the membrane [21].

The storage of RC leads to several changes in the RBCcm composition. Protein [11] and lipid [14, 22, 23, 23] oxidation, together with an externalization of charged phosphatidylserine lipids [24]. In addition, changes in band 3 are associated with the aggregation and binding of haemoglobin to the membrane and an increased RBC removal from the circulation [25]. In this context, the high-affinity binding of . Controversial information exists on the relative amount of cholesterol in the bilayer. An increase in membrane cholesterol levels during storage has been reported, and speculated to be a result of lipid loss [26, 27], while other articles challenge these findings [28].

Here, we investigated the implications of storage on the molecular structure and bending stiffness of hemoglobin depleted RBCcms. RBCs were stored in commercial blood bags for 2 weeks and 5 weeks, respectively, and membranes were isolated. We determined membrane thickness, domain sizes and the membrane's bending modulus using a combined suite of X-ray diffraction (XRD) and X-ray diffuse scattering (XDS) experiments. We further determined the lipid composition from mass spectrometry to develop coarse grained Molecular Dynamics (MD) models for fresh and stored RBCcms. While the structural changes were altogether small, they indicate a stiffening of RBCcms as function of storage time.

Materials and methods

This research was approved by the Hamilton Integrated Research Ethics Board (HIREB) under approval number 1354-T and by the Canadian Blood Services Research Ethics Board under approval number # 2015.022.

Preparation of Solid Supported RBC Cytoplasmic Membranes

Leukocyte reduced transfusion RCs were provided by the Canadian Blood Services Network Centre for Applied Development (netCAD, Vancouver, BC) and stored in standardized PVC plastic bags in a citrate phosphate dextrose and saline-adenine-glucose-mannitol (CPD-SAGM) solution. The storage bag was stored at 4 °C and samples were collected after 2 and 5 weeks, respectively. In addition, fresh blood was collected from volunteers in 10 ml heparinized blood collection tubes. RBC

liposomes were then prepared from all samples simultaneously following a previously published protocol [29, 30]. Briefly: The whole blood was washed twice and the RBCs were isolated by successive centrifugation and replacing the supernatant with phosphate saline buffer (PBS). The cells were exposed to osmotic stress by mixing hematocrit with lysis buffer (3 % PBS buffer, pH 8) at a concentration of 3 vol%. The lysis buffer was pre-chilled to 4 °C and the reaction tubes were immediately stored on ice to prevent a fast re-closing of the ruptured cells. Hemoglobin and other cellular compartments were removed through multiple washing steps, as demonstrated in [29]. The protocol results in a white pellet containing empty RBC liposomes. The resulting solution was tip sonicated 20 times for 5 s each at a power of 100 W. The reaction tube was placed on ice during sonication to prevent the sample from overheating. Afterwards, the tube was centrifuged for 15 min at 20,000 g. The supernatant consists of a solution of small, nanometer-sized liposomes at a membrane concentration of ≈14 mg/ml [29].

Multi-lamellar, solid supported membranes were prepared for the X-ray experiments. Membranes were applied onto single-side polished silicon wafers. 100 mm diameter, 300 μm thick silicon wafers were pre-cut into 10×10 mm^2 chips. The wafers were functionalized with a solution of 15 ml sulfuric acid and 5 ml hydrogen peroxide (Piranha solution) resulting in a hydrophilic surface. This strong oxidizing agent removes all organic contaminants on the surface, but does not disturb the native silicon oxide layer. Each wafer was then thoroughly rinsed with ≈50 ml of ultra pure water (18.2 MΩ·cm) and placed on a hot plate (37 °C) in a 3-dimensional orbital shaker. 100 μl of the hybrid membrane solution was pipetted slowly onto the wafer. The sample was covered with a tilted lid of a petri dish to allow the membrane solution to slowly dry within ≈12 h. The dried wafers were then incubated for 24 h at 97 % relative humidity (RH) and 37 °C by placing the samples in a sealed container with a saturated K_2SO_4 solution. The subsequent drying and incubation of the sample results in a fusion of the RBC liposomes on the silicon surface producing a stack of several hundreds RBCcms, which is a prerequisite for the structural X-ray investigations [29].

X-ray Diffraction

X-ray diffraction was performed on a RIGAKU Smartlab diffractometer using a 9 kW (45 kV, 200 mA) CuKα rotating anode source with a wavelength of 1.5418 Å and a Rigaku HyPix-3000 2-dimensional semiconductor detector with an area of 3000 mm^2 and 100 μm^2 pixel size. Both source and detector are mounted on movable arms such that the membranes remained horizontal throughout the measurements. The $q_{||}$-axis probed the lateral structure, parallel to the wafer surface, and the perpendicular axis, q_z, probed out-of-plane structure, perpendicular to the substrate. The focusing multi-layer optics provided a high intensity beam of ≈200 μm with monochromatic X-ray intensities of up to 10^8 counts/s. The samples were mounted in a custom-built humidity chamber during the experiments. The temperature inside the machine was kept constant at 37 °C. Two measurements were performed: perpendicular membrane structure and the electron densities were determined at 88% RH while bending fluctuations were measured at a high humidity of 99.9% RH.

The membrane orientation H was determined by first extracting the X-ray intensity along the meridional angle Φ at $|\vec{q}| = q_1$, the first order lamellar diffraction peak, and fitting the resulting profile with a Gaussian distribution centered at 0. Hermans orientation function

$$H = \frac{3 < \cos^2(\delta) > -1}{2} \tag{1}$$

was then used to determine the membrane orientation.

The relative electron density, ρ(z), was approximated by a 1-dimensional Fourier analysis [31]:

$$\rho(z) \quad = \quad \frac{2}{d_z}\sum_{n=1}^{N}\sqrt{I_n q_n}\nu_n \cos\left(\frac{2\pi n z}{d_z}\right). \tag{2}$$

Here, N is the highest order of the lamellar peaks observed. $F(q_n) = \sqrt{I_n q_n}$ is the membrane's form factor [31] and is generally a complex quantity. However, in case of centro-symmetry, the form factor becomes real and the phase problem of crystallography, therefore, simplifies to a sigmoidal problem with phase factors $v_n = \pm 1$ [31]. An X-ray diffraction experiment probes the form factor at discrete values of q_z, and a continuous function, $T(q_z)$, can be fitted to the data [32].

$$T(q_z) = \sum_n \sqrt{I_n q_n}\mathrm{sinc}\left(\frac{1}{2}d_z q_z - \pi n\right). \tag{3}$$

Once an analytical expression for $T(q_z)$ has been determined from fitting the experimental peak intensities, the phases v_n can be assessed from $T(q_z)$. The phase array $v_n = [-1\ \ -1\ \ 1\ \ -1\ 1]$ was used for all samples.

The electron densities determined by Eq. (2) are on a relative scale and were normalized for comparison. $\rho(z{=}0)$ was set to 0 and the electron density at the boundaries were scaled to 1.

The average size of the different lipid and peptide domains was estimated from the widths of the corresponding in-plane correlation peaks by applying Scherrer's equation:

$$L = \frac{0.94\lambda}{B(2\theta)\cos(\theta)}, \tag{4}$$

where λ is the wavelength of the X-ray beam, θ is the diffraction angle and $B(2\theta)$ is the width of the correlation peak in radians. This relation is an established method to estimate crystalline domain sizes of up to ≈100 nm in X-ray diffraction experiments. L corresponds to the edge size of rectangular domains in cubic lattices. We note that this method has limitations to quantitatively determine sizes of small irregular domains of a few nanometers, only. The measured values present the upper limits of the domain sizes.

The membrane interaction modulus B and the membrane bending modulus κ can be determined independently from measurements of the diffuse scattering when the membranes are hydrated close to 100% RH [33–35]. The structure factor of a well hydrated membrane is given by [33]:

$$\begin{aligned} S(q_z, q_r) \quad &= \quad \sum_{n=-\infty}^{n=\infty} H_z(nD)\cos(q_z n D) \\ &\times \quad \int_0^\infty r dr H_r(r) J_0 \exp(-q_z^2 \delta u_n(r,\zeta,\eta)/2), \end{aligned} \tag{5}$$

where J_0 is the zero order bessel function, $H_r(r)$ and $H_z(z)$ account for the finite size of the membrane stack and $\delta u_n(r)$ is the height-height pair correlation function of a lipid bilayer. The definitions of all functions can be found in Lyatskaya *et al.* [33]. The bending modulus κ and membrane compression modulus B can be determined by simultaneously fitting Eq. (6) to two $q_{||}$-line cuts (at $q = 2\frac{2\pi}{d}$ and $q = 2.5\frac{2\pi}{d}$ for instance) [33]. The parameters η and ξ are the Caillé parameter [36] and the in-plane correlation length that are related to both the bending modulus κ and the membrane interaction modulus B by

$$\eta = \frac{k_B T q_1^2}{8\pi\sqrt{B\kappa}} \quad and \quad \xi^4 = \frac{\kappa}{B}. \tag{6}$$

The numerical procedure for calculating $S(q_z, q_r)$ has been described in [33].

Errors were determined as fit standard errors, corresponding to 95 % confidence bounds, equivalent to two standard deviations, σ. Errors for calculated parameters, such as peak area, were then calculated by applying the proper error propagation.

Molecular Dynamics simulations

MD simulations were performed on a GPU accelerated computer workstation using GROMACS Version 5.1.4. The device is equipped with a 40 Core central processing unit (CPU, Intel(R) Xeon(R) CPU E5-2630 v4 @ 2.20GHz), 130 GB random-access memory (RAM) and three graphic processing units (GPU, 2 × NVIDIA 1080 TDI + 1 × GeForce GT 730). RBCcm models were created using the CHARMM-GUI membrane-builder (http://charmm-gui.org/) [37,38] and the Martini forcefield 2.2 [38]. The system represents a membrane patch of ≈ 34 nm × 34 nm with about 2,500 lipid molecules on each leaflet and 37 water molecules per lipid corresponding to a well hydrated state of the membrane. Two models replicating the lipidomics of membranes from fresh RBC and stored RBC were prepared. The lipid composition of the membrane patch was adjusted to match the experimental lipidomic findings determined from mass spectrometry experiments. Each lipid species was mapped to available models in the Martini 2.2 force field: An error coefficient was calculated for every available model lipid describing the difference in the tail length and the difference in tail saturation between the model and the experimental lipid. The Martini lipid with the smallest error value was then used for each experimental lipid respectively. The membrane's asymmetry, *i.e.*, the unequal distribution of lipids among both leaflets, was adjusted by using values for the compositional asymmetry published in previous coarse grained plasma membrane simulations [39]. For instance, from all simulated PC lipids 75 % were placed in the upper and 25 % were placed in the lower leaflet. Details about the exact lipid composition of each model can be found in the *Supplementary Material* in Table S1. Fig. S1 and Fig. S2 visualize the relative concentrations of lipid species in both membrane models. In addition, simulations of the 30 mol% membrane patch were repeated on two symmetrized membrane patches. The lipid composition from the upper and lower leaflet of the asymmetric model were taken, respectively, and used in the creation of models with symmetric leaflets.

Simulations were equilibrated for 80 ns using the NPT ensemble (constant pressure and temperature), and then run for 2 μs. Only the final 1,800 ns were analyzed, after affirming the membrane had reached equilibrium by determining the area per lipid. Prior to each simulation run, the system was allowed to equilibrate for simulated 5 ns. The simulation used a 1 fs time step, a short range van der Waal cutoff of 1.1 nm and a potential-shift-verlet coulomb modifier. Periodic boundary conditions were applied to all spacial directions. Neighbor lists were updated in intervals of 20 steps. The temperature coupling was controlled by a v-rescale thermostat at a constant pressure of 1 bar using Parrinello-Rahman semi-isotropic weak coupling (τ=12 ps; compressibility β=3·10^{-4} bar^{-1}). Cholesterol density maps were calculated using the gmx densmap function provided by GROMACS. Out-of-plane density profiles were calculated using the GROMACS build-in gmx density function. The domain size of cholesterol rich areas was determined by manually selecting 40 points on the edges of the observed clusters in the calculated density maps and measuring the distance between the points, respectively. The domain sizes of cholesterol depleted areas were determined the same way.

Fluctuation spectra for both membrane models were determined. Index files containing C1 Beads from DPGG, OPGG, FPGG, and DFGG; GL1 beads from FPMG, OPMG, DPMG and PO4 beads from POPC were created for each leaflet respectively. Trajectories for all index groups were exported between 200 ns and 2 μs in steps of 4 ns from the simulation. The location of these coarse grained beads corresponds to the

location of the lipid head groups in the simulated bilayer. The undulation profile at a given time step was determined by first interpolating the z-position of all beads for both leaflets respectively and calculating the average undulation of the upper and lower leaflet. The 2-dimensional spectrum was then determined using built-in MATLAB functions. The scaling of the spectrum was verified using the program provided by the authors of [40].

The spectrum is governed by a q^4 dependency according to the Helfrich–Canham (HC) theory. The bending modulus can be thus determined by fitting the lower q-regime (q <0.1 Å^{-1}) to

$$\left\langle |h(q)|^2 \right\rangle = \frac{k_B T}{\kappa q^4} \tag{7}$$

Lipidomics Analysis

Lipidomics

Samples were resolved as described [41], over an ACQUITY HSS T3 column (2.1 × 150 mm, 1.8 μm particle size (Waters, MA, USA) using an aqueous phase (A) of 25 % acetonitrile and 5 mM ammonium acetate and a mobile phase (B) of 50 % isopropanol, 45 % acetonitrile and 5 mM ammonium acetate. Samples were eluted from the column using either the solvent gradient: 0-1 min 25 % B and 0.3 ml/min; 1-2 min 25-50 % B and 0.3 ml/min, 2-8 min 50-90 % B and 0.3 ml/min, 8-10 min 90-99 % B and 0.3 ml/min, 10-14 min hold at 99 % B and 0.3 ml/min, 14-14.1 min 99-25 % B and 0.3 ml/min, 14.1-16.9 min hold at 25 % B and 0.4 ml/min, 16.9-17 min hold at 25 % B and resume flow of 0.3 ml/min. Isocratic elution of 5 % B flowed at 250 μl/min and 25 °C or a gradient from 0- 5 % B over 0.5 min; 5-95 % B over 0.6 min, hold at 95 % B for 1.65 min; 95-5 % B over 0.25 min; hold at 5 % B for 2 min, flowed at 450 μl/min and 35 °C [42]. The Q Exactive mass spectrometer (Thermo Fisher Scientific, San Jose, CA, USA) was operated independently in positive or negative ion mode, scanning in Full MS mode (2 μscans) from 150 to 1500 m/z at 70,000 resolution, with 4 kV spray voltage, 45 sheath gas, 15 auxiliary gas.

MS2 analyses for untargeted lipidomics

For untargeted lipidomics, dd-MS2 was performed at 17,500 resolution, AGC target = $1 \cdot 10^5$, maximum IT = 50 ms, and stepped NCE of 25, 35 for positive mode, and 20, 24, and 28 for negative mode, as described in Stefanoni *et al.* [43] and applied to similar samples (*i.e.*, stored RBCs) in D'Alessandro *et al.* [44].

Quality control and data processing

Calibration was performed prior to analysis using the PierceTM Positive and Negative Ion Calibration Solutions (Thermo Fisher Scientific). Acquired data was then converted from .raw to .mzXML file format using Mass Matrix (Cleveland, OH, USA). Samples were analyzed in randomized order with a technical mixture (generated by mixing 5 μl of all samples tested in this study) injected every 10 runs to qualify instrument performance. This technical mixture was also injected three times per polarity mode and analyzed with the parameters above, except CID fragmentation was included for unknown compound identification (10 ppm error for both positive and negative ion mode searches for intact mass, 50 ppm error tolerance for fragments in MS2 analyses – further details about the database searched below).

Metabolite assignment and relative quantitation

Metabolite assignments, isotopologue distributions, and correction for expected natural abundances of deuterium, ^{13}C, and ^{15}N isotopes were performed using MAVEN (Princeton, NJ, USA) [45], against an in house library of deuterated lipid standards (SPLASH LIPIDOMIX Mass Spec Standard, Avanti Lipids) and in house libraries of 3,000 unlabeled (MSMLS, IROATech, Bolton, MA, USA; IroaTech ; product A2574 by ApexBio; standard compounds for central carbon and nitrogen pathways from SIGMA Aldrich, St Louis, MO, USA) and labeled standards (see below for the latter). Untargeted lipidomics analyses were performed with the software LipidSearch (Thermo Fisher, Bremen, Germany). Results from lipidsearch were exported as a library and additional discovery mode analyses were performed with standard workflows using Compound Discoverer 2.1 SP1 (Thermo Fisher Scientific, San Jose, CA). From these analyses, metabolite IDs or unique chemical formulae were determined from high-resolution accurate intact mass, isotopic patterns, identification of eventual adducts (e.g., Na^+ or K^+, etc.) and MS2 fragmentation spectra against the KEGG pathway, HMDB, ChEBI, and ChEMBL databases.

Results

Table 1. Structural parameters and membrane bending modulus κ determined from XRD and XDS experiments.

	Fresh	2Weeks	5Weeks
Lamellar Spacing (Å)	55.4±0.5	56.9±0.2	57.3±0.1
HH-Distance (Å)	43±1	46±1	45±1
Water-Layer Thickness (Å)	11.9±0.5	11.25±0.5	11.65±0.5
Membrane Order Parameter (%)	88.4±0.7	89.9±0.5	91.5±0.5
Fractions l_d:l_o	60 : 40	59 : 41	54: 46
Tail distance a (Å)			
Protein	10.88±0.22	10.54 ± 0.07	10.33 ± 0.06
l_d	5.39±0.03	5.39 ± 0.004	5.413 ± 0.005
l_o	4.69±0.27	4.20 ± 0.01	4.22 ± 0.01
Area per Lipid Tail A_T (Å^2)			
l_d	25.18 ± 0.13	25.173 ± 0.008	25.383 ± 0.008
l_o	19.04 ± 1.10	15.29 ± 0.02	15.44 ± 0.03
Domain Size ζ (Å)			
l_d	29 ± 2	24.6 ± 0.31	22.7 ± 0.1
l_o	16± 3	14.2 ± 0.3	12.1 ± 0.4
Bending Modulus κ (k_BT)	1.9±0.2	4.6±0.4	5.3±0.4

Structure of RBCcm from X-ray Diffraction and X-ray Diffuse Scattering

Two-dimensional X-ray intensity maps for membranes from fresh RBC, and 2 weeks and 5 weeks old RC, all measured at 88% RH, are depicted in Fig. 1 A. Structural features are typically enhanced at this slightly reduced hydration. Series of pronounced lamellar peaks were observed in all samples indicating a lamellar organization of the membranes. The maximal observed order of lamellar peaks was found to be 4 for a fresh RBCcms, and up to 6 in case of samples prepared from RC. q_1 will hereafter refer to the position of the first order lamellar peak. The specular reflectivity was analyzed by first

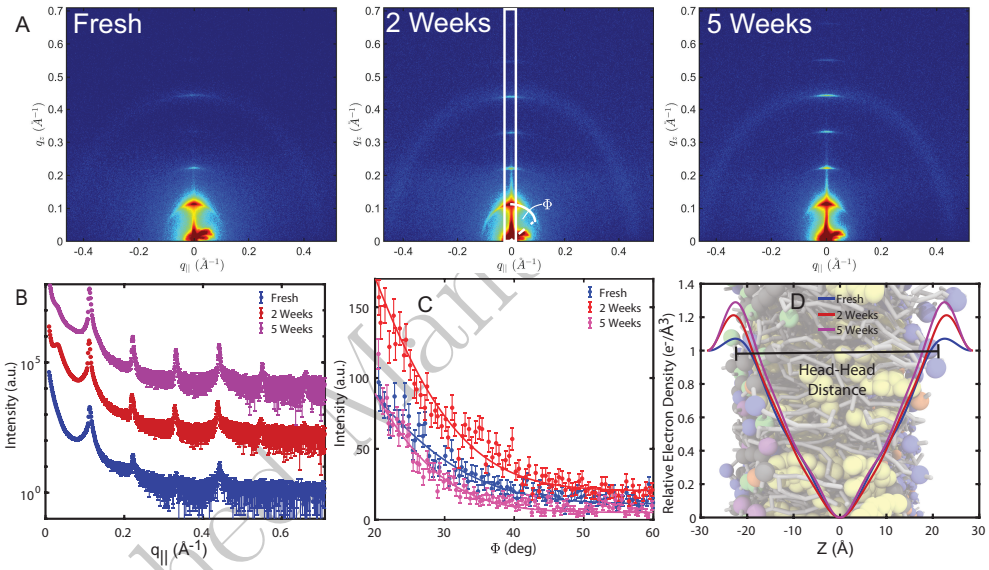

Fig 1. **A** Two-dimensional X-ray intensity maps measured at 88% RH for a fresh RBCcm sample and RBC collected from RC that was stored for 2 and 5 weeks respectively. Up to 6 orders of lamellar peaks were observed. **B** Specular reflectivity as determined from the integrated intensity marked as white rectangle. **C** X-ray intensity determined along the meridional angle Φ as indicated by the white line in **A**. The degree of orientation was determined by fitting Hermans orientation function. **C** Relative electron density profile determined from a 1-dimensional Fourier analysis. Maxima around $|z|$=20 Å indicate the location of the electron-rich head-groups of the membranes while the electron density is reduced in the bilayer center.

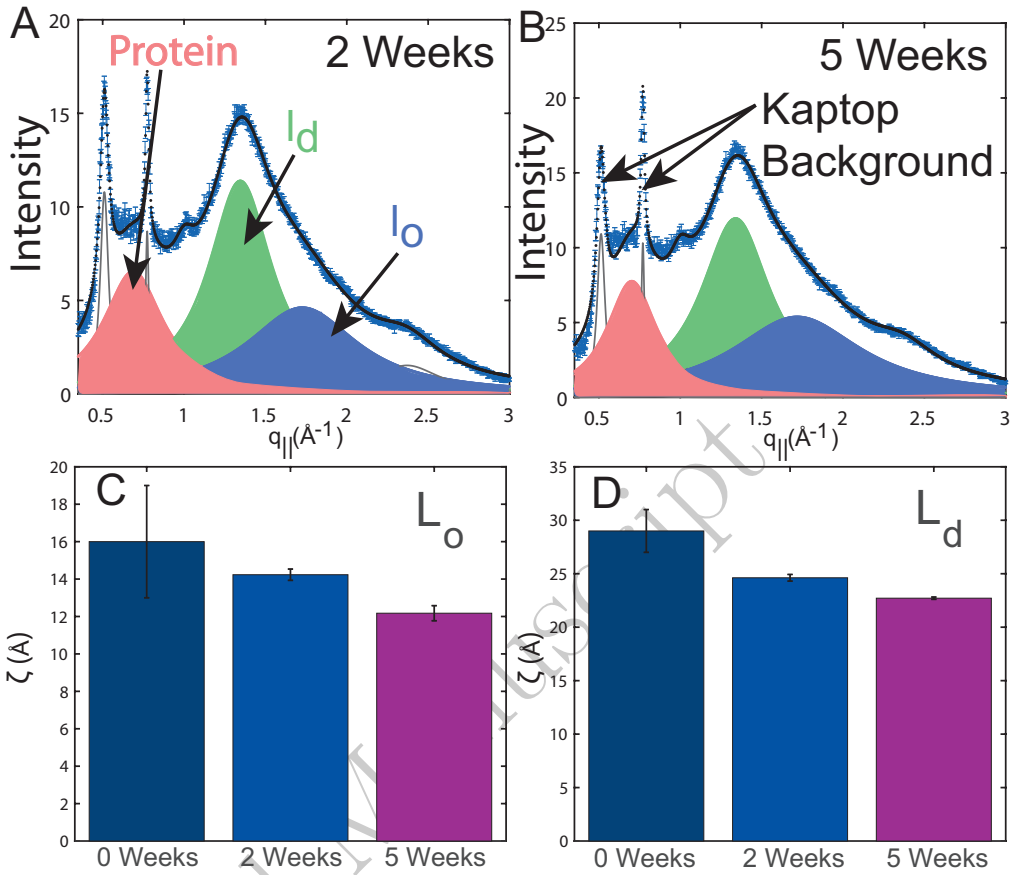

Fig 2. **A** Background corrected in-plane X-ray intensity profiles. Three peaks resulting from liquid ordered l_o and liquid disordered l_d lipid domains, as well as α-helical protein structures were observed and fits are shown in blue, green and red respectively. The domain sizes were determined as described in *Materials & Methods* and are expressed as the edge size of the domain. They are graphed in **C** and **D**.

integrating the 2-dimensional X-ray intensity map along the marked rectangle. The resulting line-cuts are shown in Fig. 1 B. The lamellar spacing d_z was determined from the peak positions and Bragg's law, $d_z = 2\pi/q_z$, as listed in Table 1. Fig. 1 C shows the X-ray intensity profile along the meridional angle Φ. The degree of order in the membrane stack was determined by fitting Hermans orientation function.

Out-of-plane electron density profiles were determined by a 1-dimensional Fourier analysis, shown in Fig. 1 D. The electron density is plotted on a relative scale. The maximal electron density was observed around $|z|$=20 Å indicating the location of the electron-rich head-groups of the membranes; it reaches a minimum in the center of the membrane. While the differences in the electron density between fresh RBCs and stored RBCs were small within the membranes, the electron density in the head-groups of the 2 and 5 weeks sample was observed to be increased by 10% and 20%, respectively, as compared to a fresh RBC sample.

The distance between the head-group peaks was defined as membrane thickness and is listed Table 1. The difference between the d_z-spacing and the membrane thickness consequently corresponds to the thickness of the water layer between neighboring membranes (also listed in Table 1).

Fig. 2 shows the in-plane diffraction signal from 2 and 5 weeks stored RBCcm.

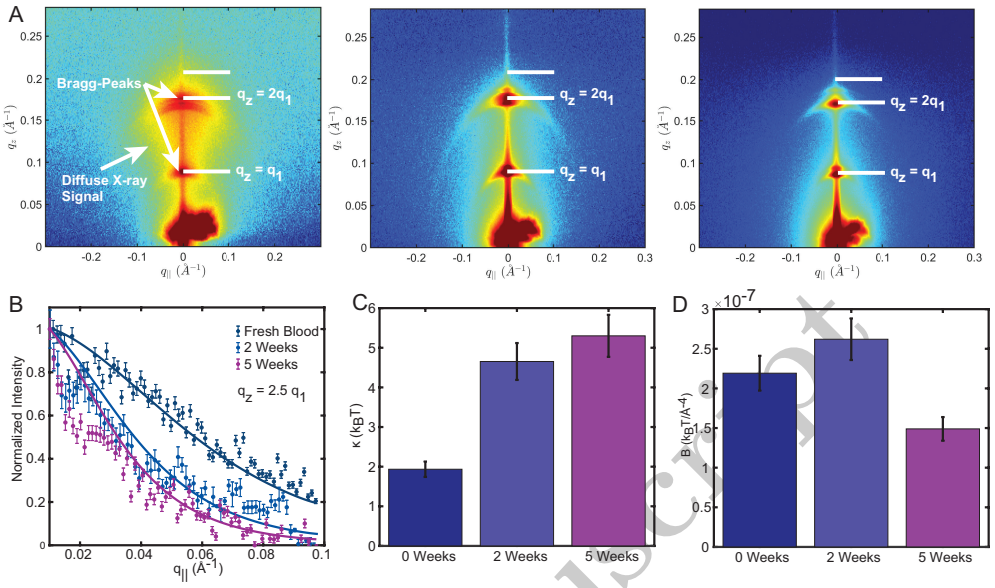

Fig 3. **A** Two-dimensional X-ray intensity maps measured at 99.9% RH. A diffuse cloud of X-ray signal was observed as the result of out-of-plane fluctuations. Line-cuts at $q_z = 2.5 \cdot q_1$ are depicted in **B**. The bending modulus κ and membrane interaction modulus B were determined by fitting $S(q)$ to the data, and are visualized as bar graph in **C** and **D**

Peaks at $q_{||}$=0.7 Å^{-1}, 1.3 Å^{-1} and 1.7 Å^{-1} were observed. The blue and green signals are the result of a hexagonal packing of the liquid disordered (l_d) and liquid ordered (l_o) lipid tails in the hydrophobic membrane core (planar group p6) [29]. A third peak shown in red was assigned to coiled-coil α-helical peptides [29]. The distance between two acyl tails was determined using $a = 4\pi/(\sqrt{3}q_{||})$, where $q_{||}$ is the position of the corresponding correlation peak. The area per lipid chain is obtained to $A_T = (\sqrt{3}/2)a^2$. All values are listed in Table 1. The tail distance in l_o domain was found to slightly decrease during storage, while changes in the tail distance of l_d domains were within statistical errors. The fraction of l_d domains was found to monotonically decrease by 6 % in favor of l_o domains. The sizes ζ of both lipid domains are graphed in Figs. 2 C and D and were found to monotonically decrease.

Diffuse scattering was measured in Fig. 3 A, showing 2-dimensional X-ray intensity maps measured at 99.9% RH. Only two orders of lamellar peaks were observed as the result of increased fluctuations at this high hydration. Importantly, a diffuse cloud of X-ray signal was detected around the peaks resulting from membrane height fluctuations. Line-cuts at $q_z = 2 \cdot q_1$ and $q_z = 2.5 \cdot q_1$ were taken, and are depicted in Fig. 3 B and Fig. S4 in the *Supplementary Material*. The membranes' bending modulus κ, and compressibility modulus B were determined by fitting the calculated structure factor $S(q)$ (in Eq. (6)) to the diffuse profiles. Bending moduli of κ =4.6 k_BT and κ =5.3 k_BT were determined for membranes extracted from RBCs after 2 and 5 weeks of storage, indicating a 2.8× fold increase as compared to fresh RBC (κ =1.9 k_BT)

The results of the structural analysis (in Table 1) can be summarized as follows: lamellar spacing and membrane thickness increase during storage and the membranes become stiffer as the order parameter increases. At the same time the fraction of l_d domains decreased from 60 % to 54 % while the fraction of l_o lipids increased from 40-46%. The size of those domains reduced from 29 Å to about 23 Å. The bending rigidity κ monotonically increased with storage time from 1.9 to 5.3 k_BT.

Membrane Lipidomics

Lipidomics of RBCcm was measured and analyzed with respect to the abundance of lipid species, tail length and degree of tail saturation. Fig. S1 A and Fig. S2 A in the *Supplementary Material* show the abundance of Phosphatidylcholine, PC; Ceramide, CER; Monoglucosyl lipids, MG; Diacylglycerol lipids, DG; Fatty acids, FA; Sphingomyelin, SM; Phosphatidylethanolamine, PE; Phosphatidylserine, PS; Phosphatidylglycerol, PG; Phosphatidic acid, PA; Phosphatidylinositol, PI for a fresh RBC sample and a sample after 42 days. Fig. S3 A and B compare the differences in tail saturation and tail length for a fresh and 42 day old RBCcm. It was found that the difference between the samples was small and in the order of a few percent, only. The abundance of tails with a length < 16 CH_2 groups was found to be decrease by 5 % in favor of shorter tails with a length of 8 and 12 CH_2 groups. At the same time the tails were found to be more unsaturated. While fatty acids accounted for less than 1 % of the RBCcm in the fresh sample, they contributed ≈5 % to the RBCcm's lipidomics in a 42 day old sample (Fig. S3 C). While this analysis method provides detailed insight into the RBCcm's lipid composition, the information about cholesterol concentrations is limited. While [27] reported that cholesterol makes up one third of the membrane in fresh cells and half of the RBCcm after 42 days of storage [27], others assume that cholesterol typically makes 50 mol% of the lipid content, and that the concentration does not change during storage [28].

MD simulations

Two coarse grained membrane models mimicking a fresh RBCcm and a RBCcm after 42 days of storage were created. To mimic the largest potential change in composition, lipidomics from fresh RBC and RBC after 42 days of storage were used with cholesterol concentrations of 30 mol% and 50 mol%, respectively.

Fig. 4 A shows 3-dimensional renders created after 2 μs of simulations, where lipid molecules are represented by rods and cholesterol molecules are displayed as red spheres. Cholesterol density maps were created and are shown in Fig. 4 B. A patchy structure is apparent, where cholesterol rich areas are shown in red; blue areas indicate cholesterol depletion. Domain sizes were measured with values of ≈50 Å for fresh, and 40 Å in 5 weeks old membranes (listed in Table 2). Fig. 4 C shows the mass density profiles of the overall membrane patch (solid lines) and the cholesterol OH-Group (dotted lines) that were determined from both simulations. A mass density of ≈1000 kg/m^3 was observed in the water layer surrounding the membrane. The density is significantly increased within the bilayer and peaks around the membrane's head-group region of the membrane. This head-group mass density is found to be increased by up to 25 kg/m^3 in the 42 day old membrane mimic as compared to the fresh membrane. The increase was 5 kg/m^3 in the bilayer center only. The cholesterol's head-group density was observed to increase by a factor of 2.3 from a maximum of 31 kg/m^3 in the fresh membrane mimic to a maximum of 71 kg/m^3 in the 42 days membrane patch.

The fluctuation spectrum is shown in Fig. 4 D. It follows a q^4 dependency in the low-q regime (q <0.1 Å^{-1}), as predicted by the Helfrich–Canham (HC) theory (Eq. (7)), which describes membrane undulations on length scales much larger than the membrane thickness [40, 46]. The spectrum deviates from the q^4 dependency for q >0.1 Å^{-1}. Fits of Eq. (7) for values of q <0.1 Å^{-1} are displayed as red solid line. There was an increase in bending modulus from κ =3.2±0.1 k_BT for fresh membranes, to κ =5.3±1.5 k_BT for the 5 week old membrane patch.

Due to a random stacking of membranes in the solid supported RBCcm samples, the XRD experiment is not sensitive to a potential asymmetry. The simulation containing 30 mol% cholesterol was thus repeated with a symmetric lower and upper leaflet

respectively. The fluctuation spectrum of both simulations is shown in Fig. S5 (*Supplementary Material*). The bending modulus was measured to be 4.12±1.36 k_BT (symmetric upper leaflet) and 3.18±0.84 k_BT (symmetric lower leaflet) and thus agrees with the asymmetric membrane patch within statistical errors.

Table 2. Structural parameters and bending modulus κ determined from MD simulations.

	fresh	5 weeks
Domain Size ζ (Å)		
l_d	52 ± 16	40 ± 17
l_o	42± 17	30 ± 1
Bending Modulus κ (k_BT)	3.2 ±0.1	5.3±1.5

The simulations thus indicate a decrease in domain size, a decrease in the fraction of l_d domains and an increase in the bending modulus, κ, of the membranes as function of storage time, in agreement with the experimental findings.

Discussion

As a general note, the observed changes in the hemoglobin depleted RBCcm structure during storage were small and require high-resolution techniques to be resolved. The majority of lipid species (PC, PE, PA, PI, PS, PG, MG and DG) were found to change only slightly, in the order of ≈1 %. Only the concentration of fatty acid was found to increase by ≈5 %. It has been previously reported that the degree of fatty acid unsaturation increased in stored RBCs as a function of oxidant stress and pyruvate/lactate ratios, perhaps as a result of residual fatty acid desaturase activity in the mature RBC or moonlighting function of other enzymes sensitive to $NADH/NAD^+$ ratios [47].

A significant change was reported in the membrane's cholesterol content by [27], who observed an increase from 30 mol% to 50 mol%, which was speculated to be a result of lipid loss [26]. The rigid cholesterol molecule is widely known to form patches with increased lipid tail order within the membrane [48–54].

Our experimental results show that the fraction of liquid disordered l_d domains decreases by 6 % in favor of liquid ordered l_o domains. At the same time the sizes of both domains were found to decrease. The same changes were observed for the cholesterol rich patches in the MD simulations, suggesting that the experimental observations are the effect of higher cholesterol concentrations resulting in a splitting and dispersion of the domains in stored RBCcm.

It may be surprising that the domain sizes in XRD experiments and simulations do not agree until the respective definition of domain sizes is taken into account. Scherrer's equation (Eq. 4) was developed for the study of crystalline structures and measures the domain size from the width and position of an in-plane correlation peak. The equation generally determines the edge size of quadratic domains in a presumably cubic lattice. However, lipid domains have a rather irregular shape, as it is apparent from the simulation. A maybe more appropriate comparison between both results are given by diagonal elements in the quadratic domains which increases the experimental sizes by a factor of $\sqrt{2}$.

The l_o domains have a decreased area per lipid tail (15 $Å^2$ *vs.* 25 $Å^2$ in l_d domains) which was found to decrease slightly (19 $Å^2$ *vs.* 15 $Å^2$) in the stored samples. Importantly, this denser packing of molecules, together with the measured larger fractions of l_o domains, explains the increase in the system's mass and electron density observed in simulations and experiments.

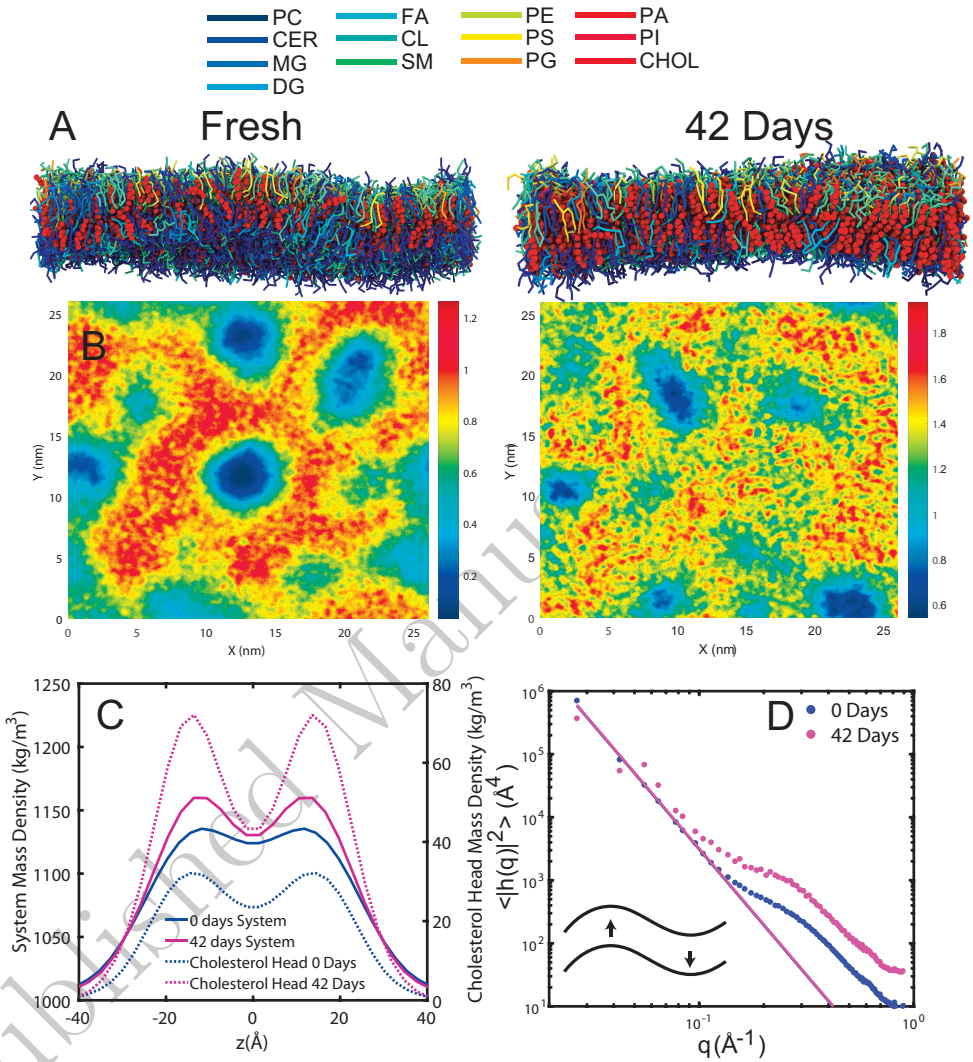

Fig 4. **A** 3-dimensional render of a simulated RBCcm patch after 2 μs. Lipid molecules are displayed as rods symbolizing molecular bonds. Cholesterol is depicted as red spheres. Each lipid species (Phosphatidylcholine, PC; Ceramide, CER; Monoglucosyl lipids, MG; Diacylglycerol lipids, DG; Fatty acids, FA; Sphingomyelin, SM; Phosphatidylethanolamine, PE; Phosphatidylserine, PS; Phosphatidylglycerol, PG; Phosphatidic acid, PA; Phosphatidylinositol, PI) are represented by different colors indicated in the legend. **C** Cholesterol density maps averaged over the last 800 ns of the simulation. Red indicates cholesterol rich areas while blue represents cholesterol depletion. **C** Mass density profiles averaged over the last 800 ns of the simulation for the entire membrane patch (System) and the cholesterol head groups. **D** Fluctuation spectrum of the 42 day old membrane patch. The bending modulus κ was determined by fitting Helfrich–Canham (HC) theory.

The increased fraction of these patches thus agrees with the observed age dependent increased electron and mass density in both experiments and simulations. The measured increased HH-distance was found to be small (2 Å). However, our lipidomic findings report negligible changes in the tail length of the lipid molecules and the increased membrane thickness can consequently be understood as the result of straightened lipid tails in cholesterol rich domains. This is also supported by the measured 6 % increase of membrane order parameter.

Cholesterol is known to reduce the non-active oxygen transport across lipid bilayers [21, 55, 56]. The denser packing of lipid tails around cholesterol molecules presents a physical barrier [56] and oxygen consequently transits the membrane at the boundaries between l_o and l_d domains [21]. The observed larger fraction of l_o domains with an denser lipid packing in stored RBCcm suggests that there is less space available for oxygen to permeate the membrane. We thus speculate that the measured changes in the RBCcm's domain landscape may influence the passive transport of oxygen across the RBCcm, which is of particular importance for this cell species.

A significant increase (2.8×) in the membrane's bending modulus was observed in XDS experiments. These observations are consistent with the RBCcm becoming stiffer during storage. It further agrees well with previous studies reporting a decreased deformability of stored RBC [15–19].

It is well known that RBCs have a composite outer "shell" formed by a cytoplasmic membrane (RBCcm) tethered to a spectrin cytoskeleton. We argue that our results measure the bending modulus of the RBCcm in the absence of the spectrin cytoskeleton. First, spectrin filaments were no longer detectable using our preparation protocol [29] by fluorescent microscopy following sonication with subsequent centrifugation of RBC ghosts. In addition, the d_z-spacing in XRD experiments together with electron density profiles are inconsistent with the presence of cytoskeleton structures between membranes in the solid supported stack.

An attempt to explain the experimentally measured increase in the membrane's bending modulus needs to consequently focus on the RBCcm only. An obvious explanation for this increase may be an increased cholesterol concentration in stored membranes. . To address this question, MD simulations were performed in the absence of proteins to explicitly probe the influence of membrane composition and in particular the effect of cholesterol.

However, the simulations show a slight increase in the membrane's bending modulus, only, substantially smaller than in the XDS experiments. This difference becomes even smaller when considering results on membrane patches with symmetric upper and lower leaflet. We conclude that the significant increase in cholesterol concentration is obviously not directly linked to increased stiffness in more realistic membrane models. Cholesterol's rigid molecular structure contrasts the flexible nature of fatty acyl tails and is known to increase the membrane's bending modulus in fully saturated model membranes [57, 58]. However, this effect is substantially reduced for mono-unsaturated bilayer and vanishes for 1,2-dioleoyl-sn-glycero-3-phosphocholine (DOPC) membranes [57, 58]. Little is known about the effect of cholesterol on the bending rigidity of multi-component lipid bilayers. Only ≈1/3 of the lipids within the RBCcm were found to be fully saturated and the findings are thus in-line with previous experiments on synthetic membranes and re-emphasize the negligible effect of cholesterol on the membrane's bending rigidity when there are unsaturated molecules present. A potential explanation for the changes in κ could be related to the effect of integral membrane proteins [40, 59–61]

Blood bags are primarily composed of polyvinyl chloride (PVC) compounded with 30-40% *wt* di(2-ethylhexyl) phthalate (DEHP) [62], a plasticizer used to improve the bags' flexibility and durability. Due to its lipophilic structure, DEHP is known to

migrate from the PVC polymer matrix into packed red blood cells (RBC) [63, 64]. 15 to 624.2 μg/ml of DEHP were detected in PVC blood bags after 20 days of storage [65, 66] and 7.4 to 36.1 μg/ml of DEHP were found in irradiated RBC concentrate products [65]. The partitioning of DEHP in RBCcms has long been suspected to change membrane properties [66, 67] and contribute to the changes observed during storage. A recent study in model lipid bilayers indeed reported that DEHP can slightly increase membrane width and area per lipid, and the deuterium order parameter, however, decrease membrane orientation, indicating the formation of thicker, stiffer membranes with increased local curvature [68]. Concentrations of DEHP in this paper were elevated, of up to 10 mol% of the lipid concentration to emphasize the potential effects of DEHP. Even though the presence of DEHP could potentially explain the observed increased stiffness in our experiments, we could not find clear evidence for the presence of DEHP molecules in the electron density of RBCcms in our X-ray diffraction results. The upper bound of experimentally reported DEHP concentrations in blood bags is ≈ 600 μg/ml [66], which corresponds to molar concentrations of less than 0.2 mol% (resulting in about 15 molecules in the computer simulations), significantly smaller than what was used in [68]. While we can not rule out that the effects of DEHP were too small to be detected in this study, we speculate that the changes in the membranes' structural parameters would be even smaller than the subtle effects reported by Bider *et al.*. In addition, the DEHP molecule is currently not available in the Martini force field such that it could not be included in our MD simulations. We can, therefore, at this point not comment on the role of DEHP in the observed changes in membrane properties.

Conclusion

The molecular structure of RBCcm was determined from RBCs that were stored for 2 and 5 weeks respectively. We provide direct experimental evidence for an increased fraction of lipid ordered lipid domains within the bilayer. This is consistent with an observed increase in the membrane thickness, membrane order parameter and head-group density as a result of straightened lipid tails in these cholesterol rich domains. The domain size of l_o and l_d lipid domains was found to decrease with storage time. X-ray diffuse scattering experiments revealed a significant increase ($2.8\times$) of the membrane's bending modulus κ. This change was not observed in Molecular Dynamics simulations and suggests that the increased bending rigidity is not a result of lipidomic changes, and especially the increased cholesterol concentrations.

Supporting information

Table S1 Lipid composition of RBCcms from fresh RBC and stored RBC as determined from mass spectrometry and corresponding mapped coarse grained molecular dynamics models.

Acknowledgements

We thank Dr. John F. Nagle from Carnegie Mellon University for helpful discussion and advice for the analysis of the X-ray diffraction experiments. M.C.R. is the recipient of

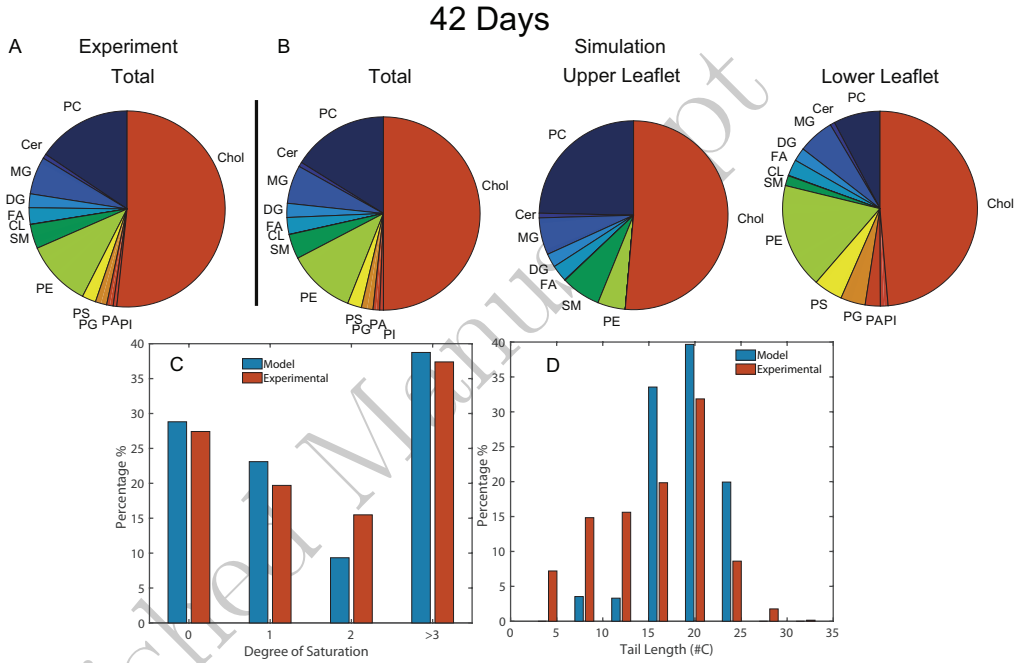

Figure S1. **A** Experimentally determined composition of red blood cell membrane as reported by [69]. **B** Lipidomics of the implemented coarse grained MD simulation model. The asymmetry of the membrane was created by distributing lipids between both leaflets according to experimental findings by [70]. **C** Comparison of the degree of tail saturation in the experimental and model membrane. **D** Comparison between the lipid tail length of the experimental and model membrane.

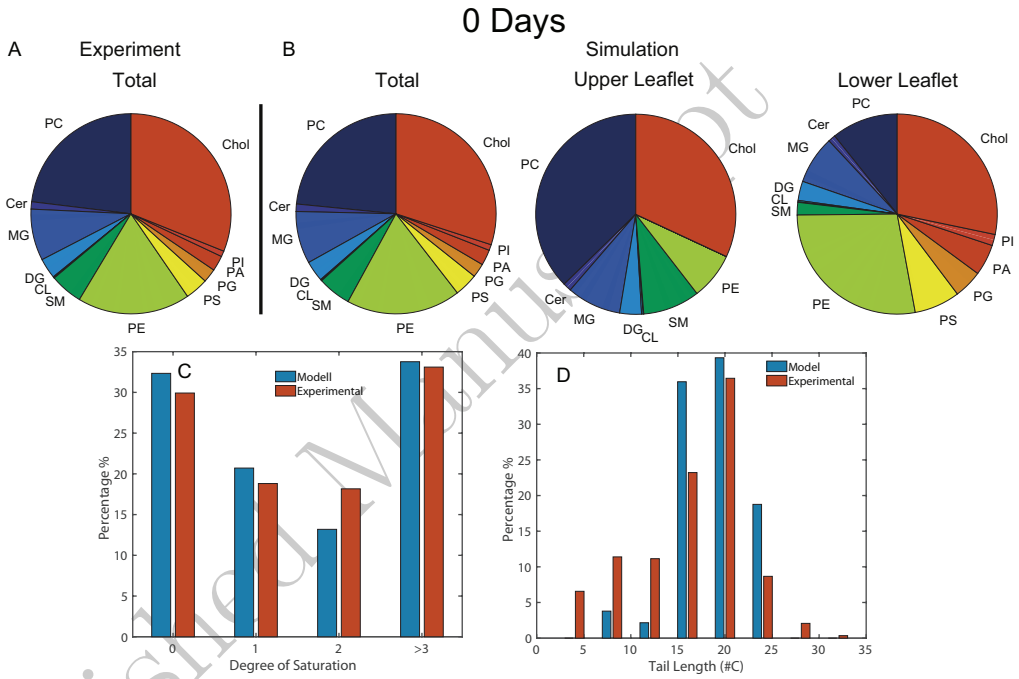

Figure S2. **A** Experimentally determined composition of red blood cell membrane as reported by [69]. **B** Lipidomics of the implemented coarse grained MD simulation model. The asymmetry of the membrane was created by distributing lipids between both leaflets according to experimental findings by [70]. **C** Comparison of the degree of tail saturation in the experimental and model membrane. **D** Comparison between the lipid tail length of the experimental and model membrane.

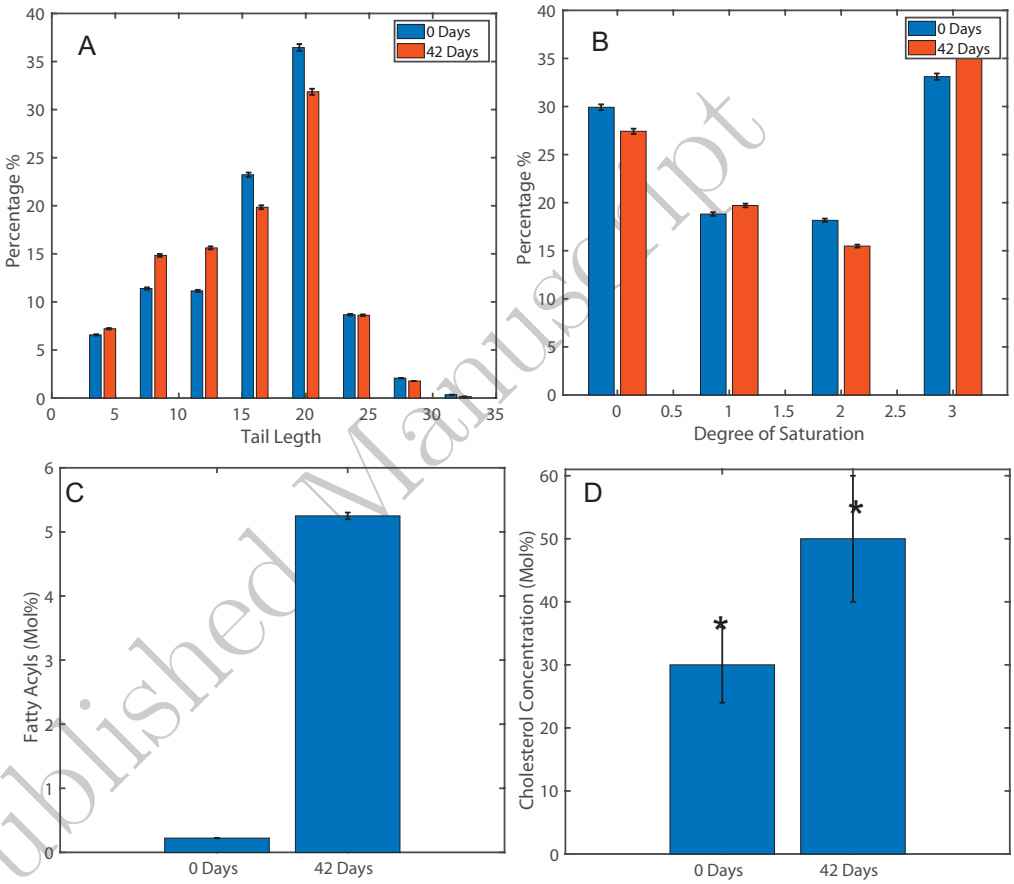

Figure S3. Comparison of the experimentally determined distribution of lipid tail lengths (**A**) and degrees of tail saturation (**B**). **C** The cholesterol concentration in fresh RBC and stored RC as determined by [27]. **D** Concentration differences of fatty acids.

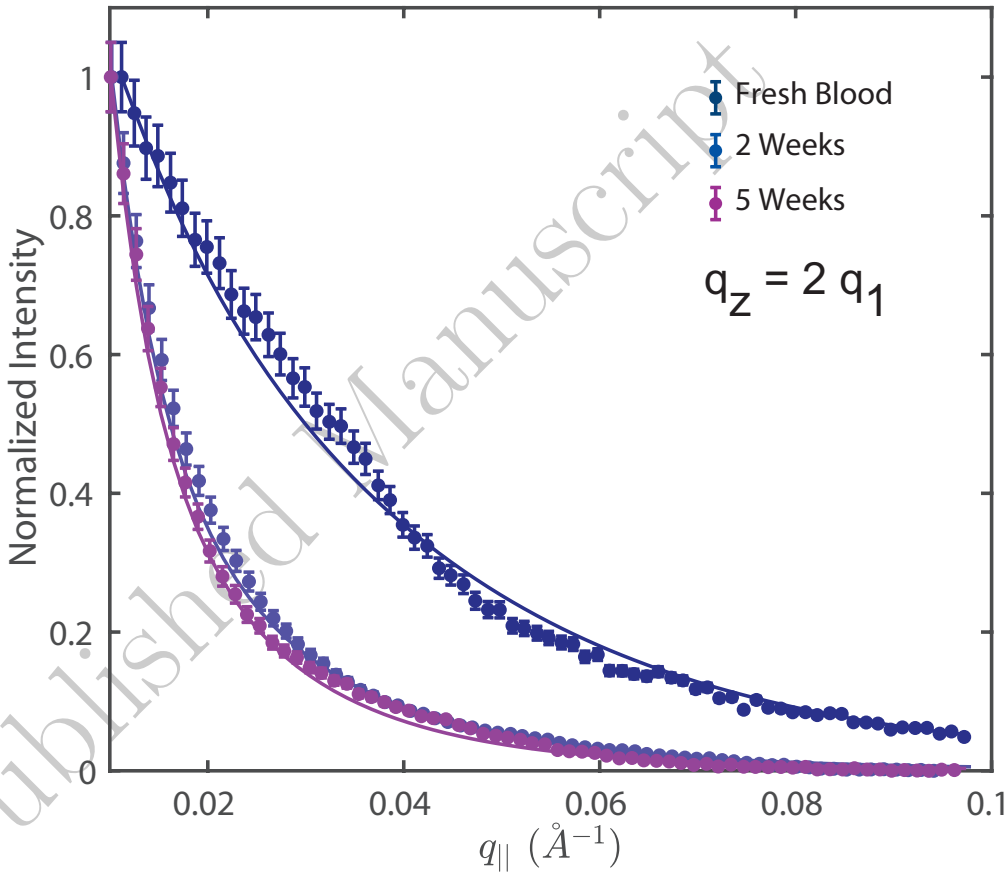

Figure S4. Line cuts at $q_z = 2q_1$ and corresponding fits of $S(q)$ (Eq. (6))

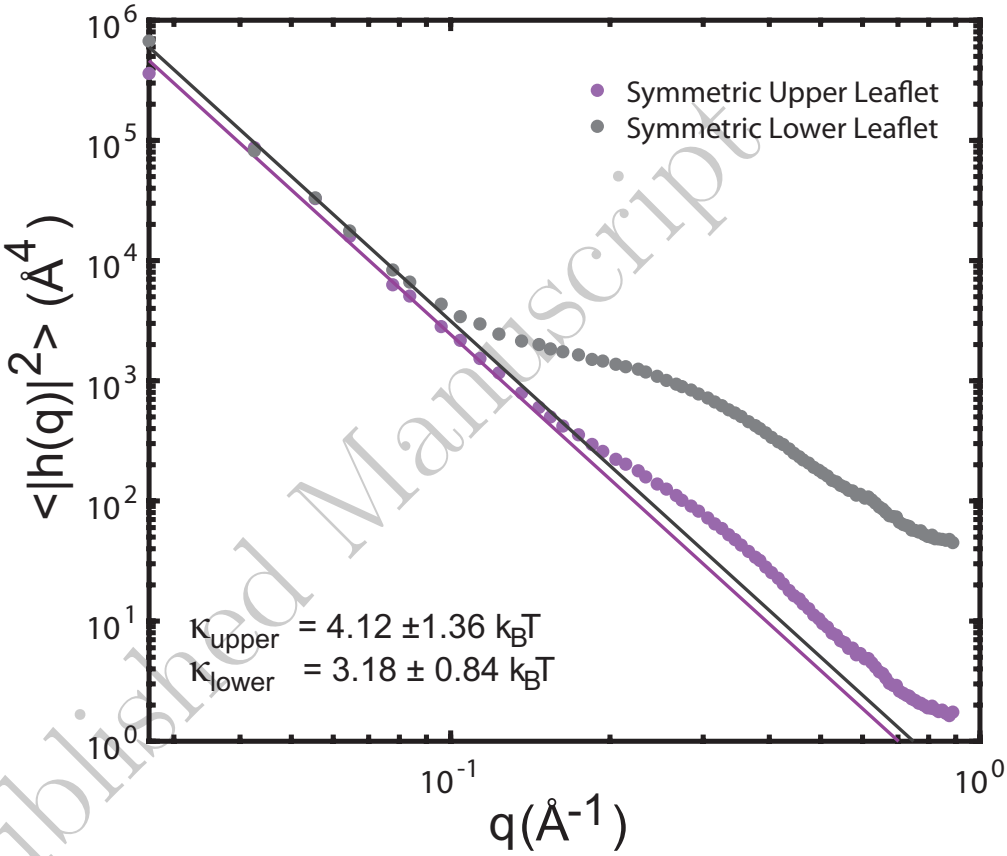

Figure S5. Fluctuation spectra determined from simulations of a symmetrisized versions of the asymmetric membrane patch (30 mol%). Bending moduli of κ=4.1±1k_BT and κ=3.1±0.8k_BT were determined for membranes with a symmetric upper and lower leaflet respectively.

an Early Researcher Award of the Province of Ontario and a University Scholar of McMaster University.

References

1. D'Alessandro A (2021) In vivo clearance of stored red blood cells. *Blood, The Journal of the American Society of Hematology* 137(17):2275–2276.

2. Roussel C, et al. (2021) Rapid clearance of storage-induced microerythrocytes alters transfusion recovery. *Blood, The Journal of the American Society of Hematology* 137(17):2285–2298.

3. Yoshida T, Prudent M, D'Alessandro A (2019) Red blood cell storage lesion: causes and potential clinical consequences. *Blood Transfusion* 17(1):27.

4. Grimshaw K, Sahler J, Spinelli SL, Phipps RP, Blumberg N (2011) New frontiers in transfusion biology: identification and significance of mediators of morbidity and mortality in stored red blood cells. *Transfusion* 51(4):874–880.

5. Spinella PC, et al. (2009) Duration of red blood cell storage is associated with increased incidence of deep vein thrombosis and in hospital mortality in patients with traumatic injuries. *Critical Care* 13(5):1–11.

6. Wang D, Sun J, Solomon SB, Klein HG, Natanson C (2012) Transfusion of older stored blood and risk of death: a meta-analysis. *Transfusion* 52(6):1184–1195.

7. Solomon SB, et al. (2013) Mortality increases after massive exchange transfusion with older stored blood in canines with experimental pneumonia. *Blood* 121(9):1663–1672.

8. Gerber DR (2012) Risks of packed red blood cell transfusion in patients undergoing cardiac surgery. *Journal of Critical Care* 27(6):737–e1.

9. Kanias T, Acker JP (2010) Biopreservation of red blood cells–the struggle with hemoglobin oxidation. *The FEBS Journal* 277(2):343–356.

10. Bosman GJ, et al. (2008) The proteome of red cell membranes and vesicles during storage in blood bank conditions. *Transfusion* 48(5):827–835.

11. Berlett BS, Stadtman ER (1997) Protein oxidation in aging, disease, and oxidative stress. *Journal of Biological Chemistry* 272(33):20313–20316.

12. D'Alessandro A, D'Amici GM, Vaglio S, Zolla L (2012) Time-course investigation of SAGM-stored leukocyte-filtered red bood cell concentrates: from metabolism to proteomics. *Haematologica* 97(1):107.

13. Kriebardis AG, et al. (2007) Storage-dependent remodeling of the red blood cell membrane is associated with increased immunoglobulin G binding, lipid raft rearrangement, and caspase activation. *Transfusion* 47(7):1212–1220.

14. Kozlova E, et al. (2017) Morphology, membrane nanostructure and stiffness for quality assessment of packed red blood cells. *Scientific Reports* 7(1):1–11.

15. Mohanty J, Nagababu E, Rifkind JM (2014) Red blood cell oxidative stress impairs oxygen delivery and induces red blood cell aging. *Frontiers In Physiology* 5:84.

16. Cluitmans JC, Hardeman MR, Dinkla S, Brock R, Bosman GJ (2012) Red blood cell deformability during storage: towards functional proteomics and metabolomics in the blood bank. *Blood Transfusion* 10(Suppl 2):s12.

17. Xu Z, et al. (2018) Stiffness increase of red blood cells during storage. *Microsystems & Nanoengineering* 4(1):1–6.

18. La Celle P (1969) Alteration of deformability of the erythrocyte membrane in stored blood. *Transfusion* 9(5):238–245.

19. Huruta R, et al. (1998) Mechanical properties of stored red blood cells using optical tweezers. *Blood, The Journal of the American Society of Hematology* 92(8):2975–2977.

20. Auth T, Safran S, Gov NS (2007) Fluctuations of coupled fluid and solid membranes with application to red blood cells. *Physical Review E* 76(5):051910.

21. Ghysels A, et al. (2019) Permeability of membranes in the liquid ordered and liquid disordered phases. *Nature Communications* 10(1):1–12.

22. Silliman CC, et al. (2011) Identification of lipids that accumulate during the routine storage of prestorage leukoreduced red blood cells and cause acute lung injury. *Transfusion* 51(12):2549–2554.

23. Chaudhary R, Katharia R (2012) Oxidative injury as contributory factor for red cells storage lesion during twenty eight days of storage. *Blood Transfusion* 10(1):59.

24. Dinkla S, et al. (2014) Phosphatidylserine exposure on stored red blood cells as a parameter for donor-dependent variation in product quality. *Blood Transfusion* 12(2):204.

25. Bosman GJCGM, Werre J, Willekens F, Novotnỳ V (2008) Erythrocyte ageing in vivo and in vitro: structural aspects and implications for transfusion. *Transfusion Medicine* 18(6):335–347.

26. Timperio AM, Mirasole C, D'Alessandro A, Zolla L (2013) Red blood cell lipidomics analysis through hplc-esi-qtof: application to red blood cell storage. *Journal of Integrated OMICS* 3(1):11–24.

27. Almizraq R, Tchir JD, Holovati JL, Acker JP (2013) Storage of red blood cells affects membrane composition, microvesiculation, and in vitro quality. *Transfusion* 53(10):2258–2267.

28. Melzak KA, Muth M, Kirschhöfer F, Brenner-Weiss G, Bieback K (2020) Lipid ratios as a marker for red blood cell storage quality and as a possible explanation for donor gender differences in storage quality. *Vox Sanguinis* 115(8):655–663.

29. Himbert S, et al. (2017) The molecular structure of human red blood cell membranes from highly oriented, solid supported multi-lamellar membranes. *Scientific Reports* 7:39661.

30. Himbert S, et al. (2020) Hybrid erythrocyte liposomes: Functionalized red blood cell membranes for molecule encapsulation. *Advanced Biosystems* 4(3):1900185.

31. Nagle JF, Wiener MC (1989) Relations for lipid bilayers. *Biophysical Journal* 55(55):309–313.

32. Barrett MA, et al. (2012) Interaction of aspirin (acetylsalicylic acid) with lipid membranes. *PLOS ONE* 7(4):e34357.

33. Lyatskaya Y, Liu Y, Tristram-Nagle S, Katsaras J, Nagle JF (2000) Method for obtaining structure and interactions from oriented lipid bilayers. *Physical Review E* 63:011907.

34. Liu Y, Nagle JF (2004) Diffuse scattering provides material parameters and electron density profiles of biomembranes. *Physical Review E* 69(4):040901.

35. Tristram-Nagle S, Nagle JF (2007) Hiv-1 fusion peptide decreases bending energy and promotes curved fusion intermediates. *Biophysical Journal* 93(6):2048–2055.

36. Caillé A (1972) X-ray scattering by smectic-A crystals. *C.R. Acad. Sci. Ser. B* 274:891–893.

37. Jo S, Kim T, Iyer VG, Im W (2008) Charmm-gui: a web-based graphical user interface for charmm. *Journal of Computational Chemistry* 29(11):1859–1865.

38. Qi Y, et al. (2015) Charmm-gui martini maker for coarse-grained simulations with the martini force field. *Journal of Chemical Theory and Computation* 11(9):4486–4494.

39. Ingólfsson HI, et al. (2014) Lipid organization of the plasma membrane. *Journal of the American Chemical Society* 136(41):14554–14559.

40. Fowler PW, et al. (2016) Membrane stiffness is modified by integral membrane proteins. *Soft Matter* 12(37):7792–7803.

41. Thomas T, et al. (2020) Evidence of structural protein damage and membrane lipid remodeling in red blood cells from covid-19 patients. *Journal of Proteome Research* 19(11):4455–4469.

42. Reisz JA, Zheng C, D'Alessandro A, Nemkov T (2019) Untargeted and semi-targeted lipid analysis of biological samples using mass spectrometry-based metabolomics in *High-Throughput Metabolomics*. (Springer), pp. 121–135.

43. Stefanoni D, et al. (2020) Red blood cell metabolism in rhesus macaques and humans: comparative biology of blood storage. *Haematologica* 105(8):2174.

44. D'Alessandro A, et al. (2021) Donor sex, age and ethnicity impact stored red blood cell antioxidant metabolism through mechanisms in part explained by glucose 6-phosphate dehydrogenase levels and activity. *Haematologica* 106(5):1290.

45. Clasquin MF, Melamud E, Rabinowitz JD (2012) Lc-ms data processing with maven: a metabolomic analysis and visualization engine. *Current Protocols in Bioinformatics* 37(1):14–11.

46. Brown FL (2008) Elastic modeling of biomembranes and lipid bilayers. *Annual Reviews Physical Chemistry* 59:685–712.

47. Thomas T, et al. (2021) Fatty acid desaturase activity in mature red blood cells and implications for blood storage quality. *Transfusion*.

48. Armstrong CL, et al. (2013) The observation of highly ordered domains in membranes with cholesterol. *PLOS ONE* 8:e66162.

49. Rheinstädter MC, Mouritsen OG (2013) Small-scale structure in fluid cholesterol–lipid bilayers. *Current Opinion in Colloid & Interface Science* 18(5):440–447.

50. Armstrong CL, Häußler W, Seydel T, Katsaras J, Rheinstädter MC (2014) Nanosecond lipid dynamics in membranes containing cholesterol. *Soft Matter* 10(15):2600–2611.

51. Toppozini L, et al. (2014) Structure of cholesterol in lipid rafts. *Physical Review Letters* 113(22):228101.

52. von Laue M (1914) Die interferenzerscheinungen an röntgenstrahlen, hervorgerufen durch das raumgitter der kristalle. *Jahrbuch der Radioaktivität und Elektronik* 11(3):308 – 345.

53. Nickels JD, et al. (2019) Lipid rafts: buffers of cell membrane physical properties. *The Journal of Physical Chemistry B* 123(9):2050–2056.

54. Levental I, Levental KR, Heberle FA (2020) Lipid rafts: controversies resolved, mysteries remain. *Trends in Cell Biology* 30(5):341–353.

55. Subczynski WK, Hyde JS, Kusumi A (1989) Oxygen permeability of phosphatidylcholine–cholesterol membranes. *Proceedings of the National Academy of Sciences* 86(12):4474–4478.

56. Dotson RJ, Smith CR, Bueche K, Angles G, Pias SC (2017) Influence of cholesterol on the oxygen permeability of membranes: insight from atomistic simulations. *Biophysical Journal* 112(11):2336–2347.

57. Pan J, Tristram-Nagle S, Nagle JF (2009) Effect of cholesterol on structural and mechanical properties of membranes depends on lipid chain saturation. *Physical Review E* 80(2):021931.

58. Pan J, Mills TT, Tristram-Nagle S, Nagle JF (2008) Cholesterol perturbs lipid bilayers nonuniversally. *Physical Review Letters* 100(19):198103.

59. Rangamani P, Mandadap KK, Oster G (2014) Protein-induced membrane curvature alters local membrane tension. *Biophysical Journal* 107(3):751–762.

60. Aimon S, et al. (2014) Membrane shape modulates transmembrane protein distribution. *Developmental Cell* 28(2):212–218.

61. Netz RR, Pincus P (1995) Inhomogeneous fluid membranes: Segregation, ordering, and effective rigidity. *Physical Review E* 52(4):4114.

62. Rock G, Labow RS, Tocchi M (1986) Distribution of di(2-ethylhexyl) phthalate and products in blood and blood components. *Environmental Health Perspectives* 65:309–316.

63. Rael LT, et al. (2009) Phthalate esters used as plasticizers in packed red blood cell storage bags may lead to progressive toxin exposure and the release of pro-inflammatory cytokines. *Oxidative Medicine and Cellular Longevity* 2(3):166–171.

64. Carmen R (1993) The selection of plastic materials for blood bags. *Transfusion Medicine Reviews* 7(1):1–10.

65. Inoue K, et al. (2005) Evaluation and analysis of exposure levels of di (2-ethylhexyl) phthalate from blood bags. *Clinica Chimica Acta* 358(1-2):159–166.

66. D'Alessandro A, Nemkov T, Hansen KC (2016) Rapid detection of dehp in packed red blood cells stored under european and us standard conditions. *Blood Transfusion* 14(2):140.

67. Horowitz B, et al. (1985) Stabilization of red blood cells by the plasticizer, diethylhexylphthalate 1. *Vox Sanguinis* 48(3):150–155.

68. Bider RC, et al. (2020) Stabilization of lipid membranes through partitioning of the blood bag plasticizer di-2-ethylhexyl phthalate (DEHP). *Langmuir* 36(40):11899–11907.

69. Stefanoni D, et al. (2020) Red blood cell metabolism in rhesus macaques and humans: comparative biology of blood storage. *Haematologica* 105(8):2174.

70. Dodge JT, Phillips GB (1967) Composition of phospholipids and of phospholipid fatty acids and aldehydes in human red cells. *Journal of Lipid Research* 8(6):667–675.

Chapter 6

Paper III: Hybrid Erythrocyte Liposomes: Functionalized Red Blood Cell Membranes for Molecule Encapsulation

6.1 Preface to Paper III

Paper I and II aim to gain insight into the molecular assembly of the RBCcm as well as the implications of this structure on the mechanical properties. Paper III is the first out of two publications where we utilize this knowledge to tune the membrane's molecular composition to functionalize this endogenous structure for technological applications. Here, we study the impact of synthetic lipid molecules on the membrane's structure, and demonstrate that small molecules can be encapsulated into liposomes that are formed from these hybrid erythrocyte membranes.

We develop an optimized protocol to fuse synthetic lipid molecules homogeneously with the RBCcm on the nanoscale (Chapter 3), and study the effect of lipid molecules of different classes (PC, PS, PG), and different degrees of saturation (14:0, 16:0-18:1). PC lipids are found to tune membrane thickness and lipid orientation while PS and PG lipids effect the charge of the synthesized hybrid membranes.

The protocols that are developed for this publication set the basis for the insertion of proteins, such as the SARS-Cov-2 Spike protein into the RBC membrane, as it will be demonstrated in Paper IV.

Status: published in Advanced Biosystems

Author Contributions:

- Experimental Concept: Sebastian Himbert, Maikel Rheinstädter
- Sample Preparation: Sebastian Himbert, Mathew J. Blacker, Alexander Kihm, Kevin Yang, Christian Wagner
- DLS Experiment: Sebastian Himbert
- X-ray Experiments: Sebastian Himbert, Maikel Rheinstädter
- MD Model Development: Sebastian Himbert, Quinn Pauli, Adree Khondker
- Microscopy Experiments: Sebastian Himbert, Sheilan Sinjari, Mitchell Johnson, Janos Juhasz, Harald D. Stöver
- Data Analysis: Sebastian Himbert, Maikel Rheinstädter
- Manuscript Preparation: Sebastian Himbert, Maikel Rheinstädter

ADVANCED BIOSYSTEMS
www.adv-biosys.com

Hybrid Erythrocyte Liposomes: Functionalized Red Blood Cell Membranes for Molecule Encapsulation

*Sebastian Himbert, Matthew J. Blacker, Alexander Kihm, Quinn Pauli, Adree Khondker, Kevin Yang, Sheilan Sinjari, Mitchell Johnson, Janos Juhasz, Christian Wagner, Harald D. H. Stöver, and Maikel C. Rheinstädter**

The modification of erythrocyte membrane properties provides a new tool towards improved drug delivery and biomedical applications. The fabrication of hybrid erythrocyte liposomes is presented by doping red blood cell membranes with synthetic lipid molecules of different classes (PC, PS, PG) and different degrees of saturation (14:0, 16:0–18:1). The respective solubility limits are determined, and material properties of the hybrid liposomes are studied by a combination of X-ray diffraction, epi-fluorescent microscopy, dynamic light scattering (DLS), Zeta potential, UV-vis spectroscopy, and Molecular Dynamics (MD) simulations. Membrane thickness and lipid orientation can be tuned through the addition of phosphatidylcholine lipids. The hybrid membranes can be fluorescently labelled by incorporating Texas-red DHPE, and their charge modified by incorporating phosphatidylserine and phosphatidylglycerol. By using fluorescein labeled dextran as an example, it is demonstrated that small molecules can be encapsulated into these hybrid liposomes.

1. Introduction

Target-oriented drug delivery is one of the biggest challenges in modern drug development. The idea of using carriers to transport and release drug molecules at specific locations in the body is intriguing, and can significantly increase the drug's efficiency and reduce potential side effects.[1–4] Hydrogels and synthetic liposomes are two common attempts to address this problem.[5,6] Despite their success, these non-endogenous drug carriers raise numerous challenges as their efficiency is often limited by the host's immune response[6] or requires costly implants.[5]

First proposed by Ihler et. al.,[7] Red blood cells (RBCs) have been in focus as potential drug carriers. The evident advantage of using RBCs is an extended natural lifespan of these cells within the body, a greater biocompatibility, and a direct access to numerous target sites.[8] With glucocorticoid analogue dexamethasone loaded RBCs, the first RBC-based therapy reached the clinical stage[9] as treatment of Ataxia-telangiectasia, a rare neurodegenerative disease.[10] The two common approaches described in the literature aim to encapsulate drugs and molecules within erythrocyte ghosts or attach reactive agents to RBCs.[11–13] For instance, Thrombomodulin[12] and plasminogen activators[11,13] have been successfully linked to RBCs resulting in an increased circulation time of these molecules.[11–14] Escherichia coli L-asparaginase loaded erythrocytes have been reported to show a ten-fold increase of the pharmacodynamic of this therapeutic enzyme in mice.[15] Although RBCs have numerous advantages over the aforementioned synthetic drug carriers, loaded RBCs or RBC ghosts typically lack specificity with respect to target sites or show a reduced biocompatibility.[16,17] To address these difficulties, recent approaches include hybrid RBC liposomes as drug carriers,[18] or combined membranes from multiple endogenous cells.[19,20]

In this paper, we describe the preparation of hybrid erythrocyte liposomes and study the effect of different lipid classes (PC, PS, and PG), as well as varying degrees of saturation and tail length (14:0, 16:0–18:1), on the material properties of RBC membranes. First, empty RBC liposomes, often referred to as RBC ghosts, were mixed with synthetic liposomes, sonicated

S. Himbert, M. J. Blacker, A. Kihm, Q. Pauli, A. Khondker, K. Yang, J. Juhasz, Dr. M. C. Rheinstädter
Department of Physics and Astronomy
McMaster University
Hamilton, ON L8S 4M1, Canada
E-mail: rheinstadter@mcmaster.ca

S. Himbert, M. J. Blacker, A. Kihm, Q. Pauli, A. Khondker, K. Yang, Dr. M. C. Rheinstädter
Origins Institute
McMaster University
Hamilton, ON L8S 4M1, Canada

A. Kihm, Dr. C. Wagner
Department of Experimental Physics
Saarland University
66123 Saarbrücken, Germany

S. Sinjari, M. Johnson, Dr. H. D. H. Stöver
Department of Chemistry and Chemical Biology
McMaster University
Hamilton, ON L8S 4M1, Canada

Dr. J. Juhasz
Juravinski Cancer Centre
Department of Medical Physics
Hamilton, ON L8V 5C2, Canada

The ORCID identification number(s) for the author(s) of this article can be found under https://doi.org/10.1002/adbi.201900185.

DOI: 10.1002/adbi.201900185

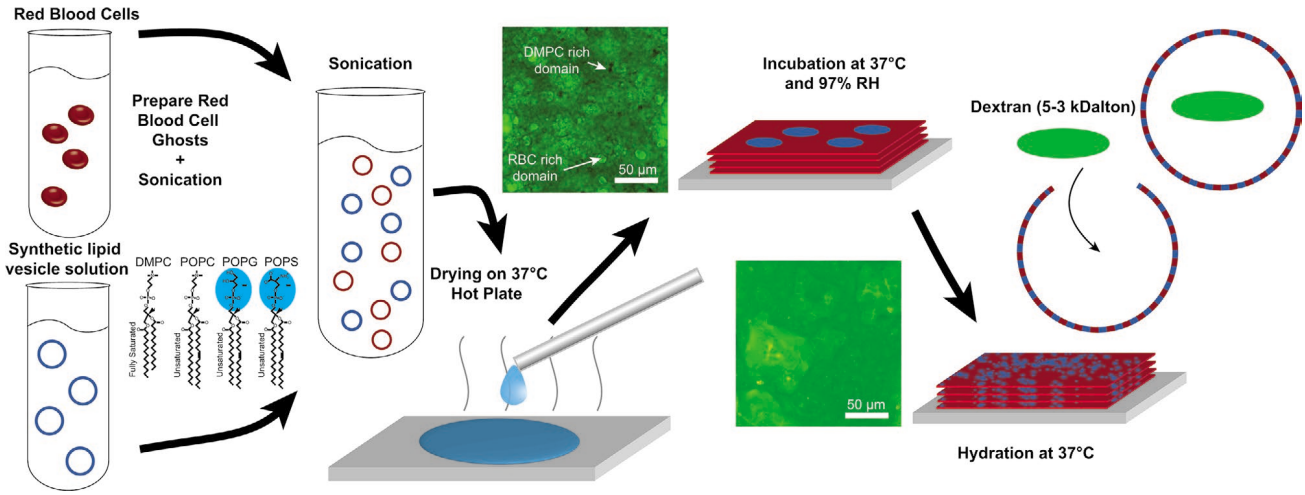

Figure 1. Erythrocyte liposomes (ghosts) are prepared from human RBCs and aqueous stock solutions of synthetic lipid molecules (DMPC, POPC, POPS, and POPG) are prepared. Blood and lipid solutions are sonicated before mixing in ratios of 1:4, 2:3, 1:1 3:2, 4:1, and 9:1. The resulting solution is sonicated 10 times in pulses of 55 s and applied onto a silicon wafer and allowed to dry and incubate. The images show epi-fluorescent microscopic images of the wafer surface. Green areas correspond to protein-rich, erythrocyte membrane rich areas. Uniform membranes form after incubation. The wafer is then immersed in a solution containing small molecules, which are encapsulated when hybrid erythrocyte liposomes form. In this work, fluorescein labeled dextran was incorporated.

and dried on a solid support. This 2D confinement promotes the fusion of both membrane species during the subsequent incubation. Hybrid liposomes were formed by re-hydrating the dry membranes. Small molecules can be incorporated within these hybrid liposomes during this step. A sketch of the preparation protocol is shown in **Figure 1**.

Molecular level structural and dynamical information was obtained using X-ray diffraction, epi-fluorescent microscopy, dynamic light scattering (DLS), Zeta potential, UV-vis spectroscopy, and Molecular Dynamics (MD) simulations. Dimyristoylphoshatidylcholine (DMPC), for instance, was found to increase the degree of order while decreasing the membrane thickness. In contrast, palmitoyloleoylglycerophosphocholine (POPC) lowers the overall bilayer thickness and reduces the degree of order. Anionic lipids, such as palmitoyloleoylglycerophosphoserine (POPS) and palmitoyloleoylglycerophosphoglycerol) (POPG), were used to alter the membranes' charge and result in a decreased Zeta-potential. On microscopic scales, synthetic lipid molecules fuse homogeneously with erythrocyte membranes when within their solubility limits. However, MD simulations, indicate the presence of dynamic nanometer sized erythrocyte rich and erythrocyte poor domains, mimicking rafts in biological plasma membranes.

2. Results

2.1. Molecular Structure of Hybrid Membranes

The molecular structure of the hybrid erythrocyte membranes was determined by X-ray diffraction. The measurements were performed on solid supported membranes after incubation but before liposomal fabrication. Scans were done in a humidity and temperature controlled chamber. The setup is depicted in **Figure 2**a. Figure 2b shows 2D X-ray intensity maps for erythrocyte membranes containing DMPC at ratios of (RBC:DMPC) 1:4, 1:1, and 9:1. Pure RBC membranes are shown as reference. The observed Bragg peaks are the result of the membrane stacking. The 1:4 sample mainly consists of synthetic DMPC and produces a well pronounced series of peaks. The intensity and number of these peaks decrease as the RBC concentration increases, indicative of a less-well ordered lamellar phase with increased mosaicity. Line-cuts along $q_{\|} = 0$ were calculated by integration along the marked rectangle and are shown in Figure 2c. The lamellar spacing, d_z, was determined from the distance of the reflectivity Bragg peaks using Bragg's law, $d_z = 2\pi/q_z$.

Electron densities perpendicular to the membranes are presented in Figure 2d, as calculated from a 1D Fourier analysis. The data show an increased electron density around $|z| \approx 20$ Å, corresponding to the electron-rich head groups of the lipid molecules, and a decreased density in the center of the bilayer ($|z| = 0$ Å). The membrane thickness was determined by the distance between the two maxima in the electron density profile, and will be referred to as head-to-head distance d_{HH}. Figure 2e shows the result of an angular integration along the dotted line in Figure 2b. A small width in the angular distribution is indicative of well-ordered membranes within the stack. The degree of order is quantified by fitting Herman's orientation function, as detailed in the Experimental Section. A degree of orientation between ≈82% and ≈97% was determined, in good agreement with previous studies on pure red blood cells,[21] and on mono- or multicomponent synthetic membranes.[22]

Figure 3a compares the reflectivity of different types of synthetic lipids, all at a ratio of 9:1. While the inclusion of DMPC and POPC was found to lead to well organized membranes, the addition of POPS and POPG significantly suppressed higher order peaks, indicative of increased disorder. The corresponding electron densities are shown in Figure S1, Supporting Information, and are in agreement with increasing tail disorder between DMPC-POPC-POPS (no electron density could be determined for the case of POPG because of the absence of higher order Bragg peaks).

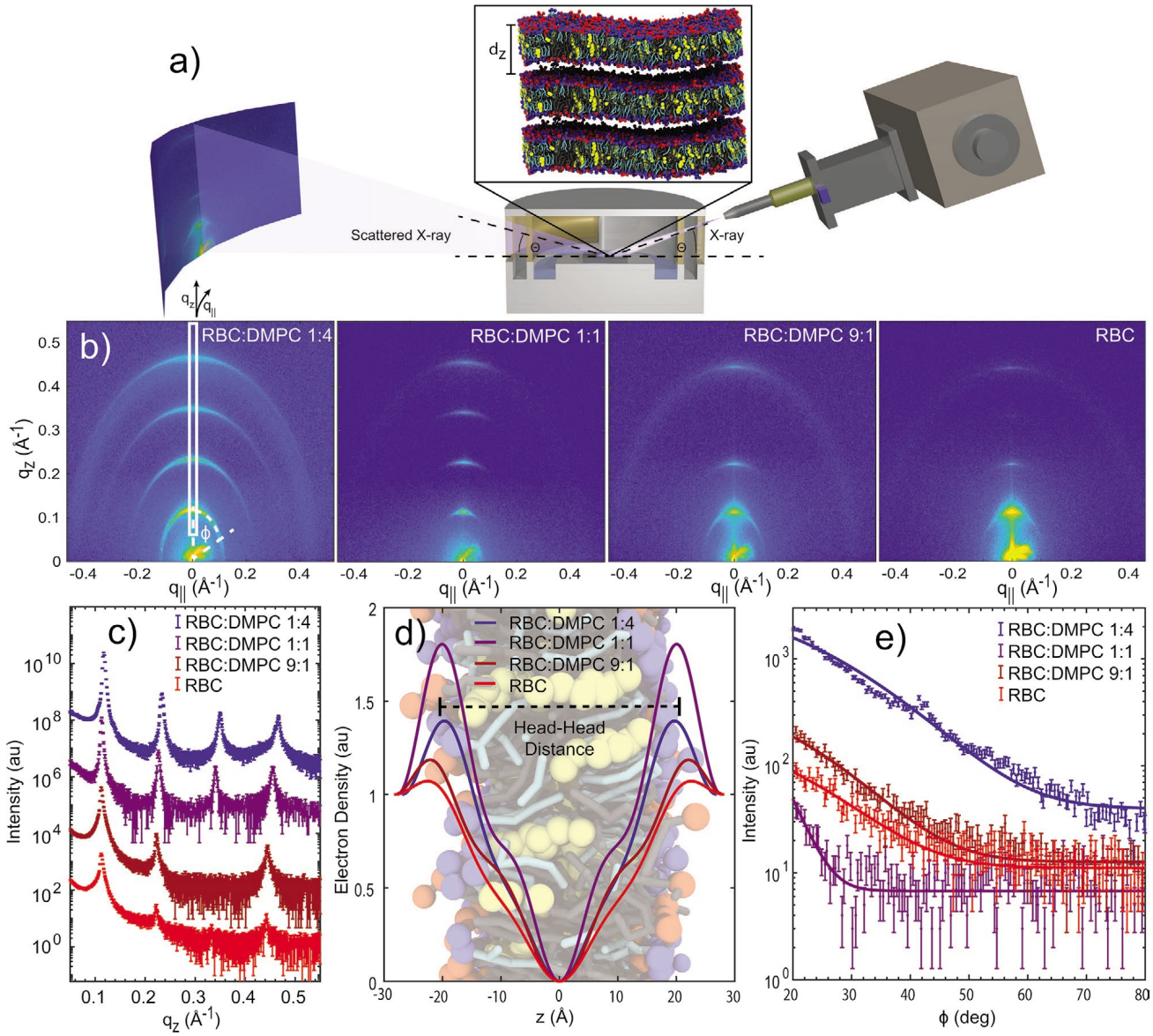

Figure 2. a) Experimental setup. The solid supported membranes are placed in a humidity controlled chamber at 88% relative humidity. The sample remains horizontal throughout the measurement. q_z measures out-of-plane structure while $q_{||}$ measures in-plane structure. b) 2D X-ray intensity maps for three selected RBC:DMPC hybrid samples: 1:4, 1:1, and 9:1. The scattering pattern of pure RBC membranes are included as reference. c) Bright prominent spots are apparent, which appear as series of Bragg-peaks in a line-cut along q_z at $q_{||} = 0$ and are result of the lamellar spacing between the stacked membranes. d) Shows the corresponding electron density data determined by a 1D Fourier Analysis. The head groups show up as increased electron density around $|z| \approx 20$ Å. e) The degree of orientation was determined by fitting a Gaussian profile to the scattered intensity along the meridional angle ϕ and using Herman's orientation function.

DMPC, POPC, and POPS show a gradual increase in lamellar spacing and head–head distance with an increasing fraction of RBC membranes, as shown in Figures 3b,c. It converges to ≈56 Å for the d_z-spacing and ≈44 Å for the head-head distance, in good agreement with previously published measurements on red-blood cell membranes.[21]

Two regimes were observed for all lipid species: a linearly increasing regime and a plateau region for higher fractions of RBC membranes. The latter one indicates minor structural differences as compared to a pure erythrocyte membrane. Consequently, we define the solubility limit as the boundary between both regimes. It was determined for all lipid species by fitting lines to both regimes and determining the x-coordinate of the intersect. The fits are indicated in Figure 3b by dotted lines using POPC as an example. The solubility limits are plotted in Figure 3d.

Figure 3e compares the membranes' orientation as function of the synthetic lipid concentration and the lipid species. The highest degree of orientation was observed for an equal ratio between erythrocyte and synthetic lipids, while a high concentration of synthetic lipids causes an overall lower degree of orientation. Values for DMPC are significantly higher as compared

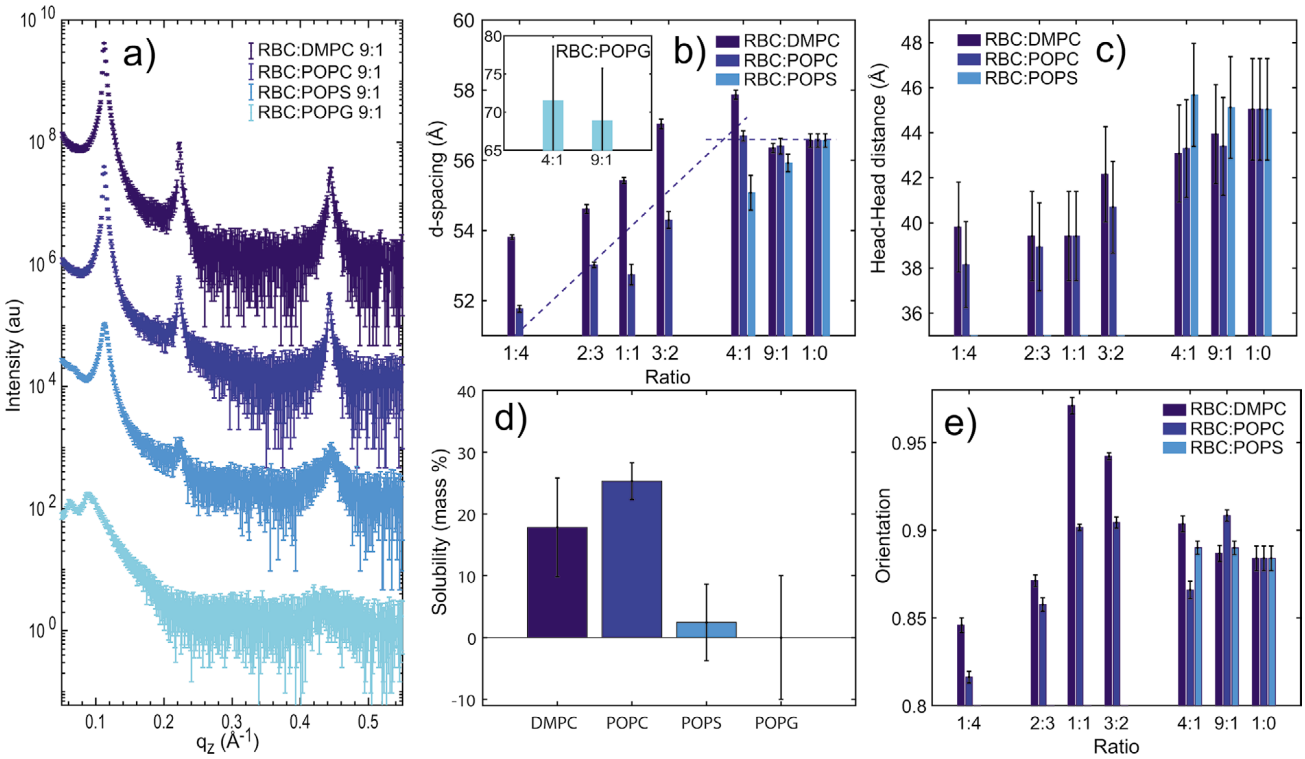

Figure 3. a) Diffraction along q_z for hybrid membranes containing 10 mass percent synthetic lipids (DMPC, POPC, POPS, and POPG). b) Lamellar spacing d_z as function of synthetic lipid concentration for the different lipid species. c) Corresponding head-head distance as function of the synthetic lipid concentration. d) The solubility limit was determined by the intercept of two linear regimes fitted to part b). The fits for POPC are shown as dotted lines. e) shows the degree of order as a function of the synthetic lipid concentration and species, as determined by Herman's orientation function.

to POPC and POPS, as fully saturated lipid molecules seem to induce additional order in the erythrocyte membrane.

2.2. Molecular Dynamics Simulations

Experiments point to a homogeneous mixing of erythrocyte and synthetic membranes. MD simulations give information about the underlying dynamical processes. Coarse grained MD simulations were performed using erythrocyte membranes containing 10 mol% (≈11.5 mass%), 50 mol% (≈54 mass%) and 80 mol% (≈82.4 mass%) DMPC to study the dynamics and in-plane organization of the hybrid membranes. Snapshots after 5 µs of simulation time are depicted in **Figure 4**a. Red and blue spheres represent the phosphate groups of lipid molecules assigned to the red blood cell fraction and synthetic DMPC lipids, respectively. Cholesterol is depicted by yellow spheres. The snapshots indicate a homogeneous mixture of both membrane species. This changes when comparing the time averaged density of the lipid molecules, as shown in Figure 4b, where dynamic small, nanometer-sized patches become visible.

The size of the erythrocyte and DMPC patches can be determined by counting the number of pixels above the median density multiplied with the resolution. Patch sizes ranging from 35.3 to 147.0 nm^2 were determined, as listed in **Table 1**. These patches are dynamic entities and undergo molecular fluctuations, which mimic the natural fluctuations observed in biological plasma membranes. Simulation videos are provided in videos S1–S3, Supporting Information, over the course of 2 µs.

2.3. Liposome Characterization and Encapsulation of Molecules

Fluorescently labeled hybrid liposomes (**Figure 5**a) were visualized using an epifluorescent microscope (Figure 5b), as detailed in the Experimental Section. Liposomes had a typical size of 10-15 µm and varied in shape, as shown in Figure 5c. The membrane appears as a bright red edge with a width of ≈550 nm, within the resolution limit of the microscopic setup used. The liposomes in Figure 5c appear to be homogeneously labeled and show no indication of phase separation or domain formation within the resolution limit of the microscope.

Size and size distribution of all hybrid liposomes were determined using DLS and are listed in **Table 2**. Liposomes were sonicated before the measurements for better comparison. The average diameter ranges from ≈120 to ≈208 nm. While pure RBC liposomes (ghosts) showed an average size of ≈200 nm, inclusion of saturated and charged lipids resulted in smaller sized liposomes. The inclusion of dextran led to a small increase of the liposome size. While the size distribution of pure RBC liposomes was found to be reasonably well defined, as indicated by the polydispersity index, the inclusion of synthetic lipids increased the size distribution in all cases.

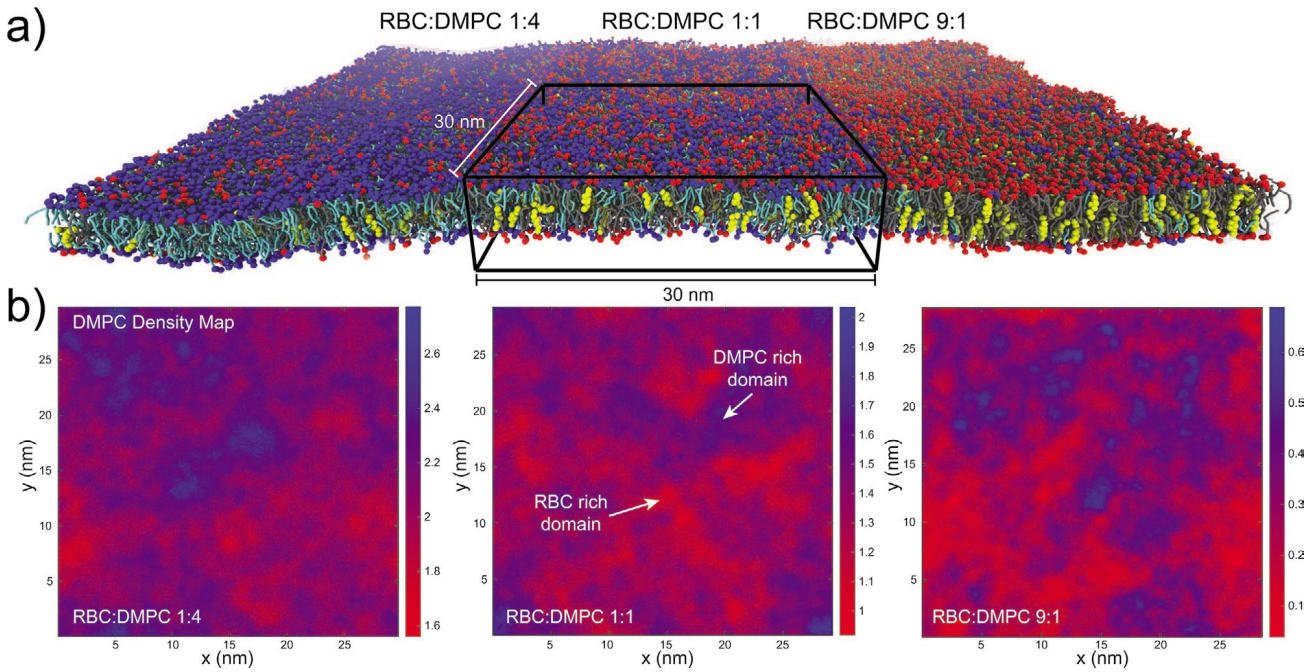

Figure 4. a) Snapshot of MD simulation at $t = 5$ µs. The phosphate group is indicated by red and blue spheres, corresponding to RBC and DMPC lipids respectively. Cholesterol is represented by yellow spheres. Gray and light blue lines represent the lipid tails of RBC and DMPC lipids respectively. The simulation box is shown as a black box and measures 30 × 30 nm. Water molecules are omitted for clarity. b) DMPC density maps for hybrid membranes containing 80, 50, and 10 mass% DMPC, respectively. Blue color indicates a high concentration of DMPC while the red regions correspond to a DMPC depletion, that is, a high concentration of RBC lipid species.

DMPC and POPC resulted in a significant broadening of the distribution while adding charged lipids (POPS and POPG) increased the distribution moderately, only. The Zeta-potential was determined for pure RBC ghosts as well as for hybrid membranes containing 10% and 20% POPS and POPG. By applying an alternating current, the Zeta-potential is a measurement of potential charge-dependent dynamics of the liposomes, as depicted in **Figure 6**a. Both anionic lipids decrease the Zeta-potential, as shown in Figure 6b. While erythrocyte membranes show a Zeta-potential of –25.7 ± 5 mV, POPS and POPG were found to lower the potential to –35.5 ± 5 mV and –47.5 ± 5 mV, respectively. Previous studies[23] have reported a linear relationship between the concentration of charged lipid molecules and the Zeta-potential. However, our data show no concentration dependence, within statistical errors.

Molecules were encapsulated in the hybrid liposomes by hydrating the solid supported membranes in an aqueous solution, as pictured in **Figure 7**a. The experimental setup is shown in Figure 7b. Figure 7c shows liposomes that were prepared in a 1 mg mL^{-1} solution of 3–5 kDa fluorescein labeled dextran. The interior of the liposomes lights up in green under the microscope indicating that the dextran is located within the hybrid liposomes. Dextran has been previously reported to interact with the RBC membrane at larger concentration of dextran (>10 mg mL^{-1}).[24–26] The homogeneous color and intensity of the liposomes, however, indicate that the molecules are homogenously distributed within the liposomes (within the resolution limit of the microscope).

Table 1. DMPC domain sizes were determined from 2-dimensional density maps by counting the number of pixels above a threshold and multiplying the results by the resolution.

Membrane System	DMPC domain size [nm^2]	
	upper leaflet	lower leaflet
RBC:DMPC 1:4	75.4	95.2
RBC:DMPC 1:1	46.1	147.0
RBC:DMPC 9:1	79.0	35.3

3. Discussion

Endogenous substances can transport drugs hidden from the immune system and allow the design of far more complex liposomes. However, controlling membrane morphology and structure is essential in generating applicable carrier systems. Recent papers[18–20] used a combination of biological and synthetic membranes. Human erythrocytes are well suited as a base for such hybrid liposomes as their membrane can be easily isolated from other cellular components. At the same time they have the potential of minimizing immune reactions and circulating in the blood stream for extended periods of time.

The protocol presented in this work allows the efficient preparation of hybrid erythrocyte membranes. Our data indicate that synthetic lipid molecules can be incorporated into RBC membranes and show no indication of phase separation, in contrast to previously published protocols.[18] The crucial intermediate step in the protocol is the preparation of solid supported hybrid membranes. The 2D confinement together with

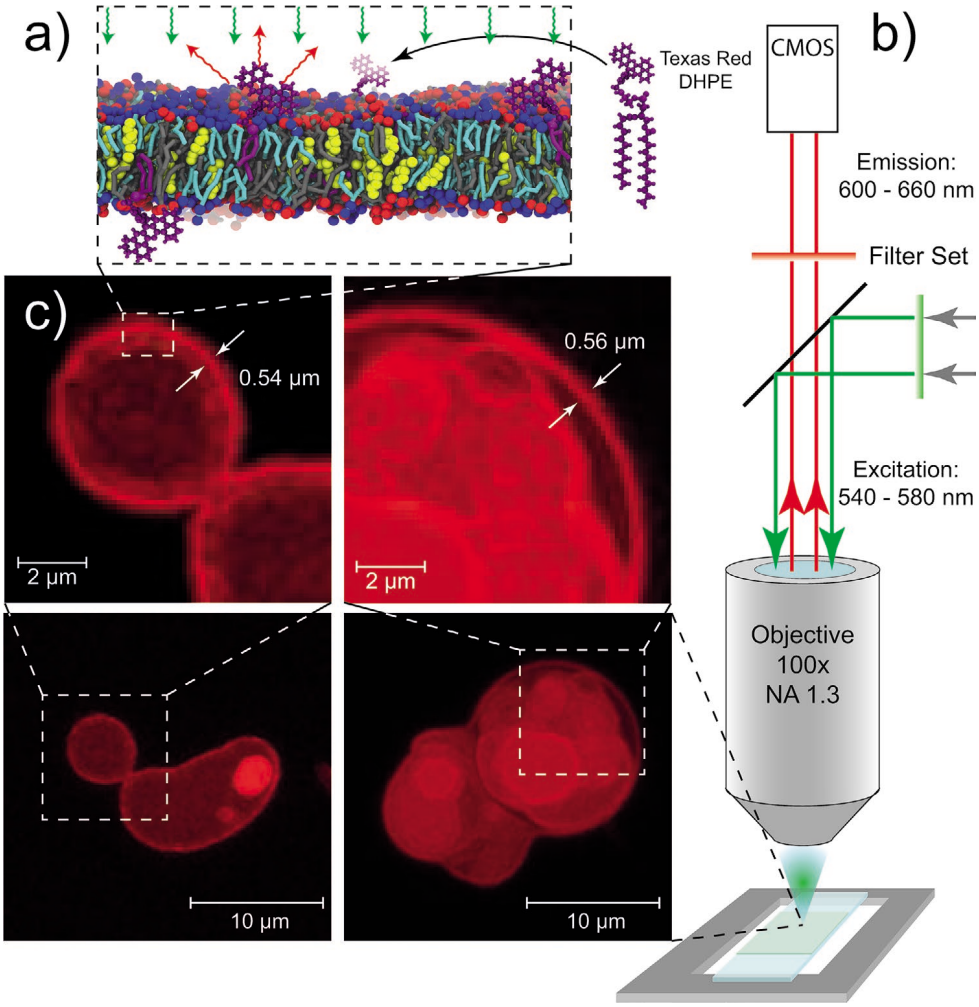

Figure 5. a) Liposomes containing 0.5 mass% head-group labeled Texas red DHPE were prepared. b) The Epi-fluorescent microscope uses an excitation filter of 540–580 nm and an emission filter of 600–660 nm. c) The membrane of the liposomes shows up as a bright, red barrier under the microscope. Complex liposome structures were observed consisting of multiple fused spherical objects. The membrane thickness was found to be 560 nm, the resolution limit of the setup.

Table 2. The diameter of the hybrid liposomes after sonication determined by dynamic light scattering (DLS). The average diameter ranges from ≈120 nm to ≈208 nm. Inclusion of saturated and charged lipids resulted in smaller sized liposomes. The inclusion of dextran led to a small increase of the liposome size. While the size distribution of pure RBC liposomes is reasonably well defined, as indicated by the polydispersity index, the inclusion of synthetic lipids increased the size distribution in all cases. DMPC and POPC resulted in a significant broadening of the distribution while adding charged lipids (POPS and POPG) increased the distribution moderately, only.

Liposomes	Diameter [nm]	Polydispersity index
pure ghosts	199.05 ± 3.34	0.14 ± 0.013
RBC:DMPC 4:1	147.8 ± 2.3	0.32 ± 0.04
RBC:DMPC 9:1	198.9 ± 12.1	0.42 ± 0.06
RBC:POPC 4:1	208.0 ± 8.8	0.48 ± 0.079
RBC:POPC 9:1	174.5 ± 6.7	0.46 ± 0.01
RBC:POPS 4:1	164.3 ± 1.0	0.174 ± 0.02
RBC:POPS 9:1	147.9 ± 1.35	0.218 ± 0.004
RBC:POPG 4:1	138.3 ± 1.6	0.241 ± 0.003
RBC:POPG 9:1	147.2 ± 1.1	0.248 ± 0.008
RBC:DMPC 4:1 with Dextran	160.0 ± 60	0.3 ± 0.08
RBC:POPG 4:1 with Dextran	119.3 ± 1.46	0.245 ± 0.01

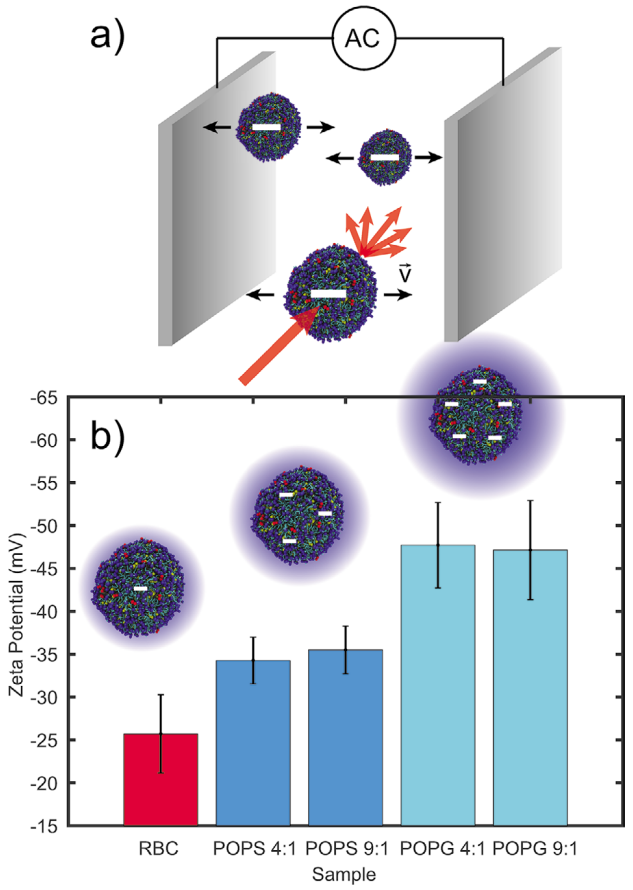

Figure 6. a) The Zeta-potential of the hybrid liposomes was determined using a Zetasizer Nano ZS from Malvern Panalytical. Alternating current is applied via two electrodes allowing the measurement of charge-dependent dynamics of the liposomes. b) Zeta-potential for RBC ghosts and hybrid liposomes containing 10 and 20 mass% POPS and POPG, respectively. Both synthetic lipid species add additional charge to the membrane.

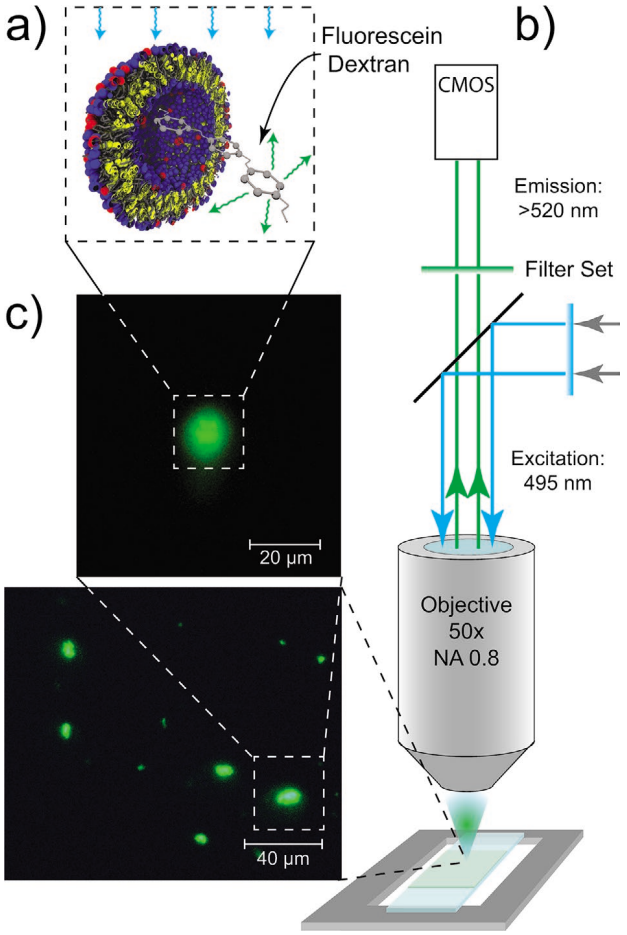

Figure 7. a) The hybrid liposomes were filled with fluorescein labeled dextran. b) The experimental setup consisted of an epi-fluorescent microscope with an excitation wavelength of 495 nm and a long-pass analysis filter with a barrier wavelength of 520 nm. ≈20 µL of the liposome solution was applied to a microscope slide and sealed by a cover slip. c) Epi-fluorescent microscopic image of the prepared liposomes, which light up as bright green circles on the image.

drying and incubation promotes the fusion of both membrane species. While microscopy is a very efficient tool to determine the topology of hybrid membranes and liposomes, X-ray diffraction gives access to nanoscale bulk information. Experiments were complemented by computer simulations, which can now model plasma membranes realistically,[27] and provide important information on nanoscopic dynamics and mixing.

The lack of split peaks in the X-ray diffraction measurements, together with the homogeneous red color of the fluorescently labeled hybrid liposomes indicate a homogenous fusion of both membrane species. A deeper insight into the mixing is provided by MD simulations. While snapshots of the simulation indicate a uniform mixture of erythrocyte and synthetic membranes, the time averaged density maps show evidence for dynamic nanometer sized patches of erythrocyte rich and poor regions.

Previous MD simulations on large-scale models show a similar de-mixing of lipid species in biological cell membranes. Ingolfsson and co-authors also demonstrated that these patches form and disappear on nano to microsecond time scales.[27] It is now widely accepted that local fluctuations are an intrinsic property of membranes.[27–31] These fluctuations typically average out on longer length and time scales leading to a uniform membrane structure. The observed small dynamic domains are, therefore, not the result of a static phase separation between both membrane species but the result of nanoscopic molecular fluctuations, typically observed in biological membranes.

We note that erythrocyte membranes are in general asymmetric.[32] POPS, for instance, is exclusively found in the inner leaflet of mammalian cell membranes. PE lipids are located on both leaflets with a preferred position on the inner leaflet. In experiments, RBC ghosts in general co-exist in inside-out and right-side out configurations, as discussed, for example, in ref. [33]. When the ghosts are dried out on the solid support there is a random stacking of the different membrane orientations and the resulting membrane layer and liposomes are on average symmetric with respect to the composition of the inner and outer leaflets. We can, therefore, not conclude on effects due to potential asymmetry of the hybrid membranes and liposomes. MD models were prepared by first modeling an

asymmetric RBC membrane. Synthetic lipids were then equally added to to both leaflets to mimic the experimental conditions. However, there was no evidence for an asymmetric distribution of the synthetic lipids between the two leaflets within the 5 µs of simulation time, which could for instance be caused by lipid flip-flop. We therefore assume a stable symmetric distribution of synthetic lipids across the leaflets.

While up to 30 mass% DMPC and POPC can be mixed with erythrocyte membranes, small amounts of charged lipids disturb the membrane assembly resulting in decreased (POPS) and increased (POPG) lamellar spacings, and the formation of smaller liposomes. In particular POPG inhibits the assembly of stacked membranes. These findings are supported by the DLS and Zeta-potential measurements. Inclusion of synthetic lipids (except for RBC:POPC 4:1) resulted in smaller sized liposomes, indicating a reduced stability. Inclusion of dextran led to a small increase of the liposome size.

While the Zeta-potential is not a direct measure of the charge density, as detailed in the paper by Bhattacharjee,[34] it determines the interfacing potential of the so-called slipping plane around the liposome. The Zeta-potential of the erythrocyte membrane was measured to be −25.7 ± 4.6 mV, in good agreement with previous studies.[35] POPS and POPG further decrease the Zeta-potential to −34.3 ± 2.7 and −35.5 ± 2.8 mV, and −47.7 ± 5 and −47.1 ± 5.8 mV, respectively, indicating an increased negative membrane charge. Previous studies reported a concentration-dependent decrease of the Zeta-potential in the presence of PS[23] and PG[35] lipids in synthetic membranes. The concentration dependent differences in our measurements, however, are within the statistical errors.

Liposomes can be loaded with molecules during the rehydration phase, when the molecule containing solution is applied onto the dried out supported membranes. The molecules are then encapsulated when the membranes re-hydrate and liposomes form. The loading efficiency is defined as the amount of encapsulated molecules relative to the initial concentration of the molecule, and was determined using UV–vis spectroscopy. We determine an encapsulation efficiency of 2.1 ± 0.7% for dextran in hybrid liposomes containing 20% DMPC and 3.5 ± 0.5% for hybrid liposomes containing 20% POPG. Both efficiencies are comparable, in the order of a few percent. While these efficiencies are only slightly smaller than typical loading efficiencies reported for synthetic liposomes of ≤10%,[36] they can likely be increased with an optimized protocol in the future.

The biocompatibility of RBC based drug delivery systems is a long standing concern. While the hybrid membranes are entirely composed of biocompatible materials,[18] previous studies have shown that loading of RBCs can have a significant impact on their biocompatibiliy.[16,17] This is, however, often a result of heavy modifications to the RBC surface. The longevity of modified RBC depends on numerous mechanisms and has been studied in detail.[37–40] However, a key factor for the biocompatibility is the resilience of the hybrid liposomes against mechanical stress. Figure S5, Supporting Information, shows the result of a lysis assay where hybrid liposomes containing 20% DMPC were exposed to increasing osmotic stress by altering the molar concentration of a phosphate buffer saline. This method has previously been described as in vitro test for biocompatibiliy of RBC membranes.[41] The data show an increase of lysed hybrid liposomes below 5.6 mM phosphate buffer saline, corresponding to a ≈150 mOsm solution, in good agreement with results for pure RBC.[41] It can, therefore, be expected that the hybrid liposomes will behave similar to RBCs in vivo. Although these results prove the biocompatible nature of these hybrid liposomes, the compatibility and longevity of the drug delivery system will be confirmed in animal studies in the future.

4. Conclusion

In summary, we prepared hybrid erythrocyte membranes by purifying and doping endogenous RBC bilayers with synthetic lipid molecules. We studied the impact of different lipid classes (PC, PS, and PG), as well as different tail saturation (14:0, 16:0–18:1), on membrane morphology and structure using X-ray diffraction, MD simulations, dynamic light scattering, Zeta potential, UV-vis spectroscopy, and epi-fluorescent microscopy. Fluorescently labeled hybrid liposomes were prepared using Texas-red DHPE (TR-DHPE) and fluorescein labeled dextran.

Different synthetic lipid species functionalize the RBC membranes by altering their thickness, order and the surface charge. As a fully saturated lipid, DMPC was found to induce additional order, while POPC led to a more disordered bilayer with increased mosaicity. Both lipids result in a significantly reduced membrane thickness. The addition of POPS and POPG led to the formation of charged liposomes, as proven by a decreased Zeta-potential.

Experimental and computational findings indicate a homogenous mixing of erythrocyte and synthetic membranes down to the nanoscale. Formation of dynamic nanometer sized patches of constantly mixing and de-mixing erythrocyte rich and poor domains was, however, observed as a result of molecular fluctuations. By using dextran as an example, we show that small molecules can be encapsulated into the hybrid liposomes.

5. Experimental Section

This research was approved by the Hamilton Integrated Research Ethics Board (HIREB) under approval number 1354-T. Informed consent was obtained from all blood donors. The authors confirm that all methods were performed in accordance with the relevant guidelines and regulations.

Preparation of Hybrid Membrane Mixtures: The preparation is based on a protocol first published by Himbert et al.[21] All blood samples were collected using sodium heparin coated venous blood collection tubes from BD (Product Number: BD 367874). The blood was washed twice and the RBC were isolated as described in ref. [21]. Hemolysis was induced by adding 50 µL of the hematocrit to 1 mL of a diluted buffer solution in a 1.5 mL reaction tube. This buffer is prepared by mixing 16 mL of Phosphate Buffered Saline (PBS) with 484 mL of 18 MΩ cm ultra pure water and adjusting the pH to a value of 8 by slowly adding potassium hydroxide. The reaction tubes were immediately stored on ice to prevent a fast re-closing of the ruptured cells. This enables the removal of hemoglobin and other cellular compartments using multiple washing steps as demonstrated in ref. [21]. The protocol results in a white pellet containing empty RBC liposomes. The pellets from 24 reaction tubes were combined and the volume was adjusted to 0.5 mL resulting in a ghosts concentration of ≈14 mg mL^{-1}.[21] The resulting solution was tip sonicated 20 times for 5 s each at a power of 100 W. Note, that the reaction tube was placed on ice during sonication to prevent the sample

from overheating. Afterwards, the tube was centrifuged for 15 min at ≈20000 g. The supernatant consists of a solution of small nanometer-sized liposomes,[21] referred to as Blood Solution.

Aqueous solutions of dispersed 1,2-dimyristoyl-sn-glycero-3-phoshatidylcholine (DMPC), 1-palmitoyl-2-oleoyl-glycero-3-phosphocholine (POPC), 1-palmitoyl-2-oleoyl-sn-glycero-3-phospho-L-serine (POPS) and 1-palmitoyl-2-oleoyl-sn-glycero-3-phospho-(1′-rac-glycerol) (POPG) were prepared by dissolving 14 mg of each lipid in 1 mL of 18.2 MΩ cm ultra pure water. The resulting solution was tip sonicated 20 times for 10 s each at a power of 100 W until the solutions were clear. This sonicated solution will be referred to as Lipid Solution.

For DMPC and POPC, assays at ratios of (*Blood Solution*:*Lipid Solution*) 1:4, 2:3, 1:1, 3:2, 4:1, and 9:1 were prepared. For POPS and POPG, both solutions were mixed in ratios of 4:1 and 9:1. The reaction tube with the final solution was placed on ice and tip sonicated 20 times for 5 s each.

Fluorescently labeled membranes were prepared by doping the bilayers with Texas Red 1,2-Dihexadecanoyl-sn-Glycero-3-Phosphoethanolamine (TR-DHPE) (Thermo Fisher, Catalog number: T1395MP) which was used previously as an indicator for liquid disordered l_d domains.[42–45] TR-DHPE was reported for its interaction with lipid molecules, such as DPPC,[46] resulting in a reduced diffusion coefficient,[46] and induced domain formation[47] at higher concentrations (>0.2 mol%). 1 mg of TR-DHPE was dissolved in 1 ml chloroform. 5.6 mg of DMPC (this corresponds to hybrid membranes containing 40 mass% DMPC) was dissolved in 1 mL chloroform. 52 µL of the TR-DHPE solution was mixed with the DMPC solution in a glass vial. Chloroform was removed by blowing dry N_2 gas in the glass vial for ≈20 min before mixing the sample with ultra pure water and tip sonicating 20 times for 10 s each at a power of 100 W. The concentration of TR-DHPE corresponds to 0.5 mol% in the Lipid Solution and 0.003 mass% when mixed with erythrocyte membranes. This solution will be referred to as Fluorescent Solution.

For the stained membrane assays, the Fluorescent Solution was mixed with 80 µL of the Blood Solution creating a 3:2 sample.

Preparation of Liposomes: The preparation of liposomes is a two-step process. First, erythrocyte ghosts and synthetic liposomes were mixed and sonicated. The solution was then applied to a surface, slowly dried, and incubated. The resulting solid supported membranes initially show large, micrometer-sized erythrocyte, and synthetic domains as depicted in Figure 1. During incubation, the large domains merge to form homogenous hybrid membranes.

Membranes were applied onto single-side polished silicon wafers. 100 mm diameter, 300 µm thick silicon wafers were pre-cut into 10 × 10 mm^2 chips. The wafers were functionalized with a solution of 15 mL sulfuric acid and 5 mL hydrogen peroxide (Piranha solution) resulting in a hydrophilic surface. This strong oxidizing agent removes all organic contaminants on the surface, but do not disturb the native silicon oxide layer. Each wafer was then thoroughly rinsed with ≈50 mL of ultra pure water with a resistance of 18.2 MΩ cm and placed on a hot plate (37 °C) in a 3D orbital shaker. 100 µL of the hybrid membrane solution was pipetted slowly onto the wafer. The sample was covered with a tilted lid of a petri dish and allowed the membrane solution to slowly dry within ≈12 h. The dried wafers were then incubated at 97% relative humidity and 37 °C for 3 days by placing the samples in a sealed container with a saturated K_2SO_4 solution. This allows the erythrocyte and synthetic membrane domains to fuse into a homogenous membrane phase, as shown in Figure 1. Sample pictures of different RBC-DMPC ratios are shown in Figure S2, Supporting Information.

Liposomes were then synthesized by placing the silicon wafers in a reaction tube filled with 2 mL of ultra pure water. The tubes were bath sonicated for 1 h at 37 °C. This re-hydrates the membrane stack and lets the membranes bleb, leaving a blank silicon wafer. The resulting solution had a concentration of ≈7 mg mL^{-1} of membrane material. Liposomes were characterized by dynamic light scattering (DLS) and the determination of the Zeta-potential, as detailed below.

To encapsulate molecules within the liposomes, the solid supported membranes were placed in 2 mL of an aqueous solution of 1 mg mL^{-1} fluorescein dextran and bath sonicated at 37 °C for ≈ 1 h. The sample was then centrifuged for 20 min at 20000 g. The supernatant was removed and replaced with ultra pure water. This washing step was repeated twice to isolate the stained liposomes. The resulting solution was applied onto a microscope slide and covered with a coverslip prior to imaging.

Liposomes prepared by this protocol showed a large polydispersity index (PDI). Measurements performed on pure RBC liposomes determined a average size of 481.0 ± 11.41 nm and a PDI of 0.53 ± 0.027. This can be optimized by an additional tip sonication (20 times for 5 s each at a power of 100 W) of the liposomes resulting in a average size of 199.05 ± 3.34 with a PDI of 0.14 ± 0.013.

X-ray Diffraction Experiment: X-ray scattering data was obtained using the Biological Large Angle Diffraction Experiment (BLADE) in the Laboratory for Membrane and Protein Dynamics at McMaster University. BLADE uses a 9 kW (45 kV, 200 mA) CuKα rotating anode at a wavelength of 1.5418 Å using a Rigaku HyPix-3000 2D semiconductor detector with an area of 3000 mm^2 and 100 µm pixel size.[48] All samples were prepared and measured in replicates to check for consistency. Both source and detector are mounted on movable arms such that the membranes stay horizontal during the measurements. Focusing multi-layer optics provides a high intensity parallel beam of ≈200 µm with monochromatic X-ray intensities of up to 10^8 counts. Note that there is no risk of sample damage using this in-house technique because of the relatively low intensity of the X-ray beam as compared to synchrotron sources. The samples were mounted in a custom-built humidity chamber during the experiments to control the humidity of the membranes. The result of an X-ray experiment is a 2D intensity map of a large area of the reciprocal space, as sketched in Figure 2a,b, covering length scales from about 2.5 to 100 Å. All scans were measured at 28 °C and 88% relative humidity (RH) hydration. As depicted in Figure 2a, the wafers were oriented in the X-ray diffractometer, such that the $q_{\|}$-axis probed lateral structure, parallel to the wafer surface, and the perpendicular axis, q_z, probed out-of-plane structure, perpendicular to the substrate.

The out-of-plane structure of the membrane was determined using specular reflectivity. The relative electron density, $\rho(z)$, is approximated by a 1D Fourier analysis.[49]

$$\rho(z) = \frac{2}{d_z}\sum_{n=1}^{N}\sqrt{I_n q_n}\,\nu_n \cos\left(\frac{2\pi n z}{d_z}\right), \tag{1}$$

where N is the highest order of the Bragg peaks observed. $F(q_n)$ is known as the form factor and is determined by multiplying the integrated peak intensity I_n with q_n[49] and is in general a complex quantity. In case of centro-symetrie, the form factor becomes real and the phase problem of crystallography, therefore, simplifies to the sign problem $F(q_z) = \pm|F(q_z)|$. A X-ray diffraction experiment probes the form factor at discrete values of q_z, and continuous function, $T(q_z)$, can be fitted to the data.[49]

$$T(q_z) = \sum_n \sqrt{I_n q_n}\,\mathrm{sinc}\left(\frac{1}{2}d_z q_z - \pi n\right). \tag{2}$$

Once an analytical expression for $T(q_z)$ has been determined from fitting the experimental peak intensities, the phases ν_n can be assessed from $T(q_z)$. The phase array $\nu_n = [-1\ -1\ 1\ -1\ 1]$ was used for all samples.

The electron densities determined by Equation (1) are on a relative scale. In order to compare the electron densities in Figure 2d and Figure S1, *Supporting Information*, ρ in the membrane center at $z = 0$ was set to 0 and the electron density at the boundaries, which probe the water layer between the stacked membranes, were scaled to 1.

To determine the degree of orientation of the membranes in the stack, the correlation peak intensities were integrated as function of the meridonal angle φ (the angle relative to the q_z axis) as depicted in Figure 2b. The corresponding intensity was fit with a Gaussian distribution centered at 0, which was then used to calculate the degree of orientation using Hermans orientation function:

$$H = \frac{3 < \cos^2 \delta > -1}{2}. \quad (3)$$

The experimental errors were determined as follows: Errors for peak positions, peak width and peak height are determined as the fit standard errors, corresponding to 95% confidence bounds, equivalent to two standard deviations, σ. Errors for calculated parameters, such as peak area, were then calculated by applying the proper error propagation.

Molecular Dynamics Simulation: MD simulations were performed on MacSim, a GPU accelerated computer workstation using GROMACS Version 5.1.4. The computer is equipped with a 40 Core central processing unit (CPU, Intel(R) Xeon(R) CPU E5-2630 v4 @ 2.20GHz), 130 GB random-access memory (RAM) and three graphic processing units (GPU, 2 × NVIDIA 1080 TDI + 1 × GeForce GT 730). Seven membrane models were designed using the CHARMM-GUI membrane-builder (http://charmm-gui.org/)[50,51] and the Martini forcefield 2.2.[51] The systems correspond to a pure red blood cell membrane and membranes containing 10%, 50%, and 80% DMPC respectively. Each system represents a membrane patch of 30 × 30 nm with 1500 lipid molecules on each leaflet and 37 water molecules per lipid representing a fully hydrated state of the membrane.

The lipid composition of the membrane patch was chosen according to the widely accepted experimental findings by Dodge et al.[32] However, the presented lipodomic analysis is limited to the ratio of lipid classes and tail saturation. Thus further approximations to the overall lipid composition had to be made. We used the same lipid species presented in the work by Ingólfsson and co-workers[27] and adapted the concentrations respectively to match the aforementioned experimental findings.[32] Note that multiple lipid species are represented by the same arrangement of atoms in the coarse-grained Martini force field. Each membrane system was charge-neutralized by the addition of (NaCl or KCl) counter-ions. The model is available from the authors upon request.

Simulations were equilibrated for 5 ns using an NPT ensemble (constant pressure and temperature), and then run for 5 µs. Only the final 3 µs were analyzed, after affirming the membrane had reached equilibrium by determining the area per lipid. All simulations used a 2 fs time step, a short range van der Waal cutoff of 1.1 nm, a potential-shift-verlet coulomb modifier and periodic boundary conditions were applied to all spacial directions. Neighbor lists were updated in intervals of 20 steps. The temperature coupling was controlled by a v-rescale thermostat at a constant pressure of 1 bar using Parrinello–Rahman semi-isotropic weak coupling (τ = 12 ps; compressibility $\beta = 3 \cdot 10^{-4}$ bar^{-1}). DMPC density maps were calculated using the gmx densmap function provided by GROMACS. For this purpose, the phosphate group of DMPC was indexed for each leaflet respectively and the density map was averaged over the last microsecond of the simulation.

The pure RBC membrane model contained 55 different lipid species from five different lipid classes. However, the exact composition was adjusted to produce the desired hybrid membrane models. Figure 4a shows a 3D render of membranes containing 10, 50, and 80 mol% DMPC. The lipid tails are represented by cyan and gray bonds for DMPC and RBC lipids, while blue and red spheres highlight the phosphate group of each membrane species respectively. Details about the exact lipid composition of each model can be found in Table S1, Supporting Information. Figure S3, Supporting Information, visualizes the relative concentrations of lipid species in the membrane model. Time-resolved DMPC density were determined by averaging the in-plane DMPC density over 1 µs between 2 and 5 µs in steps of 100 ns. The data were visualized using Matlab and were rendered with ffmpeg (Version 2.8.15).

Epi-Fluorescent Microscopy: Hybrid liposomes were visualized on a Nikon Eclipse Ti2-E inverted microscope, equipped with a CFI Plan Fluor 100× Oil immersion objective with a numerical aperture of 1.30 and a Tu Plan Fluor BD 50× objective with a numerical aperture of 0.8. The instrument was used in episcopic illumination mode using a X-Cite 120 LED combined with an excitation filter of 540–580 nm and an emission filter of 600–660 nm. Images were taken with an Andor Zyla 5.5 sCMOS camera with a resolution of 2560 × 2160 pixels and a pixel size of 6.5 µm and processed by cropping the image to the size of the liposomes shown. For each picture, brightness and contrast has been adjusted using ImageJ (Version 1.52i). Edges were detected in ImageJ and the contrast was further increased by adding both the original data and the edge detected picture.

Dynamic Light Scattering and Determination of the Zeta-Potential: The size distribution and the Zeta-potential of the prepared liposomes were determined on a Zetasizer Nano ZS from Malvern Panalytical. The instrument utilizes a 4 mW He–Ne laser (Wavelength: 633 nm) in combination with a non-invasive backscattering optics to measure a dynamic light scattering (DLS) spectrum allowing the diffusion constant D of the liposomes to be determined. This is related to the particle size via the Stokes–Einstein relation: $D = \frac{K_B T}{6\pi\eta r}$, where η is the dynamic viscosity of the solution, K_B is the Boltzmann Constant, T is the sample temperature and r is the radius of a presumably spherical particle. The Zeta-potential is determined by Laser Doppler Micro-Electrophoresis. Here, an alternating electric field is applied to the solution and the velocity of the particles is determined via the patented phase analysis light scattering (M3-PALS, patent reference: US7217350). This allows for the determination of the charge dependent mobility of the particles. All measurements were performed at 25 °C on 1 mL sample containing ≈14 mg mL^{-1} of membrane material.

UV–Visible Light Spectroscopy: The encapsulation efficiency and the resistance to mechanical stress was determined using UV–visible light spectroscopy using a Nanophotometer from IMGEN. The liposomes were prepared in a 1 mg mL^{-1} solution of fluorescein dextran, as described above. The liposomes were then isolated by centrifuging for 60 min at 20 000 g, and refilled to a total volume of 2 mL. UV–visible spectra were taken before and after the centrifugation process. Before centrifugation, the absorbance contains contributions from free dextran in the solution and from dextran encapsulated in liposomes. After centrifugation and liposome isolation, only encapsulated dextran contributes to the signal.

The efficiency E is calculated by

$$E = \frac{(I_{enc} - I_{pure\ liposomes})}{I_{enc+free}}, \quad (4)$$

where I_{enc} and $I_{enc+free}$ are the integrated intensities of the characteristic absorbance peak of fluorescein (430–520 nm) for the encapsulated and encapsulated+free dextran molecules, respectively. Corresponding absorbance spectra for hybrid liposomes containing 20% DMPC are shown in Figure S4, Supporting Information.

The resistance to mechanical stress was determined by a lysis essay. Liposomes were prepared according to the previously described protocol using phosphate buffer saline containing 1 mg mL^{-1} fluorescein labeled dextran. The solution was then centrifuged for 60 min at 20 000 g. The supernatant was removed and replaced by phophate buffer saline at varying molar concentrations (1–10 mM) increasing the osmotic and mechanical stress. The samples were allowed to rest for 30 min and afterward centrifuged for additional 60 min at 20 000 g. The degree of lysis was determined by determine the absorbance of the fluorescein peak. A low degree of lysis results in a low concentration of free dextran in the supernatant while a increased lysis is indicated by a leveled dextran concentration and thus a higher absorbance.

Statistical Analysis: All samples were prepared and measured in replicates and checked for consistency. Errors were determined by the respective experimental errors and consequent error propagation. Details are provided at the appropriate places in the manuscript.

Supporting Information

Supporting Information is available from the Wiley Online Library or from the author.

Acknowledgements

This research was funded by the Natural Sciences and Engineering Research Council of Canada (NSERC), the Canada Foundation for Innovation (CFI) and the Ontario Ministry of Economic Development and Innovation. M.C.R. is the recipient of an Early Researcher Award of the Province of Ontario and a University Scholar of McMaster University. C.W. acknowledges support by the DFG FOR 2688, project WA 1336/12. The funders had no role in study design, data collection and analysis, decision to publish, or preparation of the manuscript.

Conflict of Interest

The authors declare no conflict of interest.

Keywords

drug delivery, erythrocyte membrane, hybrid erythrocyte membranes, membrane material properties, red blood cells, synthetic lipids

Received: August 14, 2019
Revised: November 26, 2019
Published online:

[1] A. Samad, Y. Sultana, M. Aqil, *Curr. Drug Delivery* **2007**, *4*, 297.
[2] A. Laouini, C. Jaafar-Maalej, I. Limayem-Blouza, S. Sfar, C. Charcosset, H. Fessi, *J. Colloid Sci. Biotechnol.* **2012**, *1*, 147.
[3] B. S. Pattni, V. V. Chupin, V. P. Torchilin, *Chem. Rev.* **2015**, *115*, 10938.
[4] L. R. C. Pedrosa, O. van Tellingen, T. Soullié, A. L. Seynhaeve, A. M. Eggermont, T. L. ten Hagen, M. Verheij, G. A. Koning, *Eur. J. Pharm. Biopharm.* **2015**, *94*, 207.
[5] T. R. Hoare, D. S. Kohane, *Polymer* **2008**, *49*, 1993.
[6] L. Sercombe, T. Veerati, F. Moheimani, S. Y. Wu, A. K. Sood, S. Hua, *Front. Pharmacol.* **2015**, *6*, 286.
[7] G. M. Ihler, R. H. Glew, F. W. Schnure, *Proc. Natl. Acad. Sci.* **1973**, *70*, 2663.
[8] V. R. Muzykantov, *Expert Opin. Drug Delivery* **2010**, *7*, 403.
[9] M. Magnani, *Am. J. Hematol.* **2017**, *92*, 979.
[10] V. Leuzzi, R. Micheli, D. D'Agnano, A. Molinaro, T. Venturi, A. Plebani, A. Soresina, M. Marini, P. F. Leali, I. Quinti, M. C. Pietrogrande, A. Finocchi, E. Fazzi, L. Chessa, M. Magnani, *Neurology-Neuroimmunology Neuroinflammation* **2015**, *2*, e98.
[11] S. Zaitsev, D. Spitzer, J.-C. Murciano, B.-S. Ding, S. Tliba, M. A. Kowalska, O. A. Marcos-Contreras, A. Kuo, V. Stepanova, J. P. Atkinson, M. Poncz, D. B. Cines, V. R. Muzykantov, *Blood* **2010**, *115*, 5241.
[12] S. Zaitsev, M. A. Kowalska, M. Neyman, R. Carnemolla, S. Tliba, B.-S. Ding, A. Stonestrom, D. Spitzer, J. P. Atkinson, M. Poncz, D. B. Cines, C. T. Esmon, V. R. Muzykantov, *Blood* **2012**, *119*, 4779.
[13] W. M. Armstead, K. Ganguly, J. W. Kiessling, X.-H. Chen, D. H. Smith, A. A. Higazi, D. B. Cines, K. Bdeir, S. Zaitsev, V. R. Muzykantov, *J. Cereb. Blood Flow Metab.* **2009**, *29*, 1463.
[14] W. M. Armstead, K. Ganguly, J. Kiessling, J. Riley, X.-H. Chen, D. H. Smith, S. C. Stein, A. A. Higazi, D. B. Cines, K. Bdeir, S. Zaitsev, V. R. Muzykantov, *J. Neurochem.* **2010**, *113*, 303.
[15] K. M. Lorentz, S. Kontos, G. Diaceri, H. Henry, J. A. Hubbell, *Sci. Adv.* **2015**, *1*, e1500112.
[16] D. Pan, O. Vargas-Morales, B. Zern, A. C. Anselmo, V. Gupta, M. Zakrewsky, S. Mitragotri, V. Muzykantov, *PLoS One* **2016**, *11*, e0152074.
[17] V. R. Muzykantov, J. C. Murciano, R. P. Taylor, E. N. Atochina, A. Herraez, *Anal. Biochem.* **1996**, *241*, 109.
[18] Y. He, R. Li, H. Li, S. Zhang, W. Dai, Q. Wu, L. Jiang, Z. Zheng, S. Shen, X. Chen, Y. Zhu, J. Wang, Z. Pang, *ACS nano* **2019**, *13*, 4148.
[19] Q. Jiang, Y. Liu, R. Guo, X. Yao, S. Sung, Z. Pang, W. Yang, *Biomaterials* **2019**, *192*, 292.
[20] Y. Liu, X. Wang, B. Ouyang, X. Liu, Y. Du, X. Cai, H. Guo, Z. Pang, W. Yang, S. Shen, *J. Mater. Chem. B* **2018**, *6*, 7033.
[21] S. Himbert, R. J. Alsop, M. Rose, L. Hertz, A. Dhaliwal, J. M. Moran-Mirabal, C. P. Verschoor, D. M. E. Bowdish, L. Kaestner, C. Wagner, M. C. Rheinstädter, *Sci. Rep.* **2017**, *7*, 39661.
[22] R. J. Alsop, R. M. Schober, M. C. Rheinstädter, *Soft Matter* **2016**, *12*, 6737.
[23] M. C. Smith, R. M. Crist, J. D. Clogston, S. E. McNeil, *Anal. Bioanal. Chem.* **2017**, *409*, 5779.
[24] M. W. Rampling, *Biochem. Pharmacol.* **1976**, *25*, 751.
[25] D. Flormann, K. Schirra, T. Podgorski, C. Wagner, *Rheol. Acta* **2016**, *55*, 477.
[26] D. Flormann, O. Aouane, L. Kaestner, C. Ruloff, C. Misbah, T. Podgorski, C. Wagner, *Sci. Rep.* **2017**, *7*, 7928.
[27] H. I. Ingólfsson, M. N. Melo, F. J. Van Eerden, C. Arnarez, C. A. Lopez, T. A. Wassenaar, X. Periole, A. H. De Vries, D. P. Tieleman, S. J. Marrink, *J. Am. Chem. Soc.* **2014**, *136*, 14554.
[28] D. Lingwood, K. Simons, *Science* **2010**, *327*, 46.
[29] M. C. Rheinstädter, O. G. Mouritsen, *Curr. Opin. Colloid Interface Sci.* **2013**, *18*, 440.
[30] C. L. Armstrong, D. Marquardt, H. Dies, N. Kučerka, Z. Yamani, T. A. Harroun, J. Katsaras, A.-C. Shi, M. C. Rheinstädter, *PLOS ONE* **2013**, *8*, e66162.
[31] L. Toppozini, S. Meinhardt, C. L. Armstrong, Z. Yamani, N. Kučerka, F. Schmid, M. C. Rheinstädter, *Phys. Rev. Lett.* **2014**, *113*, 228101.
[32] J. T. Dodge, G. B. Phillips, *J. Lipid Res.* **1967**, *8*, 667.
[33] V. L. Lew, A. Hockaday, C. J. Freeman, R. M. Bookchin, *J. Cell Biol.* **1988**, *106*, 1893.
[34] S. Bhattacharjee, *J. Controlled Release* **2016**, *235*, 337.
[35] M. Ribeiro, M. Domingues, J. Freire, N. Santos, M. Castanho, *Front. Cell. Neurosci.* **2012**, *6*, 44.
[36] T. Nii, F. Ishii, *Int. J. Pharm.* **2005**, *298*, 198.
[37] A. Zaltzman, C. Van den Berg, V. Muzykantov, B. Morgan, *Biochem. J.* **1995**, *307*, 651.
[38] V. R. Muzykantov, M. D. Smirnov, A. L. Klibanov, *FEBS Lett.* **1993**, *318*, 108.
[39] V. R. Muzykantov, M. D. Smirnov, G. P. Samokhin, *Biochimica et Biophysica Acta (BBA)-Biomembranes* **1992**, *1107*, 119.
[40] V. R. Muzykantov, M. D. Smirnov, A. L. Klibanov, *J. Immunol. Methods* **1993**, *158*, 183.
[41] C. H. Villa, D. C. Pan, I. H. Johnston, C. F. Greineder, L. R. Walsh, E. D. Hood, D. B. Cines, M. Poncz, D. L. Siegel, V. R. Muzykantov, *Blood Adv.* **2018**, *2*, 165.
[42] S. L. Veatch, S. L. Keller, *Biochim. et Biophys. Acta (BBA)-Mol. Cell Res.* **2005**, *1746*, 172.
[43] J. Juhasz, F. J. Sharom, J. H. Davis, *Biochim. et Biophys. Acta (BBA)-Biomemb.* **2009**, *1788*, 2541.
[44] J. Juhasz, J. H. Davis, F. J. Sharom, *Biochem. J.* **2010**, *430*, 415.
[45] J. Juhasz, F. J. Sharom, J. H. Davis, *Biochim. et Biophys. Acta (BBA)-Biomemb.* **2009**, *1788*, 2541.
[46] M. J. Skaug, M. L. Longo, R. Faller, *J. Phys. Chem. B* **2011**, *115*, 8500.
[47] N. F. Morales-Penningston, J. Wu, E. R. Farkas, S. L. Goh, T. M. Konyakhina, J. Y. Zheng, W. W. Webb, G. W. Feigenson, *Biochimica et Biophysica Acta (BBA)-Biomembranes* **2010**, *1798*, 1324.
[48] A. Khondker, D. J. Malenfant, A. K. Dhaliwal, M. C. Rheinstädter, *ACS Infect. Dis.* **2018**, *4*, 926.
[49] J. F. Nagle, M. C. Wiener, *Biophys. J.* **1989**, *55*, 309.
[50] S. Jo, T. Kim, V. G. Iyer, W. Im, *J. Comput. Chem.* **2008**, *29*, 1859.
[51] Y. Qi, H. I. Ingólfsson, X. Cheng, J. Lee, S. J. Marrink, W. Im, *J. Chem. Theory Comput.* **2015**, *11*, 4486.

ADVANCED BIOSYSTEMS

Supporting Information

for *Adv. Biosys.*, DOI: 10.1002/adbi.201900185

Hybrid Erythrocyte Liposomes: Functionalized Red Blood Cell Membranes for Molecule Encapsulation

*Sebastian Himbert, Matthew J. Blacker, Alexander Kihm, Quinn Pauli, Adree Khondker, Kevin Yang, Sheilan Sinjari, Mitchell Johnson, Janos Juhasz, Christian Wagner, Harald D. H. Stöver, and Maikel C. Rheinstädter**

Supplementary Material to: Hybrid erythrocyte liposomes: functionalized red blood cell membranes for molecule encapsulation

Sebastian Himbert,[1,2] Matthew J. Blacker,[1,2] Alexander Kihm,[1,2,3] Quinn Pauli,[1,2] Adree Khondker,[1,2] Kevin Yang,[1,2] Sheilan Sinjari,[4] Mitchell Johnson,[4] Janos Juhasz,[1,5] Christian Wagner,[3] Harald D. H. Stöver,[4] and Maikel C. Rheinstädter[1,2,*]

[1] *Department of Physics and Astronomy, McMaster University, Hamilton, ON, Canada*

[2] *Origins Institute, McMaster University, Hamilton, ON, Canada*

[3] *Department of Experimental Physics, Saarland University, Saarbrücken, Germany*

[4] *Department of Chemistry and Chemical Biology, McMaster University, Hamilton, ON, Canada*

[5] *Juravinski Cancer Centre, Department of Medical Physics, Hamilton, ON, Canada*

(Dated: November 26, 2019)

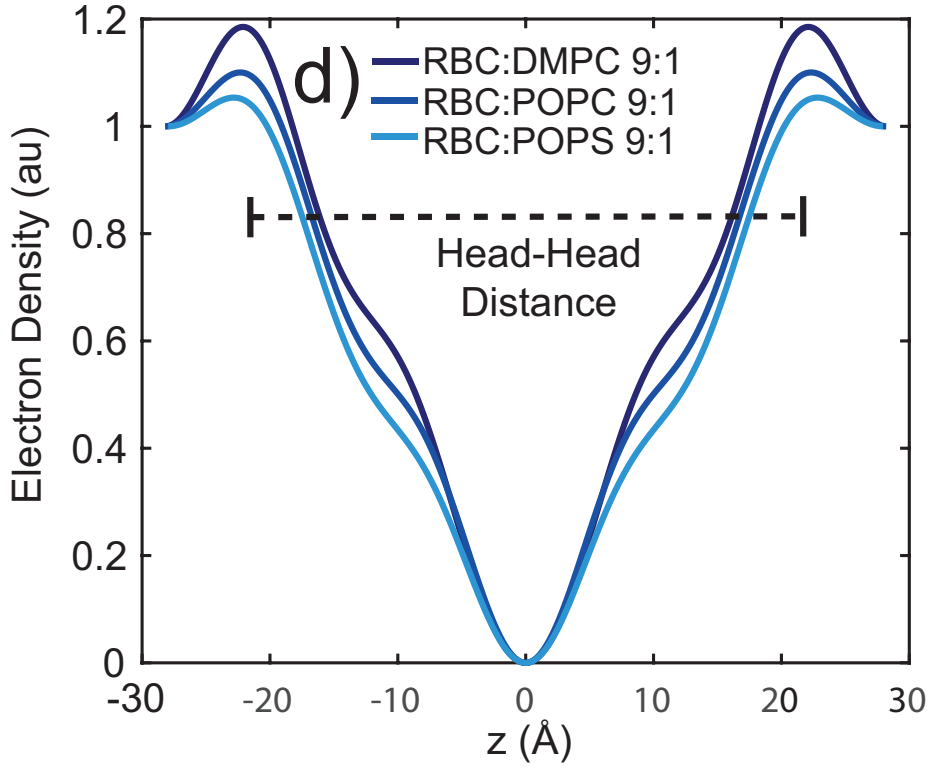

Supplementary Material, Figure S1. Corresponding electron density to Fig. 3a) in the main text determined by a 1-dimensional Fourier analysis.

* Department of Physics and Astronomy, McMaster University, ABB-241, 1280 Main Street West, Hamilton, Ontario L8S 4M1, Canada; Phone: +1-(905)-525-9140-23134, Fax: +1-(905)-546-1252, E-mail:rheinstadter@mcmaster.ca

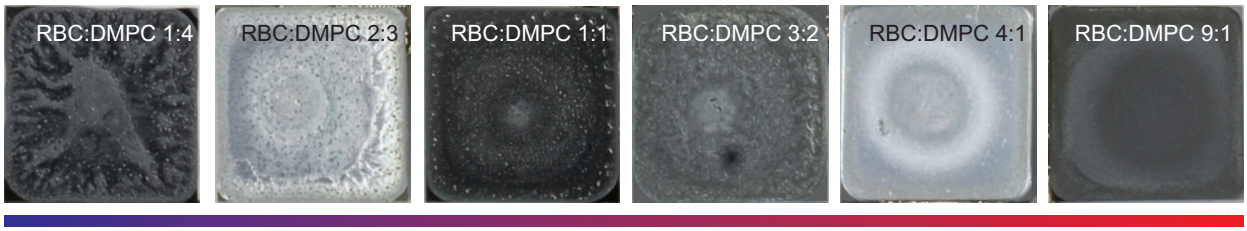

Supplementary Material, Figure S2. Photos of the prepared silicon wafers coated with hybrid membranes containing 10, 20, 50, 60, and 80 % DMPC.

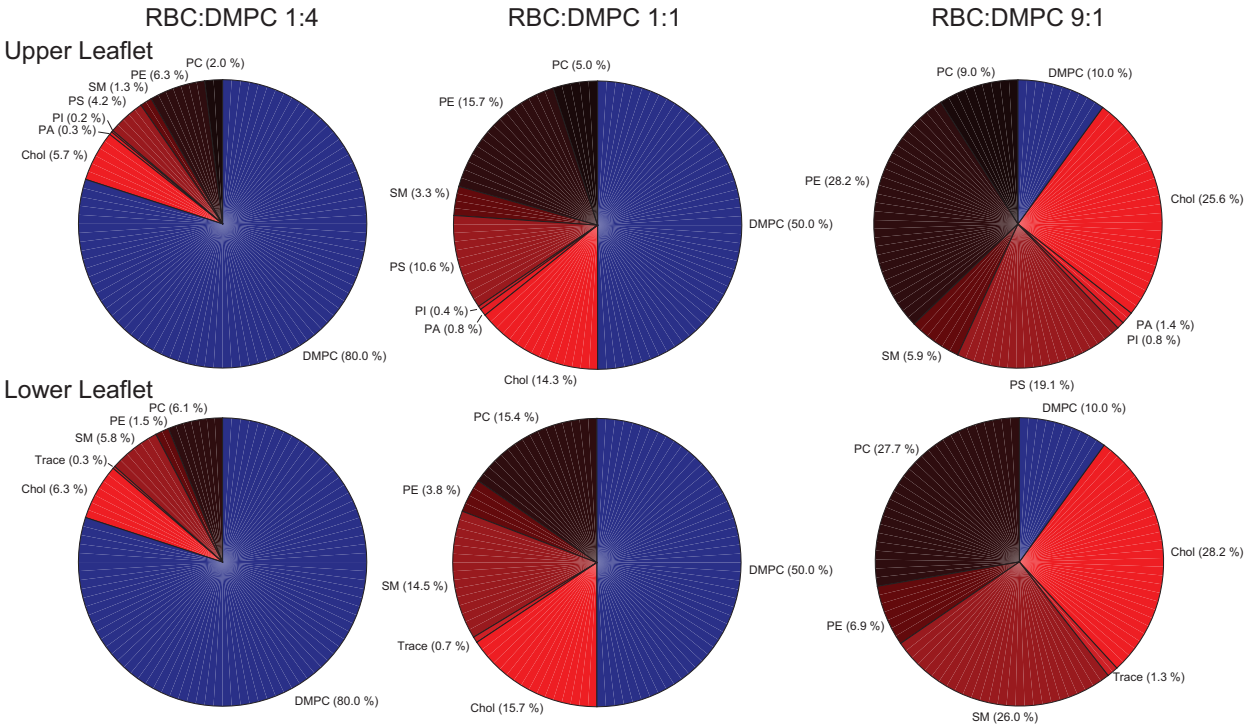

Supplementary Material, Figure S3. Relative concentrations of lipid species within the simulated membrane patches.

	Lipid Species	RBC:DMPC 1:4		RBC:DMPC 1:1		RBC:DMPC 9:1	
Layers		upper	lower	upper	lower	upper	lower
PC Lipids	POPC	10	31	26	79	46	141
	DOPC	1	3	2	7	4	12
	PIPC	15	46	38	116	68	208
	PEPC	1	2	1	5	3	8
	PAPC	2	7	6	18	11	33
	DAPC	0	1	1	2	1	4
	PUPC	1	2	1	5	3	8
PE Lipids	POPE	23	6	56	14	102	25
	DOPE	0	0	0	0	0	0
	PIPE	15	4	38	9	68	17
	PQPE	4	1	9	2	17	4
	PAPE	21	5	52	13	93	23
	DAPE	21	5	52	12	90	22
	PUPE	8	2	19	5	34	8
	DUPE	4	1	9	2	17	4
Sphingomylin	DPSM	9	39	23	97	41	175
	DBSM	4	18	10	44	18	79
	DXSM	6	28	15	69	28	125
	POSM	0	0	0	1	0	1
	PGSM	0	0	0	1	0	1
	PNSM	0	1	0	2	1	4
	BNSM	0	0	0	1	0	2
	XNSM	0	1	0	2	1	3
PS Lipids	POPS	1	0	3	0	6	0
	PIPS	5	0	13	0	23	0
	PQPS	8	0	20	0	37	0
	PAPS	35	0	88	0	158	0
	DAPS	1	0	3	0	6	0
	PUPS	11	0	29	0	51	0
	DUPS	1	0	3	0	6	0

	Lipid Species	RBC:DMPC 1:4		RBC:DMPC 1:1		RBC:DMPC 9:1	
Layers		upper	lower	upper	lower	upper	lower
PI Lipids	POPI	0	0	1	0	1	0
	PIPI	1	0	1	0	2	0
	PAPI	1	0	2	0	4	0
	PUPI	0	0	1	0	2	0
PA Lipids	POPA	2	0	4	0	7	0
	PIPA	1	0	3	0	6	0
	PAPA	1	0	3	0	6	0
	PUPA	1	0	1	0	3	0
Others	PPC	0	2	0	0	0	9
	OPC	0	1	0	0	0	3
	IPC	0	1	0	0	0	3
	APC	0	1	0	0	0	3
	UPC	0	0	0	0	0	1
Cholesterol		85	94	214	235	384	423
RBC		300	300	750	750	1350	1350
DMPC		1200	1200	750	750	150	150

Supplementary Material, Table S1. Number concentration of lipid molecules within the simulated coarse grained RBC membrane model.

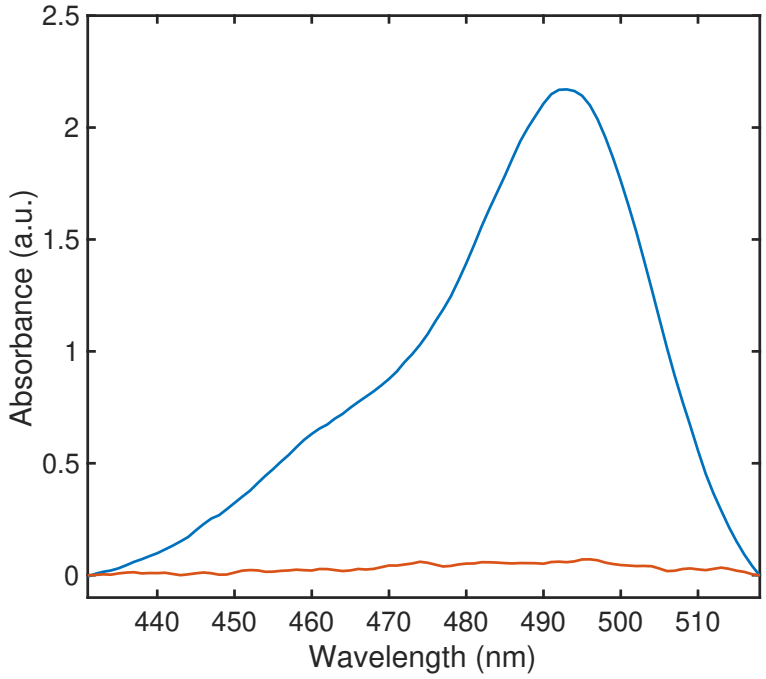

Supplementary Material, Figure S4. UV-vis absorbance spectra of hybrid liposomes containing 20% DMPC in a solution of 1 mg/ml fluorescein labeled dextran (blue), and isolated liposomes (red). The first curve contains contributions from free and encapsulated dextran while the second curve shows encapsulated dextran, only.

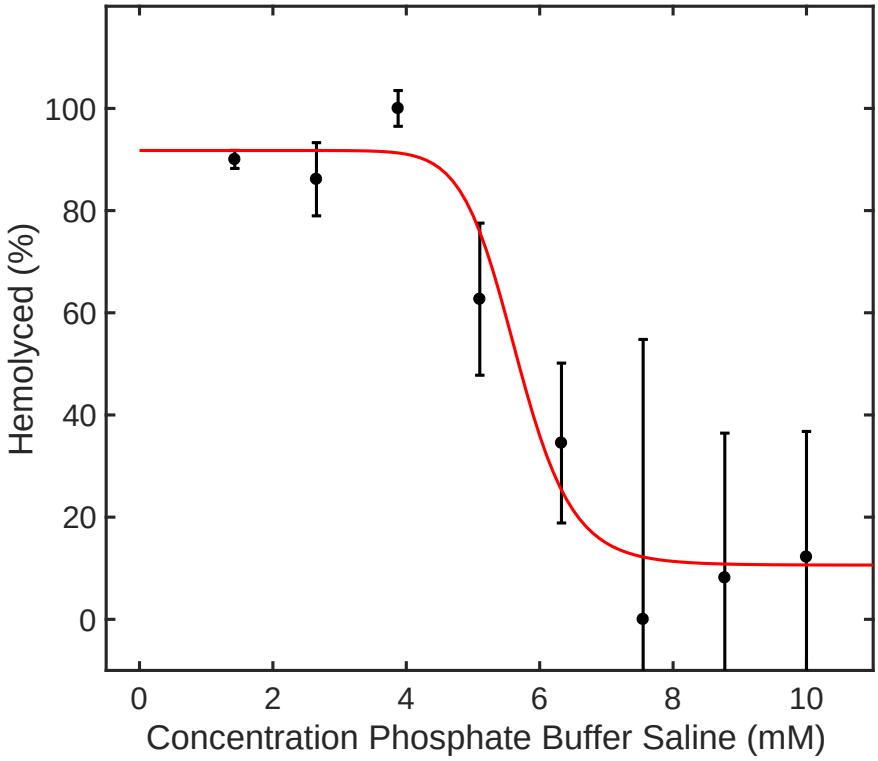

Supplementary Material, Figure S5. Lysis curve for hybrid liposomes containing 20% DMPC. The liposomes were prepared in a PBS solution containing 1 mg/ml fluorescein labeled dextran. The liposomes were then exposed to mechanical and osmotic stress by placing the liposomes in a solution with varying concentrations of phosphate buffer saline. The increase of lysed hybrid liposomes below 5.6 mM phosphate buffer saline is in good agreement with results for pure RBC [1].

[1] C. H. Villa, D. C. Pan, I. H. Johnston, C. F. Greineder, L. R. Walsh, E. D. Hood, D. B. Cines, M. Poncz, D. L. Siegel and V. R. Muzykantov, *Blood advances*, 2018, **2**, 165–176.

Chapter 7

Paper IV: Erythro-VLPs: anchoring SARS-CoV-2 spike proteins in erythrocyte liposomes

7.1 Preface to Paper IV

Paper IV was strongly motivated by the outbreak of the coronavirus disease 19 (COVID-19) pandemic and shall be seen as a proof of concept, where tuned RBC membranes are being used to deliver antigens to the immune system. We prepare Erythrocyte-membrane based virus-like particles (erythro-VLPs) by anchoring the S-protein in the RBCcm following the protocol introduced in Chapter 3. These functionalized liposomes have a diameter of ≈200 nm and are characterized with scanning confocal microscopy and dynamic light scattering, and exhibit dose-dependent binding in Biolayer Interferometry experiments. Further, the Triton-X 100 mediated insertion protocol is studied in MD simulations. A coarse grained model of the S-Protein is simulated in an aqueous solution with and without Triton-X100 and it is observed that this detergent stabilizes the proteins transmembrane domain prior to insertion. The protein model is simulated in two stages of the insertion process: in close proximity to a RBC membrane mimic and in an embedded configuration.

The pharmaceutical efficacy of the erythro-VLP is tested in mouse models where two mice received erythro-VLPs and a third mouse received a placebo that contained non-modified RBC liposomes. It was decided to administer three doses of 5 μg of S-protein, each, intravenously over the course of 20 days. This intravenous administration differs from the intramuscular injection that is preferred for vaccines, but allows utilizing the natural life cycle of RBCs to trigger seroconversion. RBCs can present antigens to the immune system when undergoing

phagocytosis in the liver and the spleen and we speculate that erythro-VLP's follow this non-inflammatory pathway.

Seroconversion is observed 14 days after the first injection and is measured through an enzyme-linked immunosorbent assay.

This publication thus demonstrates that erythro-VLP can present a viable alternative for creating anti-spike antibodies and underlines the biotechnological potential of functionalized RBC membranes.

Author Contributions:

- Experimental Concept: **Sebastian Himbert**, Maikel Rheinstädter
- Sample Preparation: **Sebastian Himbert**, Isabella Passos Gastaldo
- MD Model Development: **Sebastian Himbert**
- Microscopy Experiments: **Sebastian Himbert**, Isabella Passos Gastaldo, Samantha Ros, Janos Juhasz, Harald D. Stöver
- BLI Experiment: **Sebastian Himbert**, Rashik Ahmed, Guiseppe Melacini
- Mouse Trial: **Sebastian Himbert**, Breaden Cowbrough, Dawn M. E. Bowdish
- Data Analysis:**Sebastian Himbert**, Maikel Rheinstädter
- Manuscript Preparation: **Sebastian Himbert**, Maikel Rheinstädter

Erythro-VLPs: anchoring SARS-CoV-2 spike proteins in erythrocyte liposomes

Sebastian Himbert,[1,2] Isabella Passos Gastaldo,[1,2] Rashik Ahmed,[3,4]
Samantha Ros,[3] Janos Juhasz,[1,5] Braeden Cowbrough,[6,7,8] Harald D. H. Stöver,[3]
Giuseppe Melacini,[3,4] Dawn M. E. Bowdish,[6,7,8] and Maikel C. Rheinstädter[1,2,*]

[1] *Department of Physics and Astronomy, McMaster University, Hamilton, ON, Canada*
[2] *Origins Institute, McMaster University, Hamilton, ON, Canada*
[3] *Department of Chemistry and Chemical Biology, McMaster University, Hamilton, ON, Canada*
[4] *Department of Biochemistry and Biomedical Sciences, McMaster University, Hamilton ON, Canada*
[5] *Juravinski Cancer Centre, Department of Medical Physics, Hamilton, ON, Canada*
[6] *Department of Pathology and Molecular Medicine, McMaster University, Hamilton, ON L8N 3Z5, Canada*
[7] *McMaster Immunology Research Centre, McMaster University, Hamilton, ON L8N 3Z5, Canada*
[8] *Michael G. DeGroote Institute for Infectious Disease Research, McMaster University, Hamilton, ON L8N 3Z5, Canada*

(Dated: September 20, 2021)

Novel therapeutic strategies are needed to control the SARS-CoV-2 (severe acute respiratory syndrome coronavirus 2) pandemic. Here, we present a protocol to anchor the SARS-CoV-2 spike (S-)protein in the membranes of erythrocyte liposomes. Molecular Dynamics simulations provide details of the insertion process, and the role of a surfactant to stabilize the S-protein's structure in the aqueous environment before insertion and solubilize the membrane to facilitate entry. The correct insertion and functional confirmation of the S-proteins was confirmed by dose-dependent binding to ACE-2 (angiotensin converting enzyme 2) in biolayer interferometry (BLI) assays. These Erythro-VLPs (erythrocyte based virus like particles) have a well defined size distribution of ∼200 nm and an average protein density on the outer membrane of ∼300 proteins/μm^2. Seroconversion was observed in mouse trials after 14 days when administered intravenously, based on enzyme-linked immunosorbent assays (ELISA). This red blood cell based platform may open novel possibilities for therapeutics for the coronavirus disease (COVID-19), and because of its versatility potentially also for variants and other viruses in the future.

Keywords: SARS-CoV-2, Covid-19, Spike Protein, Red Blood Cell Membranes, Erythrocytes, Virus-Like-Particles

The outbreak of the coronavirus disease 19 (COVID-19) challenges the world in an unprecedented manner. It has led to over 191 million infections and more than 4,000,000 deaths globally[1] (as of July 20, 2021). The adverse effects of this global crisis, which has permeated all aspects of day-to-day living, including personal life, economy, and health care systems, substantiates an urgent need for novel diagnostics, therapeutics and vaccines.

The severe acute respiratory syndrome-coronavirus-2 (SARS-CoV-2) is mainly transmitted via respiratory droplets and aerosols[2,3]. In the lung, both SARS-CoV-2, as well as its precursor SARS-CoV, primarily infect the ciliated bronchial epithelial cells and type 2 pneumocytes[4–6] through the angiotensin converting enzyme 2 (ACE-2). This triggers a cascade of reactions leading to the fusion of the virus with the host cell and its reproduction, ultimately causing COVID-19.

SARS-CoV-2 is an enveloped, single and positive stranded RNA virus[4,7]. Of the three protein components on the viral envelope, the spike (S-)protein binds to the human ACE-2 receptor with a high affinity[7–10], and catalyzes the viral and host membrane fusion to initiate the infection[10,11]. It is a densely glycosylated transmembrane protein that forms the characteristic surface spikes of the corona virus[10]. The protein also induces neutralizing antibody and T-cell responses, and is, therefore, an important target for vaccine development[12]. The structure and conformations of the SARS-CoV-2 S-protein have been elucidated, however, this is still a highly active field of research[7,9,11]. The basic structure consists of an ectodomain trimer that includes the receptor binding domain (RBD), a trans-membrane domain (TMD), and a cytoplasmic domain (CPD).

The development of diagnostics, therapeutics and vaccines for SARS-CoV-2 challenges our current nanomedical manufacturing capabilities. Several SARS-CoV-2 vaccines have been developed[13,14]. Protein-based vaccines (including AstraZeneca, Johnson & Johnson) include whole-inactivated virus, individual viral proteins or subdomains, or viral proteins assembled as particles[15]. Gene-based vaccines (including Pfizer/BioNTech, Moderna) deliver genetic sequences that encode protein antigens that are produced by host cells. These mRNA vaccines have shown a high potency[16], however, require carriers, such as nanoparticles, as mRNA is quickly degraded by cellular processes. The candidate vaccine mRNA-1273, for instance, encodes the stabilized prefusion SARS-CoV-2 S-protein[17].

* Department of Physics and Astronomy, McMaster University, ABB-241, 1280 Main Street West, Hamilton, Ontario L8S 4M1, Canada; Phone: +1-(905)-525-9140-23134, Fax: +1-(905)-546-1252, E-mail:rheinstadter@mcmaster.ca

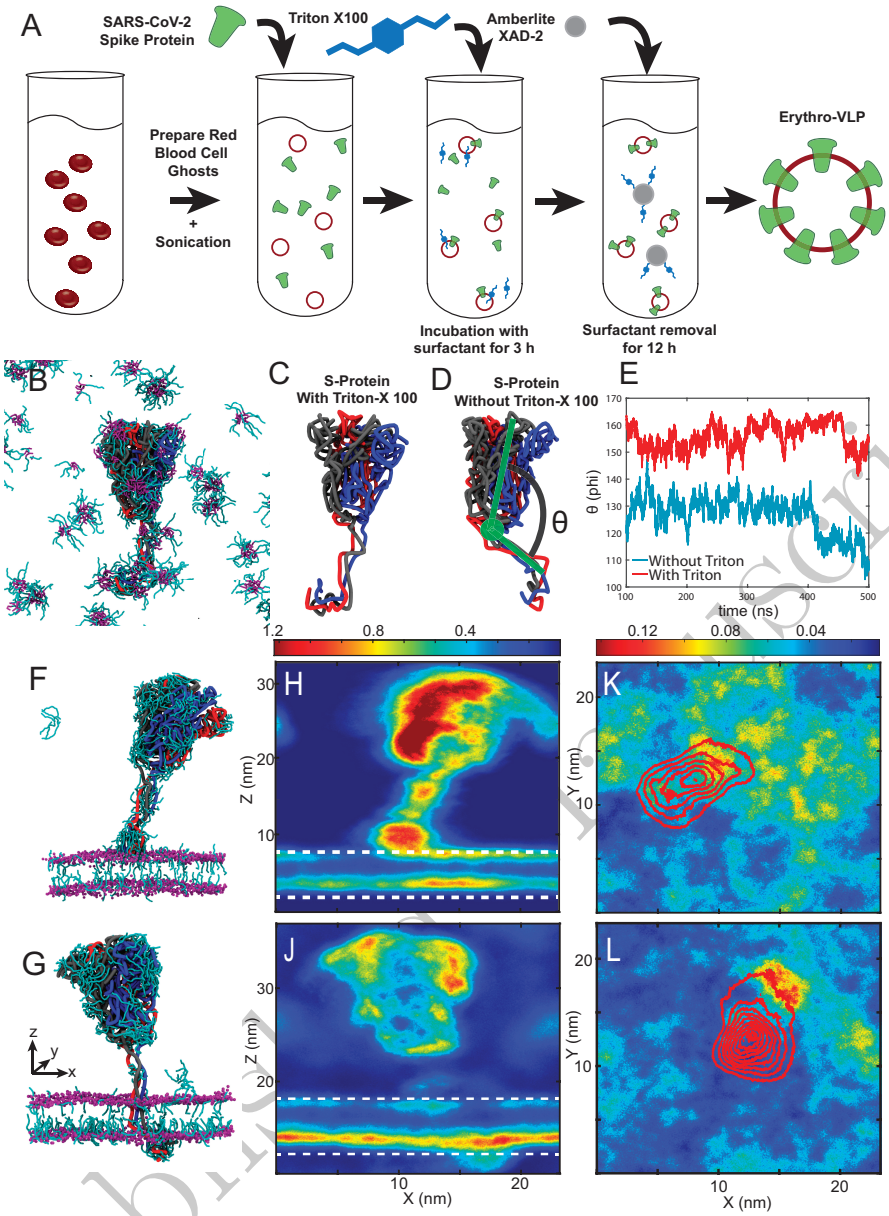

FIG. 1. **A:** Preparation protocol for Erythro-VLPs: Erythrocyte liposomes were prepared from human RBCs. 14 mg/ml erythrocyte liposomes were incubated in a 3 μM and 25 mM Triton-X100 solution. The detergent was removed by Amberlite XAD-2 and SEC. **B:** Snapshot of a MD simulation of the S-protein in a 25 mM aqueous Triton-X 100 solution after 500 ns. The three chains of the protein are visualized as black, red and blue tubes; Triton-X 100 is represented by cyan rods (hydrophilic head group) and purple rods (hydrocarbon tails). **C** and **D**: Snapshots of the S-protein in aqueous solution after 500 ns with and without Triton-X 100, respectively. The angle Θ measures the tilt of the TMD relative to the ectodomain trimer and is plotted in **E**. **F** MD snapshot after 50 ns of the S-protein insertion process into the RBC membrane mimic. **G** Snapshot after 500 ns, with the S-protein fully embedded in the membrane. Triton-X 100 density maps from both simulations averaged along the y-axis are displayed in **H** and **J**, maps averaged along the z-axis in **K** and **L**.

Here, we present an alternative approach to administer the S-protein using endogenous carriers by the *in-vitro* functionalization of red blood cells (RBC) through directly anchoring the SARS-CoV-2 S-protein into the RBCs' membranes. RBCs have been reported previously to catch immune complexes and bacteria and present them to Kupffer cells in the liver and Antigen-Presenting Cells (APCs) in the spleen[18,19]. Through this mechanism, these erythrocyte based virus like particles (Erythro-VLPs) can potentially lead to antibody production, higher central memory T cell, and lower regulatory T cell response[20] when delivered to the spleen. As will be shown below, the Erythro-VLPs exhibit dose-dependent binding to ACE-2 in biolayer interferometry

assays and seroconversion in mouse trials and enzyme-linked immunosorbent assays.

RESULTS & DISCUSSION

Erythro-VLPs were prepared as sketched in Fig. 1 A. Briefly, erythrocyte liposomes were prepared as detailed in[21], and incubated with a 3 μM S-protein solution. A surfactant (Triton-X 100) was used to facilitate the insertion of the S-protein (at a concentration of 25 mM). The surfactant was then removed by Amberlite XAD-2 beads and subsequent size exclusion chromatography (SEC).

The transport of the the CPD across the hydrophobic membrane core is essential to anchor the S-protein in the membrane of the erythrocyte liposomes. Surfactants are often used to facilitate these insertion processes[22–24]. An S-protein model was taken from[25] and simulated in coarse grained MD simulations in an aqueous solution with and without 25 mM Triton-X 100. Three-dimensional renders of the simulation are depicted in Figs. 1 B, C and D. Triton-X 100 was found to form micelles (Fig. 1 B). In addition, the surfactant molecules were found to bind to the protein, particularly to the TMD and CPD. While the hydrophobic hydrocarbon moiety (tail) of Triton-X 100 was found to associate with the TMD, likely to shield its hydrophobic core region from the aqueous environment, the hydrophilic head groups preferably interacted with the CPD. The angle Θ (in Fig. 1 D) measures the tilt of the membrane domain relative to the protein's ectodomain trimer. Fig. 1 E shows the time-behavior of this tilt-angle for simulations with and without Triton-X 100. An average angle of $\Theta = 155 \pm 5\ ^\circ$ was determined in the presence of Triton-X 100 while the angle was significantly reduced ($\Theta = 126 \pm 7\ ^\circ$) in the absence of this surfactant (Figs. 1 C and D). It is plausible that the straight orientation of the TMD may facilitate membrane entry, in contrast to the tilted structure in the absence of the surfactant.

MD snaphots of the S-protein's insertion process are shown in Figs. 1 F and G. Triton-X density maps, averaged along the y-axis, are depicted in Figs. 1 H and J (the membrane is indicated by white dotted lines); lateral Triton-X distribution within the membrane, averaged along the z-direction, is shown in Figs. 1 K and L. When the S-protein is close to the membrane (in Figs. 1 F, H and K), the CPD is the first point of contact. A high surfactant density is observed around the CPD, which likely facilitates insertion and passage through the membrane by lowering the hydrophobic mismatch between CPD and hydrophobic membrane core. The intra-membrane surfactant density is also increased in both leaflets, around the protein's lateral location. Once the protein is fully anchored (Figs. 1 G, J and L), surfactant density around the TMD is significantly reduced and remains concentrated around the CPD and the surrounding lower leaflet. This leaflet was observed to have a slightly larger area per lipid of 0.54 nm^2, as compared to 0.52 nm^2, in the upper leaflet, and it can be speculated that this additional space promotes the asymmetric distribution of Triton-X 100 between both leaflets.

The Erythro-VLPs were purified using size exclusion chromatography (SEC), shown in Fig. 2 A, detected between an elution volume of 7 ml and 12 ml. Remaining Triton-X 100 micelles were detected between an elution volume of 15 ml and 30 ml, showing that the Amberlite XAD-2 beads do not completely remove Triton-X 100 and subsequent separation with SEC is essential for the purification of the Erythro-VLPs. The size distribution of the purified erythrocyte liposomes with and without S-protein was determined by dynamic light scattering (DLS) and is shown in Fig. 2 B. While erythrocyte liposomes measured 102 nm (polydispersity: 0.19), in good agreement with previous results[26], an average diameter of 222 nm (polydispersity: 0.32) was determined for the Erythro-VLPs.

The concentration of proteins on the liposomes can be estimated using the following assumptions: 70% of the RBC membrane's mass are known to be lipids[21], with an average molecular mass of 700 g/mol. A liposome with a diameter of 100 nm has a surface area of $\sim$126000 nm^2. Assuming a typical area per lipid of 0.6 nm^2 in each leaflet, each liposome contains $\sim$42,000 lipid molecules. Cholesterol is well known to affect the area per lipid in a multi-component plasma membrane[27] and thus may effect this calculation. The RBC membrane is composed of approximatly 50 mol% cholesterol which can be assumed to have an area per molecule of 0.4 nm^2 [27] and one can assume a average area per lipid in the membrane of (0.6 nm^2 + 0.4 nm^2)/2 = 0.5 nm^2. This increases the estimated number of lipid molecules per vesicle to $\sim$51,000. An initial concentration of erythrocyte liposomes of 14 mg/ml then corresponds to a liposome concentration of 27-33 nM. A loading efficiency of 40 % was determined in an ELV-protein co-sedimentation assay (shown in Fig. S2 in the *Supporting Information*). The average number of proteins per liposome is then calculated by dividing the molar concentration of proteins in solution (3 μM) by the liposome concentration to 36-44 proteins/Erythro-VLP (on average). This corresponds to an average protein density of $\sim$280-350 proteins/μm^2.

Binding to ACE-2 was confirmed through biolayer interferometry (BLI)[28] (sketched in Fig. 2 E). When incorrectly embedded, the S-protein can not bind to the ACE-2 receptor. This assay is thus important to assess the correct functional conformation of the S-protein in the membrane-embedded state. A dose-dependent reduction in BLI signal was observed upon exposure of the ACE-2 immobilized biosensors to increasing concentrations of Erythro-VLPs, consistent with the binding of large particles to the optical biosensor (Fig. 2 C). Interestingly, addition of higher concentrations of Erythro-VLPs ($> 4\times$) resulted in more prominent binding at earlier time points which saturates at smaller negative λ values. This observation is consistent with a concentration-dependent clustering of Erythro-VLPs, which when bound to the sen-

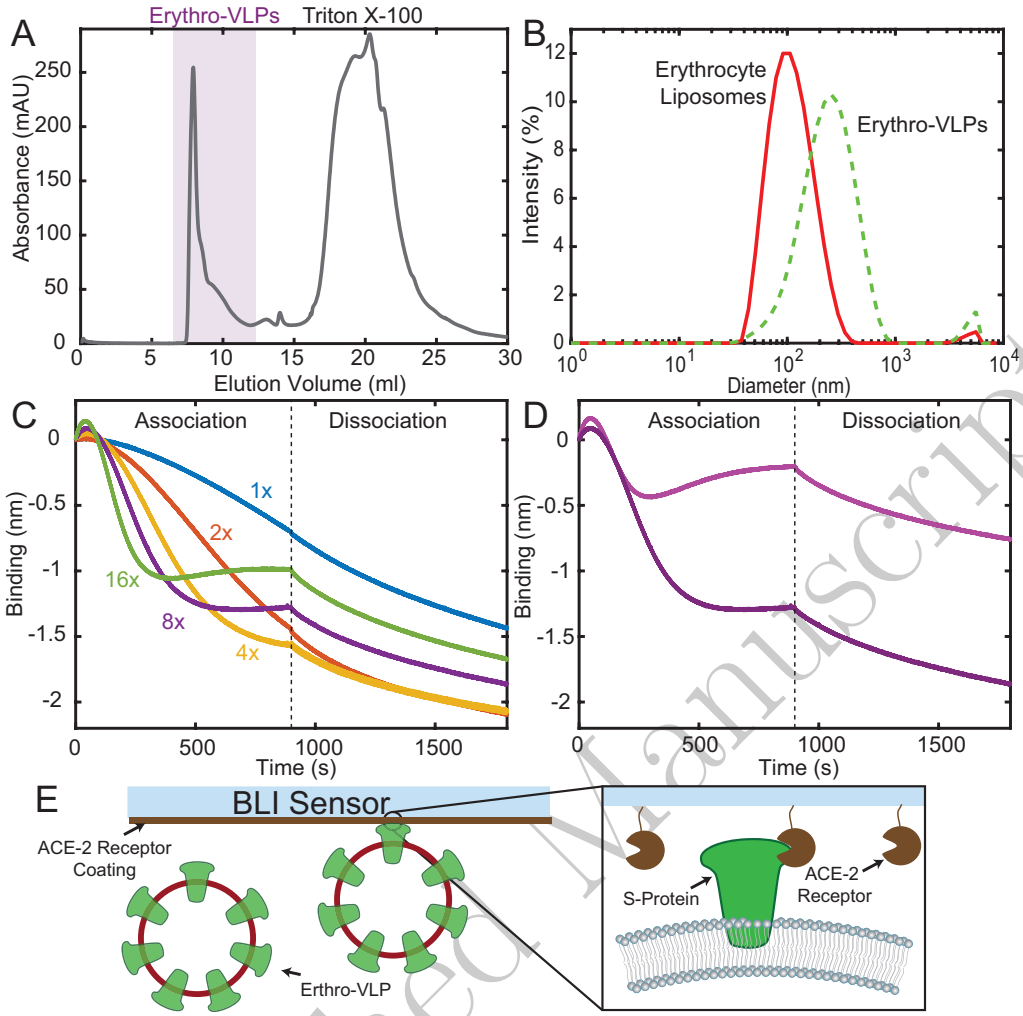

FIG. 2. **A:** SEC chromatogram of the Erythro-VLPs showing two signals from Erythro-VLPs and Triton-X100. **B:** Size distribution of Erythro-VLPs, as determined by DLS. While erythrocyte liposomes measured 102 nm (polydispersity: 0.19) an average diameter of 222 nm (polydispersity: 0.32) was determined for the spike carrying liposomes. **C:** Binding of Erythro-VLPs to human ACE-2 protein was measured by biolayer interferometry (BLI). A dose-dependent reduction in BLI signal was observed upon exposure of the ACE-2 immobilized biosensors to increasing concentrations of Erythro-VLPs, consistent with the binding of large particles to the optical biosensor. **D:** Association and dissociation curves for Erythro-VLPs in the absence (light purple) and presence (dark purple) of human ACE-2 immobilized onto the biosensor. The dark purple curve is reproduced from C (8×) for the purpose of comparison. **E:** Schematic of the BLI. Biotinylated human ACE-2 was immobilized onto the Streptavidin BLI sensor. The sensor was then exposed to Erythro-VLPs and association and dissociation was monitored.

sor chip sterically hinder[29] binding of further Erythro-VLPs. To exclude the possibility of additional binding contributions from the erythrocyte liposomes, we titrated erythrocyte liposomes lacking the S-protein to the ACE-2 immobilized sensor ship. Unlike the binding of the Erythro-VLPs, addition of erythrocyte liposomes to ACE-2 resulted in a positive wavelength change ($\Delta\lambda$) (see Fig. S3 in the *Supporting Information*). This observation not only suggests that the binding of Erythro-VLPs to ACE-2 is distinct, as compared to the erythrocyte liposomes, but also implies that the saturation of BLI signal at lower negative λ values observed at higher Erythro-VLP concentrations could arise from weaker binding contributions from erythrocyte liposomes.

Notably, in the absence of ACE-2 conjugation to the biosensor, the wavelength change due to binding is significantly diminished, suggesting that the S-protein - ACE-2 interaction is the predominant source of binding probed through BLI (Fig. 2 D). Overall, these findings indicate that the S-protein's RBD recognizing human ACE-2 remains solvent-exposed after embedding into the erythrocyte liposomes (Fig. 2 E). While it can not be excluded that that the S-protein embeds in two orientations, with the RBD domain facing outwards or inwards on the erythrocyte liposomes, the observation of a positive binding affinity of the Erythro-VLPs (as well as the positive immune response in mouse models further below) confirms that a significant fraction of S-proteins are facing out-

wards and remain in an active conformation.

Giant unilamellar vesicles (GUVs) were prepared to visualize the partitioning of the S-proteins in the erythrocyte liposomes. While electroformation is commonly used to fabricate GUVs, this method is difficult in physiological buffers because of electrolysis and the corresponding gas formation in the presence of salts[22,23]. Giant Erythro-VLPs were, therefore, prepared using gel-assisted swelling where the Erythro-VLPs were first dried on an agarose gel. Giant Erythro-VLPs then formed spontaneously when the gel-liposome film was rehydrated. The procedure is known to lead to a homogeneous protein distribution among the liposomes and allows a rapid preparation in physiological buffers[22].

The RBC membranes were doped with TR-DHPE (red); The S-protein was stained using Alexa Fluor 488 maleimide (AF488, green) which binds to the thiol group of cysteine[30]. The S-protein is shown as ribbon diagram in Fig. 3 A) with the cysteine groups highlighted as red and green spheres. The solvent accessible surface area (SASA) for each of the cysteine residues is shown in Fig. 3 B). Following this analysis, only two cysteine residues (136 and 166) per chain are directly accessible for staining with AF488 (green bars in Fig. 3 B)). Thus, each protein is expected to be stained with 6 AF488 molecules at most, as marked by the green spheres in Fig. 3 A.

The giant Erythro-VLPs were imaged using a combination of epifluorescent and confocal laser scanning microscopy (CLSM), shown in Fig 3 C. The image was taken on the agarose gel, before harvesting the vesicles. The liposomes appear as spherical orange objects with sizes of $\sim$50 μm; however, such large liposomes were no longer observed after harvesting, likely due to shear stress induced damage during harvesting. The harvested liposomes show typical sizes between $\sim$5-10 μm and were investigated using CLSM, as depicted in Fig. 3 D. Fig. 3 E shows one representative liposome in magnification. Separate imaging of the green (excitation: 488 nm) and red (excitation: 561 nm) channels shows that the S-proteins are located in the membranes (within the resolution of the microscope). The orange color is the result of the superposition of the red and green dye and the images thus indicate a uniform distribution of the S-proteins in the liposomes. A vesicle with a diameter of 8 μm has an estimated surface area of 200 μm^2. Given the calculated average protein density of $\sim$300 proteins/μm^2, each giant Erythro-VLP contained approximately 60,000 proteins and $1.8 \cdot 10^6$ AF488 molecules.

A mouse study was conducted over a period of 33 days involving three female mice at an age of 3 months to confirm seroconversion. A timeline of the study including all injections and blood collections is displayed in Fig. 4 A. The mice were divided into 2 groups: Two mice received three doses of Erythro-VLPs suspended in 50 μL of sterile saline buffer at days 0, 5, and 10 of the study. The liposome concentration in each dose was approximately 30 nM, containing 8 μg of the S-protein. The third mouse received erythrocyte liposomes without the S-protein at an equal liposome concentration. Venous blood was collected at days 0, 7, and 28, and antibody levels were determined by ELISA (Fig. 4 B). Mice were immunized for the total S-protein; however, it is well documented that antibodies to the RBD are required to prevent viral entry and infection. Therefore, anti-RBD IgG antibodies were measured by ELISA. Serum was diluted (1/20, 1/50/, 1/100) and absorbance values are shown as a ratio of the post-vaccination/pre-vaccination levels in sera in Fig. 4 C and D. Since de novo antibody responses generally take 10 days to develop and can be low and transient in the absence of a booster dose, no signal was observed at days 0 and 7. Vaccinated mice (Mouse 1 & 2) demonstrated and increase in these ratios (up to 83 and 112, respectively) on days 14 and 28 of the study. The control (Mouse 3) showed no change in the optical density throughout the samples collected.

Drug delivery by nanocarriers is often limited by liver uptake and limited target organ deposition. Nanocarriers adsorbed on RBCs have been shown to improve delivery for a wide range of carriers and viral vectors[31,32]. However, their potential for therapeutic applications, such as drug delivery[33,34] and immunological functions[35–38] has been started to be exploited only recently. The biocompatibility of RBCs[39] and their bioavailability[40], coupled with the phagocytic capacity of RBCs in the spleen, suggests that RBCs can be effective vehicles for the presentation of viral immunopathogens, such as the SARS-CoV-2 S-protein, to APCs and the immune system.

A prerequisite for the efficacy of the Erythro-VLPs in generating an antibody-based immune response is that the S-protein retains its functional conformation in the membrane-embedded state[15]. The increased optical density in the ELISA assays 14 days after injection is a clear evidence for a successful seroconversion. Importantly, while the mice received Erythro-VLP with the full-length S-protein, antibodies to the RBD sub-domain were measured, which is required for viral entry[41,42]. This implies that the conformation of the S-protein in the Erythro-VLPs is not changed in such a way that the RBD domain is 'hidden' or modified, which is often challenging when injecting soluble proteins.

The Erythro-VLPs can present immunopathogens to the immune system[18–20] when the cells are being phagocytized in the spleen. This pathway has been utilized in the past to present antigens to APCs in the spleen by attaching nanoparticles to red cells[20], and for hybrid RBC based nanovesicles[43]. An interesting point is that IgG production was triggered without an adjuvant (such as aluminium hydroxide[44,45]), which points to some sort of a depot effect, likely related to the circulation of the Erythro-VLPs in the blood stream before they are processed in the spleen. While these first results demonstrate the potential of this pathway and the erythrocyte platform, future work is needed to elucidate its potential therapeutic use. These include, for instance, *in-vivo* toxicity evaluations and pathological analysis including vasculitis, and options for intramuscular administration.

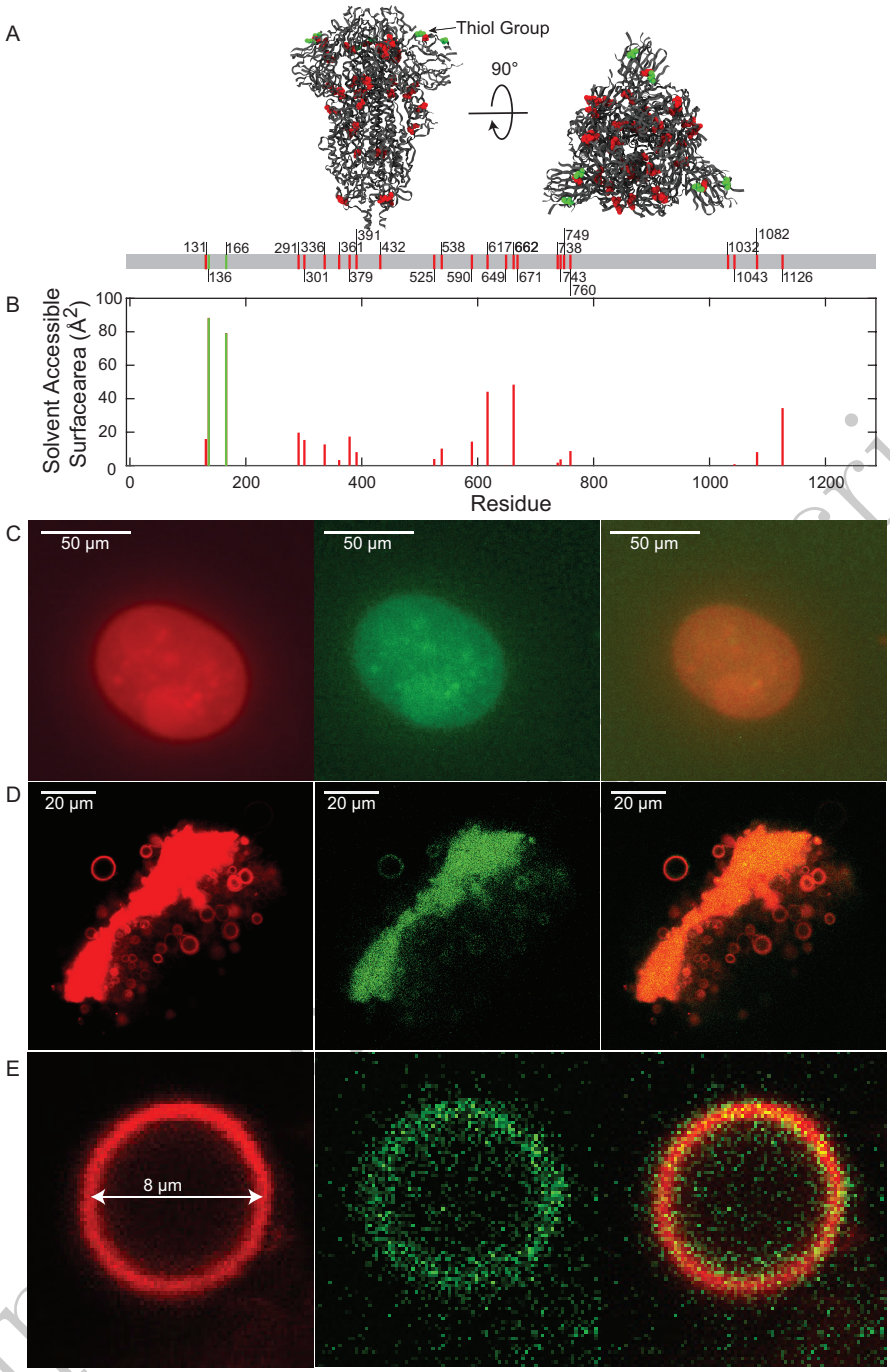

FIG. 3. **A:** Protein structure of the SARS-CoV-2 S-protein. The protein is shown as ribbon diagram and cysteine is shown as sphere. The red and green color indicates solvent accessible and non-accessible cysteine residues. The Solvent Accessible Surface Area (SASA) was determined by the Getarea software and is graphed in **B**. **C:** Epifluorescent microscopy images of giant Erythro-VLPs grown on agarose gel. The membrane was stained in red using TR-DHPE; the SARS-CoV-2 S-protein was stained in green using Alexa Fluor 488 maleimide. **D:** CLSM images of a cluster of giant liposomes after harvesting from the agarose. **E:** Magnified image of one isolated giant Erythro-VLP taken with CLSM. Images in C-E show the red-, green-, and combined fluorescent channel, respectively.

CONCLUSION

The SARS-CoV-2 Spike (S-)protein was successfully anchored in the membranes of erythrocyte liposomes to create 'Erythro-VLPs'. These ∼200 nm sized liposomes carry up to 36 S-proteins on average (corresponding to an average protein density of ∼300 proteins/μm^2). The correct insertion and functionality of the S-proteins was

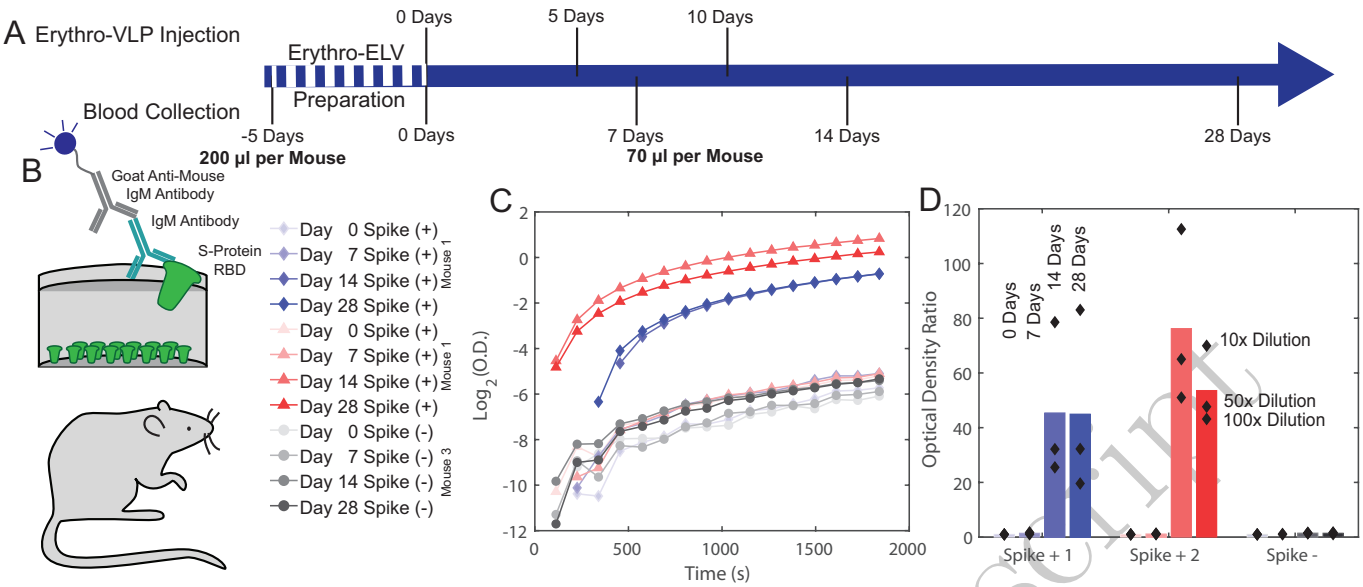

FIG. 4. **A:** Time line of the mouse study. Each mouse received 3 injections of Erythro-VLPs suspended in sterile saline buffer at 0, 5, and 10 days. The liposome concentration in each dose was approximately 30 nM containing 8 μg of the S-protein. Blood was drawn at 0 (control), 7, and 14 days. Final draw was after 28 days. **B:** An enzyme-linked immunosorbent assay (ELISA) was used for antibody detection. **C:** Optical density as function of time for the ELISA essay for all samples. **D:** Measured optical density ratios. Bars represent the mean optical density ratio averaged over all three dilution runs. Values above 1 ratio are considered positive in the SARS-CoV-2 antibody ELISA. A strong antibody response was observed in both mice after 14 days; no response was observed in the control.

shown through ACE-2 binding assays. Seroconversion was observed in mice after 14 days, after two injections, and the production of antibodies was confirmed in ELISA. The results show that the Erythro-VLPs are an effective way to present the S-protein to the immune system and induce antibody production. With a large number of similar viruses circulating in bats and camels[46], and the emergence of variants, the possibility of additional outbreaks poses major threats to global public health. The erythrocyte platform that we present in this work may have therapeutic potential and can rapidly be adapted to different variants and viruses by embedding the corresponding antigenic proteins.

MATERIALS & METHODS

Ethics approval

This research was approved by the Hamilton Integrated Research Ethics Board (HIREB) under approval number 1354-T. Informed consent was obtained from all blood donors by signing a written consent form. The authors confirm that all methods were performed in accordance with the relevant guidelines and regulations. All animal procedures for this study were approved by the McMaster University Animal Research Ethics Board (Animal Utilization Protocol 17-05-19 and Amendment #20-111 to AUP #17-05-19) in accordance with the guidelines of the Canadian Council of Animal Care.

Immunization experiments

Three female C57BL/6J mice were obtained from the Jackson Laboratory (Bar Harbor, ME, Strain 000664), maintained in a single standard mouse cage in the same room with a constant temperature of 25°C and a 12 h light, 12 h dark cycle, and fed a control standard diet (17% kcal fat, 29% kcal protein, 54% kcal CHO, 3 kcal/g; Harlan 8640 Teklad 22/5 Rodent Diet) and provided water ad libitum. Pre-immunizaiton blood (200 μl) was collected retro-orbitally in heparinized tubes. RBCs were then isolated through centrifugation and washed twice using sterile saline solution and Erythro-VLPs were prepared as described. The lysing buffer was exchanged to sterile buffer saline after the preparation of red blood cell ghosts, in compliance with the approved animal utilization protocol. The mice were allowed to rest and acclimate for 5 days before immunization. Mice were immunized by injecting 50 μl of Erythro-VLP in the tail vein injection and monitored daily for adverse reactions or inflammatory reactions at the injection site. Venous blood (70 μl) was collected from the tail vein in heparinized tubes at days 0, 7, 14 and 28. No adverse reactions were observed.

Preparation of small erythrocyte liposomes

The detailed protocol is described elsewhere[21]. Briefly: Heparinized blood samples were collected. The blood was washed twice and the RBCs were isolated by successive centrifugation and replacing the supernatant with phosphate saline buffer (PBS). The cells were exposed to to osmotic stress by mixing hematocrit with lysis buffer (3% PBS buffer, pH 8) at a concentration of 5 vol%. The lysis buffer was pre-chilled to ∼4 °C and the reaction tube were immediately stored on ice to prevent a fast re-closing of the ruptured cells. Hemoglobin and other cellular compartments can be removed through multiple washing steps as shown in[21]. The protocol results in a white pellet containing empty erythrocyte liposomes. The resulting solution was tip sonicated 20 times for 5 s each at a power of 100 W. The reaction tube was placed on ice during sonication to prevent the sample from overheating. Afterwards, the tube was centrifuged for 15 min at ∼20,000 g. The supernatant consists of a solution of small, nanometer-sized liposomes and will be hereafter referred to as the *Blood Solution*. The protocol results in a membrane concentration of ∼14 mg/ml[21].

Preparation of Erythro-VLPs

S-proteins were purchased from Acrobiosystems (SPN-C52H4). The cryoprotectants, glycerol and trehalose, were removed from the ACE-2 and S-proteins, respectively, by analytical size-exclusion chromatography using a Superdex 200 increase 10/300 analytical gel filtration column (GE Healthcare). The S-protein was eluted with ultrapure H_2O and lyophilized and resuspended by adding 50 μl of the *Blood Solution*. Triton-X 100 (9002-93-1, Sigma-Aldrich) was added to achieve a concentration of 25 mM; above the critical micelle concentration (CMC) of the surfactant. The size distribution of erythrocyte liposomes at varying Triton-X 100 concentrations (in Fig. S1 in the *Supporting Information*) shows 3 phases: Liposomes with an average diameter of 244.8±175.9 nm were observed at a Triton-X 100 concentration of 0.1 mM; below the critical micelle concentration (CMC = 0.25 mM). This liposome signal co-exists with micelles with a diameter of ∼10 nm between concentrations of 3 and 20 mM. Concentrations higher than 25 mM eventually led to an aggregation of the liposomes causing the formation of aggregates with a diameter of up to 2±0.3 μm. A concentration of 25 mM was, therefore, chosen to facilitate the protein insertion as it is the upper limit of the coexistence phase of liposomes and micelles.

The sample was incubated for 3 h before adding an excess of Amberlite XAD-2 (9003-70-7, Sigma-Aldrich). These non-polar polystyrene beads are commonly used to remove surfactant, such as Triton-X 100. The sample was incubated at room temperature for 12 h. To remove potential excess Triton-X 100, which was not extracted by the beads, the supernatant containing S-protein embedded RBC membranes (Erythro-VLPs) was injected into an analytical gel filtration column and eluted with 8-fold diluted PBS. The purified fraction was then concentrated 8-fold to a working volume of 500 μL (∼ 80 μg/ml of total S-protein) using a Vacufuge plus from Eppendorf for subsequent BLI (Octet Red 96, ForteBio) analysis. The resulting solution will be referred to as *Erythro-VLP Solution*.

Staining of Erythro-VLPs

The RBC membrane was fluorescently labeled by doping the bilayers with Texas Red 1,2-Dihexadecanoyl-sn-Glycero-3-Phosphoethanolamine (TR-DHPE) (Thermo Fisher, Catalog number: T1395MP). It is known to interact with liquid disordered l_d lipid patches and has been previously used to investigate domain formation in membranes[47,48]. 10 mg/ml 1-Palmitoyl-2-Oleoyl-sn-Glycero-3-Phosphocholin (POPC) in chloroform was prepared containing 1 mol% TR-DHPE. POPC has been previously shown to homogenously fuse with RBC membranes[26] and facilitates the incorporation of stained lipids into the membrane. 50 μl of this solution was dried in a glass vial under a constant dry nitrogen flow before adding 250 μl (∼3.5 mg) of the *Blood Solution*. This solution has a concentration of TR-DHPE of 0.001 mass% and will be referred to as *Fluorescent Solution*.

SARS-Cov-2 S-protein was purchased from ACRO-Biosystems (SPN-C_52H_4) and was delivered in a Tris buffer (50 mM Tris (Tris(hydroxymethyl)aminomethan), 150 mM NaCl, pH 7.5 with 10% trehalose) at a concentration of 0.2 μg/ml. The protein was separated in aliquots of 20 μg. After thawing, the protein was incubated for 20 min with a 100× excess of TCEP (Tris-(2-carboxyethyl)-phosphin). This reduces the disulfide bonds preparing the protein for staining with Alexa Fluor 488 maleimide (SCJ4600016, Sigma-Aldrich). A stock solution of 1 μmol in 0.1 ml DMSO of Alexa Fluor 488 maleimide was prepared. 1 μl was then added to the protein solution and incubated over night at 4°C. The protein was separated from the excess dye through centrifugation at 20,000 g for 6 h. A brown pallet was observed and the supernatant was replaced by fresh HEPES Buffer (20 mM Hepes, 150 mM NaCl).

The *Fluorescent Solution* was concentrated to 30 mg/ml using a Vacufuge plus from Eppendorf. The protein solution was brought to a total volume of 70 μl. 5 μl of the concentrated *Fluorescent Solution* was then added. Triton-X 100 (9002-93-1, Sigma-Aldrich) was added to achieve a concentration of 25 mM. The sample was incubated for 3 h before adding an excess of Amberlite XAD-2 (9003-70-7, Sigma-Aldrich) and incubating at room temperature for another 12 h.

Preparation of giant Erythro-VLPs

Giant Erythro-VLPs were prepared using the gel assisted swelling method[22]. Briefly; Microscope cover slips were coated with a thin layer of agarose gel. Then, 12 × 1 μl droplets of the Erythro-VLP solution were applied onto the gel and allowed to fully dry for ∼10 min under a nitrogen atmosphere. The glass slides were then placed in a petri dish and covered with 1 ml of growth buffer (20 mM Hepes, 150 mM NaCl, 200 mM sucrose) and incubated at room temperature for 30 min. This allows liposomes to grow on the surface of the agarose gel. Compared to the commonly known electroformation of GUV, the method produces more heterogeneous liposomes, however, has the advantage of using a saline based buffer during growth. However, it was reported to have a lower yield in isolated defect free GUV[22]. The giant Erythro-VLPs were harvested by gently pipetting ∼20 μL from near the surface of the agarose and mixing it in a ratio of 1:1 with imaging buffer (20 mM Hepes, 150 mM NaCl, 200 mM glucose)

Epi-fluorescent microscopy

Epi-fluorescent Microscopy was conducted using an Nikon Eclipse LV100 ND Microscope. The instrument is equipped with a Plan Fluor BD 10× and 20× objective with numerical apertures of 0.3 and 0.5, respectively. Images were recorded using a Nikon DS-Ri2 Camera with a resolution of 4908×3264 pixels and a pixel-size of 7.3×7.3 μm. The camera is mounted via a 2.5× telescope to the microscope. All images were recorded in episcopic illumination mode using a halogen lamp. Images were recorded using the Nikon control software (NIS Elements, Version 4.60.0).

Confocal laser scanning microscopy

Liposomes were imaged on a Nikon A1 Confocal Eclipse Ti microscope with Nikon A1plus camera. The microscope was equipped with a Plan Apo 40×/0.9 NA objective lens. Images were recorded using a resolution of 2048 × 2048 pixels and the recording speed was adjusted to ensure a optimized signal to noise ratio for each channel respectively. Two excitation modes were used: 561 nm (TR-DHPE) and 488 nm (Alexa Fluor 488 maleimide) allowing the identification of the membrane and the S-protein, respectively. The instrument was controlled by the Nikon NIS Elements software.

Dynamic light scattering

A Zetasizer Nano ZS from Malvern Panalytical was used to determine the size distribution of the liposomes. The instrument is equipped with a 4 mW He-Ne laser (wavelength: 633 nm) and a non-invasive backscattering optics. The diffusion constant, D, of the liposomes is determined by measuring the dynamic light scattering (DLS) spectrum. This is related to the particle size via the Stokes-Einstein relation: $D = \frac{k_B T}{6\pi\eta r}$, where η is the dynamic viscosity of the solution, k_B is the Boltzmann constant, T is the sample temperature and r is the radius of a spherical particle. All measurements were performed at 25°C on 1 ml sample containing ∼0.5 mg/ml of membrane material.

Biolayer interferometry (BLI)

Biotinylated human ACE-2 was purchased from Acrobiosystems (AC2-H82F9). The cryoprotectants, glycerol and trehalose, were removed from the ACE-2 proteins, respectively, by analytical size-exclusion chromatography using a Superdex 200 increase 10/300 analytical gel filtration column (GE Healthcare). The ACE-2 protein was eluted with PBS at pH 7.4 and stored at 4°C until use.

The biotinylated human ACE-2 protein (∼11 μg/ml) was immobilized onto Streptavidin (SA) biosensors (ForteBio) until a threshold of 1 nm wavelength change was reached for all sensor chips. Excess non-immobilized ACE-2 was washed off by dipping the sensor into PBS at pH 7.4 for 120 s. Subsequently, the SA biosensor was dipped into solutions of Erythro-VLPs or erythrocyte liposomes of varying doses ranging from 1× to 16× for 900 s to allow for association. Dissociation was monitored by dipping the biosensor in PBS at pH 7.4 for 900 s.

Solvent accessible surface area (SASA) of SARS COV-2 S-protein

The SASA of the S-protein was computed through the Getarea software (http://curie.utmb.edu/getarea.html) based on the PDB ID: 6VXX S-protein structure reported by Walls and colleagues[7]. The total (backbone and sidechain) SASA was computed for all three protomers and the average and standard deviation of these three measurements are reported for each residue.

SARS-CoV-2 ELISA

A high-throughput serological assay to identify SARS-CoV-2 antibodies in COVID-19 patients has been developed previously[49]. In brief, 384 well plates (Nunc Maxisorp, Rochester, NY, USA) were coated overnight at 4°C with 25 μL/well of RBD (2 μg/ml) suspended in 50 mM carbonate-bicarbonate buffer (pH 9.6). The plates were then blocked with 100 μL/well of 3% skim milk prepared in PBS with 0.05% Tween 20 at room temperature for 2 h. The blocking solution was removed, and diluted mouse serum samples (1/100 prepared in 1% skim milk

in PBS/0.05% Tween 20) was added to the plates for 1 h at room temperature. The plates were washed twice with PBS/0.05% Tween 20 and thrice with PBS. Bound mouse antibodies (IgG, IgA, or IgM) were detected with alkaline phosphatase conjugated goat anti-mouse IgG (γ-chain-specific, 1/2000, Jackson ImmunoResearch Laboratories, Inc, Westgrove, PA, USA), goat anti-mouse IgA (α-chain-specific; 1/500, Jackson ImmunoResearch Laboratories, Inc, Westgrove, PA, USA) antibody, or goat anti-mouse IgM (γ-chain-specific; 1/1000, Jackson ImmunoResearch Laboratories, Inc, Westgrove, PA, USA) antibody prepared in PBS/0.05% Tween 20. Plates were washed as before and followed with the addition of 50 μL substrate (4-nitrophenylphosphate disodium salt hexahydrate in diethanolamine; MilliporeSigma, St. Louis, MO, USA). The optical density at 405 nm and 490 nm (as a reference) was measured using a BioTek 800TS microplate reader (BioTek, Winooski, VT, USA).

Values are represented as a ratio of of the observed optical density after 1840 s to the determined optical density at day 0. This value will be referred as *optical density ratio*. Values above 1 ratio are considered positive in the SARS-CoV-2 antibody ELISA.

Molecular dynamics simulations

MD simulations were performed on a GPU accelerated computer workstation using GROMACS Version 5.1.4. The device is equipped with a 40 Core central processing unit (CPU, Intel(R) Xeon(R) CPU E5-2630 v4 @ 2.20GHz), 130 GB random-access memory (RAM) and three graphic processing units (GPU, 2 × NVIDIA 1080 TDI + 1 × GeForce GT 730)[26]. A total of 4 simulation systems were created. First, a coarse grained model of a single S-protein was created using the CHARMM-GUI Martini Solution-builder (http://charmm-gui.org/)[50]. The S-protein model from[25] which bases on the RBD-down protein structure (PDB database: 6VXX) was used in all simulation. Model 1 (see[25] for naming convention) was used for the heptad repeat linker 2 (HR2), the transmembrane-domain (HR2-TM) and the CPD. The System was charge-neutralized by adding Na^+ and Cl^- counter-ions. A second model was created by first removing water from the simulation box and adding Triton-X 100 molecules to archive a concentration of 25 mM. The system was re-dissolved with MARTINI water and neutralizing ions were added.

Two membrane-S-protein complexes containing one SARS-CoV-2 S-protein, a RBC membrane mimic respectively were designed using the CHARMM-GUI membrane-builder (http://charmm-gui.org/)[50]. The bilayer composition was chosen to match the lipid concentrations of a RBC membrane as has been shown previously[26]. In one model, the protein's TMD was embedded into the membrane. For the second model, the CPD was placed in close proximity to the membrane mimic. Triton-X 100 at a concentration of 25 mM was added to both simulations. All models are available from the authors upon request. All models were energy-minimized using steepest descent and equilibrated for 5 ns in the NPT ensemble (constant pressure and temperature). A short range van der Waal cutoff of 1.1 nm and a potential-shift-verlet coulomb modifier were used and periodic boundary conditions were applied to all three dimensions. Neighbor lists were updated in intervals of 20 steps. The temperature was coupled through a v-rescale thermostat at a constant pressure of 1 bar using Parrinello-Rahman semi-isotropic weak coupling (τ=12 ps; compressibility β=$3{\cdot}10^{-4}$ bar^{-1}). All simulations were run for a total of 500 ns. The model containing a single S-protein in close proximity to the membrane mimic was first run for 500 ns with position constraints applied to the protein in all spacial direction. The constraints were removed and the system was simulated for additional 500 ns.

The GROMACS built-in function angle was used to calculate the tilt angle Θ indicated in Fig. 1 D.

ELV-protein co-sedimentation assay

The S-protein loading efficiency onto the Erythro-VLP was determined using UV–visible light spectroscopy using a Nanophotometer NP80 from IMPLEN. Erythro-VLP carrying Alexa-fluor 488 labeled S-protein were prepared as described above. A UV-vis spectra was measured and the the sample was incubated for 12 h with an excess of Amberlite XAD-2 (9003-70-7, Sigma-Aldrich). The samples were centrifuged for 2 h and a UV-vis spectrum was measured. Both spectra are graphed in Fig. S2. A peak at 488 nm was observed in both samples resulting from the stained proteins. The signal was observed to decrease by 40%. This decrease is assumed to be the result of sedimented liposomes and we consequently estimate a loading efficiency of ∼40%.

Determining the Triton-X 100 - erythrocyte liposome phase diagram

Red blood cell ghosts where first prepared according to the protocol described above. 10 samples, 1 ml each, containing ∼0.5 mg/ml of membrane material were prepared with Triton-X 100 at concentrations of 0.1, 1, 3, 5, 10, 15, 20, 25, 30, 35 mM. The size distribution of the liposomes and Triton-X 100 micelles were then determined using a Zetasizer Nano ZS from Malvern Panalytical. All measurements were performed at 25°C.

ACKNOWLEDGEMENTS

This research was funded by the Natural Sciences and Engineering Research Council of Canada (NSERC,

RGPIN-2021-03926), the Canada Foundation for Innovation (CFI) and the Ontario Ministry of Economic Development and Innovation. M.C.R. is the recipient of an Early Researcher Award of the Province of Ontario and a University Scholar of McMaster University. The funders had no role in study design, data collection and analysis, decision to publish, or preparation of the manuscript.

SUPPORTING INFORMATION

Supporting Information Available: Phase diagram of erythrocyte liposomes at varying Triton-X 100 concentrations, ELV-protein co-sedimentation assay, and BLI assay of erythrocyte liposomes.

REFERENCES

[1] Dong E, Du H, Gardner L. An interactive web-based dashboard to track COVID-19 in real time. The Lancet Infectious Diseases. 2020;20(5):533–534.

[2] Anfinrud P, Stadnytskyi V, Bax CE, Bax A. Visualizing speech-generated oral fluid droplets with laser light scattering. New England Journal of Medicine. 2020;.

[3] Somsen GA, van Rijn C, Kooij S, Bem RA, Bonn D. Small droplet aerosols in poorly ventilated spaces and SARS-CoV-2 transmission. The Lancet Respiratory Medicine. 2020;.

[4] Aiello F, Afflitto GG, Mancino R, Li JPO, Cesareo M, Giannini C, et al. Coronavirus disease 2019 (SARS-CoV-2) and colonization of ocular tissues and secretions: a systematic review. Eye. 2020; p. 1–6.

[5] Li W, Moore MJ, Vasilieva N, Sui J, Wong SK, Berne MA, et al. Angiotensin-converting enzyme 2 is a functional receptor for the SARS coronavirus. Nature. 2003;426(6965):450–454.

[6] Yeo C, Kaushal S, Yeo D. Enteric involvement of coronaviruses: is faecal–oral transmission of SARS-CoV-2 possible? The Lancet Gastroenterology & Hepatology. 2020;5(4):335–337.

[7] Walls AC, Park YJ, Tortorici MA, Wall A, McGuire AT, Veesler D. Structure, function, and antigenicity of the SARS-CoV-2 spike glycoprotein. Cell. 2020;181(2):281–292.

[8] Wu F, Zhao S, Yu B, Chen YM, Wang W, Song ZG, et al. A new coronavirus associated with human respiratory disease in China. Nature. 2020;579(7798):265–269.

[9] Wrapp D, Wang N, Corbett KS, Goldsmith JA, Hsieh CL, Abiona O, et al. Cryo-EM structure of the 2019-nCoV spike in the prefusion conformation. Science. 2020;367(6483):1260–1263.

[10] Masters PS. The molecular biology of coronaviruses. Advances in virus research. 2006;66:193–292.

[11] Cai Y, Zhang J, Xiao T, Peng H, Sterling SM, Walsh RM, et al. Distinct conformational states of SARS-CoV-2 spike protein. Science. 2020;369(6511):1586–1592.

[12] Du L, He Y, Zhou Y, Liu S, Zheng BJ, Jiang S. The spike protein of SARS-CoV—a target for vaccine and therapeutic development. Nature Reviews Microbiology. 2009;7(3):226–236.

[13] Le TT, Andreadakis Z, Kumar A, Roman RG, Tollefsen S, Saville M, et al. The COVID-19 vaccine development landscape. Nat Rev Drug Discov. 2020;19(5):305–306.

[14] Chung YH, Beiss V, Fiering SN, Steinmetz NF. COVID-19 vaccine frontrunners and their nanotechnology design. ACS Nano. 2020;14(10):12522–12537.

[15] Graham BS. Rapid COVID-19 vaccine development. Science. 2020;368(6494):945–946.

[16] Pardi N, Hogan MJ, Porter FW, Weissman D. mRNA vaccines—a new era in vaccinology. Nature Reviews Drug Discovery. 2018;17(4):261.

[17] Jackson LA, Anderson EJ, Rouphael NG, Roberts PC, Makhene M, Coler RN, et al. An mRNA Vaccine against SARS-CoV-2 — Preliminary Report. New England Journal of Medicine. 0;0(0):null. doi:10.1056/NEJMoa2022483.

[18] Baum J, Ward RH, Conway DJ. Natural selection on the erythrocyte surface. Molecular Biology and Evolution. 2002;19(3):223–229.

[19] Minasyan H. Phagocytosis and oxycytosis: two arms of human innate immunity. Immunologic Research. 2018;66(2):271–280.

[20] Ukidve A, Zhao Z, Fehnel A, Krishnan V, Pan DC, Gao Y, et al. Erythrocyte-driven immunization via biomimicry of their natural antigen-presenting function. Proceedings of the National Academy of Sciences. 2020;117(30):17727–17736.

[21] Himbert S, Alsop RJ, Rose M, Hertz L, Dhaliwal A, Moran-Mirabal JM, et al. The Molecular Structure of Human Red Blood Cell Membranes from Highly Oriented, Solid Supported Multi-Lamellar Membranes. Scientific Reports. 2017;7:39661.

[22] Garten M, Aimon S, Bassereau P, Toombes GE. Reconstitution of a transmembrane protein, the voltage-gated ion channel, KvAP, into giant unilamellar vesicles for microscopy and patch clamp studies. JoVE. 2015;(95):e52281.

[23] Dezi M, Di Cicco A, Bassereau P, Lévy D. Detergent-mediated incorporation of transmembrane proteins in giant unilamellar vesicles with controlled physiological contents. Proceedings of the National Academy of Sciences. 2013;110(18):7276–7281.

[24] Skar-Gislinge N, Johansen NT, Høiberg-Nielsen R, Arleth L. Comprehensive study of the self-assembly of phospholipid nanodiscs: what determines their shape and stoichiometry? Langmuir. 2018;34(42):12569–12582.

[25] Woo H, Park SJ, Choi YK, Park T, Tanveer M, Cao Y, et al. Developing a fully glycosylated full-length SARS-CoV-2 spike protein model in a viral membrane. The Journal of Physical Chemistry B. 2020;124(33):7128–7137.

[26] Himbert S, Blacker MJ, Kihm A, Pauli Q, Khondker A, Yang K, et al. Hybrid Erythrocyte Liposomes: Functionalized Red Blood Cell Membranes for Molecule Encapsulation. Advanced Biosystems. 2020;4(3):1900185.

[27] Cathcart K, Patel A, Dies H, Rheinstädter MC, Fradin C. Effect of cholesterol on the structure of a five-component mitochondria-like phospholipid membrane. Membranes. 2015;5(4):664–684.

[28] Verzijl D, Riedl T, Parren PWHI, Gerritsen AF. A novel label-free cell-based assay technology using biolayer interferometry. Biosensors and Bioelectronics. 2017;87:388 – 395.

[29] Müller-Esparza H, Osorio-Valeriano M, Steube N, Thanbichler M, Randau L. Bio-Layer Interferometry Analysis of the Target Binding Activity of CRISPR-Cas Effector Complexes. Frontiers in Molecular Biosciences. 2020;7:98.
[30] Wiesner S, Helfer E, Didry D, Ducouret G, Lafuma F, Carlier MF, et al. A biomimetic motility assay provides insight into the mechanism of actin-based motility. The Journal of Cell Biology. 2003;160(3):387–398.
[31] Pan DC, Myerson JW, Brenner JS, Patel PN, Anselmo AC, Mitragotri S, et al. Nanoparticle properties modulate their attachment and effect on carrier red blood cells. Scientific Reports. 2018;8(1):1–12.
[32] Brenner JS, Pan DC, Myerson JW, Marcos-Contreras OA, Villa CH, Patel P, et al. Red blood cell-hitchhiking boosts delivery of nanocarriers to chosen organs by orders of magnitude. Nature Communications. 2018;9(1):1–14.
[33] Kravtzoff R, Colombat P, Desbois I, Linassier C, Muh J, Philip T, et al. Tolerance evaluation of L-asparaginase loaded in red blood cells. European Journal of Clinical Pharmacology. 1996;51(3-4):221–225.
[34] Glassman PM, Villa CH, Ukidve A, Zhao Z, Smith P, Mitragotri S, et al. Vascular Drug Delivery Using Carrier Red Blood Cells: Focus on RBC Surface Loading and Pharmacokinetics. Pharmaceutics. 2020;12(5):440.
[35] Chiarantini L, Argnani R, Zucchini S, Stevanato L, Zabardi P, Grossi MP, et al. Red blood cells as delivery system for recombinant HSV-1 glycoprotein B: immunogenicity and protection in mice. Vaccine. 1997;15(3):276–280.
[36] Boberg A, Dominici S, Brave A, Hallermalm K, Hinkula J, Magnani M, et al. Immunization with HIV protease peptides linked to syngeneic erythrocytes. Infectious Agents and Cancer. 2007;2(1):1–4.
[37] Grimm AJ, Kontos S, Diaceri G, Quaglia-Thermes X, Hubbell JA. Memory of tolerance and induction of regulatory T cells by erythrocyte-targeted antigens. Scientific Reports. 2015;5:15907.
[38] Anderson HL, Brodsky IE, Mangalmurti NS. The evolving erythrocyte: red blood cells as modulators of innate immunity. The Journal of Immunology. 2018;201(5):1343–1351.
[39] Zaitsev S, Spitzer D, Murciano JC, Ding BS, Tliba S, Kowalska MA, et al. Sustained thromboprophylaxis mediated by an RBC-targeted pro-urokinase zymogen activated at the site of clot formation. Blood, The Journal of the American Society of Hematology. 2010;115(25):5241–5248.
[40] Zaitsev S, Kowalska MA, Neyman M, Carnemolla R, Tliba S, Ding BS, et al. Targeting recombinant thrombomodulin fusion protein to red blood cells provides multifaceted thromboprophylaxis. Blood, The Journal of the American Society of Hematology. 2012;119(20):4779–4785.
[41] Yang J, Wang W, Chen Z, Lu S, Yang F, Bi Z, et al. A vaccine targeting the RBD of the S protein of SARS-CoV-2 induces protective immunity. Nature. 2020;586(7830):572–577.
[42] Wang Q, Zhang Y, Wu L, Niu S, Song C, Zhang Z, et al. Structural and functional basis of SARS-CoV-2 entry by using human ACE2. Cell. 2020;181:894–904.
[43] He Y, Li R, Li H, Zhang S, Dai W, Wu Q, et al. Erythroliposomes: Integrated Hybrid Nanovesicles Composed of Erythrocyte Membranes and Artificial Lipid Membranes for Pore-Forming Toxin Clearance. ACS Nano. 2019;13(4):4148–4159. doi:10.1021/acsnano.8b08964.
[44] Krammer F. SARS-CoV-2 vaccines in development. Nature. 2020;586(7830):516–527.
[45] Petrovsky N. Comparative safety of vaccine adjuvants: a summary of current evidence and future needs. Drug Safety. 2015;38(11):1059–1074.
[46] Hu B, Ge X, Wang LF, Shi Z. Bat origin of human coronaviruses. Virology Journal. 2015;12(1):1–10.
[47] Veatch SL, Keller SL. Seeing spots: complex phase behavior in simple membranes. Biochimica et Biophysica Acta (BBA)-Molecular Cell Research. 2005;1746(3):172–185.
[48] Juhasz J, Sharom FJ, Davis JH. Quantitative characterization of coexisting phases in DOPC/DPPC/cholesterol mixtures: comparing confocal fluorescence microscopy and deuterium nuclear magnetic resonance. Biochimica et Biophysica Acta (BBA)-Biomembranes. 2009;1788(12):2541–2552.
[49] Huynh A, Arnold DM, Smith JW, Moore JC, Zhang A, Chagla Z, et al. Characteristics of anti-SARS-CoV-2 antibodies in recovered COVID-19 subjects. Viruses. 2021;13(4):697.
[50] Qi Y, Ingólfsson HI, Cheng X, Lee J, Marrink SJ, Im W. CHARMM-GUI martini maker for coarse-grained simulations with the martini force field. Journal of Chemical Theory and Computation. 2015;11(9):4486–4494.

SUPPORTING INFORMATION TO: ERYTHRO-VLPS: ANCHORING SARS-COV-2 SPIKE PROTEINS IN ERYTHROCYTE LIPOSOMES

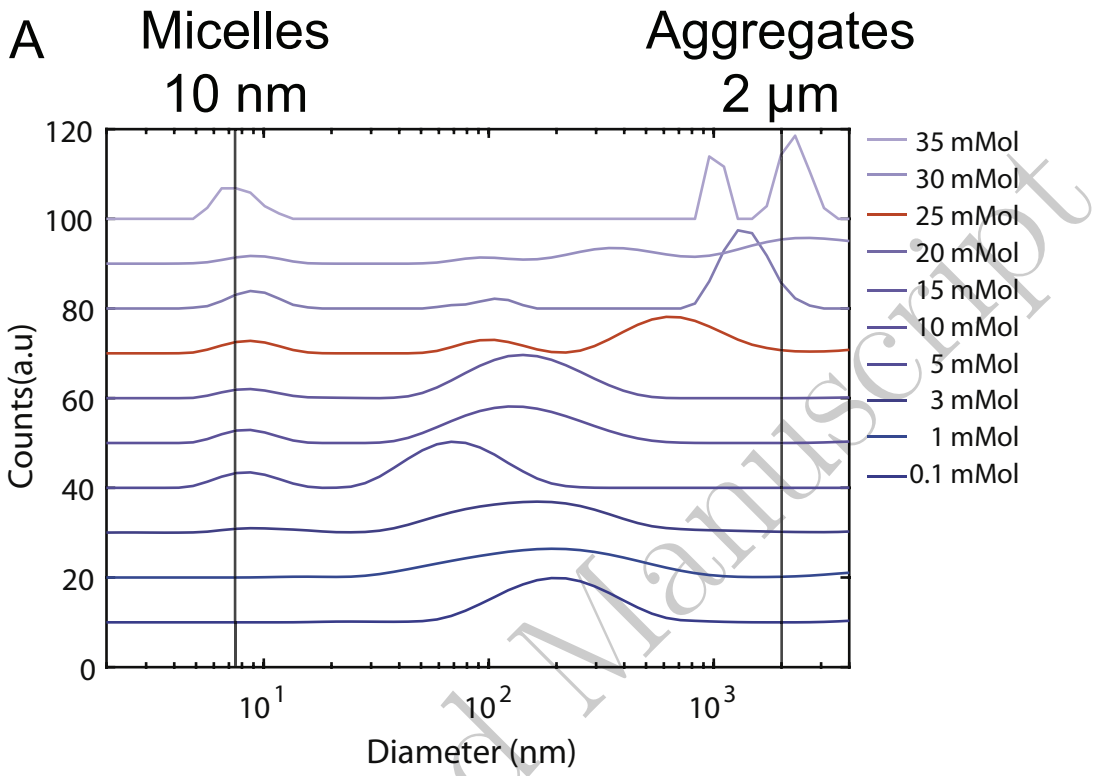

Supporting Information, Figure S1. DLS spectra of erythrocyte liposomes in aqueous solution and Triton-X 100 concentrations ranging from 0.1 mM to 35 mM. A single distribution 244.8±175.9 nm resulting from liposomes was observed at a Triton-X 100 concentration of 0.1 mM; below the critical micelle concentration (CMC = 0.25 mM). This Liposome signal co-exists with micelles with a diameter of 10 nm at concentrations from 3 mM to 20 mM. Concentrations higher than 20 mM eventually lead to an aggregation of the liposomes to form aggregates with a diameter of up to 2±0.3 μm.

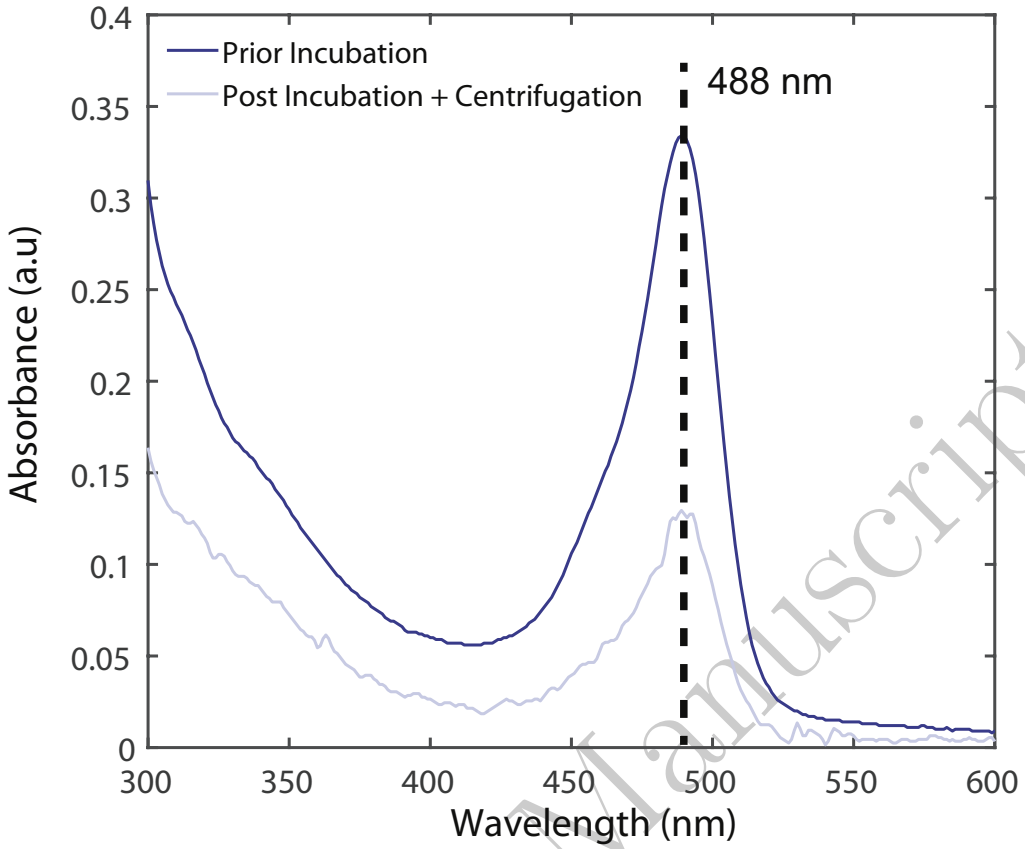

Supporting Information, Figure S2. UV-Visible spectra of Erythro-VLP carrying Alexa Fluor 488 maleimide tagged S-protein before and after incubation.

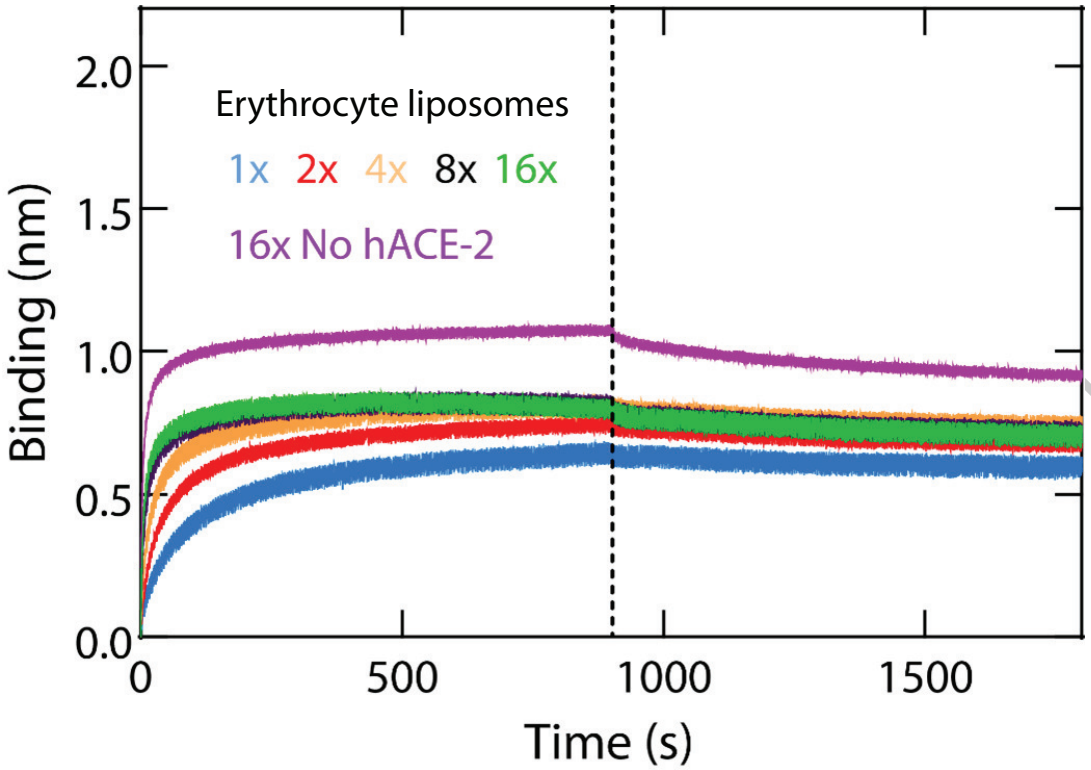

Supporting Information, Figure S3. Biolayer interferometry analysis of the binding of erythrocyte liposomes to the human ACE-2 receptor. Association and dissociation curves for the binding of various concentrations of erythrocyte liposomes to the human ACE-2 receptor is shown in accordance with the color coding in the figure inset. Control association and dissociation curves for erythrocyte liposomes in the absence of human ACE-2 immobilized onto the biosensor are shown in purple.

Chapter 8

Conclusion

The scientific achievements in this thesis divide in two parts; the analysis of the structure and mechanical properties of the RBCcms and the functionalization of this biological structure on a molecular level.

The first two publications demonstrate that the use of X-ray and Neutron scattering can provide unique insight into the molecular organization and mechanical properties of RBCcms. I measured bending moduli of order of 2 to 4 k_BT, relatively small compared to literature values for intact RBCs, and for most single component lipid bilayers. This demonstrates that RBCcms are highly flexible and deformable structures on the nanoscopic length scales. The extreme softness is likely a result of a large variety of lipids (see lipid composition in Chapter 2) in these biological membranes. When applied to stored RBCs, the developed methods reveal an increased fraction of liquid ordered membrane domains and an increased bending rigidity.

This is a good place to re-emphasize the limitations of the performed analysis. Both X-ray and neutron experiments require optimized sample preparation, which includes the isolation of the RBCcm from the cell. It is possible that this preparation may introduce artifacts. In addition, the interpretation of the scattering experiments is based on models that were developed for symmetric lipid bilayer. There are two caveats that need to be addressed.

First, the RBCcm is an asymmetric structure, which contradicts the centrosymmetry that is required for a 1-dimensional Fourier analysis. However, the sample preparation processes generally does not allow control of the membrane's orientation within the stack and we consequently measure an ensemble of different membrane orientations. Hence, it is plausible to assume an average symmetric membrane.

The second caveat concerns the observed fluctuations of RBCcms in XDS and

NSE experiments. The determination of static material properties from these fluctuations requires a good theoretical understanding of the membrane dynamics. The underlying model becomes especially critical in NSE experiments where it is required to decouple both the area compression modulus and the bending modulus. The agreement of the measured intermediate scattering function with the ZG-Theory and the performed MD simulations encourage the approximation of the observed fluctuations by lipid bilayer dynamics. However, potential influences from transmembrane proteins can not be ruled out. A coherent mathematical description that takes all aspects of the membrane's composition into account is currently missing but would be desirable to better understand the observed membrane dynamics.

A major innovation in this thesis is the synthesis of functionalized RBCcms. I have demonstrated that the membrane can be modified with synthetic lipid molecules to tune membrane thickness, order, and charge. Furthermore, I successfully anchored the SARS-CoV-2 S-Protein into the RBCcm to synthesize virus-like particles that eventually lead to seroconversion in mouse models.

RBC liposomes are *a priori* superior over synthetic pharmaceutical carriers as they provide an enhanced biocompatibility and an increased circulation time within the body. However, they often lack specificity. Functionalization of the RBCcm is thus critical in overcoming these limitations.

Of course, large disturbances of the endogenous structure can limit the biocompatibility of these engineered hybrid liposomes. Paper III is thus critical in understanding these limitations as we determined the solubility limits of synthetic lipid molecules in the RBCcm. It further sets the foundation for anchoring much larger structures such as the SARS-CoV-2 S-Protein into the RBCcm.

While the preparation of hybrid RBCcms was tested with a variety of different lipid species, the insertion of proteins was thus far solely investigated for the SARS-CoV-2 S-Protein. Proteins, such as ion channels, have been routinely embedded into synthetic liposomes using detergent mediated protocols [98] and it can thus be speculated that the developed protocol is also applicable for other protein structures. Potential other protein candidates are of course spike proteins from other viruses.

The functionalization of RBCcms should be evolved further as they provide a unique tool to deliver pharmaceuticals across the body. Importantly, they can provide direct access to pathways that are intrinsically related to the RBC's life cyle. For instance, RBCs can present antigens to the immune system when undergoing

phagocytosis in the liver and the spleen [2]. We speculate in Paper IV that erythro-VLPs are being processed in the same manner. This platform of engineered RBC-cms thus presents a potential vaccine candidate against the coronavirus disease (COVID-19) and can potentially also be applied to variants and other viruses in the future.

Appendix A

Common Lipid Molecules And Their Abbreviation

Abbreviation	Name	Tails (Length 1: Saturation 1 - Length 2: Saturation 2)
di13:0 PC	1,2-ditridecanoyl-sn-glycero-3-phosphocholine	13:0-13:0
DMPC	1,2-dimyristoyl-sn-glycero-3-phosphocholine	14:0-14:0
POPC	1-palmitoyl-2-oleoyl-glycero-3-phosphocholine	16:0-18:1
SOPC	1-stearoyl-2-oleoyl-sn-glycero-3-phosphocholine	18:0-18:1
DOPC	1,2-dioleoyl-sn-glycero-3-phosphocholine	18:1-18:1
POPS	1-palmitoyl-2-oleoyl-sn-glycero-3-phospho-L-serine	16:0-18:1
POPG	1-palmitoyl-2-oleoyl-sn-glycero-3-phospho-(1′-rac-glycerol)	16:0-18:1
di22:1 PC	1,2-dierucoyl-sn-glycero-3-phosphocholine	22:1-22:1

TABLE A.1: A summary of values reported for the bending rigidity κ in the literature

Appendix B

Copyright Information

B.1 Figure 2.2 B

The permission to republish Figure 2.2 B in this Thesis was obtained from *Rockefeller University Press* as detailed in the attached certificate.

Copyright Clearance Center Marketplace™

Rockefeller University Press - License Terms and Conditions

This is a License Agreement between Sebastian Himbert ("You") and Rockefeller University Press ("Publisher") provided by Copyright Clearance Center ("CCC"). The license consists of your order details, the terms and conditions provided by Rockefeller University Press, and the CCC terms and conditions.

All payments must be made in full to CCC.

Order Date	31-May-2021	**Type of Use**	Republish in a thesis/dissertation
Order license ID	1122824-1		
ISSN	0021-9525	**Publisher**	ROCKEFELLER UNIVERSITY PRESS
		Portion	Image/photo/illustration

LICENSED CONTENT

Publication Title	The Journal of cell biology	**Rightsholder**	Rockefeller University Press
Article Title	Visualization of the hexagonal lattice in the erythrocyte membrane skeleton.	**Publication Type**	Journal
		Start Page	527
Author/Editor	ROCKEFELLER INSTITUTE., AMERICAN SOCIETY FOR CELL BIOLOGY.	**End Page**	536
		Issue	3
		Volume	104
Date	01/01/1962		
Language	English		
Country	United States of America		

REQUEST DETAILS

Portion Type	Image/photo/illustration	**Distribution**	Worldwide
Number of images / photos / illustrations	1	**Translation**	Original language of publication
Format (select all that apply)	Print, Electronic	**Copies for the disabled?**	No
		Minor editing privileges?	No
Who will republish the content?	Academic institution	**Incidental promotional use?**	No
Duration of Use	Life of current edition	**Currency**	USD
Lifetime Unit Quantity	Up to 499		
Rights Requested	Main product		

NEW WORK DETAILS

Title	The Physics of Red Blood Cells	**Institution name**	Mcmaster University
Instructor name	Maikel C. Rheinstadter	**Expected presentation date**	2021-09-01

ADDITIONAL DETAILS

Order reference number	N/A	**The requesting person / organization to appear on the license**	Sebastian Himbert

REUSE CONTENT DETAILS

Title, description or numeric reference of the portion(s)	Figures 2 and 3	**Title of the article/chapter the portion is from**	Visualization of the hexagonal lattice in the erythrocyte membrane skeleton.
Editor of portion(s)	Liu, S C; Derick, L H; Palek, J	**Author of portion(s)**	Liu, S C; Derick, L H; Palek, J
Volume of serial or monograph	104	**Issue, if republishing an article from a serial**	3
Page or page range of portion	527-536	**Publication date of portion**	1987-03-01

CCC Republication Terms and Conditions

1. Description of Service; Defined Terms. This Republication License enables the User to obtain licenses for republication of one or more copyrighted works as described in detail on the relevant Order Confirmation (the "Work(s)"). Copyright Clearance Center, Inc. ("CCC") grants licenses through the Service on behalf of the rightsholder identified on the Order Confirmation (the "Rightsholder"). "Republication", as used herein, generally means the inclusion of a Work, in whole or in part, in a new work or works, also as described on the Order Confirmation. "User", as used herein, means the person or entity making such republication.

2. The terms set forth in the relevant Order Confirmation, and any terms set by the Rightsholder with respect to a particular Work, govern the terms of use of Works in connection with the Service. By using the Service, the person transacting for a republication license on behalf of the User represents and warrants that he/she/it (a) has been duly authorized by the User to accept, and hereby does accept, all such terms and conditions on behalf of User, and (b) shall inform User of all such terms and conditions. In the event such person is a "freelancer" or other third party independent of User and CCC, such party shall be deemed jointly a "User" for purposes of these terms and conditions. In any event, User shall be deemed to have accepted and agreed to all such terms and conditions if User republishes the Work in any fashion.

3. Scope of License; Limitations and Obligations.

    3.1. All Works and all rights therein, including copyright rights, remain the sole and exclusive property of the Rightsholder. The license created by the exchange of an Order Confirmation (and/or any invoice) and payment by User of the full amount set forth on that document includes only those rights expressly set forth in the Order Confirmation and in these terms and conditions, and conveys no other rights in the Work(s) to User. All rights not expressly granted are hereby reserved.

    3.2. General Payment Terms: You may pay by credit card or through an account with us payable at the end of the month. If you and we agree that you may establish a standing account with CCC, then the following terms apply: Remit Payment to: Copyright Clearance Center, 29118 Network Place, Chicago, IL 60673-1291. Payments Due: Invoices are payable upon their delivery to you (or upon our notice to you that they are available to you for downloading). After 30 days, outstanding amounts will be subject to a service charge of 1-1/2% per month or, if less, the maximum rate allowed by applicable law. Unless otherwise specifically set forth in the Order Confirmation or in a separate written agreement signed by CCC, invoices are due and payable on "net 30" terms. While User may exercise the rights licensed immediately upon issuance of the Order Confirmation, the license is automatically revoked and is null and void, as if it had never been

issued, if complete payment for the license is not received on a timely basis either from User directly or through a payment agent, such as a credit card company.

3.3. Unless otherwise provided in the Order Confirmation, any grant of rights to User (i) is "one-time" (including the editions and product family specified in the license), (ii) is non-exclusive and non-transferable and (iii) is subject to any and all limitations and restrictions (such as, but not limited to, limitations on duration of use or circulation) included in the Order Confirmation or invoice and/or in these terms and conditions. Upon completion of the licensed use, User shall either secure a new permission for further use of the Work(s) or immediately cease any new use of the Work(s) and shall render inaccessible (such as by deleting or by removing or severing links or other locators) any further copies of the Work (except for copies printed on paper in accordance with this license and still in User's stock at the end of such period).

3.4. In the event that the material for which a republication license is sought includes third party materials (such as photographs, illustrations, graphs, inserts and similar materials) which are identified in such material as having been used by permission, User is responsible for identifying, and seeking separate licenses (under this Service or otherwise) for, any of such third party materials; without a separate license, such third party materials may not be used.

3.5. Use of proper copyright notice for a Work is required as a condition of any license granted under the Service. Unless otherwise provided in the Order Confirmation, a proper copyright notice will read substantially as follows: "Republished with permission of [Rightsholder's name], from [Work's title, author, volume, edition number and year of copyright]; permission conveyed through Copyright Clearance Center, Inc. " Such notice must be provided in a reasonably legible font size and must be placed either immediately adjacent to the Work as used (for example, as part of a by-line or footnote but not as a separate electronic link) or in the place where substantially all other credits or notices for the new work containing the republished Work are located. Failure to include the required notice results in loss to the Rightsholder and CCC, and the User shall be liable to pay liquidated damages for each such failure equal to twice the use fee specified in the Order Confirmation, in addition to the use fee itself and any other fees and charges specified.

3.6. User may only make alterations to the Work if and as expressly set forth in the Order Confirmation. No Work may be used in any way that is defamatory, violates the rights of third parties (including such third parties' rights of copyright, privacy, publicity, or other tangible or intangible property), or is otherwise illegal, sexually explicit or obscene. In addition, User may not conjoin a Work with any other material that may result in damage to the reputation of the Rightsholder. User agrees to inform CCC if it becomes aware of any infringement of any rights in a Work and to cooperate with any reasonable request of CCC or the Rightsholder in connection therewith.

4. Indemnity. User hereby indemnifies and agrees to defend the Rightsholder and CCC, and their respective employees and directors, against all claims, liability, damages, costs and expenses, including legal fees and expenses, arising out of any use of a Work beyond the scope of the rights granted herein, or any use of a Work which has been altered in any unauthorized way by User, including claims of defamation or infringement of rights of copyright, publicity, privacy or other tangible or intangible property.

5. Limitation of Liability. UNDER NO CIRCUMSTANCES WILL CCC OR THE RIGHTSHOLDER BE LIABLE FOR ANY DIRECT, INDIRECT, CONSEQUENTIAL OR INCIDENTAL DAMAGES (INCLUDING WITHOUT LIMITATION DAMAGES FOR LOSS OF BUSINESS PROFITS OR INFORMATION, OR FOR BUSINESS INTERRUPTION) ARISING OUT OF THE USE OR INABILITY TO USE A WORK, EVEN IF ONE OF THEM HAS BEEN ADVISED OF THE POSSIBILITY OF SUCH DAMAGES. In any event, the total liability of the Rightsholder and CCC (including their respective employees and directors) shall not exceed the total amount actually paid by User for this license. User assumes full liability for the actions and omissions of its principals, employees, agents, affiliates, successors and assigns.

6. Limited Warranties. THE WORK(S) AND RIGHT(S) ARE PROVIDED "AS IS". CCC HAS THE RIGHT TO GRANT TO USER THE RIGHTS GRANTED IN THE ORDER CONFIRMATION DOCUMENT. CCC AND THE RIGHTSHOLDER DISCLAIM ALL OTHER WARRANTIES RELATING TO THE WORK(S) AND RIGHT(S), EITHER EXPRESS OR IMPLIED, INCLUDING

WITHOUT LIMITATION IMPLIED WARRANTIES OF MERCHANTABILITY OR FITNESS FOR A PARTICULAR PURPOSE. ADDITIONAL RIGHTS MAY BE REQUIRED TO USE ILLUSTRATIONS, GRAPHS, PHOTOGRAPHS, ABSTRACTS, INSERTS OR OTHER PORTIONS OF THE WORK (AS OPPOSED TO THE ENTIRE WORK) IN A MANNER CONTEMPLATED BY USER; USER UNDERSTANDS AND AGREES THAT NEITHER CCC NOR THE RIGHTSHOLDER MAY HAVE SUCH ADDITIONAL RIGHTS TO GRANT.

7. Effect of Breach. Any failure by User to pay any amount when due, or any use by User of a Work beyond the scope of the license set forth in the Order Confirmation and/or these terms and conditions, shall be a material breach of the license created by the Order Confirmation and these terms and conditions. Any breach not cured within 30 days of written notice thereof shall result in immediate termination of such license without further notice. Any unauthorized (but licensable) use of a Work that is terminated immediately upon notice thereof may be liquidated by payment of the Rightsholder's ordinary license price therefor; any unauthorized (and unlicensable) use that is not terminated immediately for any reason (including, for example, because materials containing the Work cannot reasonably be recalled) will be subject to all remedies available at law or in equity, but in no event to a payment of less than three times the Rightsholder's ordinary license price for the most closely analogous licensable use plus Rightsholder's and/or CCC's costs and expenses incurred in collecting such payment.

8. Miscellaneous.

    8.1. User acknowledges that CCC may, from time to time, make changes or additions to the Service or to these terms and conditions, and CCC reserves the right to send notice to the User by electronic mail or otherwise for the purposes of notifying User of such changes or additions; provided that any such changes or additions shall not apply to permissions already secured and paid for.

    8.2. Use of User-related information collected through the Service is governed by CCC's privacy policy, available online here:https://marketplace.copyright.com/rs-ui-web/mp/privacy-policy

    8.3. The licensing transaction described in the Order Confirmation is personal to User. Therefore, User may not assign or transfer to any other person (whether a natural person or an organization of any kind) the license created by the Order Confirmation and these terms and conditions or any rights granted hereunder; provided, however, that User may assign such license in its entirety on written notice to CCC in the event of a transfer of all or substantially all of User's rights in the new material which includes the Work(s) licensed under this Service.

    8.4. No amendment or waiver of any terms is binding unless set forth in writing and signed by the parties. The Rightsholder and CCC hereby object to any terms contained in any writing prepared by the User or its principals, employees, agents or affiliates and purporting to govern or otherwise relate to the licensing transaction described in the Order Confirmation, which terms are in any way inconsistent with any terms set forth in the Order Confirmation and/or in these terms and conditions or CCC's standard operating procedures, whether such writing is prepared prior to, simultaneously with or subsequent to the Order Confirmation, and whether such writing appears on a copy of the Order Confirmation or in a separate instrument.

    8.5. The licensing transaction described in the Order Confirmation document shall be governed by and construed under the law of the State of New York, USA, without regard to the principles thereof of conflicts of law. Any case, controversy, suit, action, or proceeding arising out of, in connection with, or related to such licensing transaction shall be brought, at CCC's sole discretion, in any federal or state court located in the County of New York, State of New York, USA, or in any federal or state court whose geographical jurisdiction covers the location of the Rightsholder set forth in the Order Confirmation. The parties expressly submit to the personal jurisdiction and venue of each such federal or state court.If you have any comments or questions about the Service or Copyright Clearance Center, please contact us at 978-750-8400 or send an e-mail to support@copyright.com.

v 1.1

B.2 Paper III

The permission to republish my article

S. Himbert, M. J. Blacker, A. Kihm, Q. Pauli, A. Khondker, K. Yang, S. Sinjari, M. Johnson, J. Juhasz, C. Wagner, H. D. H. Stover, M. C. Rheinstädter, Hybrid erythrocyte liposomes: functionalized red blood cell membranes for molecule encapsulation, Advanced Biosystems, 1900185.

in this Thesis was obtained from *John Wiley & Son* as detailed in the attached certificate.

Advanced Biosystems

Article Hybrid Erythrocyte Liposomes: Functionalized Red Blood Cell Membranes for Molecule Encapsulation.

GENERAL INFORMATION

Request ID	600043709	Request Date	31 May 2021
Request Status	Accepted	Price	0.00 USD Special Terms

ALL DETAILS

ISSN:	2366-7478	Publisher:	John Wiley & Sons
Type of Use:	Republish in a thesis/dissertation	Portion:	Chapter/article

LICENSED CONTENT

Publication Title	Advanced Biosystems	Rightsholder	John Wiley & Sons - Books
Article Title	Hybrid Erythrocyte Liposomes: Functio...	Publication Type	e-Journal
Date	01/01/2017	Issue	3
Country	United States of America	Volume	4

REQUEST DETAILS

Portion Type	Chapter/article	Rights Requested	Main product and any product related ...
Page range(s)	1-11	Distribution	Worldwide
Total number of pages	11	Translation	Original language of publication
Format (select all that apply)	Print, Electronic	Copies for the disabled?	No
Who will republish the content?	Academic institution	Minor editing privileges?	No
Duration of Use	Life of current edition	Incidental promotional use?	No
Lifetime Unit Quantity	Up to 499	Currency	USD

NEW WORK DETAILS

Title	Physics of Red Blood Cells	Institution name	McMaster University
Instructor name	Dr. Maikel C. Rheinstadter	Expected presentation date	2021-09-01

ADDITIONAL DETAILS

The requesting person / organization to appear on the license	Sebastian Himbert

REUSE CONTENT DETAILS

Title, description or numeric reference of the portion(s)	I would like to use the entire article	Title of the article/chapter the portion is from	Hybrid Erythrocyte Liposomes: Functio...
Editor of portion(s)	Rheinstädter, Maikel C; Stöver, Harald ...	Author of portion(s)	Rheinstädter, Maikel C; Stöver, Harald ...
Volume of serial or monograph	4	Publication date of portion	2020-03-01
Page or page range of portion	1-11		

COMMENTS

Add Comment / Attachment

31 May 2021 2:27:52 PM, by Sebastian Himbert

Dear Sir or Madam, I am the lead author on the publication entitled 'Hybrid Erythrocyte Liposomes: Functionalized Red Blood Cell Membranes for Molecule Encapsulation' (https://onlinelibrary.wiley.com/doi/full/10.1002/adbi.201900185) and I would like to utilize the article as material in my PhD thesis at McMa View More

Bibliography

1. Auth, T., Safran, S. & Gov, N. S. Fluctuations of coupled fluid and solid membranes with application to red blood cells. *Physical Review E* **76,** 051910 (2007).
2. Ukidve, A. *et al.* Erythrocyte-driven immunization via biomimicry of their natural antigen-presenting function. *Proceedings of the National Academy of Sciences* **117,** 17727–17736 (2020).
3. Müller, W. A. & Frings, S. *Tier-und Humanphysiologie: Eine Einführung* (Springer-Verlag, 2009).
4. Liu, S.-C., Derick, L. H. & Palek, J. Visualization of the hexagonal lattice in the erythrocyte membrane skeleton. *The Journal of Cell Biology* **104,** 527–536 (1987).
5. Popescu, G. *et al.* Optical measurement of cell membrane tension. *Physical Review Letters* **97,** 218101 (2006).
6. Singer, S. & Nicolson, G. The fluid mosaic model of the structure of cell membranes. *Science* **175,** 720–731 (1972).
7. Mohandas, N. & Gallagher, P. G. Red cell membrane: past, present, and future. *Blood* **112,** 3939–3948 (2008).
8. Himbert, S. *et al.* The Molecular Structure of Human Red Blood Cell Membranes from Highly Oriented, Solid Supported Multi-Lamellar Membranes. *Scientific Reports* **7,** 39661 (2017).
9. Van Meer, G., Voelker, D. R. & Feigenson, G. W. Membrane lipids: where they are and how they behave. *Nature Reviews Molecular Cell Biology* **9,** 112–124 (2008).
10. Falck, E., Patra, M., Karttunen, M., Hyvönen, M. T. & Vattulainen, I. Lessons of slicing membranes: interplay of packing, free area, and lateral diffusion in phospholipid/cholesterol bilayers. *Biophysical Journal* **87,** 1076–1091 (2004).
11. Dodge, J. T. & Phillips, G. B. Composition of phospholipids and of phospholipid fatty acids and aldehydes in human red cells. *Journal of Lipid Research* **8,** 667–675 (1967).

12. Almizraq, R., Tchir, J. D., Holovati, J. L. & Acker, J. P. Storage of red blood cells affects membrane composition, microvesiculation, and in vitro quality. *Transfusion* **53,** 2258–2267 (2013).
13. Nickels, J. D. *et al.* Lipid rafts: buffers of cell membrane physical properties. *The Journal of Physical Chemistry B* **123,** 2050–2056 (2019).
14. Kučerka, N. *et al.* Cholesterol in Bilayers With PUFA Chains: Doping With DMPC or POPC Results in Sterol Reorientation and Membrane-Domain Formation. *Biochemistry* **49,** 7485 (2010).
15. Rheinstädter, M. C. & Mouritsen, O. G. Small-scale structures in fluid cholesterol-lipid bilayers. *Curr. Opin. Colloid Interface Sci.* **18,** 440–447 (2013).
16. Ciana, A., Achilli, C. & Minetti, G. Membrane rafts of the human red blood cell. *Molecular Membrane Biology* **31,** 47–57 (2014).
17. Mikhalyov, I. & Samsonov, A. Lipid raft detecting in membranes of live erythrocytes. *Biochimica et Biophysica Acta (BBA)-Biomembranes* **1808,** 1930–1939 (2011).
18. Pan, J., Mills, T. T., Tristram-Nagle, S. & Nagle, J. F. Cholesterol Perturbs Lipid Bilayers Nonuniversally. *Physical Review Letters* **100,** 198103 (2008).
19. Simons, K. & Gerl, M. J. Revitalizing membrane rafts: new tools and insights. *Nat Rev Mol Cell Biol* **11,** 688–699 (2010).
20. Ingólfsson, H. I. *et al.* Lipid organization of the plasma membrane. *Journal of the American Chemical Society* **136,** 14554–14559 (2014).
21. Himbert, S. *et al.* Hybrid Erythrocyte Liposomes: Functionalized Red Blood Cell Membranes for Molecule Encapsulation. *Advanced Biosystems* **4,** 1900185 (2020).
22. Kirchhausen, T. Bending membranes. *Nature Cell Biology* **14,** 906–908 (2012).
23. McMahon, H. T. & Gallop, J. L. Membrane curvature and mechanisms of dynamic cell membrane remodelling. *Nature* **438,** 590–596 (2005).
24. McMahon, H. T. & Boucrot, E. Membrane curvature at a glance. *Journal of Cell Science* **128,** 1065–1070 (2015).
25. Phillips, R., Kondev, J., Theriot, J., Garcia, H. G. & Orme, N. *Physical Biology of the Cell* (Garland Science, 2012).
26. Evans, E. A. Bending elastic modulus of red blood cell membrane derived from buckling instability in micropipet aspiration tests. *Biophysical Journal* **43,** 27–30 (1983).

27. Evans, E. A., Waugh, R & Melnik, L. Elastic area compressibility modulus of red cell membrane. *Biophysical Journal* **16,** 585–595 (1976).

28. Evans, J., Gratzer, W., Mohandas, N., Parker, K. & Sleep, J. Fluctuations of the red blood cell membrane: relation to mechanical properties and lack of ATP dependence. *Biophysical Journal* **94,** 4134–4144 (2008).

29. Evans, E & Rawicz, W. Entropy-driven tension and bending elasticity in condensed-fluid membranes. *Physical Review Letters* **64,** 2094 (1990).

30. Dimova, R. Recent developments in the field of bending rigidity measurements on membranes. *Advances in Colloid and Interface Science* **208,** 225–234 (2014).

31. Li, Y., Lipowsky, R. & Dimova, R. Membrane nanotubes induced by aqueous phase separation and stabilized by spontaneous curvature. *Proceedings of the National Academy of Sciences* **108,** 4731–4736 (2011).

32. Campillo, C. *et al.* Unexpected membrane dynamics unveiled by membrane nanotube extrusion. *Biophysical Journal* **104,** 1248–1256 (2013).

33. Brochard, F & Lennon, J. Frequency spectrum of the flicker phenomenon in erythrocytes. *Journal de Physique* **36,** 1035–1047 (1975).

34. Zilker, A, Ziegler, M & Sackmann, E. Spectral analysis of erythrocyte flickering in the 0.3–4-μm^{-1} regime by microinterferometry combined with fast image processing. *Physical Review A* **46,** 7998 (1992).

35. Strey, H, Peterson, M & Sackmann, E. Measurement of erythrocyte membrane elasticity by flicker eigenmode decomposition. *Biophysical Journal* **69,** 478–488 (1995).

36. Park, Y. *et al.* Measurement of red blood cell mechanics during morphological changes. *Proceedings of the National Academy of Sciences* **107,** 6731–6736 (2010).

37. Kučerka, N., Tristram-Nagle, S. & Nagle, J. F. Structure of fully hydrated fluid phase lipid bilayers with monounsaturated chains. *The Journal of Membrane Biology* **208,** 193–202 (2006).

38. Tristram-Nagle, S. *et al.* Structure and water permeability of fully hydrated diphytanoylPC. *Chemistry and Physics of Lipids* **163,** 630–637 (2010).

39. Rheinstädter, M. C., Häussler, W. & Salditt, T. Dispersion Relation of Lipid Membrane Shape fluctuations by Neutron Spin-Echo Spectrometry. *Physical Review Letters* **97,** 048103 (2006).

40. Nagao, M., Kelley, E. G., Ashkar, R., Bradbury, R. & Butler, P. D. Probing elastic and viscous properties of phospholipid bilayers using neutron spin echo spectroscopy. *The Journal of Physical Chemistry Letters* **8,** 4679–4684 (2017).

41. Kelley, E. G., Butler, P. D., Ashkar, R., Bradbury, R. & Nagao, M. Scaling relationships for the elastic moduli and viscosity of mixed lipid membranes. *Proceedings of the National Academy of Sciences* **117,** 23365–23373 (2020).

42. Pabst, G., Kučerka, N., Nieh, M.-P., Rheinstädter, M. & Katsaras, J. Applications of neutron and X-ray scattering to the study of biologically relevant model membranes. *Chemistry and Physics of Lipids* **163,** 460 –479 (2010).

43. Bouvrais, H. in *Advances in Planar Lipid Bilayers and Liposomes* 1–75 (Elsevier, 2012).

44. Nagle, J. F., Jablin, M. S., Tristram-Nagle, S. & Akabori, K. What are the true values of the bending modulus of simple lipid bilayers? *Chemistry and Physics of Lipids* **185,** 3–10 (2015).

45. Rappolt, M. & Pabst, G. *Flexibility and structure of fluid bilayer interfaces* 2008.

46. Rawicz, W, Olbrich, K. C., McIntosh, T, Needham, D & Evans, E. Effect of chain length and unsaturation on elasticity of lipid bilayers. *Biophysical Journal* **79,** 328–339 (2000).

47. Pan, J., Mills, T. T., Tristram-Nagle, S. & Nagle, J. F. Cholesterol perturbs lipid bilayers nonuniversally. *Physical Review Letters* **100,** 198103 (2008).

48. Pan, J., Tristram-Nagle, S. & Nagle, J. F. Effect of cholesterol on structural and mechanical properties of membranes depends on lipid chain saturation. *Physical Review E* **80,** 021931 (2009).

49. Rawicz, W, Smith, B., McIntosh, T., Simon, S. & Evans, E. Elasticity, strength, and water permeability of bilayers that contain raft microdomain-forming lipids. *Biophysical Journal* **94,** 4725–4736 (2008).

50. Gracia, R. S., Bezlyepkina, N., Knorr, R. L., Lipowsky, R. & Dimova, R. Effect of cholesterol on the rigidity of saturated and unsaturated membranes: fluctuation and electrodeformation analysis of giant vesicles. *Soft Matter* **6,** 1472–1482 (2010).

51. Sorre, B. *et al.* Curvature-driven lipid sorting needs proximity to a demixing point and is aided by proteins. *Proceedings of the National Academy of Sciences* **106,** 5622–5626 (2009).

52. Tian, A., Capraro, B. R., Esposito, C. & Baumgart, T. Bending stiffness depends on curvature of ternary lipid mixture tubular membranes. *Biophysical Journal* **97,** 1636–1646 (2009).

53. Brüning, B, Stehle, R, Falus, P & Farago, B. Influence of charge density on bilayer bending rigidity in lipid vesicles: A combined dynamic light scattering and neutron spin-echo study. *The European Physical Journal E* **36,** 1–8 (2013).

54. Liu, Y. & Nagle, J. F. Diffuse scattering provides material parameters and electron density profiles of biomembranes. *Physical Review E* **69,** 040901 (2004).

55. Kelley, E. G., Butler, P. D., Ashkar, R., Bradbury, R. & Nagao, M. Scaling relationships for the elastic moduli and viscosity of mixed lipid membranes. *Proceedings of the National Academy of Sciences* **117,** 23365–23373 (2020).

56. Peralta, M. F., Smith, H., Moody, D., Tristram-Nagle, S. & Carrer, D. C. Effect of anti-leishmania drugs on the structural and elastic properties of ultradeformable lipid membranes. *The Journal of Physical Chemistry B* **122,** 7332–7339 (2018).

57. Kumagai, A. *et al.* Elastic behavior of model membranes with antimicrobial peptides depends on lipid specificity and D-enantiomers. *Soft Matter* **15,** 1860–1868 (2019).

58. Danielczok, J. G. *et al.* Red blood cell passage of small capillaries is associated with transient Ca2+-mediated adaptations. *Frontiers in Physiology* **8,** 979 (2017).

59. Betz, T., Lenz, M., Joanny, J.-F. & Sykes, C. ATP-dependent mechanics of red blood cells. *Proceedings of the National Academy of Sciences* **106,** 15320–15325 (2009).

60. Himbert, S. *et al.* The Bending of Red Blood Cell Membranes. *In Preparation* (2021).

61. Himbert, S. *et al.* Blood bank storage of red blood cells alters RBC membrane order and bending rigidity. *Submitted* (2021).

62. Liu, Y. *New Method To Obtain Structure Of Biomembranes Using Diffuse X-Ray Scattering: Application To Fluid Phase Dopc Lipid Bilayers* Advisor Dr. John Nagle. PhD thesis (Carnegie Mellon University, Pittsburg, Pennsylvania, USA, Sept. 2003).

63. Als-Nielsen, J. & McMorrow, D. *Elements of Modern X-Ray Physics* ISBN: 0-471-498572 (John Wiley & Sons, Ltd, New York, 2001).

64. Lei, N., Safinya, C. & Bruinsma, R. Discrete harmonic model for stacked membranes: theory and experiment. *Journal de Physique II* **5,** 1155–1163 (1995).

65. Lyatskaya, Y., Liu, Y., Tristram-Nagle, S., Katsaras, J. & Nagle, J. F. Method for obtaining structure and interactions from oriented lipid bilayers. *Physical Review E* **63,** 011907 (2000).

66. Nagle, J. F. & Tristram-Nagle, S. Structure of lipid bilayers. *Biochim. Biophys. Acta* **1469,** 159–195 (2000).

67. Barrett, M. A. *et al.* Interaction of Aspirin (Acetylsalicylic Acid) with Lipid Membranes. *PLoS ONE* **7,** e34357 (Apr. 2012).

68. Himbert, S. *et al.* Anesthetics significantly increase the amount of intramembrane water in lipid membranes. *Soft Matter* **16,** 9674–9682 (2020).

69. Rheinstädter, M. C., Häussler, W. & Salditt, T. Dispersion Relation of Lipid Membrane Shape fluctuations by Neutron Spin-Echo Spectrometry. *Physical Review Letters* **97,** 048103 (2006).

70. Tristram-Nagle, S. & Nagle, J. F. HIV-1 fusion peptide decreases bending energy and promotes curved fusion intermediates. *Biophysical Journal* **93,** 2048–2055 (2007).

71. Kučerka, N. *et al.* Structure of Fully Hydrated Fluid Phase DMPC and DLPC Lipid Bilayers Using X-Ray Scattering from Oriented Multilamellar Arrays and from Unilamellar Vesicles. *Biophysical Journal* **88,** 2626–2637 (2005).

72. Rosov, N., Rathgeber, S. & Monkenbusch, M. Neutron spin echo spectroscopy at the NIST Center for Neutron Research (2000).

73. Willis, B. T. M. & Carlile, C. J. *Experimental Neutron Scattering* (Oxford University Press, 2017).

74. Mezei, F. Neutron spin echo: A new concept in polarized thermal neutron techniques. *Zeitschrift für Physik A Hadrons and Nuclei* **255,** 146–160 (1972).

75. Zilman, A. & Granek, R. Undulations and Dynamic Structure Factor of Membranes. *Physical Review Letters* **77,** 4788–4791 (1996).

76. Alsop, R. *PHARMACEUTICALS AND PHYSICS: DRUGS AND MEMBRANES* Advisor Dr. Maikel Rheinstädter. PhD thesis (McMaster University, Hamilton, Ontario, Canada, Sept. 2017).

77. Mell, M. *et al.* Bending stiffness of biological membranes: What can be measured by neutron spin echo? *The European Physical Journal E* **36,** 75 (2013).

78. Nagle, J. F. On measuring the bending modulus of lipid bilayers with cholesterol. *ArXiv Preprint arXiv:2108.04653* (2021).

79. Yi, Z., Nagao, M. & Bossev, D. P. Bending elasticity of saturated and monounsaturated phospholipid membranes studied by the neutron spin echo technique. *Journal of Physics: Condensed Matter* **21,** 155104 (2009).

80. Takeda, T. *et al.* Neutron spin–echo investigations of membrane undulations in complex fluids involving amphiphiles. *Journal of Physics and Chemistry of Solids* **60,** 1375–1377 (1999).

81. Watson, M. C., Penev, E. S., Welch, P. M. & Brown, F. L. Thermal fluctuations in shape, thickness, and molecular orientation in lipid bilayers. *The Journal of Chemical Physics* **135,** 244701 (2011).

82. Safran, S. *Statistical thermodynamics of surfaces, interfaces, and membranes* (CRC Press, 2018).

83. Nagle, J. F. *et al.* A needless but interesting controversy. *Proceedings of the National Academy of Sciences* **118.** ISSN: 0027-8424. eprint: https://www.pnas.org/content/118/20/e2025011118.full.pdf. https://www.pnas.org/content/118/20/e2025011118 (2021).

84. Pan, J., Tristram-Nagle, S. & Nagle, J. F. Effect of cholesterol on structural and mechanical properties of membranes depends on lipid chain saturation. *Physical Review E* **80,** 021931 (2009).

85. Huang, J. & MacKerell Jr, A. D. CHARMM36 all-atom additive protein force field: Validation based on comparison to NMR data. *Journal of Computational Chemistry* **34,** 2135–2145 (2013).

86. Bider, R.-C. *et al.* Stabilization of lipid membranes through partitioning of the blood bag plasticizer di-2-ethylhexyl phthalate (DEHP). *Langmuir* **36,** 11899–11907 (2020).

87. Brandt, E. G. *Molecular dynamics simulations of fluid lipid membranes* PhD thesis (KTH Royal Institute of Technology, 2011).

88. Marrink, S. J., Risselada, H. J., Yefimov, S., Tieleman, D. P. & De Vries, A. H. The MARTINI force field: coarse grained model for biomolecular simulations. *The Journal of Physical Chemistry B* **111,** 7812–7824 (2007).

89. Himbert, S. *et al.* Erythro-VLPs: Embedding SARS-CoV-2 spike proteins in red blood cell based proteoliposomes leads to pronounced antibody response in mouse models. *Submitted.*

90. Dodge, J. T., Mitchell, C. & Hanahan, D. J. The preparation and chemical characteristics of hemoglobin-free ghosts of human erythrocytes. *Archives of Biochemistry and Biophysics* **100,** 119–130 (1963).

91. D'Amici, G. M. *et al.* Red blood cell storage in SAGM and AS3: a comparison through the membrane two-dimensional electrophoresis proteome. *Blood Transfusion* **10,** s46 (2012).

92. NVIDIA. *CUDA, release: 10.2.89* 2021. https://docs.nvidia.com/cuda/cuda-c-programming-guide/index.html#features-and-technical-specifications.

93. Gough, B. *GNU scientific library reference manual* (Network Theory Ltd., 2009).

94. Rosov, N., Rathgeber, S. & Monkenbusch, M. in *ACS Symposium Series* 103–116 (American Chemical Society, July 1999). https://doi.org/10.1021/bk-2000-0739.ch007.

95. Azuah, R. *et al.* DAVE: A comprehensive software suite for the reduction, visualization, and analysis of low energy neutron spectroscopic data. *Journal of Research of the National Institute of Standards and Technology* **114,** 341 (2009).

96. Jo, S., Kim, T., Iyer, V. G. & Im, W. CHARMM-GUI: a web-based graphical user interface for CHARMM. *Journal of Computational Chemistry* **29,** 1859–1865 (2008).

97. Qi, Y. *et al.* CHARMM-GUI martini maker for coarse-grained simulations with the martini force field. *Journal of Chemical Theory and Computation* **11,** 4486–4494 (2015).

98. Garten, M., Aimon, S., Bassereau, P. & Toombes, G. E. Reconstitution of a transmembrane protein, the voltage-gated ion channel, KvAP, into giant unilamellar vesicles for microscopy and patch clamp studies. *JoVE (Journal of Visualized Experiments),* e52281 (2015).